Surface states
in the topological material
HgTe

Dissertation zur Erlangung des naturwissenschaftlichen
Doktorgrades der Julius-Maximilians-Universität Würzburg

vorgelegt von

David Mahler

aus Würzburg

Würzburg, 2021

CONTENTS

ACRONYMS

2DEG two dimensional electron gas.

3D-TI three dimensional topological insulator.

AMR anisotropic magneto-resistance.

ARPES angle-resolved photoemission spectroscopy.

DFT density functional theory.

DOS density of states.

FFT fast Fourier transformation.

HH heavy hole.

LH light hole.

LL Landau level.

MBE molecular beam epitaxy.

MR magneto-resistance.

PHE planar Hall effect.

QH quantum Hall.

QHE quantum Hall effect.

SdH Shubnikov-de Haas.

TI topological insulator.

TSS topological surface state.

VPS Volkov-Pankratov state.

WAL weak anti-localization.

I

INTRODUCTION

1

MOTIVATION

The goal of physics is understanding and describing the world around us with the help of preferably simple models. The macroscopic world surrounding us and its intuitively accessible phenomena, as the movement of cars or the ball in soccer games, is well described by classical mechanics governed by Newton's laws. The validity of such a classical theory has been challenged by the observations of quantized energies, as in the Frank and Hertz experiment in the spectrum of a mercury gas lamp. This observation is seen as the first experimental evidence for the existence of quantized energy levels. The physics of such quantized systems, usually represented by small particles, smaller than $\lesssim 10^{-8}$ m, can be described with the help of the Schrödinger equation. It turns out, that the Schrödinger equation can also be used to describe properties, such as the conductivity of materials, in arbitrary shapes and sizes which vary over orders of magnitudes. The study and use of such rigid materials is the field of solid-state physics, which constitutes a workhorse for technological advance. The development of smaller and smaller and more potent devices could in foreseeable future reach the border of the possible in this framework.

One possible way to avoid such limitations is the inclusion of concepts and theories developed in other disciplines. Namely, the adaptation of the concept of topology originally concerned with the classification of geometric objects, which lead to the discovery of new classes of materials, hence called topological materials [1]. The first predicted and experimentally realized topological materials have been topological insulators [2–8]. These insulators host massless surface states at the interface to trivial insulators. An adequate description of such massless states can be adopted from particle physics, which routinely deals with particles with vanishingly small rest mass. Since such particles possess high kinetic energies they have to be described in the framework of the relativity theory. The Schrödinger equation has been extended by Dirac correspondingly to describe such relativistic quantum particles [9]. The resulting equation is named after its discoverer Dirac equation. The limit of zero mass, nowadays used to describe the properties of topological surface states, has been proposed by Weyl and is thus called Weyl equation [10]. While the Dirac equation describes relativistic electrons, no particles have been found in nature that obeys the Weyl equation. Three-dimensional quasi-particle representations of both, the Weyl and the Dirac equation, can be found in gapless solid-state systems. These systems are called Weyl and Dirac semi-metals and depict another new class of topological materials [11]. The vast interest in these topological semi-metals started with the prediction

1

of exotic surface states with a non-closed Fermi surface accordingly dubbed Fermi-arcs in Ref. [12]. These novel states are not only of interest for basic research but also of importance for potential applications. One much sought-after path for technological advancement is the development of quantum computers [13]. Alternatively to the momentarily most advanced realization of a quantum computer based on superconducting qubits, also different possible realizations of topological qubits exist. These are either based on topological superconductivity (realizable by induced superconductivity in topological surface states [14]) or in so-called chiral qubits based on the chiral anomaly observed in topological semi-metals [15].

These ambitious far-distant applications contrast the poor understanding of topological materials. A comprehensive and deep understanding of the components and thus the topological materials is inevitable for the successful development of these applications. This work expands the understanding and possibilities for manipulation of the topological materials based on the investigation of HgTe. Conveniently, HgTe can be prepared in a three dimensional topological insulator (3D-TI) phase with topological surface states as well as in a three-dimensional Dirac semi-metal phase. The first part of this work describes the identification and manipulation of topological surface states, which represent one building block for topological superconductivity. Additionally, Volkov-Pankratov states [16, 17] are found, which are induced by applied electric fields and need to be accounted for in actual devices. The second part investigates the novel field of topological semi-metals. The transport signature, called chiral anomaly, due to the apparent anomaly in the bulk band structure is investigated. The search for the predicted peculiar disjoint surface states, called Fermi-arcs, reveals the existence of topological surface states also in inversion induced Dirac semi-metals. HgTe is chosen since it represents a well-established and controllable model system. The insights gained for HgTe are relevant for all topological insulator and inversion induced Dirac semi-metals and have important implications for topological materials in general.

2

THE VERSATILE TOPOLOGICAL MATERIAL HGTE

To build actual devices or even investigate more complex physical phenomena, as the above-mentioned topological superconductivity or the chiral anomaly, first, a suitable material has to be found and its properties well understood. In this Chapter, HgTe is presented as a perfect candidate. The introduction is split into two parts: A few theoretical considerations on the HgTe material system are discussed before existing experimental results are reviewed. HgTe is a semi-metal with a quadratic band touching point. It can be transformed into an insulator and a Dirac semi-metal by strain engineering. A trivial insulator phase is accessible via the addition of Cd. In HgTe/$Cd_x Hg_{1-x}$Te heterostructures is the formation of specific interface states predicted. The concept of topology is introduced. Topology identifies the gap-less linear surface state as a general consequence of topological non-trivial systems such as HgTe. The existing experiments evolve around tensilely strained HgTe. Its band structure is discussed based on angle-resolved photoemission spectroscopy (ARPES) measurements and calculations performed with density functional theory (DFT) as well as $k \cdot p$. The established fabrication process HgTe samples for transport experiments via high-quality molecular beam epitaxy (MBE) growth and optical lithography is reviewed. The topological surface state (TSS) have been verified by magneto-transport experiments via the observation of quantum Hall effect (QHE) and have been interpreted based on the Dirac screening model. Still, a few open questions exist and are shortly summarized. These open questions together with the experimental results on tensile strained HgTe represent the starting point for the research and results presented in the remainder of this work.

2.1. Bulk band structure of HgTe

HgTe is chosen because of two reasons. HgTe is a well-established material system that can be fabricated in high quality and HgTe possesses an adjustable band structure. The band structure of unmodified HgTe is introduced as semi-metal with quadratic band touching based on its lattice structure. This Section introduces possibilities to adjust the band structure and describes the consequences of the experimentally used material. Strain can be used to alter the symmetry of the lattice and thus the band structure. An insulator and semi-metal phase with linear dispersion can be accessed. Surface/interface states form since the experimental samples are effectively HgTe/$Cd_x Hg_{1-x}$Te heterostructures.

2.1.1. The semi-metal HgTe

HgTe crystallizes in a cubic close-packed crystal lattice with a two-atom basis called zinc blende lattice. The symmetry of such a lattice sets important constraints and conditions for the material properties, which are expressed in their band structure. A zincblende lattice is a face-centered cubic lattice with a two-atom basis along $(\frac{1}{4},\frac{1}{4},\frac{1}{4})$ like a diamond lattice [1], but with two different atoms occupying the two positions of the basis. Alternatively, one could picture the zinc blende lattice as two face-centered cubic lattices (one for Hg and Te each) offset by $(\frac{1}{4},\frac{1}{4},\frac{1}{4})$ to each other. For HgTe these two atoms are Hg and Te and the corresponding lattice is shown in Fig. 2.1a).
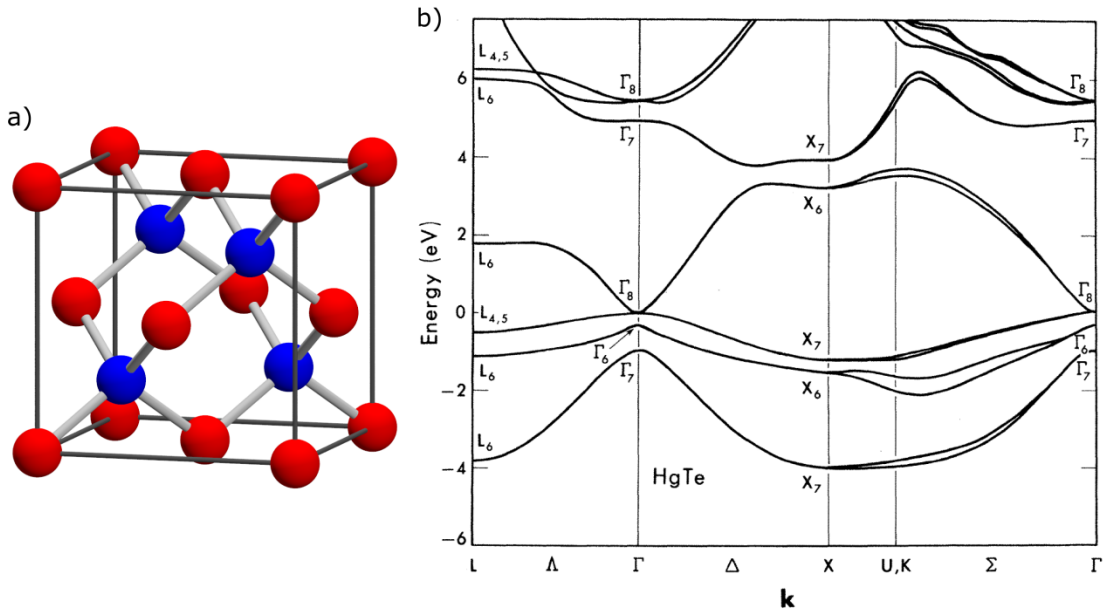
Figure 2.1: The crystal structure of HgTe in its zinc blende crystal structure is shown in a) with the Hg and Te atoms highlighted in red and blue, respectively. The resulting band structure of HgTe is shown along various directions in the Brillouin zone in b), as determined by pseudopotential calculations. b) is reprinted from D. J. Chadi *et al.*, Reflectivities and electronic band structures of CdTe and HgTe, PRB **5**, 3058 (1972) [18]. Copyright 1972 by The American Physical Society.

---

[1]The diamond lattice is inversion symmetric with the point group O_h.

To simplify the deduction of information such crystal lattices are assigned to space and point groups based on their symmetries. For HgTe the space group is the symmorphic group $T_d^2 \equiv F\bar{4}3m$ based on the inversion asymmetric point group $T_d \equiv \bar{4}3m$. Since the inversion symmetry breaking is relatively small, its influence on the band structure is minor. The point group is thus often treated as O_h [19]. The character of the irreducible representations of the respective point group can be determined at specific k values and is used to name the respective bands accordingly. For example, the relevant bands in HgTe close to the Fermi Energy are located around the Γ point ($k = 0$) and according to the respective irreducible representations are called Γ_6, Γ_8 and Γ_7, as discussed in Ref. [20]. The different symmetries of these bands can be traced back to the orbital character. The Γ_6 band is composed of the Hg S-like band, while the Γ_8 and Γ_7 bands are constituted of the Te P-like band, as explicitly written down in Sec. 4.2. The band structure of HgTe as determined by empirical pseudopotential calculations in Ref. [18, 21] is shown for high symmetry directions of the Brillouin zone in Fig. 2.1b). The low energy bands which determine the transport properties are indeed located at the Γ point. These are the Γ_8-bands and the Γ_6-band. The so-called split-off Γ_7 band lies $0.94\,\mathrm{eV}$ below the Fermi energy and is thus irrelevant for the transport properties. The low energy part of the band structure of HgTe can be well described by the Kane model [22]. The Kane model can be written as six band model only including the Γ_6 and Γ_8 bands or an eight-band model, which also considers the Γ_7 band, depending on the relevance of band structure details. This is also true for many other semi-conductors as GaAs, InSb, and CdTe. It is noteworthy, that the Luttinger model [23] with an appropriate parameterization can be sufficient as well [24]. These models are discussed in more detail in Sec. 8.4. Due to the spin-orbit coupling in HgTe the orbital character is described by the total angular momentum quantum number $j = |l \pm s|$, where l is the angular quantum number and s the spin, together with its projection $m_j \leq j$. The Γ_6 band is two times degenerate with $j = \frac{1}{2}$ and $m_j = \pm\frac{1}{2}$ and traditionally called electron (E) band. The Γ_8 band is four times degenerate with $j = \frac{3}{2}$. The Γ_8 bands with $m_j = \frac{3}{2}$ are called heavy hole (HH) bands and $m_j = \frac{1}{2}$ light hole (LH) bands. This nomenclature is traditional and motivated by the band structure of GaAs and CdTe. In these materials, the order of bands corresponds to the expectation from the atomic limit. Namely, the $j = \frac{1}{2}$ band lies above the Fermi energy with an electron-like dispersion, while the $j = \frac{3}{2}$ lie below the Fermi energy with a hole-like dispersion. The m_j quantum number distinguishes the two different effective masses of the hole like $j = \frac{3}{2}$ bands. The split of Γ_7 band with $j = \frac{1}{2}$ and $m_j = \pm\frac{1}{2}$ is typically neglected for the discussion of the low energy dispersion. The calculations presented in this work nevertheless account for the Γ_7 band to facilitate the best possible quantitative agreement. HgTe has two bands (the two Γ_8 bands) that touch at the Fermi energy and is thus a semi-metal, as shown in Fig. 2.1b). Sticking to the traditional definition of the bandgap in semiconductors (between the Γ_6 and Γ_8 bands), the bandgap is defined as $\Delta E_{\Gamma_6-\Gamma_8} = -0.3\,\mathrm{eV}$ making HgTe a quadratic semi-metal with an inverted band ordering indicated by the negative bandgap. It should be noted that in HgTe the relativistic correction due to the heavy mass of Hg is responsible for the resulting band inversion compared to the topological trivial order in CdTe.

2.1.2. THREE PHASES OF HGTE - ACCESSIBLE BY STRAIN

While HgTe as a semi-metal with quadratic dispersion, constitutes an interesting phase in itself, as discussed in Sec. 7.5.4, this Section addresses the versatility of HgTe due to the possibility of altering the bulk band structure by strain. The low energy band structure relevant for transport is given by the Γ_8 bands. The Γ_8 bands are degenerate at the high symmetry point Γ of the Brillouin zone and disperse quadratically for finite k. This touching of the Γ_8 bands at $k = 0$ (the Γ point) is protected by the cubic crystal symmetry of the zinc blende crystal structure and thus stabilizes the semi-metal phase with quadratic dispersion, which is depicted in Fig. 2.2b). Altering this quadratic band touching requires a reduction of the symmetry of the crystal. The cubic crystal symmetry can be reduced to a tetragonal symmetry by elongating the crystal along one direction. Experimentally, the bi-axial strain is realized via growth on an appropriate substrate. The stiffness of the crystal transfers this bidirectional strain into unidirectional strain in the third crystal direction. For small strains, this effect follows Hooks's law, see Ref. [8, 25, 26].
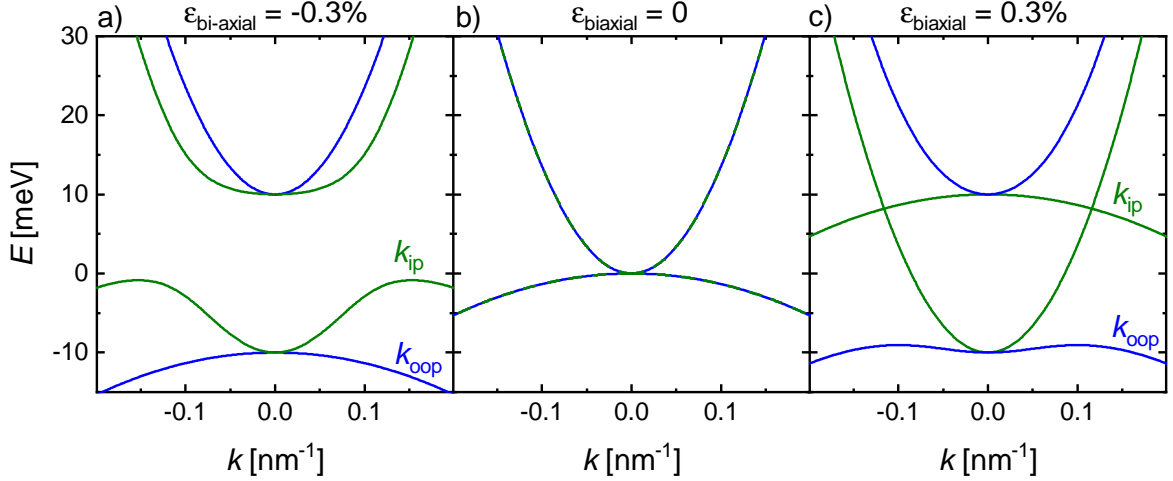
Figure 2.2: Shown is the energy dispersion of bulk HgTe for different biaxial strains, namely a) tensile strain, b) strain-free and c) compressive strain, for k_{ip} (green) along the strain direction and k_{oop} (blue) perpendicular to it.

The influence of uniaxial strain onto the shape of the two low-energy bands $(\Gamma_8)^2$ is discussed in Ref. [27] based on the low energy band structure model for Ge, which also has a direct bandgap at the Γ point with two degenerate points with the same underlying symmetry, as introduced by Ref. [28]. The crystal is thereby assumed to be a simple cubic satisfying inversion symmetry. The energy dispersion $E(\boldsymbol{k})$ is given by

$$E(\boldsymbol{k}) = A\boldsymbol{k}^2 \pm \left[B^2 \boldsymbol{k}^4 - C^2 \left(k_x^2 k_y^2 + k_y^2 k_z^2 + k_z^2 k_y^2 \right) \right]^{1/2}, \tag{2.1}$$

where k_z is along the uniaxial strain direction, while k_x and k_y are perpendicular and equivalent due to the cubic symmtery in this model. The effective band mass parameters for HgTe are $A = 611\,\mathrm{meVnm^2}$, $B = 745\,\mathrm{meVnm^2}$, and $C = 571\,\mathrm{meVnm^2}$ as taken from Ref. [25]. The band dispersion of this reduced model reproduces the one obtained by the eight-band Kane model discussed in Sec. 8.4.

---

[2]For the sake of simplicity and readability we will always refer to the bands by the Γ notation introduced in Section 2.1, although some of the models presented possess slightly different symmetries.

Tensile biaxial (compressive uniaxial) [3] strain lifts the degeneracy at the Γ point by opening a bandgap between the two Γ_8 bands forming an insulator phase. If the Γ_6 band would be included, the inverted band ordering would identify this phase as a three-dimensional topological insulator, as discussed in Sec. 8.4. As shown in Fig. 2.2a) the LH Γ_8 band forms the conduction band which disperses quadratically with some flattening for small k for the dispersion inside the sample plane (along k_{ip}). The valence band is formed by the HH Γ_8 band, which starts with an electron-like dispersion with a comparably small effective mass m_{eff}, up to a local maximum at finite k and proceeding with a hole-like dispersion with a comparably high m_{eff}. This shape of the valence band is often called camelback. This phase is addressed in more detail in Part II.

Compressive biaxial (tensile uniaxial) strain shifts the HH band towards higher energies and the LH band towards lower energies preserving their quadratic dispersion around the Γ point but causing the two bands to cross at finite k (see Fig. 2.2c)). This crossing is linear and protected by the remaining symmetry of the crystal. Since at the touching point these two bands disperse linearly, their dispersion can be described by the mass-less Dirac equation, hence the modern name Dirac semi-metal [11]. The semi-metal phase is addressed in more depth in Part III.

2.1.3. HETEROSTRUCTURES OF HGTE/CD$_x$HG$_{1-x}$TE
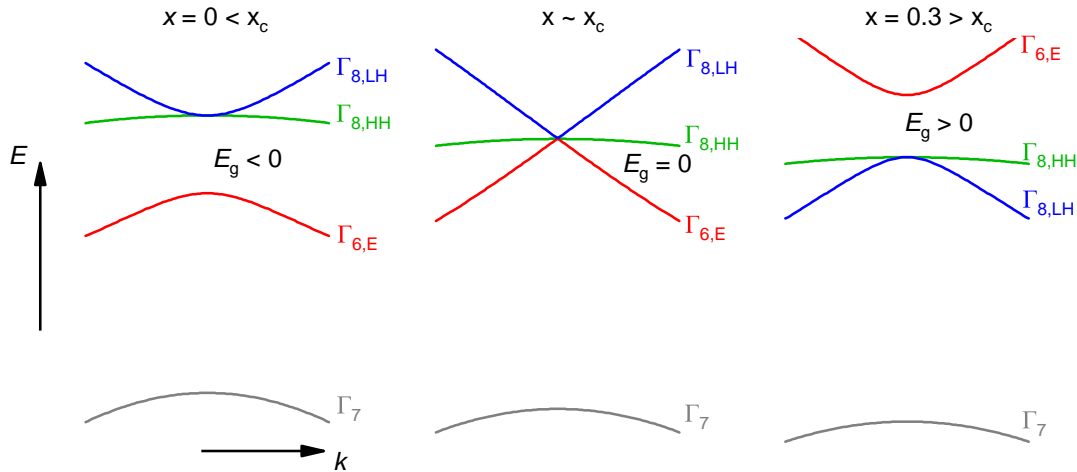
Figure 2.3: Shown is the energy spectrum of Cd$_x$Hg$_{1-x}$Te around the Γ point for different Cd concentrations x determined using the program "kdotpy" [29] with $x_c \sim 0.17$.

The experimentally investigated HgTe samples are surrounded by protective Cd$_{0.7}$Hg$_{0.3}$Te layers. The dependence of the band structure on the Cd content x is reviewed to understand the properties of the interfaces. As a starting point, the band structure of HgTe is taken, as already introduced in Sec. 2.1. The band structure of HgTe is conceptually equivalent to the one shown on the left of Fig. 2.3 for Cd$_x$Hg$_{1-x}$Te with a Cd concentration x smaller than the critical content x_c ($x < x_c$). The admixed Cd with the relative content x only renormalizes the size of the bandgap $\Delta E_{\Gamma_6 - \Gamma_8}$ but preserves the band ordering of the Γ_6 band relative to the Γ_8 bands. The bandgap $\Delta E_{\Gamma_6 - \Gamma_8}$ of Hg$_{1-x}$Cd$_x$Te varies from $-0.3\,\mathrm{eV}$ for HgTe to $1.6\,\mathrm{eV}$ for CdTe approximately linearly with the relative Cd content x [30]. On

---

[3]As long as not otherwise indicated in this work the strain direction refers to the biaxial direction.

the right of Fig. 2.3 the band structure of $Cd_xHg_{1-x}Te$ with $x > x_c$ consequently represents the band structure of CdTe with the accordingly renormalized bandgap. This order of the bands with the Γ_6 band above the Γ_8 bands represents the expected band ordering from the atomic limit. Connecting the two different insulator phases with different band ordering, a semi-metal phase with no bandgap must exist and can experimentally be realized by fine-tuning the Cd content x to the critical concentration x_c. The respective theoretically expected band structure for $x = x_c$ is shown in the middle of Fig. 2.3. The value for the critical concentration is typically assumed to be $x_c \sim 0.16$ [30] ($x_c \sim 0.17$ [31]). This value depends on a variety of parameters like temperature, strain, and confinement [32]. This semi-metal phase with linear dispersing bands and a flat band is called in literature massless Kane fermion/semi-metal [31] and experimentally examined by Ref. [32].
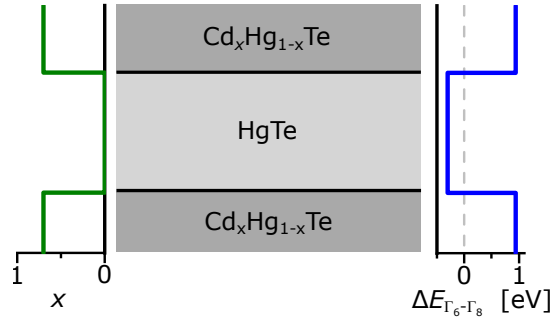
Figure 2.4: Shown is a semi-finite slab of HgTe surrounded by $Hg_{1-x}Cd_xTe$ together with the local distribution of the relative Cd content x (left) and the bandgap $\Delta E_{\Gamma_6-\Gamma_8}$ (right).

The interface between HgTe and $Cd_{0.7}Hg_{0.3}Te$ resembles a very sharp Cd content transition from $x = 0$ to $x = 0.7$ across the critical thickness $x = x_c$. The semi-finite layer stack is shown in Fig. 2.4. On the left, the variation of the relative Cd content x along the finite direction z is shown. The resulting characteristic band gap $E_g = \Delta E_{\Gamma_6-\Gamma_8}$ is shown on the right of Fig. 2.4 determined by

$$\Delta E_{\Gamma_6-\Gamma_8}(x) = -0.302 + 1.93x - 0.810x^2 + 0.832x^3 \tag{2.2}$$

for the temperature $T = 0\,K$ [30]. Since the sign of $\Delta E_{\Gamma_6-\Gamma_8}$ changes at the interface the formation of a local gap-less state is required. Intuitively one expects this state to be similar to the linearly dispersing gap-less state formed in $Hg_{1-x_c}Cd_{x_c}Te$, as shown in the middle of Fig. 2.3. B. A. Volkov and O. A. Pankratov describe a similar interface with a four-band model using the Dirac equation and making the bandgap dependent on the growth direction z in Ref. [16] [4]. This means the seemingly uninvolved flat HH Γ_8 band is ignored for this description. The HH band only alters the details of the dispersion of the surface state due to hybridization but does not change the qualitative behavior [33]. The model yields linear dispersing non-degenerate states at the interface for sharp interfaces together with additional massive surface states for smooth interfaces, as shown in Fig. 2.5. Since these states satisfy the Weyl equation, they are called Weyl states in their publication. In more recent literature such states are usually called Dirac surface states or Dirac cones and are discussed in more detail in Chapter III. The states are dubbed massless Volkov-Pankratov states after the names of the authors who predicted such states [34].

---

[4]The model is originally motivated by the band structure of $Pb_{1-x}Sn_xTe$.
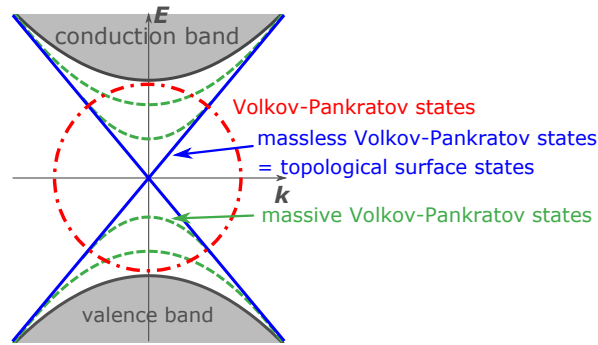
Figure 2.5: Shown are the expected interface states for an interface with smooth Cd content transition from HgTe to $Cd_{0.7}Hg_{0.3}$Te according to Ref. [16]. The nomenclature of Ref. [34] is used.

2.2. TOPOLOGY IN SOLID STATE SYSTEMS

More recently it has been recognized, that the formation of these surface states is a consequence of topology. Traditionally materials in solid-state physics are classified using their band structure and position of the Fermi energy E_F into metals, semi-metals, and insulators [5]. For metals, the Fermi energy lies deep inside a band and for insulators inside the bandgap. A semi-metal is characterized by a Fermi energy close to the band edge and overlapping bands at this energy. This classification has been found to be incomplete, and the mathematical concept of topology [6] is used to classify materials via a topological invariant. The classification via topology first found its entrance to solid-state physics to explain the stability of the QHE, the occurrence of superconductivity and superfluidity in thin layers, and the description of spin chains, leading to the Nobel Prize in 2016 for D. J. Thouless, F. D. M. Haldane and J. M. Kosterlitz [35]. Topology has subsequently been used to classify insulators in 2007 by L. Fu and C. L. Kane in Ref. [5]. $Bi_{1-x}Sb_x$ has been reported as the first experimental realization based on the observation of the topological surface states with ARPES in 2008 in Ref. [6], and soon after the Bi and Sb chalcogenides in Ref. [36]. The first verification of topological surface states using magneto-transport measurements has been reported in Ref. [8] for tensilely strained HgTe.

The classification via topology sorts materials into one class of insulators, whose band structure can be continuously transformed into each other without closing their bandgap. Members of the class of topological trivial insulators possess the band ordering as expected from their atomic limits. The strong topological insulator phase is distinguished from the topological trivial insulator phase via the topological invariant ν_0, which is a $\mathbb{Z}_2$ invariant. Topological non-trivial insulators are identified by $\nu_0 = 1$, while topological trivial insulators yield $\nu_0 = 0$. In this work, only the strong topological insulator phase is considered, even though there are a variety of other interesting topological phases. At the boundary of a topological insulator and a topological trivial insulator the above (see Sec. 2.1.3) introduced argument of the continuity of bands requires the formation of gap-less surface states. These topological surface states disperse linearly and possess a helical spin texture with the spin direction locked to the momentum. A more rigorous description of topology in solid-state systems is given in a variety of textbooks as Ref. [17, 37] and review papers

---

[5]Here Half-metals are taken as metals and semiconductors as insulators.
[6]Two objects are equivalent (belong to the same group) if they can be transformed into each other by a Homeomorphism (a continuous deformation).

as Ref. [38, 39]. An experimentally motivated description can be found in Ref. [40]. The same classification has recently been extended to gapless systems as Weyl semi-metals with their respective topological surface states, called Fermi-arcs [12]. Another class of topological semi-metals is the Dirac semi-metal, which is the degenerate counterpart of the Weyl semi-metal [11]. Topology generalizes the interface/surface states of HgCdTe/HgTe heterostructures to a variety of materials. Examples are the Bi and Sb chalcogenides, Dirac semi-metals as Cd_3As_2, Na_3Bi, and compressively strained HgTe.

2.3. STATE OF THE ART: TENSILELY STRAINED HGTE

This section establishes the starting point for this work by reviewing the research on the three-dimensional insulator phase of tensilely strained HgTe. The Section starts non-chronological with the observation of the band structure including the topological surface states via ARPES experiments. The measured band structure is compared to results obtained using DFT and $k \cdot p$ calculations. The MBE growth of HgTe samples is reviewed, including the established further processing via lithography. The verification of the TSS with magneto-transport experiments via the observation of the QHE is described. The results have been interpreted based on the so-called Dirac screening model. The Section closes with a summary of open research questions.

2.3.1. TOPOLOGICAL SURFACE STATES IN TENSILELY STRAINED HGTE

The described theoretical expectations of peculiar topological surface states are in this Section compared to the band structure of actual tensilely strained HgTe samples. ARPES measurements enable direct experimental access to the band structure. Ref. [8] presents ARPES data for a sample with a (100) surface grown by MBE. The (100) direction is also the growth direction for the samples investigated by magneto-transport measurements in this work. The result is shown in Fig. 2.6a). In Fig. 2.6b) the ARPES data from Ref. [41] on cleaved samples with a (110) surface is depicted. At first glance, both ARPES measurements look similar. The Fermi-energy, which is indicated as a dashed line, lies at the valence band etch. A quadratically and linear dispersing band is visible in both measurements. The quadratically dispersing band is identified as the bulk valence band and is indicated as BB [7] in Fig. 2.6a). The linear dispersing band is highlighted with dashed orange lines and indicated as SSB[8]. It is identified as a surface state by its non-existing k_z dispersion. In Fig. 2.6b) for $E < -0.5\,\text{eV}$ an other linear dispersing band with high intensity can be seen. Its intensity vanishes for small k. This band is identified as the second valence band. An additional third quadratically dispersing valence band at $E \sim -1\,\text{eV}$ is visible. The constant energy measurements are shown in d) reveal a fourfold symmetric dispersion in the measured plane, consistent with the cubic symmetry of the lattice.

The experimentally identified bulk and surface states are compared to the DFT calculation results shown in Fig. 2.6c) [42]. The first valence band in the DFT calculation shows a quadratic dispersion consistent with the ARPES measurements. For small k a flattening with potentially local extrema can be surmised. In agreement with the ARPES results, a surface state is found. It is identified by its spectral weight on the surface, which is used as the color code. Surface states appear red and bulk states blue. The surface state is lo-

---

[7]BB represents the bulk band.
[8]SSB represents surface state band.

calized inside the first valence and disperses linearly towards the second valence band. In the DFT band structure the second valence band appears to disperse linearly consistent with the ARPES results. It should be mentioned that the distinction between a linear and a quadratic dispersion with a small band mass is difficult. At $E \sim 0.7\,$eV the third valence band can be seen. It appears thus for slightly higher energy than in the ARPES measurements. The band structure obtained by ARPES is well reproduced by the DFT calculation.

These band structures are now compared to the widely used eight-band Kane model [22] described in Sec. 4.2. The bulk band structure of an infinite 0.3% tensilely strained HgTe layer in the Kane model is shown in Fig. 2.6e). The $k \cdot p$ calculations are performed with the program "kdotpy" [29] which uses the material parameters of Ref. [43]. The energetic positions of the bulk bands match reasonably well. To compare the character of the surface state, the band structure is also calculated for a finite 70 nm thick HgTe slab sandwiched by $Cd_{0.7}Hg_{0.3}Te$ layers as boundary conditions. The resulting band structure is shown in Fig. 2.6f). The first valence band, the $\Gamma_{8,HH}$-band also disperses quadratically for big k, but shows a deviation from the quadratic behavior for small $|k| < 0.2\,$nm, which is not resolvable in the ARPES measurements. A surface state dispersing inside the valence $\Gamma_{8,HH}$-band is found, which is consistent with the results obtained by ARPES and DFT. This surface state is the topological surface state induced by the inversion between the light-hole conduction $\Gamma_{8,LH}$-band and the Γ_6-band. The surface state coexists with the $\Gamma_{8,HH}$ band. While comparing the results obtained with ARPES and DFT with the $k \cdot p$ model, its limited k-range has to be kept in mind. The $k \cdot p$ model only allows the calculation of a small fraction of the k-range covered by the ARPES and DFT in Fig. 2.6. The k-range accessible with $k \cdot p$ calculations is nevertheless sufficient to describe the density range accessed by the magneto-transport experiments performed in this work. This k-range can also be translated into an energy range using a crude estimate. Taking the value of the maximum accessible charge carrier densities $n_{max} < 2 \times 10^{12}\,cm^{-2}$ and assuming double degenerate states, yields a maximum k of $k_{max} < 0.35\,nm^{-1}$ by using $k = \sqrt{2\pi n}$. The double degeneracy thereby stems either from the existence of two surfaces, one at the top and the other at the bottom, or the degeneracy of the first valence subband. Taking the band structure as shown in Fig. 2.6f) and assuming only the occupation of the surface state and the highest valence sub-band, this k_{max} translates into an energy window relevant for our transport experiments of $-20\,meV \lesssim E \lesssim 100\,meV$ as shown in Fig. 2.6g).

2
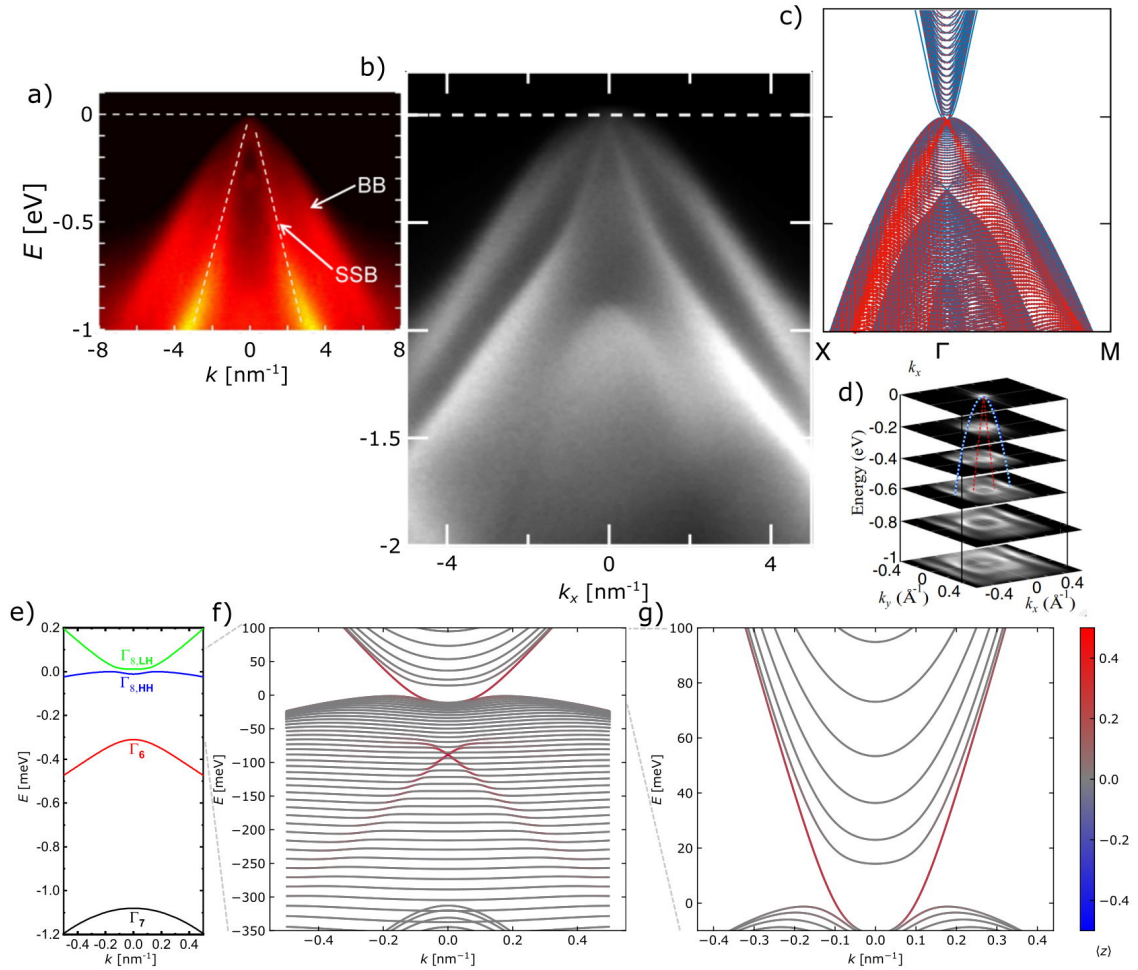
Figure 2.6: a) shows the ARPES measurement of the (001) surface of a relaxed 1 μm thick HgTe sample. The raw ARPES data of the (110) surface of HgTe is shown along k_x ($\Gamma - K$) in b). Constant energy maps measured by ARPES of the $k_x - k_y$-plane are shown in d). c) Band structure calculation by DFT of 60 nm thick 0.3 % strained HgTe film with the surface atom character proportional to the size of the red circles. Eight-band $k \cdot p$ calculation of HgTe as infinite layer e) and finite 70 nm slab with sandwiching $Cd_{0.7}Hg_{0.3}Te$ layers as the boundary condition in f) and g) with a reduced energy range indicating the maximum available energy range for transport experiments. The z-expectation value is color-coded via the use of a small electric field to split the degeneracy of the top and bottom sides. Calculated with the program "kdotpy" [29]. a) reprinted from C. Brüne *et al.*, Quantum Hall Effect from the Topological Surface States of Strained Bulk HgTe, PRL **106**, 126803 (2011) [8]. Copyright 2011 by The American Physical Society. b) and d) reprinted from C. Liu *et al.*, Tunable spin helical Dirac quasiparticles on the surface of three-dimensional HgTe, PRB **92**, 115436 (2015). Copyright 2015 by The American Physical Society. c) is taken from [42].

2.3.2. Established fabrication process for HgTe devices

As growth method MBE is chosen because of the achievable high layer quality and the possibility to realize the necessary strain to obtain the three-dimensional topological insulator phases of HgTe, as described in Sec. 2.1.2. The MBE growth process is simplified the evaporation of the different material components, onto a substrate in an ultra-high vacuum chamber. This way the hetero-structure of choice is produced. The actual procedure of the MBE growth is of course much more sophisticated and details can be found in Ref. [25]. Here we will limit ourselves to the functionality of the resulting heterostructure as schematically shown in Fig. 2.7a). The HgTe layer is grown on a substrate with appropriate lattice constant to create the desired strain of $\epsilon = (a_{HgTe} - a_{sub})/a_{HgTe}$ with a_{HgTe} and a_{sub} being the lattice constant of HgTe and the substrate of choice. The 3D-TI phase requires bi-axial tensile strain, which is realized by growth on commercially available CdTe substrates [8, 44]. The HgTe layer is sandwiched in between protective $Cd_{0.7}Hg_{0.3}Te$ layers. The layer underneath the HgTe layer is called buffer layer and ranges from $5-100\,nm$ thickness. The upper protective layer is dubbed capping layer and is typically $5-15\,nm$ thick. The layer total layer thickness is thereby limited to ensure fully strained growth to $\sim 155\,nm$ of HgTe, where the $Cd_{0.7}Hg_{0.3}Te$ due to their smaller lattice constant contribute less than their actual thickness [44].
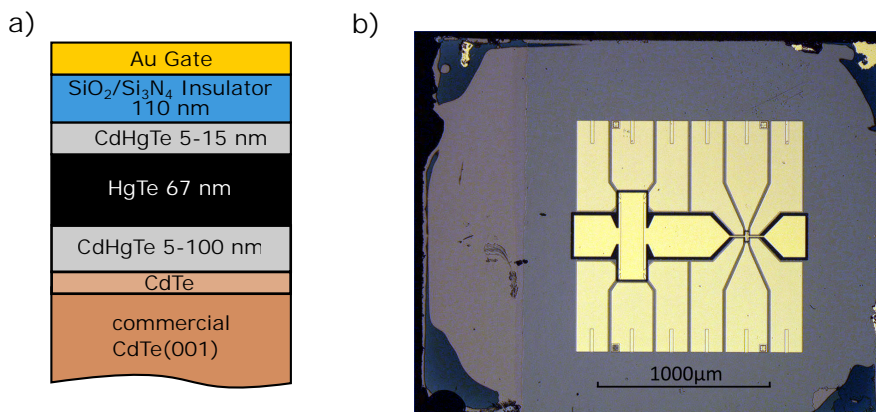
Figure 2.7: In a) the total MBE grown and lithographed layer stack is sketched. The MBE grown layers on top of the commercial CdTe substrate are a CdTe layer followed by a $Cd_{0.7}Hg_{0.3}Te$ buffer layer, the HgTe layer, and a capping $Cd_{0.7}Hg_{0.3}Te$ layer. These layers are covered with a SiO_2/Si_3N_4 insulator deposited by plasma-enhanced chemical vapor deposition and an Au layer applied by electron beam evaporation. In b) the optical photograph of the structure consisting of $600\,\mu m \times 200\,\mu m$ and a $30\,\mu m \times 10\,\mu m$ Hall-bar is shown. The mesa can be seen underneath the black SiO_2/Si_3N_4 covered by the yellow Au gate and the Au/Ge contacts covering the current leads and voltage probes.

To perform magneto-transport measurements the hetero-structure is shaped into a $600\,\mu m \times 200\,\mu m$ Hall-bar. A Hall-bar consists of a current path with transversal and longitudinal voltage probes. These probes enable measurements in the four-probe configuration to exclude the resistance of the contacts. The Hall-bars are produced by optical lithography following the standard Hall-bar recipe as described in Ref. [45] and shortly summarized in the following. The HgTe layer (including the sandwiching $Cd_{0.7}Hg_{0.3}Te$ layer) is etched into a Hall-bar shape using Ar^+ sputtering. The structure defined by etching is usually referred to as mesa. The Hall-bar is covered by a SiO_2-Si_3N_4 insulator deposited by $80°$ Plasma-enhanced chemical vapor deposition. This layer acts as the dielectric for the $100\,nm$ thick

2

Au electrode which is deposited together with a 5 nm Ti sticking layer by electron beam evaporation. The contacts to the mesa are made by cleaning the $Cd_{0.7}Hg_{0.3}Te$ capping layer of the mesa leads with Ar^+ sputtering and depositing in situ 50 nm AuGe and 50 nm Au by electron beam deposition. The final device is shown as a schematic cut in Fig. 2.7a) together with a microscopic picture of the lithographed sample in Fig. 2.7b).

2.3.3. MAGNETO-TRANSPORT ON TENSILELY STRAINED HGTE

Tensilely strained HgTe has been established as three-dimensional topological insulator (TI) by the observation of its topological surface states in Ref. [8]. QHE has been observed in a three-dimensional layer, which requires the existence of a two-dimensional state. This two-dimensional state is identified as the TSS due to the observed phase of the Shubnikov-de Haas (SdH) oscillations and the QHE. It shall be mentioned, that in Ref. [46] a similar observation is made, but the interpretation is different. There a part of the observed conductance is contributed to bulk states. The possibility to change the carrier density is introduced by the addition of a top gate electrode in Ref. [47]. The top gate allows to match the carrier densities of the top and bottom TSS and equivalently their quantum Hall (QH)-indices. The obtained Hall resistance R_{xy} as a function of the magnetic field shows different QH-plateau sequences for different gate voltages. This is shown in Fig. 2.8a), including the expected odd QH-plateau sequence for degenerate TSSs according to

$$\sigma_{xy,\mathrm{TI}} = \left(j_\mathrm{t} + j_\mathrm{b} + \frac{1}{2} + \frac{1}{2} \right) \frac{e^2}{h},$$ (2.3)

where j_t and j_t are the QH-indices for the top and bottom TSS. Such an odd QH-sequence has later also been observed in $BiSbTeSe_2$ in Ref. [48]. Compared to the bulk band gap in HgTe of $\Delta E \sim 20\,\mathrm{meV}$ (see Fig. 2.2 and Sec. 2.3.1) the QHE is observed over a surprisingly large density range. The two-dimensional transport hence dominates over a much wider energy range than expected from the size of the bulk energy gap.

Furthermore, protective top and bottom $Cd_{0.7}Hg_{0.3}Te$ layers sandwiching the HgTe layer have been introduced to improve the quality of the HgTe interface [49, 50]. The resulting layer stack is described in Sec. 2.3.2. This improvement of the layer quality leads to an increased mobility and the observation of QHE not only in the electron but also hole transport regime, as shown in Fig. 2.8b). In the p-conducting regime for low magnetic fields, the Hall signal starts with a positive slope, indicating an electron regime, which turns into a negative slope with increasing magnetic field, as expected for hole transport. This indicates the involvement of at least two transport channels with opposite carrier types. More specifically an electron type channel with a higher mobility than the hole type channel with higher carrier density. The total carrier density is thus effectively hole-like. The mobility of the electron channel is not only higher than the hole channel, but also absolutely with $\mu \sim 0.5 \times 10^6\,\mathrm{cm^2/Vs}$. The high mobility is emphasized by the observation of quantum oscillations in the R_{xx} and R_{xy} down to magnetic fields below $B = 100\,\mathrm{mT}$, as shown in Fig. 2.8c). The frequency of these oscillations as well as the fit of the Hall and longitudinal resistance with the classical Drude model for two contributing channels yields a carrier density around $0.5 - 0.6 \times 10^{11}\,\mathrm{cm^{-2}}$, which is stable for a vast number of samples [50, 51]. The low magnetic field value for the observed onset of the quantum oscillations is a confirmation of the high mobility of these samples determined by the two carriers Drude fits to $\mu \sim 0.5 \times 10^6\,\mathrm{cm^2/Vs}$. Comparing the onset magnetic field of the oscillations to mea-
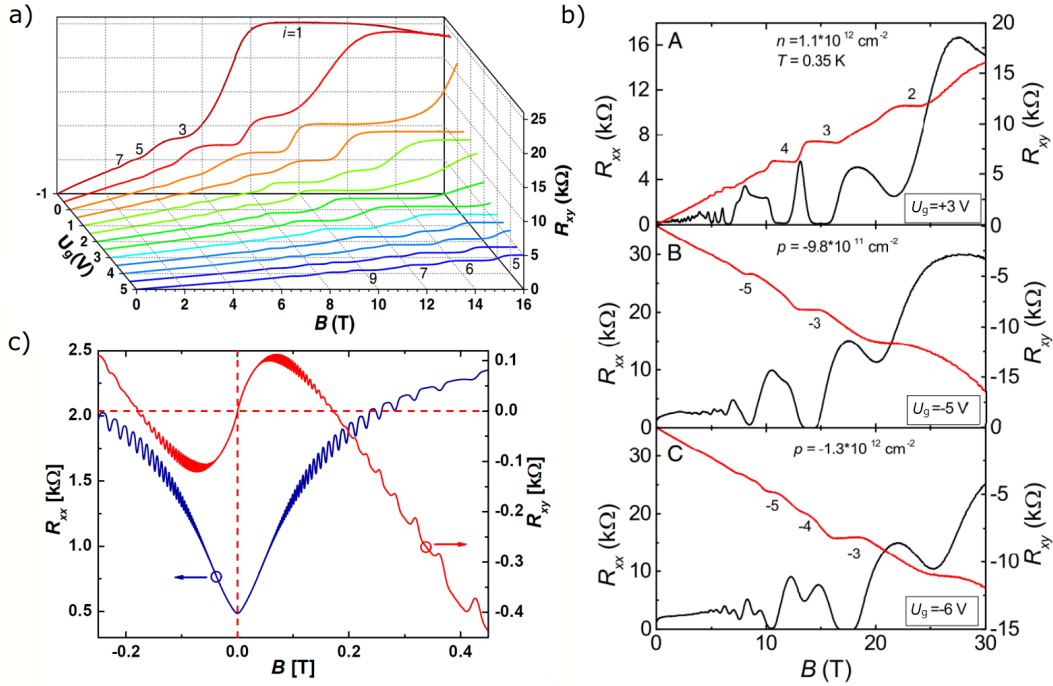
Figure 2.8: a) shows the Hall resistance R_{xy} of a top gated uncapped tensilely strained HgTe sample as a function of the magnetic field B for various gate voltages U_g. b) shows the longitudinal resistance R_{xx} in black and the R_{xy} in red of a HgTe sample with a 5 nm capping $Hg_{0.3}Cd_{0.7}Te$ layer. SdH oscillations and QHE is observed for the electron and hole transport regime. c) shows the observation of SdH oscillations in R_{xx} and R_{xy} for another capped HgTe sample for low magnetic fields at the temperature $T = 0.05\,K$. a) is reprinted from C. Brüne *et al.*, Stabilized Surface-State Transport in a Topological Insulator, PRX **4**, 41045 (2014) [47], Attribution 3.0 Unported (CC BY 3.0). b) is reprinted from A. Jost *et al.*, PNAS **113**, 8648 (2016), Copyright 2016 National Academy of Sciences [49]. c) is reprinted from C. Thienel, Exploring the transport properties of the three-dimensional topological insulator material HgTe, Dissertation, Universität Würzburg (2015) [50].

surements of $GaAs/Al_{0.3}Ga_{0.7}As$ two dimensional electron gas (2DEG)s with with mobilities of $\mu = 11.9 \times 10^6\,cm^2/Vs$, it is indeed comparable [52]. These oscillations are observed in samples with different interfaces, thicknesses and are independent of the applied top gate voltage. Their origin is still under discussion and some potential origins are named in Ref. [50]. An additional potential mechanism is the appearance of quantum oscillations without a Fermi surface, as described in Ref. [53, 54]. This mechanism is discussed in Appendix B, since it might also be relevant for topological Kondo insulators as SmB_6 [55, 56]. A in Ref. [50] mentioned potential origin of the oscillations is the bottom TSS, which is suggested based on $k \cdot p$ modeling in Ref. [57]. The bottom TSS is the most likely origin and thus addressed in Sec. 4 and in more detail in Ref. [58].

2.3.4. The Dirac screening model

As mentioned above in Sec. 2.3.3 the observed QHE in Ref. [47] for electron densities up to $2.0 \times 10^{12}\,cm^{-2}$ with quantization to the expected integer fractions of the Klitzing constant, as shown in Fig. 2.8a) seems to be in contradiction to the small bulk band gap compared to the presumably accessed energy range, as presented in Fig. 2.6g). Additional states manifest themselves in transport either as parallel conductance leading to a deviation of QH-plateaus from $\frac{h}{j \cdot e^2}$ for three-dimensional states or as additional oscillation frequencies for two-dimensional states. Neither of the two has been observed. Because of this, the authors

of Ref. [47] model the topological insulator as an insulator wrapped by a thin metal sheet. This metal sheet formed by the TSSs screens the applied electric field. In other words, a change of the top gate voltage only causes a change in the occupation of the TSSs, but the Fermi energy E_F in the bulk is unaffected. Due to the Dirac nature of the topological surface states, this model is called Dirac-screening [47].

This Dirac screening concept is implemented in Ref. [47] by using an effective Hartree potential as shown in Fig 2.9a). This effective Hartree potential determines the overall carrier density distribution in the sample. The shape of the Hartree potential is thereby equivalent to the expected distribution of the potential over the layer stack by a dielectric constant of $\epsilon_{TSS} = 3$ for the TSS and $\epsilon_{bulk} = 21$ for the HgTe bulk. The resulting band structures are shown for two example gate voltages in Fig. 2.9b) and c). The Fermi energy stays inside the bulk band gap and only the dispersion of the top TSS in red and bottom TSS in blue changes with respect to the bulk bands in black due to the applied potential. The chosen form of the Hartree potential ensures consequently a change of the occupation of both TSSs with the applied gate voltage without the occupation of bulk states. This is consistent with the observed QHE over a wide density range. The observed irregular QH-plateau sequences indicate the contribution of two two-dimensional transport channels.
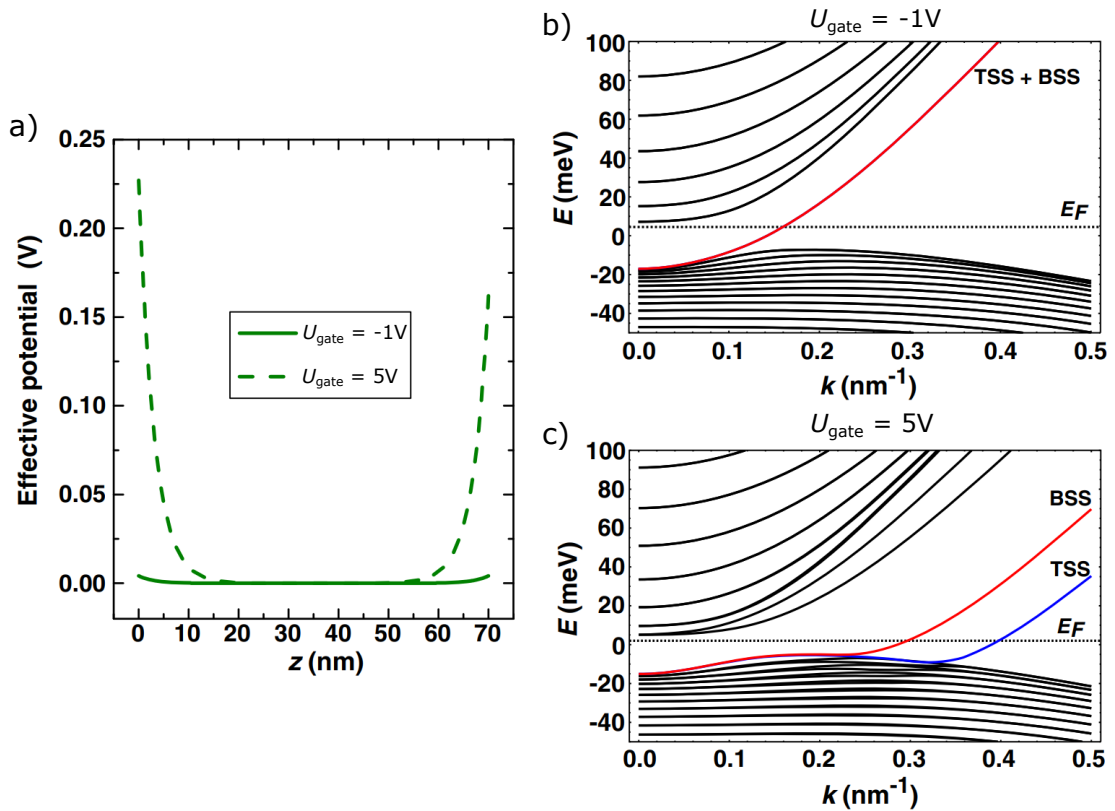
Figure 2.9: Model Hartree potentials representing the respective applied gate voltages $U_{gate} = -1\,\text{V}$ and $U_{gate} = 5\,\text{V}$. are shown in a) and are used to calculate the band structure of a 70 nm thick 0.3 % tensilely strained HgTe layer with a 6-band $k \cdot p$ Kane model which is shown in b) and c). The Fermi energy E_F is indicated as a dotted black line and the top and bottom TSS are highlighted in blue and red, respectively. Reprinted from C. Brüne *et al.*, Dirac-Screening Stabilized Surface-State Transport in a Topological Insulator, PRX **4**, 41045 (2014) [47], Attribution 3.0 Unported (CC BY 3.0).

An alternative interpretation is presented in Ref. [57]. It is based on a self-consistent $k \cdot p$ analysis with the six band Kane model parameterized to represent a 40 nm thick 0.3 % tensilely strained HgTe layer. This analysis yields a change of only the carrier density of the top surface state with the gate voltage, while the density of the bottom surface state stays unchanged. Since this result seems in contrast to the observed magneto-transport data for high magnetic field in Ref. [47] and shown in Fig. 2.8a) and it is only valid for a small density range, the Dirac-screening model has been used in Ref. [47].

2.3.5. Open questions

Tensilely strained HgTe is established as a topological insulator with accessible topological surface states. Nevertheless, open questions remain: The first question is already mentioned in Sec. 2.3.3. It concerns the origin of the pronounced quantum oscillations at low magnetic fields shown in Fig. 2.8c). This observation raises the question, whether additional states exist next to the TSS. If indications for the existence of other states can be found, of which nature are these states? Are these states additional surface states? The stability of the TSS is another interesting topic. Is a bulk bandgap necessary for TSS to exist? How high gate voltages can be applied and TSS are still observed? The top gate is so far the only possibility to adjust the occupation of the TSS. Is there a way to create specific occupations of the TSS? Does a simpler way to create specific occupations exist? Can we implement additional nobs to vary the carrier density in the TSS? These and other questions will be addressed in the remainder of this work.

II

HGTE AS THREE-DIMENSIONAL TOPOLOGICAL INSULATOR

<div align="right">

3

</div>

Magneto-transport on high mobility tensilely strained HgTe

This Chapter is the natural continuation of the above (in Sec. 2.3) described state of the art of research. New insights are gained by adjustments to the MBE grown layer stack and access to newly developed less invasive lithographic methods. The consequently increased mobility enables the analysis of SdH oscillations and the QHE at lower magnetic fields. This additional information allows the separation and identification of the involved transport channels and their individual dependencies on the gate voltage. The magnetotransport is compared to the band structure of HgTe.

3.1. Sample quality improvements and their verification

The modifications to the layer stack and the fabrication process are introduced, which lead to the increased sample quality. The increased sample quality is verified by magneto-transport experiments. The experimental setup is introduce. The semi-classical magneto-transport regime is used to extract the mobility as a figure of merit for the sample quality based on the shortly reviewed Drude model. As another indicator for the high sample quality, the occurrence of the QHE and SdH oscillations at low magnetic fields is described.

3.1.1. New layer stack and fabrication method

As summarized in Sec. 2.3, the quality of the tensilely strained HgTe has been improved by introducing a $Cd_{0.7}Hg_{0.3}Te$ buffer layer underneath the HgTe layer and a thin $Cd_{0.7}Hg_{0.3}Te$ capping layers of $5 - 15\,nm$ on top of the HgTe layer [50]. Based on developments introduced for HgTe quantum wells where with increasing capping and buffer layer thicknesses enhanced mobilities are obtained in Ref. [59], the thickness of the capping is increased to $\sim 70\,nm$. This thickness is chosen, since the overall thickness of the strained portion of the layer stack, namely the HgTe layer together with its protective $Cd_{0.7}Hg_{0.3}Te$ layers, has to be sufficiently thin to prevent relaxation. Relaxation would cause a reduction in the desired strain and layer quality. For a HgTe layer directly grown on CdTe a critical thickness of $d_c \sim 155\,nm$ is found [25, 44]. $Cd_{0.7}Hg_{0.3}Te$ contributes approximately only with half its thickness due to smaller mismatch of the lattice constant to CdTe. This means the desired thickness of the HgTe layer and $Cd_{0.7}Hg_{0.3}Te$ protective layers of $d \sim 70\,nm$ is realizable

[25]. The thicker capping layer reduces the available hysteresis free gate range. The intrinsic nature of the samples ensures the access of the electron and hole transport regime of interest without the need of big changes of the carrier density. The range is sufficient to introduce a modulation doping layer into the buffer layer, as sketched in Fig. 2.7a). This layer provides a finite starting electron density by modulating the chemical potential landscape of the hetero-structure. As dopants iodine is used and incorporated into a 9 nm thick layer inside the $Cd_{0.7}Hg_{0.3}Te$ buffer layer 65 nm below the HgTe layer. This procedure is well established for HgTe quantum wells [60].

To preserve the high mobility of these samples, less invasive etching methods have been developed in the group [45, 58]. The first method is the as new standard established wet etching method using an aqueous solution of $KI/I_2/HBr$ as presented in Ref. [45] or in more detail in Ref. [61]. The second option is inductively coupled plasma etching which combines low energy Ar^+ etching with chemical etching by CH_4. The energy of the Ar^+ ions is thereby drastically reduced from the former pure Ar^+ ion milling from 1 kV to 35 V. Details to this etching process can be found in Ref. [58].
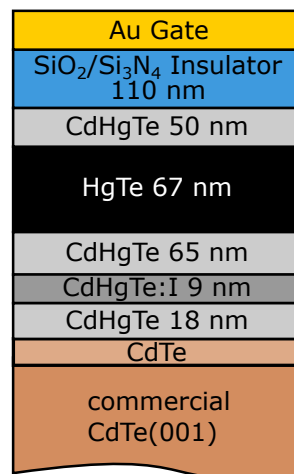
Figure 3.1: Shown is the total layer stack consistent of the commercial CdTe substrate followed by MBE grown HgTe layer, $Cd_{0.7}Hg_{0.3}Te$ buffer with a CdTe:I modulation doping layer inside, HgTe layer and a $Cd_{0.7}Hg_{0.3}Te$ cap covered with a $SiO_2Si_3N_4$ insulator and a Au gate layer.

3.1.2. MEASUREMENT SETUP

The magneto-transport measurements are perforemd to analyze the properties of the charge carrier system of HgTe and reconstruct the corresponding band structure. Low temperatures are chosen to isolate the properties of the charge carrier system from the crystal lattice by staying below $T < 20$ K, which is the temperature where optical phonons become relevant in HgTe [62]. To supply these conditions a He_3/He_4 dilution refrigerator is used to achieve temperature of $T = 0.05$ K. The dilution refrigerator is equipped with a superconducting magnet capable of magnetic fields up to $B = 16$ T. The electrical wiring is fitted with appropriate electrical filters to keep the electron temperature close to the lattice temperature of the sample. The measurements are performed by applying a constant low-frequency ac-voltage excitation and measuring the resulting voltages with lock-in amplifiers. Low excitations of $U_{exc} \sim 100 \, \mu V$ are used to stay in the linear response regime and prevent heating of the sample. The low frequencies, like $f_{exc} = 37$ Hz are employed to en-

sure that the response of the investigated samples is only resistive. Generally, the measured voltage U is proportional to the impedance $Z = R + iX$. The reactance X is thereby due to the capacitance or inductance of the device and R due to its resistance. Since the capacitance and inductance of the device are neglectable for low frequencies, the signal can be treated as the only originating from the resistance R of the device. This allows, for example, to correct for the stray capacitance of the cryostat wiring which causes a finite reactance contribution that shifts the phase of the measured signal. This shift is for the chosen measurement conditions typically in the range of a few degrees and can be corrected by determining the phase of the signal maximum and use this stray capacitance corrected phase for the measurement. The measured voltages U allow to determine the resistances R of interest by using Ohm's law $R = \frac{U}{I}$ and a known reference resistor R_{ref} to determine the current I. To access these resistances as accurately as possible the samples are shaped into a Hall-bar geometry with separate current leads and voltage probes as shown in Fig. 3.2. This allows measuring in the four-point geometry, which excludes the contact resistance since no current flows through the voltage probes. The voltage probes can hence be treated as local potential probes. The measurement configuration is shown in Fig. 3.2.
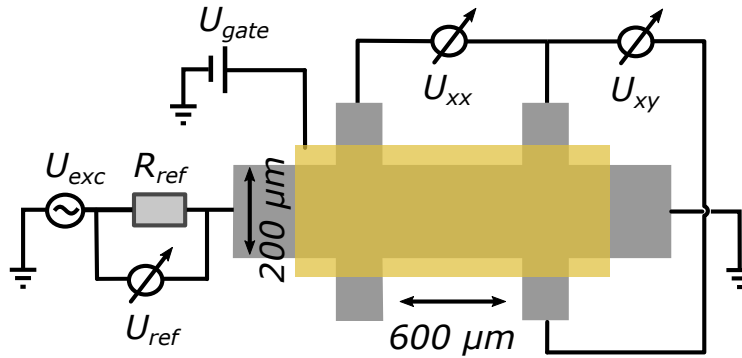
Figure 3.2: A schematic of a Hall bar in the applied measurement scheme is shown. U_{exc} is the low-frequency constant excitation voltage, U_{gate} the dc voltage applied on the Au top gate. The measured voltages are U_{ref} which is the voltage dropping over a known reference resistor R_{ref}, the longitudinal voltage U_{xx} and the Hall voltage U_{xy}.

3.1.3. QUANTIFICATION OF THE SAMPLE QUALITY

The above-introduced measurement scheme is used to quantify the improvements made by adjusting the layer stack and the etching method. The semi-classical low magnetic field regime is measured and the Drude model is used to extract the mobility μ and carrier density n. The mobility μ is chosen as figure of merit for the quality of the sample since it is a measure of the number of impurities in the sample. In the following some generally useful quantities are introduced using the conventional nomenclature. The specific resistance $\boldsymbol{\rho}(B)$ [1] of the Hall bar in dependence of the magnetic field B reads

$$\boldsymbol{\rho} = \begin{bmatrix} \rho_{xx} & R_{xy} \\ -R_{xy} & \rho_{xx} \end{bmatrix} = \begin{bmatrix} 1/\sigma_0 & -\frac{B}{ne} \\ \frac{B}{ne} & 1/\sigma_0 \end{bmatrix}. \tag{3.1}$$

---

[1]Bold symbols indicate the vector character of the quantities.

The indices here indicate the direction with respect to a two-dimensional Cartesian coordinate system. The first index indicates the current direction and the second index the direction of the resulting voltage. The conductivity without magnetic field B is

$$\sigma_0 = \sigma_{xx}(B = 0\,\mathrm{T}) = en\mu \tag{3.2}$$

with e being the electron charge, n the carrier density, and μ the carrier mobility. In this work, electron densities are positively defined, while hole densities are indicated by a minus sign. The slope of the Hall resistance $R_{xy}(B)$ given by

$$R_{xy}(B) = \frac{1}{ne}B \tag{3.3}$$

can be used to determine the carrier density n. Together with the zero-field conductivity of Eq. 3.2 gives the mobility μ. The mobility μ contains additional to the amount of scattering information about the band structure of the material, since in the relaxation time approximation the mobility is given by

$$\mu = e\tau / m_{\mathrm{eff}}, \tag{3.4}$$

where τ is the relaxation (=scattering) time and m_{eff} is the effective electron mass. The effective mass is the renormalized electron mass accounting for the movement of an electron (hole) through a crystal instead of the vacuum and is given by the curvature of the respective band. A more in-depth discussion on magneto-transport can be found in Ref. [63].

Figure 3.3: The longitudinal resistance R_{xx} in black and the Hall resistance R_{xy} in red is shown as function of the magnetic field B for the gate voltage $U_{\mathrm{gate}} = 0\,\mathrm{V}$ and the temperature $T = 0.05\,\mathrm{K}$. The theoretically expected QH-plateau values are indicated as dashed blue lines and zero is marked as dashed grey line.

The mobility is used to verify the improvements to the layer stack and the sample fabrication described in Sec. 3.1.1. The magnetoresistance data of sample QC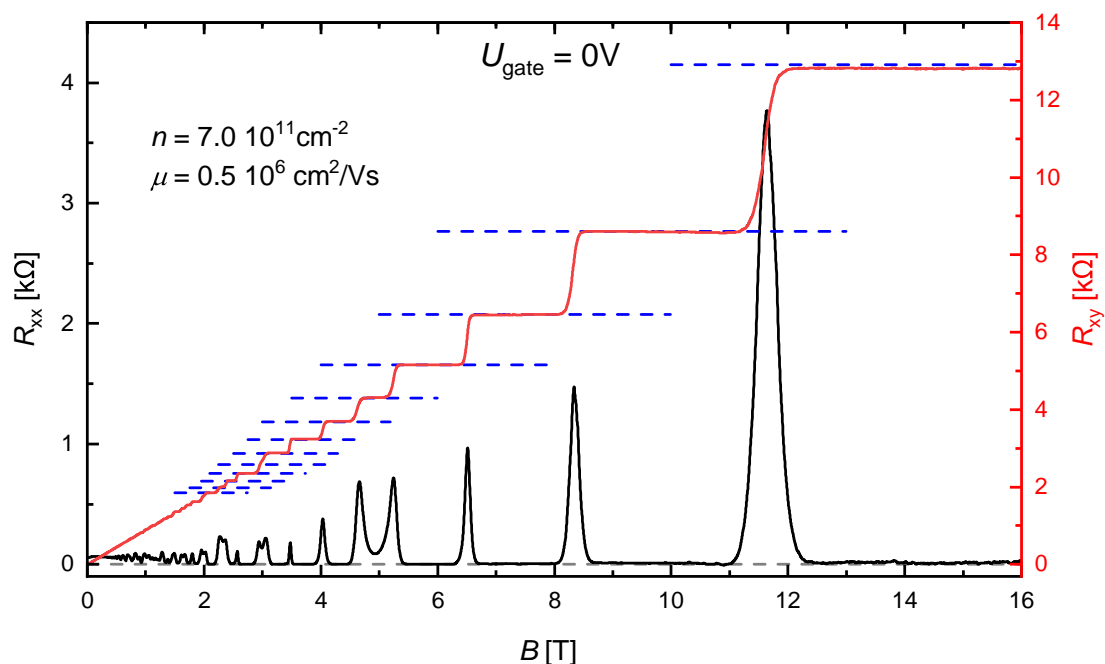0501 is shown in Figure 3.3. The sample consists of a 50 nm thick capping layer and a modulation doping layer in the buffer and is fabricated by inductively coupled plasma reactive-ion etching as shown schematically in Fig. 3.1. It should be noted, that we had to choose a non-ideal measurement configuration for this sample. One of the current contacts did not work so that we had to use one of the voltage probes as a current lead. Most importantly, in the edge channel transport regime of interest, identifiable by the observation of QH-plateaus the chosen configuration is identical to the ideal configuration. In the Drude transport, regime artifacts could arise due to the non-ideal current distribution. We checked the symmetry of the signal by measuring for positive and negative magnetic fields. The observed symmetry validates this measurement configuration and consequently the extracted numbers for density and mobility. Additionally, the results were reproduced in multiple other devices, see for example Fig. 3.4. At first glance, the measurement shows quantum effects, namely QHE and SdH-oscillations. These indicate a high sample quality. To quantify this impression the mobility is determined by first evaluating the density n using a linear fit to $R_{xy}(B)$ for the low magnetic field region $0\,\text{T} < B < 1\,\text{T}$ and Eq. 3.3. Eq. 3.2 allows by knowing the length to width ratio $l/b = 3$ and $R_{xx}(B = 0\,\text{T})$ to determine the mobility μ. This procedure yields for $U_{\text{gate}} = 0\,\text{V}$ a density of $n = 7.0 \times 10^{11}\,\text{cm}^{-2}$ with the high mobility of $\mu = 0.5 \times 10^6\,\text{cm}^2/\text{Vs}$ as indicated in Fig. 3.3 which confirms the high sample quality. To put this number into perspective it ~ 10 times higher than the mobility of uncapped HgTe samples of $\mu_{\text{uncapped}} \sim 0.03 \times 10^6\,\text{cm}^2/\text{Vs}$ for $n = 9.0 \times 10^{11}\,\text{cm}^{-2}$ [47] and about double as high as the mobility of HgTe samples with thin caps $\mu_{\text{than cap}} \sim 0.30 \times 10^6\,\text{cm}^2/\text{Vs}$ for $n \leq 11 \times 10^{11}\,\text{cm}^{-2}$ [49] as well as more than a factor 100 higher than the mobility of BiSbTeSe$_2$ $\mu_{\text{BSTS}} \sim 0.003 \times 10^6\,\text{cm}^2/\text{Vs}$ for $n = 5 \times 10^{11}\,\text{cm}^{-2}$ [48]. This high mobility manifests itself in the sharp transitions between the QH-plateaus observed in the Hall resistance R_{xy} and the narrow peaks in the longitudinal resistance R_{xx} as shown in Fig. 3.3. The QH-plateaus also quantize on the expected plateau values of $\frac{h}{\nu e^2}$ within the measurement accuracy and are accompanied by zero resistance plateaus in the R_{xx} between the peaks down to low magnetic fields of $B \lesssim 2\,\text{T}$. The sharp peaks in R_{xx} and plateau transitions in R_{xy} indicate a small broadening of the Landau levels, which can be compared to the broadening observed in the samples with thinner capping Cd$_{0.7}$Hg$_{0.3}$Te as shown in Fig. 2.8b). The quantization of the QH-plateaus up to the measurement accuracy together with the vanishing longitudinal resistance has been observed in samples with lower mobilities before [50], and shall not be claimed as new here, the focus lies solely on showing the high quality of investigated samples. The analysis of the semi-classical low magnetic field regime confirms the high sample quality and motivates further and more sophisticated investigations.

3.2. Analyzing magneto-transport measurements

The QHE and SdH oscillations contain more information about the properties of the sample. A short reminder on the Landau level (LL) formation as the underlying physical mechanism is given. Afterwards, a routine to extract information from the SdH oscillations and QHE is described. This routine is presented on an exemplary magnetic field dependent measurement. This procedure gives access to the underlying band structure of the investigated HgTe layer.

3.2.1. Consequences of Landau level formation in magneto-transport

The underlying mechanism for QHE and SdH oscillations is the restriction of charge carriers by the Lorentz force due to a magnetic field B onto cyclotron orbits in the plane perpendicular to B (see for example [63]). These states are called Landau levels and their energies are quantized to

$$E_L = (j + 1/2)\hbar eB/m_{eff}, \tag{3.5}$$

where $\hbar = \frac{h}{2\pi}$ is the reduced Planck constant and j the Landau level index. The degeneracy of these Landau levels is given by

$$n_L = g_s g_v \frac{e}{h} B \tag{3.6}$$

with h being the Planck constant and g_s (g_v) the spin (valley) degeneracy. The number of filled Landau levels in a system is given by the filling factor

$$\nu = \frac{n}{n_L} = \frac{n}{g_s g_v} \frac{h}{e} \frac{1}{B} \tag{3.7}$$

This modulation of the density of states (DOS) with magnetic field also alters the conductance following Eq. 3.2 and thus the resistance in a oscillating fashion called SdH oscillations, as shown in Fig. 3.3. In a finite two-dimensional system, the energies of the Landau levels are locally enhanced at the edges due to the edge potential. Fully occupied Landau levels, which lie below the Fermi-energy E_F in the bulk, bend upwards and cross E_F at the sample edges. The Hall conductance σ_{xy} of these states is quantized and proportional to the number of occupied Landau levels in the bulk

$$\sigma_{xy} = \nu \frac{e^2}{h}. \tag{3.8}$$

This effect is called QHE. Since all LLs in the bulk are completely occupied, no four-point longitudinal conductivity σ_{xx} is expected according to Eq. 3.2. Consequently, not only the Hall conductivity σ_{xy}, but also the Hall-resistance R_{xy} is quantized, as visible in Fig. 3.3 and 3.4. The carrier density is treated as two-dimensional carrier density despite the three-dimensional extension of the sample, since QHE is observed. QHE is expected to only exist in even dimensions, meaning two dimensions for our purposes. Abstract arguments can be made for this fact. Here an intuitive motivation is given by looking at the different shapes of the Fermi energy contours and Landau level energy contours for different dimensions. In two dimensions the Landau levels, as well as the Fermi energy, are circles, making it possible to push the Fermi energy circle through one Landau level circle into the gap between to Landau level circles without them intersecting, allowing for a bandgap in the full Brillouin zone. In three dimensions the Fermi surface is a sphere and the Landau levels are tubes

making a crossing of the spherical Fermi surface with the tube-shaped Landau levels un-
avoidable. The spacing of SdH-oscillation peaks can be used together with the definition
of the filling factor in Eq. 3.7 to determine the charge carrier density in a system up to a
degeneracy factor via

$$\Delta\left(\frac{1}{B}\right) = \frac{e}{h}\frac{4\pi}{k^2} = \frac{e}{h}\frac{g_s g_v}{n}. \tag{3.9}$$

This carrier density is equivalent to the extremal Fermi surface perpendicular to B. The
measurements of the SdH-oscillations frequency in dependence of the angle of the applied
magnetic field allow to map out the shape of the Fermi surface of a material. Such a Fermi
surface mapping has been widely used in metals by measuring the magnetization using
the de Haas-van Alphen effect [64]. The determination of the carrier density based on the
frequency of the observed oscillation is the main tool for the sample investigation in this
work.

3.2.2. EXTRACTING INFORMATION FROM THE QUANTUM HALL EFFECT AND SHUBNIKOV-DE HAAS OSCILLAITONS
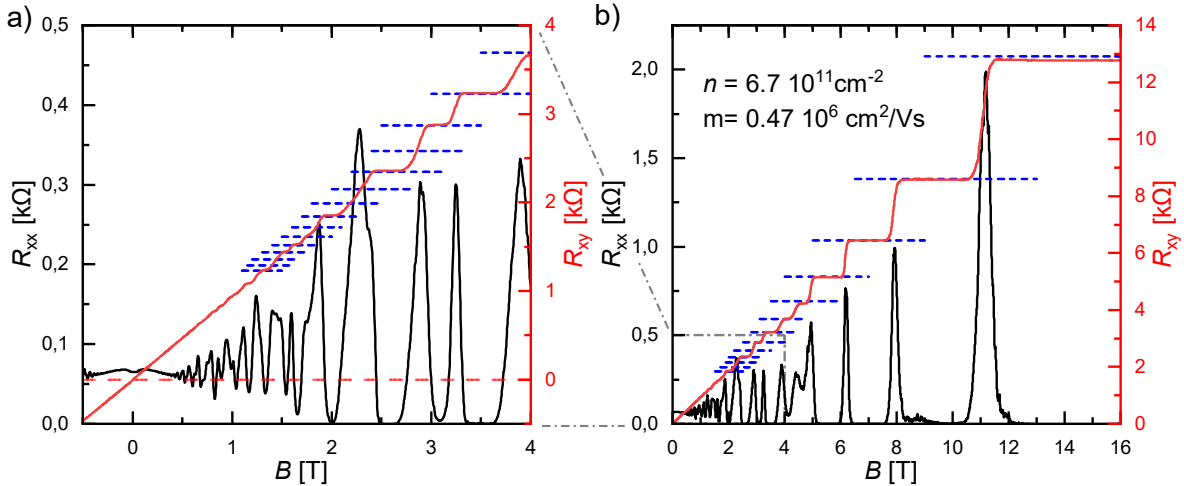
Figure 3.4: The longitudinal resistance R_{xx} in black and the Hall resistance R_{xy} in red is shown as a function of
the magnetic field B for a gate voltage $U_{\text{gate}} = 0\,\text{V}$ and the temperature $T = 0.05\,\text{K}$ together with the expected
QH-plateau values as dashed blue lines for the $30 \times 10\,\mu\text{m}$ sample up to $B = 4\,\text{T}$ in a) (with $R_{xy} = 0$ indicated
as dashed red line) and over the full available magnetic field range up to $B = 16\,\text{T}$ in b).

The reproducibility of the results and the homogeneity of the layers is demonstrated by
additional measurements on the $30\,\mu\text{m} \times 10\,\mu\text{m}$ Hall-bar structure [2] in Fig. 3.4. This Hall-
bar is simultaneously on the same chip prepared as the $600\,\mu\text{m} \times 200\,\mu\text{m}$ Hall-bar shown in
Fig. 2.7. The measurements for the $600\,\mu\text{m} \times 200\,\mu\text{m}$ Hall-bar is shown in Fig. 3.3. The den-
sity and mobility numbers extracted from the semi-classical transport regime agree well
for both Hall-bars, as shown in Fig. 3.3 and 3.4. Also, the positions of the SdH peaks and
the QH-plateaus in the magnetic field coincide reasonably well. This resemblance moti-
vates a deeper analysis, which is started with the semi-classical transport regime to extract
information on the type of the involved charge carriers. In Fig. 3.4a) the Hall resistance

---

[2]For this Hall-bar all contacts have been available and the measurements are performed in the usual Hall-bar
  measurement geometry.

R_{xy} increases monotonically with the magnetic field B. Accounting for the direction of the magnetic field this increase indicates electron transport. The increase of R_{xy} is linear for low magnetic fields, except for very small deviations for $B \sim 0\,\mathrm{T}$, yielding an overall density of $n = 6.7 \times 10^{11}\,\mathrm{cm}^{-2}$. The longitudinal resistance R_{xx} shows a weak dependence on the magnetic field for low magnetic fields B and a symmetric dip around $B = 0\,\mathrm{T}$. Such a dip of $R_{xx}(B \sim 0\,\mathrm{T})$ can have different origins.

One possible mechanism that is reported in the literature to describe a similar dip observed in the magneto-transport measurements on Bi/Sb chalcogenide TIs (e.g. [65]) is weak anti-localization (WAL). WAL is a correction to the conductance due to a positive self-interference of the different possible coherent scattering paths of the charge carriers. WAL is considered an unlikely mechanism due to the big magnetic field range of a few T reported for the Bi/Sb chalcogenides. A stronger indication is the independence of the measured dip in $R_{xx}(B)$ from the temperature in our tensilely strained HgTe samples. This temperature independence is shown in Fig. C.1 of appendix C, which depicts multiple $R_{xx}(B)$ traces for different temperatures. Another mechanism is the Sharvin-effect [66] which leads to an increase of the resistance with magnetic field in small samples due to the device geometry or impurities. Indeed an additional dip is observed in even narrower structures in Ref. [58], which excludes the Sharvin-effect as the origin for the here observed dip. The most probable mechanism is the involvement of multiple transport channels with sufficient different carrier densities and mobilities. Figuratively speaking, for $B = 0\,\mathrm{T}$ the channel with high carrier mobility dominates, while with increasing magnetic field strength the concept of mobility loses its validity, and effectively all carriers contribute equally to the transport.

The contribution of two transport channels can cause the above-described dip in R_{xx} around $B = 0\,\mathrm{T}$, which is usually accompanied by a change of slope of the Hall resistance, which might only appear as a kink or a small non-linearity around $B = 0\,\mathrm{T}$. For two contributing transport channels, the Hall slope for low magnetic fields can be approximated by the involved carrier densities n_1, n_2 and respective mobilites μ_1, μ_2 using

$$\Delta R_{xy}/\Delta B = \frac{1}{e} \frac{1}{n_1 + \frac{\mu_2}{\mu_1} n_2}. \tag{3.10}$$

For the measurement shown in Fig. 3.4 the change in the Hall resistance R_{xy} around $B \sim 0\,\mathrm{T}$ is not strong enough to be analyzable. Only one Hall slope can be determined, which gives the overall carrier density $n = 6.7 \times 10^{11}\,\mathrm{cm}^{-2}$ as mentioned above. The multiple carrier behavior is established as the origin for the observed dip in the longitudinal resistance R_{xx} in Ref. [50]. The longitudinal $R_{xx}(B)$ and Hall resistance $R_{xy}(B)$ data is for various gate voltages reproduced using the Drude model while accounting for multiple transport channels. This model reproduces the data well. Summarizing, the dip in the longitudinal resistance together with the positive Hall slope indicates the involvement of at least two electron-like transport channels.

For small magnetic fields $B \gtrsim 0.5\,\mathrm{T}$ distinct oscillations are visible in the longitudinal resistance R_{xx}, together with plateaus in the Hall resistance R_{xy} for $B \gtrsim 1\,\mathrm{T}$. For moderate magnetic fields $B < 5\,\mathrm{T}$ varying distances between SdH peaks and amplitudes in a beating fashion together with omitted QH-plateaus are observed. The observation of beating patterns suggests the involvement of multiple oscillation frequencies originating from multiple transport channels. A fast Fourier transformation (FFT) analysis is used to unambiguously identify the number of involved channels with their corresponding oscillation frequencies. These frequencies are proportional to the respective carrier densities. The data

has to be prepared for the FFT analysis because the SdH oscillations are periodic in B^{-1}, while the data is recorded at fixed time intervals with a constantly driven magnetic field, which makes the data points effectively equidistant in B. This is why the longitudinal resistance R_{xx} data is linearly interpolated in the inverse magnetic field B^{-1} to provide the necessary equidistant sampling points for the numerical FFT analysis. The longitudinal resistance R_{xx} is shown as function of the inverse magnetic field B^{-1} in Fig. 3.5a). The FFT results shown in Fig. 3.5b) are obtained for $0.2\,\text{T} < B < 16\,\text{T}$ using the "Welch" window function with "Origin 2018". The exact analyzed magnetic field range and the window function have been varied yielding consistent results (see appendix D). For FFT analyses in this work, the magnetic field step size in B^{-1} is chosen, so that the maximum detectable frequency is above the highest expected frequency. While for Fig. 3.5b) nearly the full measured magnetic field range of $0.2\,\text{T} < B < 16\,\text{T}$ is used, the analyzed magnetic field range is sometimes adapted to only include oscillations that are sufficiently sinusoidal to avoid FFT-artifacts. The stability of the FFT result to the chosen magnetic field range is also shown in appendix D.
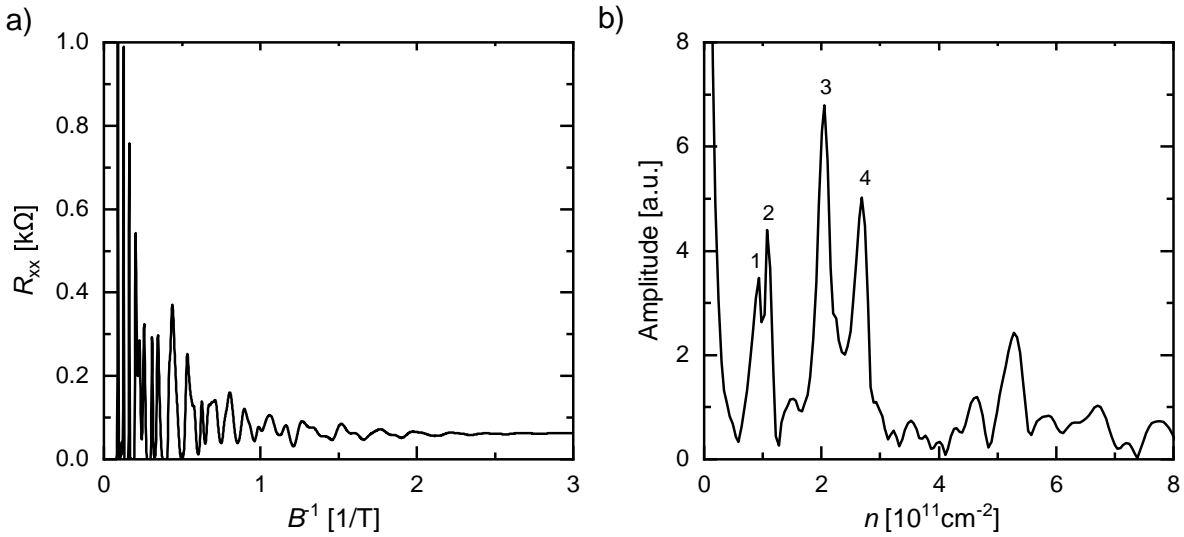
Figure 3.5: The longitudinal resistance R_{xx} as shown in Fig. 3.4 is linearly interpolated to be equidistant in B^{-1} and shown as a function of the inverse magnetic field B^{-1} in a). In b) the FFT spectrum of the data from a) is shown as a function of a rescaled frequency axis to represent the equivalent non-degenerate carrier density n.

The x-axis of the FFT spectrum in Fig. 3.5b) is transformed from frequency f to the more intuitive quantity carrier density n following Eq. 3.9 assuming non-degenerate bands via $n = \frac{e}{h} f$. This assumption is made based on the observation of odd and even QH-plateaus indicating the crossing of single LLs with the occasional exception when multiple SdH peaks coincide. The FFT spectrum shows two close peaks at $n_1 = 0.9 \times 10^{11}\,\text{cm}^{-2}$ and at $n_2 = 1.1 \times 10^{11}\,\text{cm}^{-2}$ as well as peaks at $n_3 = 2.1 \times 10^{11}\,\text{cm}^{-2}$ and $n_4 = 2.7 \times 10^{11}\,\text{cm}^{-2}$. Additionally, higher-order peaks are observed, requiring a closer investigation of the origination of peak 3, since it sits roughly at $n_3 \sim 2 \times n_{1,2}$ making it potentially a higher-order peak of peak 1 or 2. Usually, higher-order peaks possess smaller amplitudes than their original peaks. The relative peak height is only a trend and not a requirement. A more rigid validation is the identification of LL with the corresponding transport channels. The densities n_{1-4} are converted to the respective periods in B^{-1}. These periods are sketched as colored sets of lines into the longitudinal resistance R_{xx} and Hall conductivity σ_{xy} data in

Fig. 3.6. The absolute position of the lines is effectively a phase and thus determined by finding the best match to the peaks in the longitudinal resistance data $R_{xx}(B^{-1})$. Each line indicates the expected position of one LL. The amount of lines between QH-plateaus in the Hall conductance σ_{xy} matches the change of the filling factor ν of the quantized values of σ_{xy} according to Eq. 3.8. Even tough some of the lines do not match the exact position of the QH-plateau transitions in the Hall conductance σ_{xy} and the SdH peaks in the longitudinal resistance R_{xx} perfectly, the overall behavior is well described down to $B^{-1} \sim 0.25\,\mathrm{T}^{-1}$ ($B \sim 4\,\mathrm{T}$). The lower B^{-1} (higher B) region is marked in grey since the lower carrier densities reach their quantum limit in this magnetic field regime obstructing the analysis in this regime. Another consistency check is the comparison of the sum of all carrier density determined by the FFT analysis to the total carrier density determined by the Hall slope. The sum of the FFT densities yields $n_{1\mathrm{to}4} = 6.8 \times 10^{11}\,\mathrm{cm}^{-2}$, which matches the Hall density of $n_{\mathrm{Hall}} = 6.7 \times 10^{11}\,\mathrm{cm}^{-2}$ well. Additionally, the analysis of further magnetic field dependent measurements for multiple gate voltages, as shown in the following Sec. 3.4, also confirm all four identified peaks as individual conducting channels.
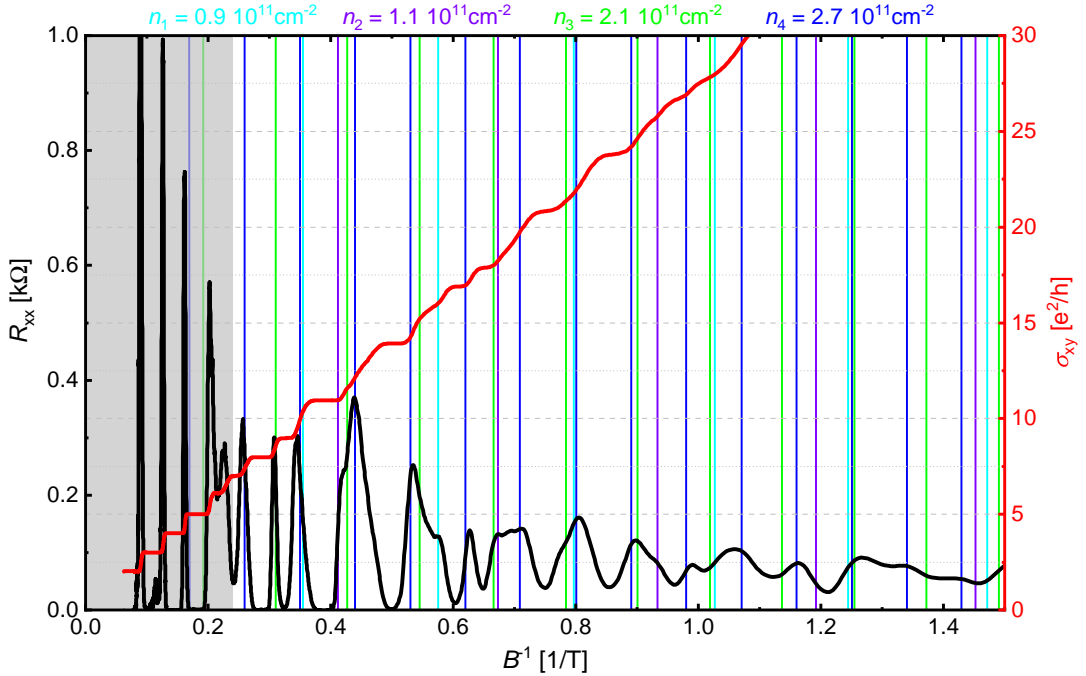
Figure 3.6: Shown is the longitudinal resistance R_{xx} (black) and the Hall conductivity σ_{xy} (red) as a function of the inverse magnetic field B^{-1} for the gate voltage $U_{\mathrm{gate}} = 0\,\mathrm{V}$ and the temperature $T = 0.05\,\mathrm{K}$. This is a repetition of the data shown in Fig. 3.5b). The periods in B^{-1} corresponding to the densities determined by the FFT analysis are shown as colored vertical lines with $n_1 = 0.9 \times 10^{11}\,\mathrm{cm}^{-2}$ (cyan), $n_2 = 1.1 \times 10^{11}\,\mathrm{cm}^{-2}$ (purple), $n = 2.1 \times 10^{11}\,\mathrm{cm}^{-2}$ (blue) and $n = 2.7 \times 10^{11}\,\mathrm{cm}^{-2}$ (green). The phase of the vertical lines is chosen to fit the observed peak positions in R_{xx}.

The observation of four transport channels might at first glance seem contradictory to the state of research magneto-transport results presented in Sec. 2.3.3. There the focus lies on the high magnetic field region for which only two transport channels are observed. These are interpreted as being the top and bottom topological surface states. To address this apparent contradiction, it has to be kept in mind, that the magnetic field strength necessary for the formation of Landau levels strongly depends on the carrier density. The visibility and contribution of the different transport channels to the overall trans-

port thus depend on the magnetic field strength. To be more explicit, for a carrier density of $n_{1,2} \sim 1 \times 10^{11}\,\mathrm{cm}^{-2}$, like the low density transport channels, the $\nu = 1$ QH-plateau is reached for $B_{\nu=1} \sim 3\,\mathrm{T}$, meaning that no further oscillations from integer Landau levels are expected (compare grey area of Fig. 3.6). In other words, an analysis for $B > 3\,\mathrm{T}$ is insensitive to transport channels with $n < 1 \times 10^{11}\,\mathrm{cm}^{-2}$, assuming that there are no further QH-plateau transitions once the filling factor $\nu = 1$ is reached. This analysis confirmed the existence of several transport channels. Two transport channels are assigned to the TSS of a 3D-TI. The origin of the other channels remains an open question. The gate voltage-dependent magneto-transport behavior in the low magnetic field regime is analyzed in more detail in the following.

3.3. QUALITATIVE ANALYSIS OF THE GATE VOLTAGE DEPENDENT MAGNETO-TRANSPORT

In this section, the influence of the top-gate onto the magneto-transport properties of the 3D-TI tensilely strained HgTe is introduced. For this analysis, the semi-classical magneto-transport regime at low magnetic fields is investigated. The obtained transport regimes are compared to the quantized high magnetic field regime, which is used to trace the dispersion of the Landau levels. The properties of the observed LL are investigated to find common properties to identify the number and type of transport channels.

3.3.1. ANALYSIS OF THE SEMI-CLASSICAL MAGNETO-TRANSPORT REGIME

As a starting point, the functionality of the gate is demonstrated. The longitudinal resistance R_{xx} is shown as a function of U_{gate} for $B = 0\,\mathrm{T}$ in Fig. 3.7a). The R_{xx} can be varied from $R_{xx}(U_{\mathrm{gate}} = 0) \sim 50\,\Omega$ by a factor ~ 4 up to a maximum of $R_{xx,\mathrm{max}} \sim 190\,\Omega$ at $U_{\mathrm{gate,max}} \sim -2.2\,\mathrm{V}$ down again to $R_{xx}(U_{\mathrm{gate}} = -5\,\mathrm{V}) \sim 120\,\Omega$. Additionally some other weak structures are visible in the $R_{xx}(B = 0\,\mathrm{T}, U_{\mathrm{gate}})$ curve for $U_{\mathrm{gate}} > -2\,\mathrm{V}$. This change of R_{xx} with U_{gate} happens over a change of the total carrier density from $n(U_{\mathrm{gate}} = 0\,\mathrm{V}) = 7.0 \times 10^{11}\,\mathrm{cm}^{-2}$ to $n(U_{\mathrm{gate}} = -5\,\mathrm{V}) = -4.3 \times 10^{11}\,\mathrm{cm}^{-2}$ as shown in Fig. 3.7b). The total carrier density n is determined by linear fits to the semi-classical Hall regime for the magnetic field range of $0.5\,\mathrm{T} < B < 1\,\mathrm{T}$, as described in Sec. 3.1.2. The Hall resistance R_{xy} is shown for exemplary gate voltages U_{gate} as a function of the magnetic field B together with the linear fits as dashed lines in Fig. 3.8. The fitting procedure works well for the electron transport regime for $U_{\mathrm{gate}} > -2.3\,\mathrm{V}$ ($n > 2 \times 10^{11}\,\mathrm{cm}^{-2}$), where the Hall slope is strictly linear (compare $U_{\mathrm{gate}} = 0\,\mathrm{V}$ in Fig. 3.8). For $U_{\mathrm{gate}} < -2.3\,\mathrm{V}$ the Hall signal shows oscillations indicating the onset of the quantum transport regime, questioning the reliability of a semi-classical analysis. These oscillations can be seen in Fig. 3.8 for $U_{\mathrm{gate}} = -2.5\,\mathrm{V}, -3\,\mathrm{V}$, and $-3.5\,\mathrm{V}$. The influence of these quantum effects depicts itself as deviation of the linear extrapolation to $B = 0\,\mathrm{T}$ from the $R_{xy}(B = 0\,\mathrm{T})$ value. This non-analyzable gate voltage range of $-2.3\,\mathrm{V} > U_{\mathrm{gate}} > -3.8\,\mathrm{V}$ is marked as grey area in Fig. 3.7b). The Hall resistance increases for all gate voltages U_{gate} for low magnetic fields and only for higher magnetic fields a change of the sign of the Hall slope for sufficiently negative gate voltages $U_{\mathrm{gate}} < -3.2\,\mathrm{V}$ is observed. The change from a positive Hall slope for low magnetic fields to a positive one for higher magnetic fields indicates the involvement of electrons and holes and consequently multiple transport channels. This multiple carrier behavior with changing positive to negative Hall slope with magnetic field is also observed for $U_{\mathrm{gate}} < -3.8\,\mathrm{V}$, but there a sufficiently linear magnetic field dependence

exists for $0.5\,\text{T} < B < 1\,\text{T}$ (see $U_{\text{gate}} = -5\,\text{V}$ in Fig. 3.8). This enables the determination of the total carrier density for $U\text{gate} < -3.8\,\text{V}$. Thereby the observed QH-plateaus for $U_{\text{gate}} = -4\,\text{V}$ and $-2\,\text{V}$ in Fig. 3.8 are treated as linear slope. This procedure is chosen, since the QHE can be treated as symmetric deformation of the Hall resistance $R_{xy}(B)$ around the semi-classical linear behavior and therefore does not change the obtained slope.
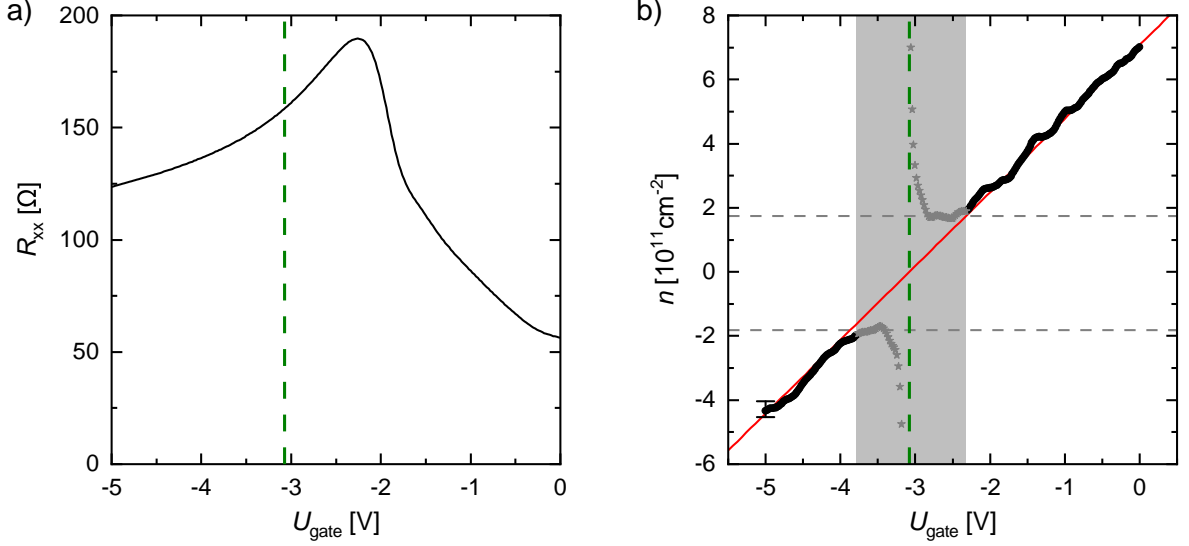
Figure 3.7: In a) the longitudinal resistance R_{xx} is shown for the magnetic field $B = 0\,\text{T}$ as function of the gate voltage U_{gate} at the temperature $T = 0.05\,\text{K}$. The expected gate voltage U_{gate} for zero density is indicated as a dashed olive line. The carrier density n is determined by linear fits to the Hall resistance $R_{xy}(B)$ for $0.5\,\text{T} < B < 1\,\text{T}$ and shown in b) as black circles. The gate voltage range with no analyzable Hall slope is marked in grey and the symbols are shown as grey stars. The red line is a linear fit disregarding the grey area. The expected value for the gate voltage for zero overall density, estimated by the linear fit, is indicated as a dashed olive line. The horizontal grey dashed lines indicate the reliable density range.

These determined densities for $U_{\text{gate}} < -3.8\,\text{V}$ and $U_{\text{gate}} > -2.3\,\text{V}$ as indicated by the white background in Fig. 3.7b) allow to determine the gate action by a linear fit. The linear fit yields a gate action of $2.3 \times 10^{11}\,\text{cm}^{-2}/\text{V}$ with $n(U_{\text{gate}} = 0\,\text{V}) = 7.0 \times 10^{11}\,\text{cm}^{-2}$, which is shown as a red line in Fig. 3.7b). This linear fit gives $U_{\text{gate,cn}} \sim -3.2\,\text{V}$ for the charge neutrality point. The possibility to describes the gating behavior for the electron and hole regime with one single linear fit points towards a gapless system, see discussion about quantum capacitance in Sec. 4.1. This is consistent with the observation of simultaneous electron and hole transport. Interestingly the maximum of the longitudinal resistance $R_{xx,\text{max}}$ at $U_{\text{gate}} \sim 2.2\,\text{V}$ does not coincide with the charge neutrality point at $U_{\text{gate,cn}} \sim 3.2\,\text{V}$ as indicated by the dashed olive line in Fig. 3.7a). The charge neutrality point is not represented by any specific features for $B = 0\,\text{T}$. The overall shape of the longitudinal resistance $R_{xx}(B = 0\,\text{T}, U_{\text{gate}})$ shall here only be noted as a zero-field peculiarity and the interested reader is referred to Ref. [58]. There the shape of the $R_{xx}(B = 0\,\text{T}, U_{\text{gate}})$ curve is modeled using a multiple channel Drude model with the respective parameters extracted from band structure calculations, like the one shown in Fig. 2.6g).
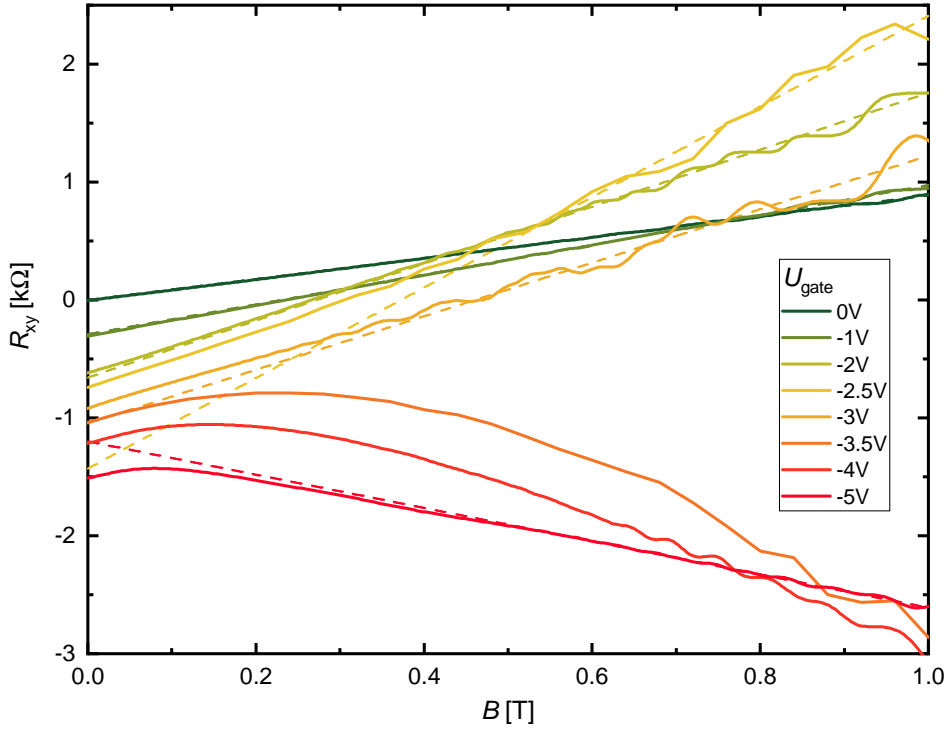
Figure 3.8: The Hall resistance R_{xy} is shown as function of the magnetic field B for gate voltages $U_{\text{gate}} = -5\,\text{V}, -4\,\text{V}, -3.52\,\text{V}, -3\,\text{V}, -2.52\,\text{V}, -2\,\text{V}, -1\,\text{V}$, and $0\,\text{V}$ (from green to red) at the temperature $T = 0.05\,\text{K}$. The curves are offset by $U_{\text{gate}} \times 300\,\Omega$ for clarity. The $U_{\text{gate}} = -3.52\,\text{V}$ and $-2.52\,\text{V}$ traces are measured at lower magnetic field resolution. Linear fits to the data for $0.5\,\text{T} < B < 1\,\text{T}$ are shown as dashed lines.

To sum up, already from the semi-classical transport regime HgTe is classified as a gapless system. The electron-dominated transport regime shows a strictly linear Hall slope, which indicates transport by one band or multiple bands with similar mobility. The hole-dominated regime is characterized by a positive slope for small magnetic fields that converts into a negative slope. Parallel to the hole channel is a more mobile electron channel present. Such behavior is consistent with a semi-metal composed of an electron-like band that overlaps with a less mobile hole-like band. More information about these bands is accessible in the quantum transport regime which is addressed in the following.

3.3.2. Qualitative investigation of the Landau level dispersion

In this Section, the focus is shifted from the low magnetic field regime to higher magnetic fields, where the transport starts to be quantized due to the formation of LLs. The aim is to trace and analyze the dispersion of the LLs with the magnetic field and gate voltage to extract further information about the underlying band structure. Intuitive access to the LLs constitute the peaks in the longitudinal resistance, which appear when LLs cross the Fermi energy, as described in Sec. 3.2. Consequently, the longitudinal resistance R_{xx} is measured as function of the gate voltage U_{gate} for various fixed magnetic field values B. The result is shown in Fig. 3.9 as color code. The blue areas represent very low values (effectively zeros) of the longitudinal resistance R_{xx} which are equivalent to no states in the bulk, while colorful areas of high resistance indicate the existence of states and the position of LLs. The colorful lines in the color plot of the longitudinal resistance R_{xx} can be seen as the dispersion of the LLs with respect to the gate voltage U_{gate} and the magnetic field B.

The dark red region around $U_{gate} \sim -3\,V$ constitutes an exception, since this U_{gate} resembles the regime of low total carrier density as determined by the semi-classical analysis depicted in Fig. 3.7. Low carrier densities, especially compensated ones [3], are expected to experience a strong increase of the longitudinal resistance with the magnetic field B called positive magneto-resistance (MR). The dark red region around $U_{gate} \sim -3\,V$ separates two regions of red lines with either positive (electron-like) slope for $U_{gate} > -3\,V$ or negative slope (hole-like) for $U_{gate} < -3$. Additionally, nearly vertical lines are visible which represent gate voltage-independent LLs. To interpret these results we first try to sort these LL based on their dispersion in B and U_{gate}, before a more quantitative analysis based on FFT analysis as in Sec. 3.2 is utilized.
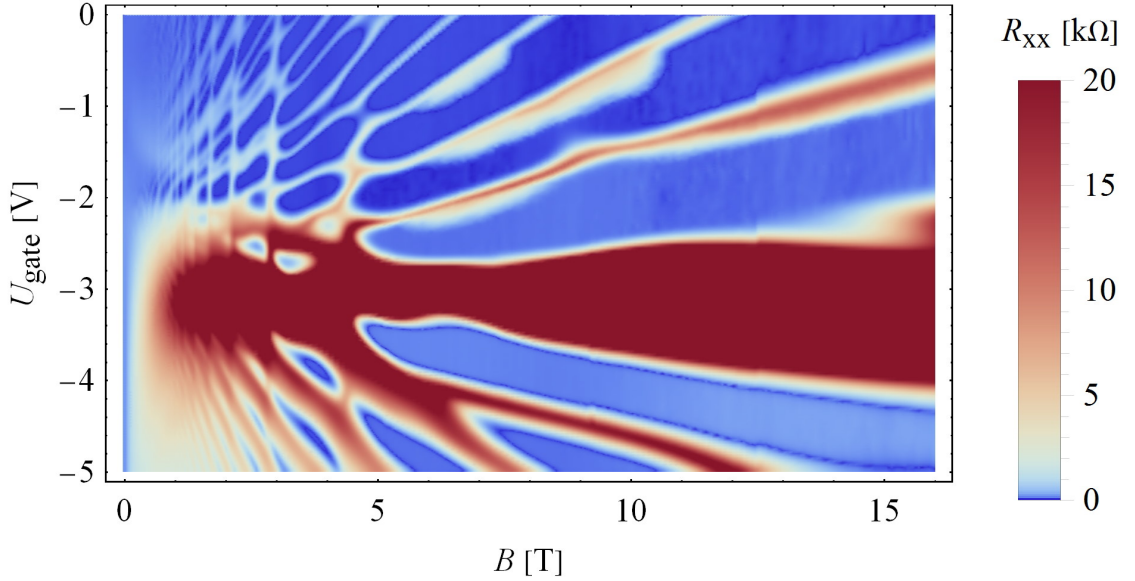
Figure 3.9: The longitudinal resistance R_{xx} is shown as color code in function of the magnetic field B and the top gate voltage U_{gate} at the temperature $T = 0.05\,K$.

As a reference, the expectation for a simple system is refreshed. According to Eq. 3.7 in a system with only one transport channel LLs disperse linearly with respect to $U_{gate} \propto n$ and B irrespective of their dispersion in energy. For high magnetic fields $B > 6\,T$, the experimental observed Landau levels indeed disperse linearly and appear to emerge from one origin for $B \to 0\,T$. To verify this observation a better resolution of the LLs in the low density regime ($U_{gate} \sim -3\,V$) is desirable. For an alternative way of visualizing the LL dispersion, which does not suffer from the strong MR, the Hall conductance σ_{xy} signal is used. Thereby the LL-position is extracted from the transition between QH-plateaus with a steep slope compared to the flat QH-plateaus. The derivative of the Hall conductance with respect to the gate voltage $\partial\sigma_{xy}/\partial U_{gate}$ is shown in Fig. 3.10, where high $\partial\sigma_{xy}/\partial U_{gate}$ values (in red) represent the LLs. The dispersion of the LLs is consistent for Fig. 3.9 and 3.10 and only differs in the visibility of the different features. The most distinct difference is that the longitudinal resistance R_{xx} data in Fig. 3.9 shows a broad region with high resistance around $U_{gate} \sim -3\,V$, while a plateau with $\partial\sigma_{xy}/\partial U_{gate} = 0$ is observed in Fig. 3.10. This plateau is enclosed by two sharp lines of high $\partial\sigma_{xy}/\partial U_{gate}$ and possesses a value of $\sigma_{xy} = 0\,e^2/h$ as shown in in Fig. 3.10b). Such a state with $\sigma_{xy} = 0$ is an interesting system in itself and could

---

[3]Compensated means the low total carrier density is due to the coexistence of electrons and holes.

be either due to a gap opening, as observed in zero-gap HgTe quantum wells in Ref. [67] or the cancellation of counter-propagating edge channels as a suggested mechanism to explain the zero QH-plateau observed in bismuth chalcogenides [48, 68]. Since the electron and hole-like LLs are observed to coexist, the most likely mechanism is the cancellation of electron and hole-like edge channels, as investigated in detail in Ref. [69].

To verify that all observed lines for $B > 6\,\mathrm{T}$ indeed behave as one set of LLs, a constant magnetic field cut at $B = 10\,\mathrm{T}$ a dashed black line at $B = 10\,\mathrm{T}$ is shown in Fig. 3.10 and equidistant steps are indicated by dotted black lines. This shows that the LL are indeed equidistant in U_{gate} as expected for a single set of LLs. The observed LL dispersion, which is consistent with the expectation for one conducting channel or equivalently one occupied band, is surprising and noteworthy in a complex material as tensilely strained HgTe (compare the band structure shown in Fig. 2.6). One possible mechanism is the in Sec. 3.2.2 motivated expected quantum limit for transport channels with low densities already at moderate magnetic fields [$B_{\mathrm{ql}}(\mathrm{n} = 1 \times 10^{11}\,\mathrm{cm}^{-2}) \sim 3\,\mathrm{T}$]. Reaching the quantum limit could cause a redistribution of the charge carriers between the transport channels in the magnetic field [70, 71]. For an assessment of this mechanism and further analysis of this transition with the magnetic field to a simple LL dispersion see Ref. [58].
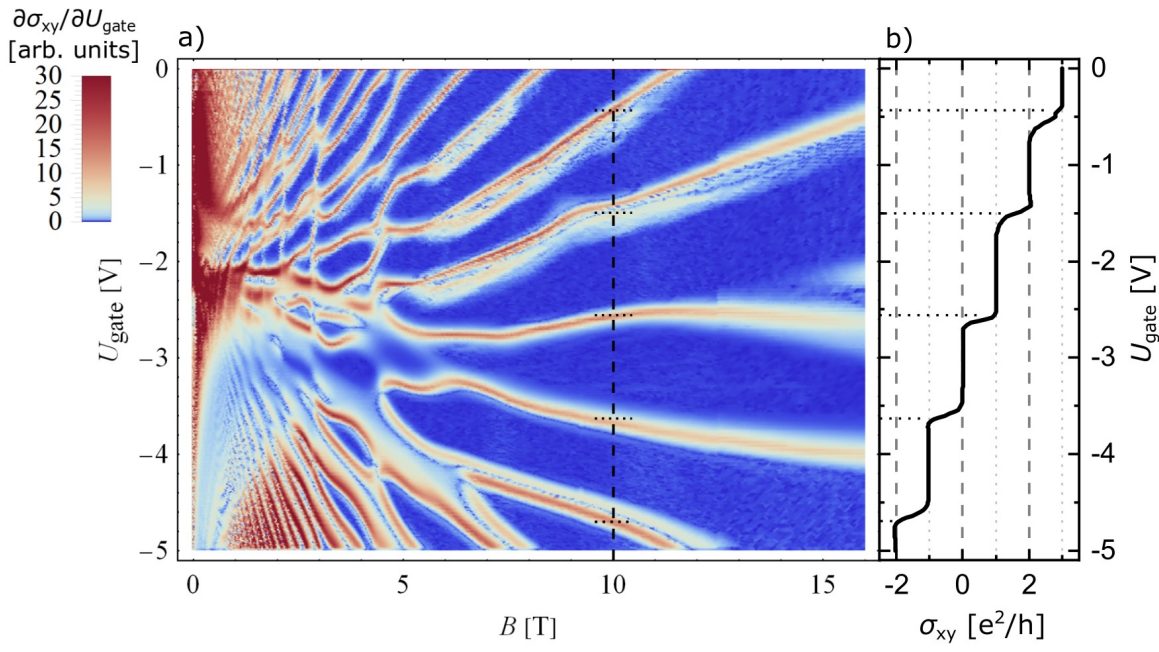
Figure 3.10: The derivative of the Hall conductivity with respect to the gate voltage $\partial\sigma_{xy}/\partial U_{\mathrm{gate}}$ is shown in color code as function of the magnetic field B and the top gate voltage U_{gate} at the temperature $T = 0.05\,\mathrm{K}$. The dashed black line marks a cut at constant magnetic field $B = 10\,\mathrm{T}$ with equidistant markers as short dotted black lines.

In contrast, the low to moderate magnetic field regime displays a completely different behavior. The LL dispersion for $B < 6\,\mathrm{T}$ in Fig. 3.9 and 3.10 seems quite overwhelming and complicated at first glance. The observed lines are grouped based on their dispersion. It shall be remarked here, that in Ref. [71] also qualitatively similar complicated LL dispersions are observed for 80 nm thick tensilely strained HgTe layers. The details of the dispersion, as the observed bending at the crossing points of some LLs, are not relevant for the assignment of the LL into groups. Such bending and deviation from the expected lin-
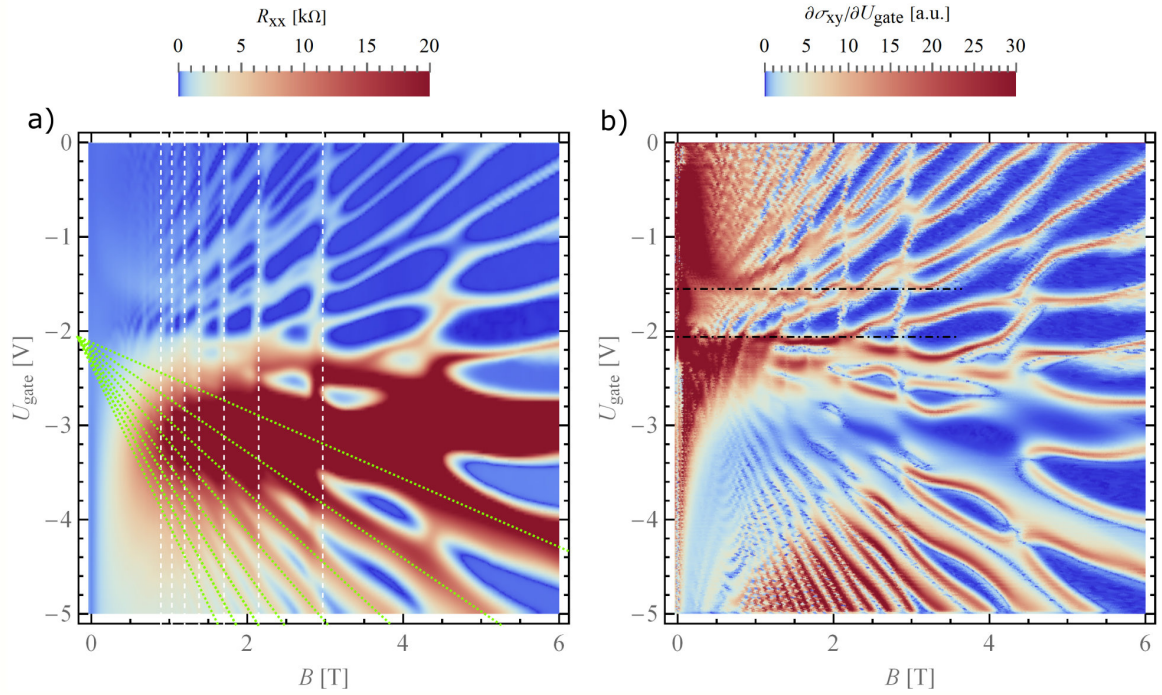
Figure 3.11: In a) the longitudinal resistance R_{xx} is presented again (see Fig. 3.9) as a function of the magnetic field B and gate voltage U_{gate} up to $B = 6$ T. The dashed white and dotted green lines are guides to the eye to mark two sets of LLs. In b) the derivative of the Hall conductivity with respect to the gate voltage $\partial\sigma_{xy}/\partial U_{gate}$ from Fig. 3.10 is re-plotted and dot-dashed black lines marking the edge of the deep red areas are added as guides to the eye.

ear behavior have been observed before in double quantum well structures for example in Ref. [72] and in 80 nm thick tensilely strained HgTe layers in Ref. [71]. The bending is there attributed to charge redistribution between the transport channels in the magnetic field. The differentiation between such charge redistribution and interaction effects is addressed in Ref. [58]. The focus of this work lies in the extraction of the involved transport channels and their identification in the band structure.

The most prominent group of LLs in Fig. 3.9 are the dark red lines with negative slope, which are marked by dotted green lines in Fig. 3.11a) and extrapolated to $B = 0$ T to one starting point at $U_{gate} \sim 2.0$ V. The shared origin is consistent with the assignment of the LL to one transport channel. Another distinct set of lines with shared gate voltage and magnetic field dependence constitute the nearly vertical lines, which are very distinct for $U_{gate} > -2$ V but persist down to the maximum investigated gate voltage $U_{gate} = -5$ V. This continuation $U_{gate} < -2$ V is best visible for $B \sim 3$ and 5 T. These LLs are marked with dashed white lines in Fig. 3.11a). These LLs are independent of the applied gate voltage, in contrast to the before discussed set of LLs (dotted green lines), which possess a hole-like gate voltage dependence. Additionally, gate voltage-dependent lines with positive slopes identifying them as electron-like LL are visible. These lines cannot straightforwardly be assigned to one set of LL due to their more complex structure with crossings. These LLs are thus not indicated as an own set of colored lines.

The same analysis is also possible for the $\partial\sigma_{xy}/\partial U_{\text{gate}}$ data, shown in Fig. 3.10 and repeated in Fig. 3.11b). The two different visualizations of the LLs illustrate different features differently well [4]. The thick p-type LLs, marked by the dotted green line in Fig. 3.11a), are revealed as each line being two weakly split LLs. This dotted green p-type set of LLs is double degenerate and appears like a normal 2DEG with its spin degeneracy lifted by the Zeeman effect. The nearly vertical set of LLs (white dashed in Fig. 3.11a)) are not as prominent, but can still be recognized for moderate magnetic fields.

Very pronounced features are the two dark red edges at $U_{\text{gate}} \sim -2.05\,\text{V}$ and $U_{\text{gate}} \sim -1.65\,\text{V}$, marked as dash-dotted black line in Fig. 3.11b). The lower black line coincides with the starting point of the dotted green lines in Fig. 3.11a). Similarly exist lines in Fig. 3.11b) that appear to start from the upper black dash-dotted line at $U_{\text{gate}} \sim -1.65\,\text{V}$. The dash-dotted black lines indicate a gap-like feature between an electron-like dispersing set of LLs and a hole-like one. In contrast to these two sets of LLs with starting points, the before mentioned vertical lines span the whole investigated gate voltage range. Between the two dash-dotted black lines are more lines with a positive dispersion visible additionally to these vertical lines visible. These lines are the fourth set of LLs. This analysis gives evidence for the existence of a spin split hole-like band for $U_{\text{gate}} < -2\,\text{V}$, a gate voltage-independent electron-like band, and two additional electron bands. One of these bands is observable over the whole accessible gate voltage range and the other one only for $U_{\text{gate}} > -1.65\,\text{V}$. The origin of these bands has to be further investigated.

3.4. QUANTITATIVE ANALYSIS OF THE LANDAU LEVEL DISPERSION

To determine the densities of the above-identified four conducting channels a FFT analysis is used as introduced in Sec. 3.2. The FFT analysis is the easiest way of determining the respective carrier densities in a system with multiple transport channels. The FFT analysis of the $R_{xx}(B, U_{\text{gate}})$ data is shown in Fig. 3.9. The amplitudes of the FFT frequencies are obtained with the program "Mathematica 12" and shown in Fig. 3.12a) color coded as function of the gate voltage U_{gate} and the corresponding frequency expressed as nondegenerate density $n_{\text{nondegenerate}}$. Yellow represents high amplitudes indicating the position of the FFT peaks corresponding to the encountered carrier densities for the respective gate voltage. The resulting peak positions of an independent FFT analysis with the program "Origin2018" are shown in Fig. 3.12 as colored circles. These colors are used to simplify the reference to the determined transport channels. The integer gate voltages are the results for separate magnetic field dependent measurements, while for the gate voltages $U_{\text{gate}} = -0.5\,\text{V}, -1.5\,\text{V}, ..., -4.5\,\text{V}$ the traces are extracted from the gate voltage-dependent measurements for a fixed magnetic field. The results are consistent independent of the analysis details, making them reliable and trustworthy. For more verification see appendix D.

The FFT results are effectively only an alternative way of representing the LL dispersion discussed in Sec. 3.3. The most prominent feature is the bright yellow nearly vertical and consequently gate voltage independent line at $n_{\text{non-degenerate}} \sim 2.0 \times 10^{11}\,\text{cm}^{-2}$ and equivalently the green dots in Fig. 3.12. These are reminiscent of the gate voltage independent lines highlighted as dashed white lines in Fig. 3.11a). The density determined by the FFT can be verified by estimating the distance of the dashed white lines in the inverse mag-

---

[4]Vertical lines are not very well depicted in the $\partial\sigma_{xy}/\partial U_{\text{gate}}$ data due to the direction of the derivative. The direction is chosen to avoid artifacts due to the measurement scheme of varying the gate voltage at a fixed magnetic field for various magnetic field values.

3
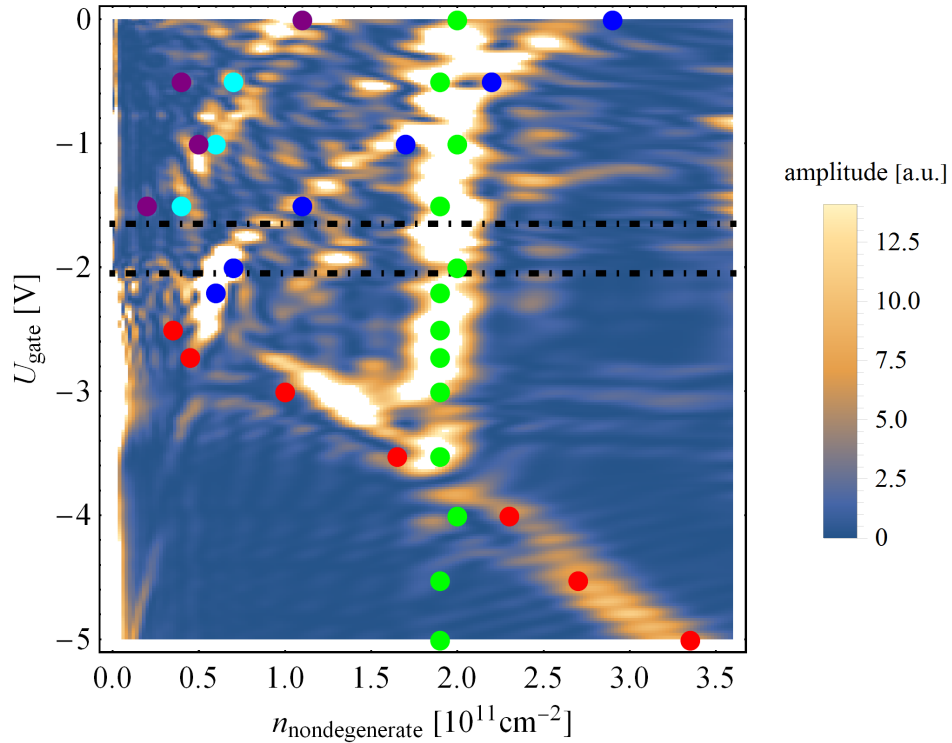
Figure 3.12: Shown is the result of the FFT analysis of the longitudinal resistance data. The respective amplitudes for the non-degenerate density $n_{\text{non-degenerate}}$ is presented as function of the applied gate voltage U_{gate}. The FFT analysis is performed with "Wolfram Mathematica 11.3" for the magnetic field range of 0.08 T to 2 T - to ensure a sufficient measurement point density and sinusoidal looking oscillations - using a Dirichlet Window following the procedure introduced by Valentin Müller in Ref. [58]. The points from an equivalent analysis with the program "Origin2018" are included as colored circles (integer voltages show analyzes from a separate data set of magnetic field-dependent measurements). Additionally guides to the eye at the same position as in Fig. 3.11b) are added for orientation.

netic field B^{-1}. This yields $n_{\text{est}} \sim 1.9 \times 10^{11}\,\text{cm}^{-2}$ consistent with the value from the FFT analysis of $n_{\text{non-degenerate}} \sim 2.0 \times 10^{11}\,\text{cm}^{-2}$. Another clear feature is the bright diagonal line or equivalently the red dots in Fig. 3.12 visible for $U_{\text{gate}} < -2.0\,\text{V}$. The red dotted density $n_{\text{non-degenerate}}$ increases with decreasing (more negative) gate voltage, identifying this transport channel as hole-like. The observed gate voltage dependence and range are reminiscent of the green dotted set of LL in Fig. 3.11a). The starting point of $U_{\text{gate}} \sim -2.0\,\text{V}$ coincides with the lower dash-dotted black line. The two dash-dotted black lines are adopted from Fig. 3.11b) to facilitate the comparison to the qualitative analysis of Sec. 3.3.

Additionally, three features in the FFT results are observed indicated by blue, cyan, and purple circles. The density of all three signals increases with increasing (less negative) gate voltage, identifying these states as electron-like. The cyan and purple lines are reminiscent of a double degenerate state with slightly lifted degeneracy, which appears to emerge from $U_{\text{gate}} \sim -1.6\,\text{V}$ consistently with the upper dash-dotted black line. In contrast, the state marked with the blue dots emerge from outside the available gate voltage range $U_{\text{gate}} < -5\,\text{V}$, as does the gate voltage-independent state marked with green dots. The FFT amplitude of this state is relatively week up to $U_{\text{gate}} \sim -2.0\,\text{V}$ and only possesses a weak dependence on U_{gate} for $U_{\text{gate}} < -2\,\text{V}$. For $U_{\text{gate}} > -2\,\text{V}$ (above the lower dash-dotted black line) the FFT amplitude and dependence on gate voltage increases abruptly.
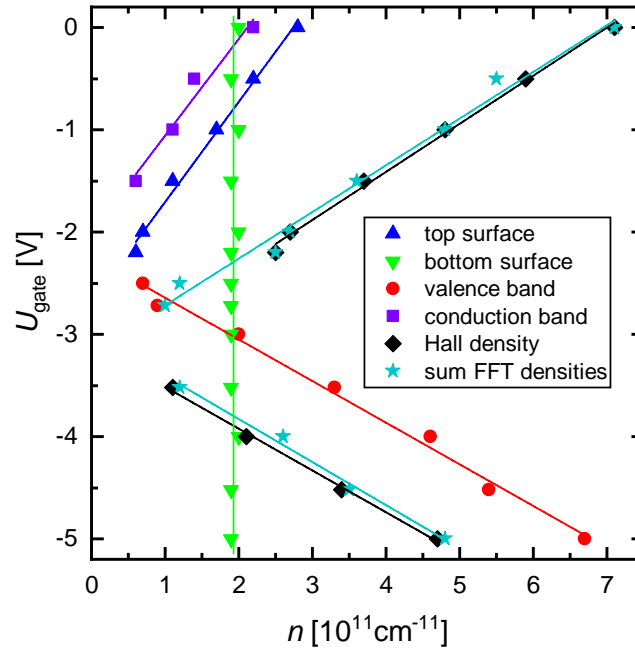
Figure 3.13: The resulting density from the FFT analysis with correctly accounted degeneracy is shown together with their sum and the total carrier density determined by the semi-classical Hall slope from Fig. 3.7b).

The identified transport channels can be grouped according to their shared properties. The first group consists of the two transport channels, which are electron-like and observable over the full gate range without any signs of degeneracy. The second group consists of the two transport channels, which are degenerate and only observable over a limited range of gate voltages despite their opposite carrier type. These two channels are the electron channel marked in cyan and purple as well as the hole channel marked with red dots. While the degeneracy of the electron states is directly visible, the degeneracy of the hole states is only visible as splitting of the hole type LL in Fig. 3.11b) for high magnetic fields. The splitting is not directly observable in the FFT analysis. The observed degeneracy of the hole LLs in the $\partial\sigma_{xy}/\partial U_{\text{gate}}$ data is not an artifact due to the derivative. This is verified by the comparison of the sum of the individual densities determined by the FFT analysis to the total carrier density determined by linear fits to the Hall slope. As shown in Fig. 3.13, a double degeneracy of the hole states is necessary to match the total densities.

Since tensilely strained HgTe is a three dimensional topological insulator with the band structure shown in Fig. 2.6, an educated guess for the origin of the respective transport channels can be made and is introduced as nomenclature to simplify the reference to the respective states. One type of state shown in the band structure is the topological surface state. These are non-degenerate and expected to exist over the whole experimentally accessible energy range (compare Fig. 2.6g)). This makes the first group likely topological surface states. Since the gate voltage is applied from the top, the surface state on the top side is expected to show a stronger gate voltage dependence, while the gate voltage dependence of the bottom surface state depends on the assumed screening scenario. The blue dotted density thus is identified as the top TSS according to its observed gate voltage dependence. Consequently, the gate voltage-independent green dotted density is assigned to the bottom TSS. The gate voltage independence of the bottom TSS is consistent with the observation in uncoupled double 2DEGs, where the electric field from the top electrode is

completely screened by the top 2DEG making the bottom 2DEG gate voltage independent (see e.g. [73]). The Thomas-Fermi screening properties of the TSS are discussed in the appendix A and support analogous this expectation of screening by the top 2DEG. In contrast, the former conduction and valence bands are expected to be spin degenerate and should only be occupied, when the Fermi level is moved into the respective band. But since these bands are expected to be three-dimensional, they are inconsistent with the observation of QHE a purely two-dimensional effect. This requires the creation of new two-dimensional states, here called Volkov-Pankratov states following Ref. [16, 34, 74]. The origin and nature of Volkov-Pankratov state (VPS) is in Sec. 4.4 discussed. The black dash-dotted line represents a bandgap between the electron-type VPS (cyan and purple circles) and the hole-like VPS (red circles). This assignment is verified with the help of model calculations in the following Section.

4

MODELING OF THE MAGNETO-TRANSPORT RESULTS

Analyzing the magneto-transport data offers insights into the number and properties of the involved transport channels. Unfortunately, the measurement data alone is not sufficient to reconstruct the band structure. Model calculations are additionally necessary. An obstacle for the unification of the experimental and theoretical results are their different accessible quantities, namely the gate voltage and the energy, respectively. Translating these two quantities into each other is not straightforward. Two different approaches are presented in this Chapter. Motivated from the experimental point of view, the sample is described as a plate capacitor. The finite DOS of the HgTe layer is accounted for by its quantum capacitance, as motivated by the high-frequency measurements discussed in Chapter 5. An equivalent capacitor circuit is created accounting for the capacitances of all involved states. This model is compared to the experimental results of Sec. 3.3. The model is translated into a relative filling and consequently respective energetic shift of the different states in the HgTe layer. The theoretical approach uses self-consistent $k \cdot p$ calculations. The Kane model is introduced, and the results of the calculations are presented. Those show indications for the formation of additional surface states called Volkov-Pankratov states.

4.1. CAPACITOR MODEL

The investigated Hall-bar device is a plate capacitor, as sketched in Fig. 4.1. The overall carrier density in the HgTe layer is thus directly proportional to the gate voltage. This linear dependence is verified in Fig. 3.7b) of Sec. 3.3, where the density determined from the slope of the Hall resistance is shown as a function of the gate voltage. Different states of the HgTe layer contribute to the capacitance of the layer. To disentangle the charge carrier density distribution inside the HgTe layer a capacitor circuit model is used. The resulting charge carrier density distribution from the model is compared to the measurement results. Eventually, an equivalent representation of capacitor circuit as band structure is presented, and its physical implications are discussed.

4.1.1. OPERATION OF THE GATE

The capacitance of a plate capacitor normalized to the area [1] C_{geo} is given by

$$C_{\text{geo}} = \frac{ne}{U_{\text{gate}}} = \epsilon_0 \epsilon_{\text{r}} \frac{1}{d}, \tag{4.1}$$

where e the elementary charge, ϵ_0 the vacuum permittivity, ϵ_{r} the relative permittivity, and d the separation of the plates. The dielectric is composed of a 110 nm thick dielectric layer consistent of 11 alternating layers of SiO_2 and Si_3N_4 with the relative permittivities $\epsilon_{SiO_2} = 3.9$ and $\epsilon_{Si_3N_4} = 7.5$ as well as the 50 nm thick $Cd_{0.7}Hg_{0.3}Te$ capping layer with an estimated relative permittivity $\epsilon_{CdHgTe} \sim 8.5$ [50, 74]. The capacitance of such a layer stack can be described as two standard plate capacitors in series yielding

$$C_{\text{tot}}^{-1} = C_{\text{geo,insulator}}^{-1} + C_{\text{geo,cap}}^{-1}. \tag{4.2}$$

The insulator multilayer is effectively also series of capacitors with the single capacitances given by Eq. 4.1. This yields for the capacitance of the multilayer

$$C_{\text{geo,insulator}}^{-1} = \sum_{i=1}^{6} \frac{d_{SiO_2}}{\epsilon_0 \epsilon_{SiO_2}} + \sum_{i=1}^{5} \frac{d_{Si_3N_4}}{\epsilon_0 \epsilon_{Si_3N_4}} \tag{4.3}$$

with $d_{SiO_2} = d_{Si_3N_4} = 10$ nm. Even though equation 4.1 assumes metal plates, the total carrier density n_{tot} introduced in the HgTe layer is well described by this simple model as shown in Fig. 3.7b). Tensilely strained HgTe is actually a topological insulator with a finite DOS $D = \frac{\partial n}{\partial E_F}$. The states of interest are its topological surface states which possess a two-dimensional linear dispersion

$$E(k) = \hbar v_F k, \tag{4.4}$$

where v_F is the Fermi-velocity. Their two-dimensional DOS is given by

$$D_{\text{lin;2D}}(E) = \frac{g}{2\pi \hbar^2 v_F^2} E \tag{4.5}$$

with $g = 1$ being the degeneracy factor. The finite DOS of the surface states causes a change of the system's energy when its carrier density is altered. This is of course not only true for a TSS with linear dispersion but all systems with a finite DOS. The energy dependence of the DOS is given by the dispersion of the band. Generally, this energy can be expressed in the form of a capacitance, called quantum capacitance

$$C_{\text{q}} = e^2 \frac{\partial n}{\partial E_F}. \tag{4.6}$$

For topological surface states the electrochemical potential dependent quantum capacitance is determined by using Eq. 4.4 and Eq. 4.6 and reads

$$C_{\text{q,lin;2D}}(E_F) = \frac{g e^2}{2\pi \hbar^2 v_F^2} E_F. \tag{4.7}$$

---

[1]The capacitance C is in this work always given normalized to the area for convenience.

A schematic illustration of the quantum capacitance is shown in Fig. 4.1. The sketched plate capacitor consists of a metal top plate (yellow), an insulator layer (black), and the HgTe layer as the bottom plate (blue). The metallic top plate is represented by an exemplary quadratic dispersion shown in the yellow frame. An experimentally realistic change in carrier density of $\Delta n \sim 5 \times 10^{11}\,\mathrm{cm}^{-2}$ only causes an insignificant change in energy. In contrast for the dispersion of a TSS leads $\Delta n \sim 5 \times 10^{11}\,\mathrm{cm}^{-2}$ to a significant change in the energy of the system in the order of $10\,\mathrm{meV}$ to $100\,\mathrm{meV}$, which cannot be neglected any longer. This additional energy cost can be expressed in the form of the quantum capacitance (see Eq.4.6), which enables the creation of equivalent circuit diagrams.
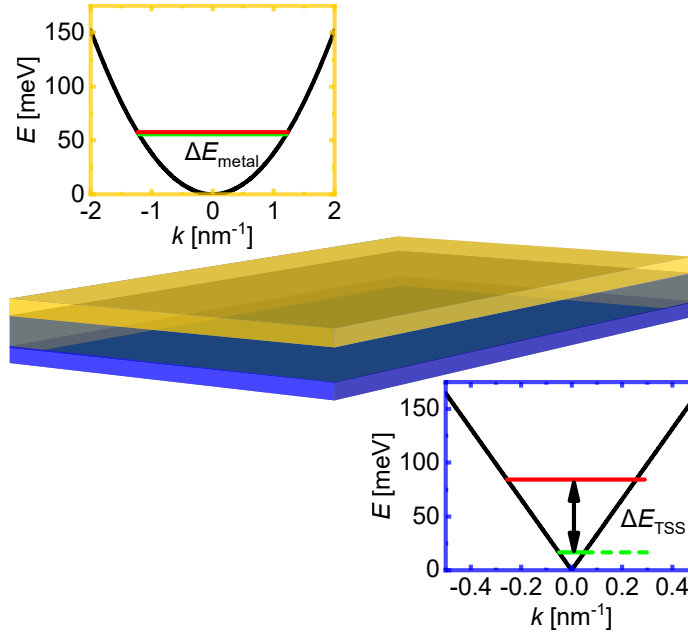
Figure 4.1: A plate capacitor composed of a metal top plate (yellow), the insulator (black), and a TI bottom plate (blue) is sketched together with the dispersion of a metal plate on the top left and the dispersion of a topological surface state on the bottom right. The expected energy difference for a density change of $\Delta n \sim 5 \times 10^{11}\,\mathrm{cm}^{-2}$ is indicated by the starting energy (green line) to the expected energy (red line).

4.1.2. THE HETEROSTRUCTURE AS CAPACITOR CIRCUIT

The above-introduced possibility to represent the band structure of HgTe as quantum capacitance is used to create an equivalent circuit diagram in this Section. This circuit diagram describes the distribution of the charge carriers in the HgTe layer. The simplest equivalent circuit diagram that describes our Hall bar structures consists of two capacitances in series, as shown in Fig. 4.2a). The first capacitance is the geometric capacitance between the Au-electrode and the HgTe layer C_{geo}. The geometric capacitance is given by the properties of the insulating and capping layer. The second capacitance is by the quantum capacitance of the HgTe layer $C_{\mathrm{q,HgTe}}$.

To determine $C_{\mathrm{q,HgTe}}$ the electrochemical potential is assumed to lie in the bulk bandgap according to the state of the art of research as described in Sec. 2.3.4. This means that only the TSSs on the top and bottom surface have to be accounted for. Since both TSS are contacted via the Au/Ge contacts, both states are connected to the ground potential, making the two TSSs act as parallel capacitances. Since the bottom TSS is located at the bottom
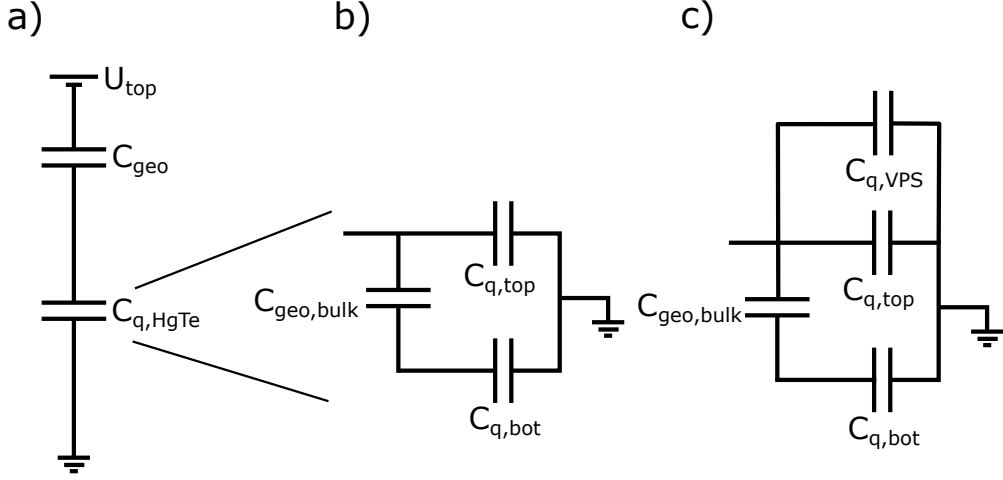
Figure 4.2: In a) the equivalent capacitor circuit is shown that represents the actual device by accounting for the quantum capacitance of the HgTe layer C_{HgTe}. In b) the equivalent circuit used to determine the quantum capacitance of the HgTe layer C_{HgTe} for the bulk bandgap is shown. In c) the equivalent circuit including either the valence or conduction band like VPS is presented.

surface of the HgTe layer, the HgTe bulk has to be taken into account as well. Since the Fermi energy is assumed to lie in the bulk bandgap as mentioned before, the HgTe bulk is an insulator and thus only contributes with its geometric capacitance. The capacitive contribution from the bottom TSS hence consists again of two capacitances in series, one being the geometric capacitance of HgTe $C_{\mathrm{geo,HgTe}}$ and the quantum capacitance of the bottom TSS $C_{\mathrm{q,bot}}$. In total the quantum capacitance of the HgTe layer $C_{\mathrm{q,HgTe}}$ is a parallel circuit of the top TSS $C_{\mathrm{q,top}}$ with the parallel capacitance given by $C_{\mathrm{q,bot}}$ in series with $C_{\mathrm{geo,HgTe}}$, as shown in Fig. 4.2b) [57, 75, 76]. To determine the voltage drop across the different contributing parts of the HgTe layer the definition of the capacitance

$$C = \frac{Q}{U} \tag{4.8}$$

is used. The equivalent circuit diagram, as shown in Fig. 4.2b), infers that mainly the top TSS will be affected by the applied top gate voltage. To quantify this statement, the actual values of the capacitances need to be determined. Taking into account the sample dimensions, as shown in Fig. 2.7a), the geometric capacitances can be determined following Sec. 4.1.1 by adding the reciprocal capacitances. Summing up the capacitances of the insulator and the $\mathrm{Cd_{0.7}Hg_{0.3}Te}$ capping layer yields $C_{\mathrm{geo}} \sim 0.33 \times 10^{-3}\,\mathrm{F/m^2}$. The exact parameters for the capping layer are not well known. Only accounting for the insulator layer, the geometric capacitance yields $C_{\mathrm{geo,only\,ins}} \sim 0.40 \times 10^{-3}\,\mathrm{F/m^2}$. Using $\epsilon_{\mathrm{HgTe}} = 21$ (see Sec. 2.3.4) the geometric capacitance of the HgTe layer reads $C_{\mathrm{geo,HgTe}} = 2.5 \times 10^{-3}\,\mathrm{F/m^2}$. To determine the quantum capacitances, the energy dependence of Eq. 4.6 is translated into the experimentally more accessible quantity density n. With the expression for the Fermi wave vector of a non-degenerate 2DEG

$$k_{\mathrm{F}} = \sqrt{4\pi n} \tag{4.9}$$

and the linear energy dispersion of the TSS according to Eq. 4.4 the quantum capacitance of a TSSs reads

$$C_{\mathrm{q,TSS}} = \frac{e^2}{h v_{\mathrm{F}}} \sqrt{4\pi n}. \tag{4.10}$$

For a TSS with a density of $n = 2 \times 10^{11}\,\text{cm}^{-2}$ this yields $C_{\text{q,surf}}(n = 2 \times 10^{11}\,\text{cm}^{-2}) = 12 \times 10^{-3}\,\text{F/m}^2$. The first result is that the quantum capacitance only contributes $\sim 2\%$ to the total capacitance. The total capacitance is thus dominated by the geometric capacitance. Because of this, the calculated geometric capacitance C_{geo} can be compared to the capacitance determined by the gate voltage-dependent magneto-transport measurements as shown in Fig. 3.7b). The dependence of the experimentally determined total carrier density on the gate voltage yields the capacitance $C_{\text{geo,exp}} = 0.38 \times 10^{-3}\,\text{F/m}^2$, which is slightly higher than the theoretically calculated value $C_{\text{geo}} \sim 0.33 \times 10^{-3}\,\text{F/m}^2$. The deviation is probably due to the uncertainty of some parameters. Especially the values for the dielectric constant of the $Cd_{0.7}Hg_{0.3}Te$ and the exact thicknesses of the layers are not well known. These uncertainties are no concern since the absolute value of the geometric capacitance is not relevant for the determination of the carrier distribution inside the HgTe layer, which is the main interest of this work. The geometric capacitance nevertheless enables a rough estimate of the bulk bandgap based on the Landau level dispersion data shown in Fig. 3.11b) and Fig. 3.12. There are band edge-like features indicated as black dash-dotted lines, which are about $\Delta U = 0.4\,\text{V}$ apart. Assuming the occupation of only the top surface state using

$$U_{\text{HgTe}} = \frac{C_{\text{total}}}{C_{\text{q,topTSS}}}\Delta U \tag{4.11}$$

yields a band gap of $\Delta E_{\text{only topTSS}} \sim 20\,\text{meV}$. The bottom surface state can also be accounted for using the equivalent circuit diagram shown in Fig. 4.2b). The quantum capacitance of the HgTe layer in the bulk band gap $C_{\text{q,HgTe,gap}}$ is then given by

$$C_{\text{q,HgTe,gap}} = C_{\text{q,topTSS}} + \left(1/C_{\text{geo,HgTe}} + 1/C_{\text{q,botTSS}}\right)^{-1}. \tag{4.12}$$

Assuming a bottom surface state density of $n_{\text{botTSS}} = 2 \times 10^{11}\,\text{cm}^{-2}$, as estimated from Fig. 3.12), yields a band gap of $\Delta E_{\text{q,HgTe}} \sim 15\,\text{meV}$. Both values are in the order of the expected band gap of $\sim 20\,\text{meV}$ according to Ref. [47]. A more refined value can be determined by the $k \cdot p$ calculations with the program "kdotpy" [29], as shown in Fig. 2.6f), yielding a value of $E_{\text{gap}} = 14 - 15\,\text{meV}$ dependent on the k-direction. This accordance is a motivating interim result. It suggests that the chosen assignment of the observed transport channels is plausible.

Now, the whole observed behavior will be reproduced with this capacitor model. All transport channels observed in the magneto-transport experiments have to be accounted for. Due to the observation of QHE these states are modeled as two-dimensional states. To simplify the nomenclature we will label these states VPS, in anticipation of the explanation given in Sec. 4.4. The dimensionality determines their DOS and consequently their quantum capacitance (see Eq. 4.6). The DOS of a two-dimensional quadratically dispersing band is

$$D_{\text{q,quad,2D}} = g_s g_v \frac{m_{\text{eff}}}{2\pi\hbar^2}, \tag{4.13}$$

where g_s and g_v are the spin and valley degeneracy, respectively. For HgTe, the relevant bands are situated at the Γ-point, which prevents any valley degeneracy making $g_v = 1$. The value of the spin degeneracy g_s depends on the type of band and is either $g_s = 1$ for the TSSs or $g_s = 2$ for the VPSs. The quantum capacitance of the additional surface states is determined using Eq. 4.6 to

$$C_{\text{q,VPS}} = g_s e^2 \frac{m_{\text{eff}}}{2\pi\hbar^2}. \tag{4.14}$$

To account for the VPSs the circuit diagram is extended by the quantum capacitance of these bands $C_{q,VPS}$ parallel to the quantum capacitances of the TSS, as shown in the circuit diagram in Fig. 4.2c). The overall quantum capacitance then reads

$$C_{q,HgTe} = C_{q,topTSS} + \left(1/C_{geo,HgTe} + 1/C_{q,botTSS}\right)^{-1} + C_{q,VPS}. \tag{4.15}$$

The relevant quantum capacitances C_q, are determined based on the observed LL dispersion in Fig. 3.11b). The amount of observed transport channels is used to determine the appropriate equivalent capacitor circuit or equivalently the contributing quantum capacitances. The dispersion of the VPS is for simplicity assumed to be quadratic, which yields the quantum capacitance according to Eq. 4.14 with with $g_s = 2$. The onset and vanishing of the VPS contribution can be translated into a gate voltage-dependent effective mass of the VPS. The values for the effective masses of the conduction band and valence band like VPS of HgTe are estimated with k·p calculations performed with "biscuit" [29] as shown in Fig. 2.6f). The gate voltage dependent effective mass for the VPS reads then

$$m_{eff}\left(U_{gate}\right) = \begin{cases} 0.2\, m_{el} & U_{gate} < -2.0\,V \\ none & -2.0 \leq U_{gate} \leq -1.6\,V \\ 0.02\, m_{el} & -1.6\,V < U_{gate}. \end{cases}$$

This $m_{eff}(U_{gate})$ enables the calculations of the quantum capacitance of the VPS over the full range using Eq. 4.14. In contrast to the quantum capacitance of quadratic bands which is independent of n, the quantum capacitance of the linearly dispersing TSS depends according to Eq. 4.10 square root like on the density. This would require an unintuitive iterative solution. This is why, instead the quantum capacitance is calculated using an appropriate average density yielding $C_{q,topTSS}(n_{avg.,top} = 0.7 \times 10^{11}\,cm^{-2}) = 7.5 \times 10^{-3}\,F/m^2$ and $C_{q,botTSS}(n_{avg.,bot} = 2.0 \times 10^{11}\,cm^{-2}) = 12 \times 10^{-3}\,F/m^2$ for the top and bottom TSS, respectively. With these values Eq. 4.15 is used to estimate the density distribution based on the ratio of the capacitances. The result is shown in Fig. 4.3 on top of the FFT data of Fig. 3.12. In the experiment, the degeneracy of the VPS can be lifted due to the Zeeman or Rashba effect. This splitting is imitated by slightly adjusting the effective mass for one spin species of the VPS. The experimentally observed density distribution is qualitatively as well as quantitatively well reproduced.

The overall good quantitative agreement is remarkable. The only very weakly gate voltage-dependent bottom TSS, as well as the strongly varying gate voltage dependence of the top TSS with the onset of the VPSs, is well reproduced. The decent agreement of the occupation of the VPSs, even though the model only includes quadratic dispersing bands, is surprising. Nevertheless, there also exist deviations. The filling of the VPSs is not perfectly reproduced. The model produces a stronger gate voltage dependence for the bottom TSS as experimentally observed. These differences between the capacitor model and the experimental results might be due to the oversimplified dispersion, the localization of the involved bands, or the uncertainty in some parameters as the dielectric constants. The simplified band structure is shown in Fig. 4.4 compared to the realistic band structure shown in Fig. 2.6. The approach of modeling the magneto-transport using a capacitor circuit is not new. Similar capacitor circuit diagrams are used in Refs. [57, 76]. The chosen circuit diagrams differ partially, however. In Ref. [57], an additional parallel geometric capacitance is added, which mimics a grounded substrate. In our experiment, the substrate is neither conducting nor contacted. This is why this capacitance is neglected. The circuit diagrams of Ref. [76] only
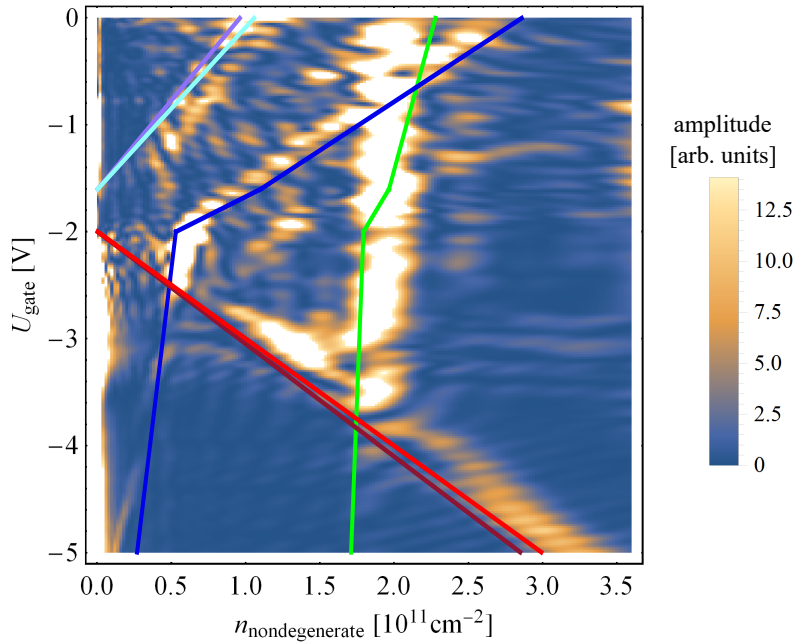
Figure 4.3: Shown is the density distribution onto the different bands of tensilely strained HgTe according to the capacitor model on top of the densities extracted by the FFT analysis from the experimental data (see Fig. 3.12). The occupation according to the capacitor model is shown for the bottom (top) TSS in green (blue), the valence band like VPS in light and dark red, and the conduction band like VPS in cyan and magenta.

differ for the regime with additional states. There a geometric capacitance is added in series to the quantum capacitance of these states. This effectively localizes the states away from the top of the sample towards its middle. In this work, these states are assumed to be localized at the top surface of the sample. This assumption is based on the localization calculated with self-consistent $k \cdot p$ calculations in Sec. 4.3. The capacitor circuit nicely visualizes the response of the different states to the applied gate voltage, as described in the next Section.

4.1.3. THE CAPACITOR CIRCUIT DEPICTED AS BAND STRUCTURE

In this Section, the gate voltage dependencies from the capacitor model are translated into its equivalent band structure to access its physical implications. The capacitor model is depicted as band structure by plotting the dispersion of the bands corresponding to the quantum capacitances of the equivalent circuit of Fig. 4.2. The resulting band structure is shown in Fig. 4.4a). The topological surface states are modeled with linear dispersion. The density of the bottom surface state (green) is increased compared to the top surface state (blue) to account for the bottom doping layer. The valence band like VPSs (red) and conduction band like VPS (purple) are assumed to disperse quadratically. The nodes in the electric circuit determine the action of the gate on the bands. The occupation of bands is indicated by the chemical potential (dashed lines). The different connections of the quantum capacitances in the circuit diagram cause effectively an energetic shift of the bands with respect to each other. Based on the circuit diagram the top TSS and the VPSs are not shifted with respect to each other and are occupied in the same fashion. This is why these states are depicted together in Fig. 4.4b). The bottom TSS is treated separately since it is occupied differently due to the geometric capacitance of the HgTe layer, as shown in Fig. 4.4c).
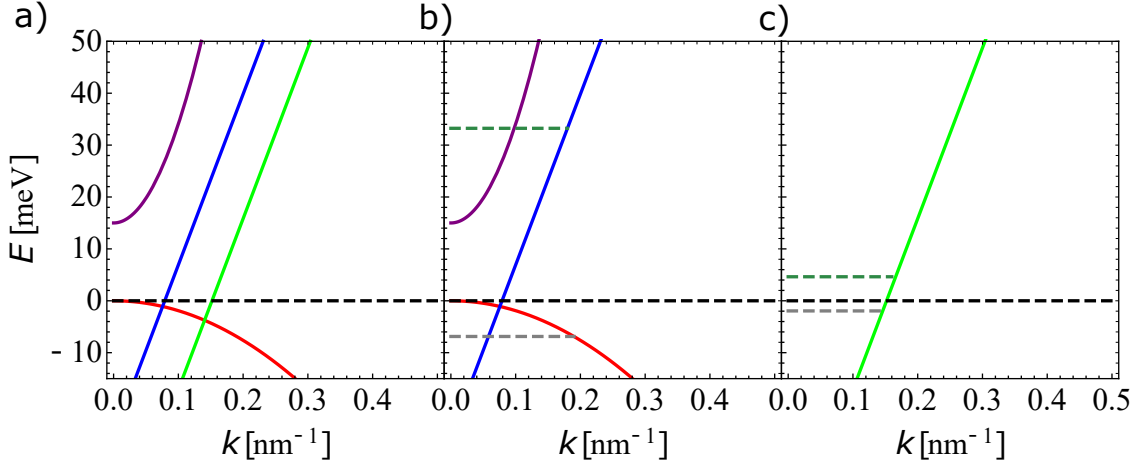
Figure 4.4: The band structure representing the capacitor model is shown in a) with the double degenerate quadratically dispersing valence and conduction Volkov-Pankratov state in red and purple and the top and bottom topological surface state in blue and green. The experimentally accessible energy range for the respective bands is indicated by the minimal (grey dashed) and maximal (olive dashed) achievable chemical potential in b) for the top TSS and VPSs in c) for the bottom TSS.

The resulting highest and lowest chemical potentials are indicated as dashed blue and grey lines in Fig. 4.4b) for the top TSS and VPSs and in Fig. 4.4c) for the bottom TSS. This gives an estimate for the energy range accessed by the experiment of $-10\,\text{meV} < E_\text{F} < 40\,\text{meV}$ for the top TSS and VPSs. Only a small change in the Fermi level in comparison to the other bands is observed for the bottom surface state. This behavior is caused by the different localization of the states on either the top or bottom side, which is accounted for in the model by the additional geometric capacitance of the HgTe layer for the bottom surface state, as mentioned before. Since the chemical potential is constant over the whole sample, this implies a relative energetic shift of the bottom TSS with respect to the top TSS and VPSs with gate voltage. A similar difference in the gate voltage dependence of the top and bottom surface state is reported based on self-consistent $k \cdot p$ calculations by Y. Baum *et. al.* in Ref. [57]. A 45 nm thick slab of 0.3 % tensilely strained HgTe is analyzed based on the six-band Kane Hamiltonian. The calculations yield a top gate voltage-independent bottom surface state together with a top gate voltage-dependent top surface state for a density range of $0.6 - 1.0 \times 10^{11}\,\text{cm}^{-2}$. For sufficiently strong gate voltages also the occupation of the conduction and the valence band is reported. The top gate voltage independence of the bottom TSS is explained by the screening of the electric field by the top TSS and the bulk states. These stats are localized towards the top surface due to the electric field. Overall the reported behavior is consistent with the capacitor model. It should be kept in mind, that only a limited gate voltage range is investigated by the self-consistent calculations in Ref. [57]. To get a better understanding of the screening effects and localization of the different involved states similar self-consistent $k \cdot p$ calculations are presented in Sec. 4.3 after first introducing the Kane model [22] in the next Section.

4.2. THE KANE HAMILTONIAN

For the self-consistent $k \cdot p$ band structure calculations the eight-band Kane model [22] is used. To be able to discuss self-consistent $k \cdot p$ calculations, the Kane model is briefly reviewed. The presented Hamiltonian is actually the six band Hamiltonian since the so-called split of bands (Γ_7) are disregarded for the discussion. The Γ_7 bands only cause quantitative corrections to the band structure, but increase the extent of the Hamiltonian and do not contribute to developing a physical understanding. The Kane Hamiltonian is given by the symmetry of the lattice of HgTe as described in Sec. 2.1.1. HgTe crystallizes in a zinc blende lattice, which is non-inversion symmetric and described by the T_d point group. Since the inversion symmetry breaking is small, the inversion symmetric O_h point group of the diamond lattice is used instead. The inversion symmetry breaking terms can be added in a perturbative fashion afterward if necessary. The basis is given by the Γ bands, which are introduced and discussed in Sec. 2.1.1. These states are

$$\left| \Gamma_6; +\frac{1}{2} \right\rangle = \left| j = \frac{1}{2}; m_j = \frac{1}{2} \right\rangle = |S; \uparrow\rangle = S \uparrow,$$

$$\left| \Gamma_6; -\frac{1}{2} \right\rangle = \left| j = \frac{1}{2}; m_j = -\frac{1}{2} \right\rangle = |S; \downarrow\rangle = S \downarrow,$$

$$\left| \Gamma_8; +\frac{3}{2} \right\rangle = \left| j = \frac{3}{2}; m_j = \frac{3}{2} \right\rangle = |HH; \uparrow\rangle = \frac{1}{\sqrt{2}} (X + iY) \uparrow,$$

$$\left| \Gamma_8; +\frac{1}{2} \right\rangle = \left| j = \frac{3}{2}; m_j = \frac{1}{2} \right\rangle = |LH; \uparrow\rangle = \frac{1}{\sqrt{6}} [(X + iY) \downarrow -2Z \uparrow],$$

$$\left| \Gamma_8; -\frac{1}{2} \right\rangle = \left| j = \frac{3}{2}; m_j = -\frac{1}{2} \right\rangle = |LH; \downarrow\rangle = \frac{1}{\sqrt{6}} [(X - iY) \uparrow +2Z \downarrow],$$

$$\left| \Gamma_8; -\frac{3}{2} \right\rangle = \left| j = \frac{3}{2}; m_j = -\frac{3}{2} \right\rangle = |HH; \downarrow\rangle = \frac{1}{\sqrt{2}} (X - iY) \downarrow.$$

Even though the detailed derivation of the Kane Hamiltonian is out of the scope of this work and the interested reader is pointed to Ref. [19, 20] for a derivation based on the analysis of the space group symmetry, a short motivation for the Hamiltonian shall be given. As the starting point, the diagonal elements are chosen. These elements describe the energy of the six bands at $k = 0$. Two bands of these bands each represent the two spin species and should have the same energy for $k = 0$. Since the Γ_8 bands originate from the P orbitals of the Te atoms, the four Γ_8 bands should be degenerate at $k = 0$ and differ from the two Γ_6 bands, which are formed by the S orbital of the Hg atoms. A quadratic dispersion with different effective masses for the $\left| \Gamma_8; \pm\frac{1}{2} \right\rangle$ and the $\left| \Gamma_8; \pm\frac{3}{2} \right\rangle$ are assumed. This procedure yields the diagonal terms of the Hamiltonian which are given in Eq. 4.16.

For the off-diagonal elements, only a few comments on the general shape of the Hamiltonian are given. Since the Hamiltonian needs to be Hermitian to ensure real eigenvalues, the condition $H_{\mathrm{Kane},ij} = H_{\mathrm{Kane},ji}^\dagger$ requires only the construction of half of the off-diagonal elements by the symmetry analysis. The k dependence of the off-diagonal elements can be motivated by looking at the magnetic quantum number m_j of the basis states, which are coupled by these elements. The $k_\pm$ can be seen as ladder operators, which can change the quantum number of a system, in this case m_j. This gives the first idea for expected k dependencies for the respective matrix elements.

The exact allowed matrix elements, as well as their actual form, have to be derived by analyzing the symmetry constraints given by the O_h point group, as mentioned above. Accounting for the spin-orbit coupling in the lowest order of perturbation theory the Kane Hamiltonian reads in the convention of Ref. [19, 75]

$$
H_{\text{Kane}} = \begin{pmatrix}
T & 0 & -\frac{1}{\sqrt{2}}Pk_+ & \sqrt{\frac{2}{3}}Pk_z & \frac{1}{\sqrt{6}}Pk_- & 0 \\
0 & T & 0 & -\frac{1}{\sqrt{6}}Pk_+ & \sqrt{\frac{2}{3}}Pk_z & \frac{1}{\sqrt{2}}Pk_+ \\
-\frac{1}{\sqrt{2]}}Pk_- & 0 & U+V & -S_- & R & 0 \\
\sqrt{\frac{2}{3}}Pk_z & -\frac{1}{\sqrt{6}}Pk_- & -S_-^\dagger & U-V & C & R \\
\frac{1}{\sqrt{6}}Pk_+ & \sqrt{\frac{2}{3}}Pk_z & R^\dagger & C^\dagger & U-V & S_+^\dagger \\
0 & \frac{1}{\sqrt{2}}Pk_- & 0 & R^\dagger & S_+ & U+V
\end{pmatrix}
\tag{4.16}
$$

using the abbreviations

$$
k_\parallel^2 = k_x^2 + k_y^2,\, k_\pm = k_x \pm i k_y,\, k_z = -i\frac{\partial}{\partial z}
$$

$$
T = E_c + \frac{\hbar^2}{2m_0}\left[(2F+1)\,k_\parallel^2 + k_z\,(2F+1)\,k_z\right],
$$

$$
U = E_v - \frac{\hbar^2}{2m_0}\left(\gamma_1 k_\parallel^2 + k_z \gamma_1 k_z\right),
$$

$$
V = -\frac{\hbar^2}{2m_0}\left(\gamma_2 k_\parallel^2 - 2k_z \gamma_2 k_z\right),
$$

$$
R = -\frac{\hbar^2}{2m_0}\left(\sqrt{3}\tilde{\gamma} k_+^2 - \sqrt{3}\overline{\gamma} k_-^2\right),
$$

$$
S_\pm = -\frac{\hbar^2}{2m_0}\sqrt{3}k_\pm\left(\{\gamma_3, k_z\} + [\kappa, k_z]\right),
$$

$$
C = \frac{\hbar^2}{m_0}k_-\,[\kappa, k_z].
$$

Thereby $\tilde{\gamma} = (\gamma_3 - \gamma_2)/2$ and $\overline{\gamma} = (\gamma_3 + \gamma_2)/2$ is used and $[A, B] = AB - BA$ represents the commutator and $A, B = AB + BA$ the anti-commutator. The parameters for HgTe are given in Table 4.1. The same arguments made to motivate the Kane Hamiltonian can be used to identify the bands responsible for the creation of the topological surface states. The Γ_6 bands possess an inverted ordering to all four Γ_8 bands compared to the expected order from the atomic limit. But only the $\left|\Gamma_8; \pm\frac{1}{2}\right\rangle$ bands possess the same quantum number as the Γ_6 bands, identifying these bands as the topologically relevant partner bands. The $\left|\Gamma_8; \pm\frac{3}{2}\right\rangle$ is in contrast only a band that happens to exist at the same energy due to symmetry constraints. Due to its subordinate relevance in a topological sense, it could be called a spectator band. Even though the $\left|\Gamma_8; \pm\frac{3}{2}\right\rangle$ is topologically irrelevant, it is important to describe the observed transport behavior as will be discussed in Sec. 4.3.

The above described Kane Hamiltonian represents unstrained HgTe which is a semi-metal with quadratically dispersing conduction and valence bands that touch at the Γ point, which is here called quadratic semi-metal. To access the different phases of HgTe, the symmetry of the Kane Hamiltonian has to be reduced. The symmetry is experimentally reduced via strained growth. The deformation of the crystal by accounting for its stiffness

$E_g = E_{\Gamma_6} - E_{\Gamma_8}$	$E_P = 2m_0 P^2/\hbar$	γ_1	γ_2	γ_3	κ	F
$-0.3\,\text{eV}$	$18.8\,\text{eV}$	4.2	0.5	1.3	-0.4	0

Table 4.1: Luttinger parameters taken from [77].

of the crystal is discussed descriptively in Ref. [25]. The resulting correction terms to the on diagonal elements as well as the coupling between the Γ_8 bands are shown explicitly in Ref. [19, 75] based on the description introduced in Ref. [26]. The Kane model including the terms for the strain, allows studying the realistic band structure for HgTe in different phases, as introduced in Sec. 2.1.2. The 3D-TI phase is investigated with self-consistent calculations in the following.

4.3. SELF-CONSISTENT $k \cdot p$ CALCULATIONS

The motivation for the self-consistent $k \cdot p$ calculations presented here is twofold. First, to double-check whether accounting for the realistic band structure using the Kane model yields the same qualitative occupation of states as the capacitor model (Sec. 4.1). Second, the orbital character and spatial distribution of the involved states can be obtained. Unfortunately, the calculation of the exact experimental layer stack and thus a quantitative comparison is not possible. A thickness of 70 nm is chosen experimentally as the thickness of the HgTe layer to ensure high crystal quality, while being thick enough to result in a small subband splitting, so that the layer can be seen as a three-dimensional structure. The resulting band structure with its subbands determined by $k \cdot p$ calculations for 70 nm thick slab is shown in Fig. 2.6f). This small subband splitting makes the self-consistent carrier distribution demanding and challenging due to the sheer amount of possible configurations. The amount of subbands is significantly reduced by choosing a thinner HgTe layer with a thickness of 40 nm, to ensure convergence for a sufficient parameter range. Interpreting these results one has to keep in mind that the reduced thickness could cause deviations due to a different potential shape and possible interaction of the surface states. The dielectric constant (=permittivity) ϵ describes the response of a material to an electric field. For HgTe the dielectric constant is space-dependent since it has to account for the different permittivity of the TSS compared to bulk HgTe (see appendix A). The dielectric constant of HgTe might even be energy-dependent, which would need to be accounted for by random phase approximation calculations [78]. Such calculations are far outside the scope of this work. With these restrictions in mind, the calculations can still be used to examine the qualitative behavior.

The calculations are performed using the program "kdotpy" kindly provided by Wouter Beugeling [29]. The calculated structure is a semi-finite HgTe slap, which is infinite along the x and y direction and finite along the z direction. The HgTe layer is 40 nm thick along the z direction and surrounded by two 10 nm thick $Cd_{0.7}Hg_{0.3}Te$ barriers as shown in Fig. 4.5. To describe this layer stack the above in Sec. 4.2 introduced Kane Hamiltonian with the material parameters of Ref. [77] is used in the program "kdotpy". The layer stack of the experimentally investigated sample possesses a bottom doping layer as shown in Fig. 3.1. This doping layer is accounted for in the calculation via a finite starting density. This is done indirectly by setting a starting chemical potential $E_F = 12\,\text{meV}$ as parameter. The electric field additionally introduced by this doping layer is neglected. For the self-consistent de-
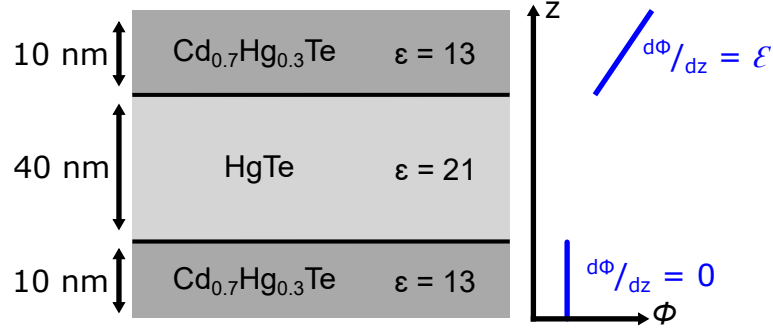
Figure 4.5: The semi-infinite slab used for the self-consistent $k \cdot p$ calculations is shown. The layer stack is sketched with the respective thickness, material, and dielectric constants ϵ of the layers indicated. On the right, the chosen boundary condition for the Hartree potential Φ is sketched. The boundary conditions are the electric field $\mathscr{E}$ which is the derivative of the Hartree potential with respect to the z direction $d\Phi/dz$.

termination of the Hartree potential via the Poisson equation two boundary conditions are necessary. Here the electric fields $\mathscr{E}$ at the boundaries of the HgTe layer are chosen, which are equivalent to the derivative of the Hartree potential Φ with respect to the z-direction $d\Phi/dz = \mathscr{E}$. For the bottom $Cd_{0.7}Hg_{0.3}Te$ layer $\mathscr{E} = 0$ is used, while for the top $Cd_{0.7}Hg_{0.3}Te$ layer an electric field representing the applied top gate voltage is chosen, as sketched in Fig. 4.5. These calculations give the dispersions shown in Fig. 4.6 for $U_{gate} = 0\,V$ meaning $d\Phi/dz = 0$ and for the highest reliable gate voltages. The presented gate voltages are the highest ones, which still yield the expected linear dependence of the total density on the applied gate voltage.

The determined density of $n_{tot} = 3.0 \times 10^{11}\,cm^{-2}$ compares reasonably well with the experimental density of $n_{TSS,gap} \sim 2.6 \times 10^{11}\,cm^{-2}$. The carrier density distribution of the simulated band structure is slightly more symmetric with $n_{TSS,bot,kp} \sim 1.7 \times 10^{11}\,cm^{-2}$ and $n_{TSS,bot,kp} \sim 1.3 \times 10^{11}\,cm^{-2}$ compared to the experimental densities of $n_{TSS,bo,exp} \sim 1.9 \times 10^{11}\,cm^{-2}$ and $n_{TSS,top,exp} \sim 0.7 \times 10^{11}\,cm^{-2}$. Even though a more quantitative agreement would be desirable, here this slightly less asymmetric starting position is accepted to calculate a sufficient gate voltage range to examine the qualitative behavior. For sufficiently strong negative voltages a band separates from the valence band. This band is called massive Volkov-Pankratov state [16, 79]. The name and properties of these states are addressed in detail in Sec. 4.4. This hole-like massive VPS is occupied as shown in Fig. 4.6b). Equivalently an electron-like massive VPS forms from the conduction band and is occupied for sufficiently positive voltages as visible in Fig. 4.6c). The occupation of the involved states for different effective gate voltages U_{eff} is summarized in Fig. 4.7a). The total density for a chosen electric field as boundary condition is calculated and then translated into U_{eff} using the experimentally determined gate action $n(U_{gate}) = \left(7.0 + 2.3\frac{1}{V} \times U_{gate}\right) \times 10^{11}\,cm^{-2}$ as determined in Sec. 3.3.1. The calculations show a range of U_{eff}, for which only the topological surface states are occupied. The occupation of the top TSS in blue changes more rapidly with U_{eff} than the occupation of the bottom TSS in green. The occupation of the first conduction band is found for $U_{eff} > -1.3\,V$ and similarly the first valence sub band for $U_{eff} < -2.5\,V$. Qualitatively this behavior is consistent with the distribution of the charge carriers found by the magneto-transport experiments. The density distribution obtained with the FFT analysis already presented in Fig. 3.12 is shown again together with the density distribution determined by the capacitor model of Fig. 4.3 in Fig. 4.7b). The comparison
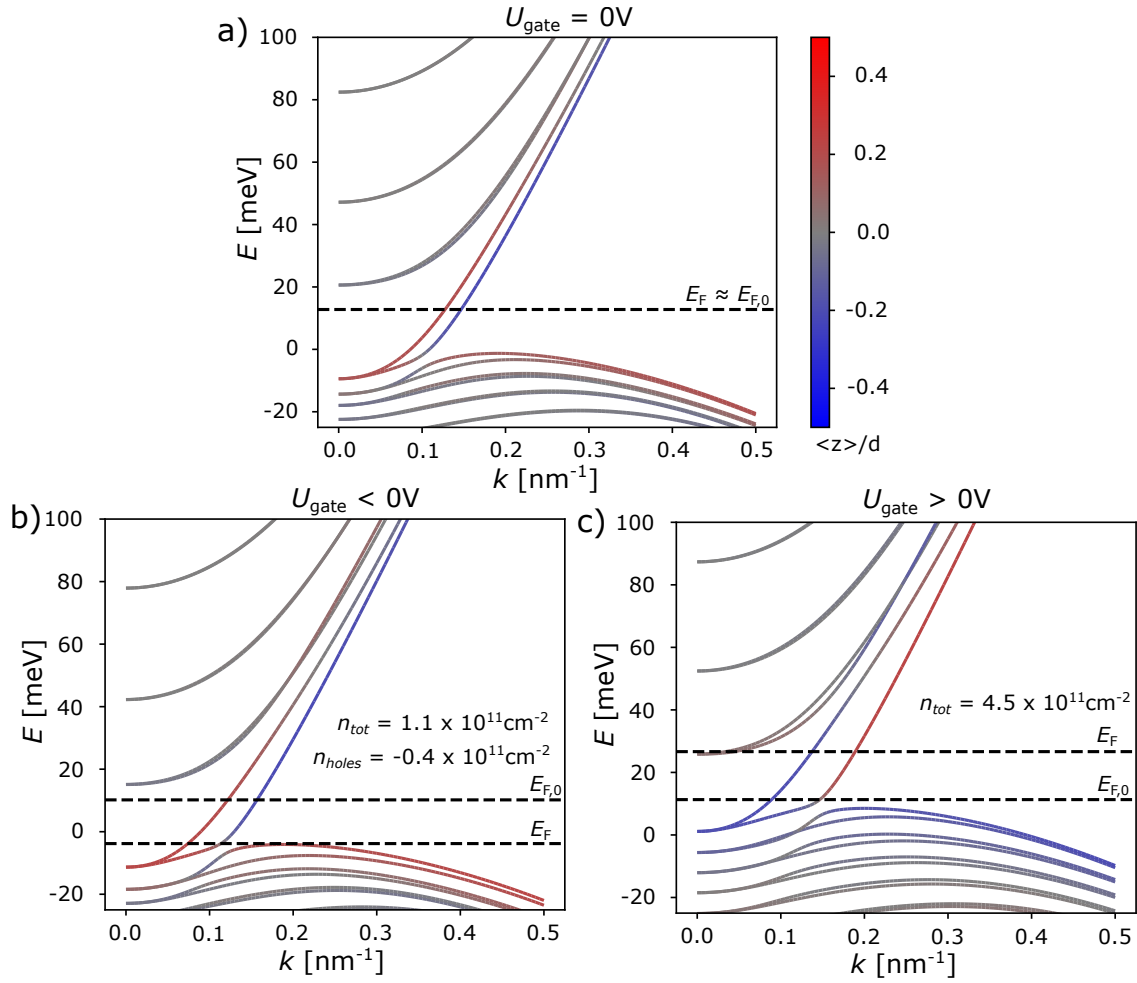
Figure 4.6: Self-consistent $k \cdot p$ calculations with the Fermi energy E_F placed in the bulk band gap for the gate voltages $U_{gate} = 0\,V$ in a), for the maximal trustworthy $U_{gate} > 0\,V$ in b), and the minimal trustworthy $U_{gate} < 0\,V$ in c). The starting Fermi energy is indicated by E_{F0} as a dashed line together with the self-consistently determined position of the electrochemical potential E_F. The corresponding total carrier densities n_{tot} are given together with the hole density n_{holes} for c). The color code indicates the spatial localization of a state via the normalized average position $< z > / d$.

of the experimental and the $k \cdot p$ calculation results show two differences. The gate voltage window between the occupation of the bulk bands is in the self-consistent $k \cdot p$ calculation with $\Delta U_{k \cdot p} \sim 1.1\,V$ more than twice as big as the experimental one of $\Delta U_{exp} \sim 0.4\,V$. The occupation of the bottom surface state changes with gate voltage for the calculation, while in the experiment the occupation of the bottom surface state is nearly independent of the top gate voltage. These effects could be due to the trade-offs needed to perform the self-consistent $k \cdot p$ calculations at all. The gate voltage dependence of the bottom TSS could be related to the thickness of 40 nm in the calculation compared to the thickness of the experimental layers of 70 nm. The layer is thinner compared to the localization length of the TSS making the surface states effectively more localized towards the middle of the sample and potentially allowing for more hybridization between the top and bottom TSS. The reduced thickness could explain the stronger top gate voltage dependence of the bottom TSS in the $k \cdot p$ calculation than in the experiment. The apparent bulk bandgap size could be altered by this hybridization or the different dielectric constants of the TSS and bulk HgTe that are

not taken into account. Similar calculations are performed for a 45 nm thick layer accessing a density range of $0.6 - 1.0 \times 10^{11} \, \text{cm}^{-2}$ in Ref. [57]. For this small density range, no change in the occupation of the bottom TSS with the top gate voltage is found, as mentioned in Sec. 2.3.4.

4
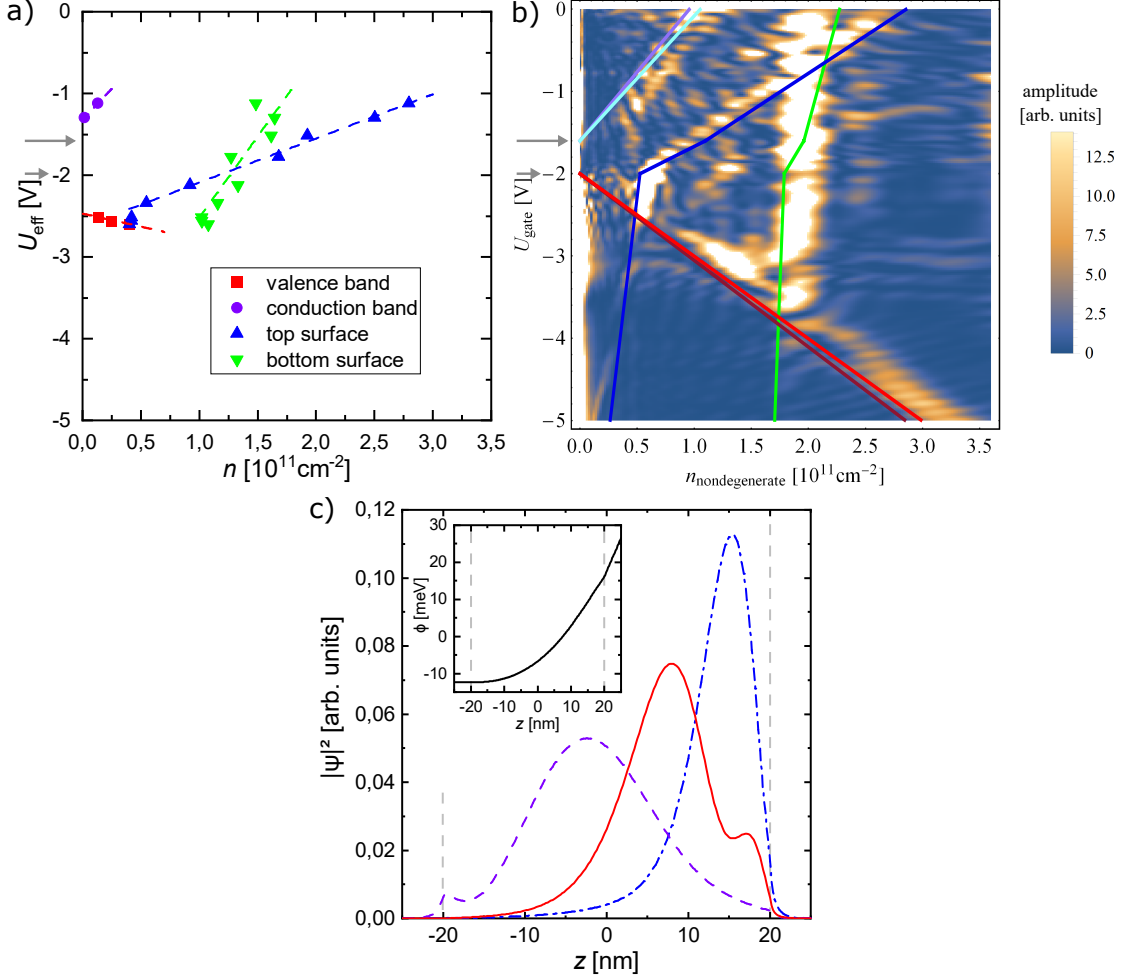
Figure 4.7: The result of the self-consistent $k \cdot p$ calculated with the program "kdotpy" [29] for different effective gate voltages U_{eff} matched to the applied gate voltage by the total carrier density are shown in a). For comparison the experimental FFT results together with the density distribution by the capacitor model (see Fig. 4.3) are shown again in b). The experimentally determined size of the bandgap is indicated as grey arrows. The inset of c) shows an exemplary chemical potential Φ as a function of the layer thickness z calculated by the self-consistent $k \cdot p$ calculation. In c) is the probability distribution $|\Psi|^2$ of the massive Volkov-Pankratov states formed from the $\Gamma_{8,\text{HH}}$ valence band at the momentum $k = 0.2 \, \text{nm}^{-1}$ (red) together with the massive Volkov-Pankratov states formed from the conduction band (purple) and the top TSS (blue) at $k = 0.07 \, \text{nm}^{-1}$ as function of the layer thickness z shown obtained by a $k \cdot p$ calculation with the spatial electrical potential function obtained by self consistent $k \cdot p$ calculations shown in the inset.

With the qualitative gating behavior reproduced, the nature of the massive VPS can be investigated. The spatial distribution of the massive VPS due to the Hartree potential is examined. The spatial probability distribution for the occupied $\Gamma_{8,\text{HH}}$ hole-like VPS is shown in Fig. 4.7c) in red for the electrical potential shown in the inset. The probability distribution is shifted towards the top half of the slab. This indicates the localization of the band with the applied electric field towards the top surface of the slab. To emphasize this shift,

the spatial distribution of the electron-like massive VPS (purple) and the top TSS (blue) are shown for comparison. This hole-like massive VPS (red) is shifted towards the top side compared to the unoccupied electron-like massive VPS (purple), but is still less localized than the top TSS (blue). This local shift is accompanied by a separation of this red hole-like massive VPS from the remaining valence-subbands in energy as shown in Fig. 4.6c). The remaining subbands are treated as the band continuum. In principle, the same effect is expected for the Γ_6 bulk conductance band. The higher mass of the valence band makes the valence band more sensitive to the variation of the electrical potential, since due to the comparably large DOS already small local changes in energy can cause a redistribution of a significant amount of charge carriers. The valence band is thus expected to follow the spatial variation of the electrical potential more strictly than the conduction band. The localization of the VPS and the top TSS onto the top surface justifies their equivalent treatment in the capacitor model. The spatial separation of the bottom TSS is accounted for by the geometric capacitance.

4.4. Massive Volkov-Pankratov states in HgTe

$Cd_xHg_{1-x}Te$ has been widely studied as an infrared detector before HgTe has been described in the framework of topology [80]. The interface of $Cd_xHg_{1-x}Te$ with $x > x_c$ on the one side and $x < x_x$ on the other side is investigated under the name band inverting contact in Ref. [33]. The band structure of the two sides is equivalent to the band structure of HgTe and $Cd_{0,7}Hg_{0,3}Te$, respectively (see Fig. 2.3). Only the size of the bandgap is renormalized according to the Cd content x. The interface is thus equivalent to the one investigated in this work. An interface state between the conduction $\Gamma_{8,LH}$ and the second valence band Γ_6 has been found. This interface state is reminiscent of the nowadays called topological surface state. A similar interface state is also reported in the gapless quadratic semi-metal unstrained HgTe based on the Luttinger model [2] in Ref. [81].

An intuitive access to the nature of the interface state is presented by B. A. Volkov and O. A. Pankratov in Ref. [16]. They discuss an inverted contact using a four-band model with mutually inverted bands motivated by the material $Pb_{1-x}Sn_xTe$. A linear dispersing non-degenerate interface state is found. This interface state is independent of the details of the interface, and forms due to the supersymmetry of the effective Hamiltonian. Additional quadratically dispersing interface states are reported for interfaces with a smooth variation of the Cd content x. The resulting band structure of such a smooth inverted interface is sketched in Fig. 4.8. The thickness of the smooth transition area determines the energy scale of the bandgap of the additional massive surface states. These states are not very likely to appear in our samples, since the length scale of such a content transition is expected to be narrow. From scanning tunneling microscopy pictures presented in Ref. [25] the thickness of the interface is estimated to $\sim 1 - 2\,nm$. For narrow interfaces, the massive surface states are only expected to exist at inaccessible high energies. This creation mechanism is extended in Ref. [17, 74] by accounting for a smooth drop of the electric potential over such an inverted interface. The smooth electric potential drop is shown to be equivalent to a smooth content variation and will also cause the formation of these additional massive surface states. Similar electric field-induced additional surface states are found by magneto-

---

[2]For a description of different model Hamiltonians typically used to describe HgTe and materials alike see Chapter 8.4.
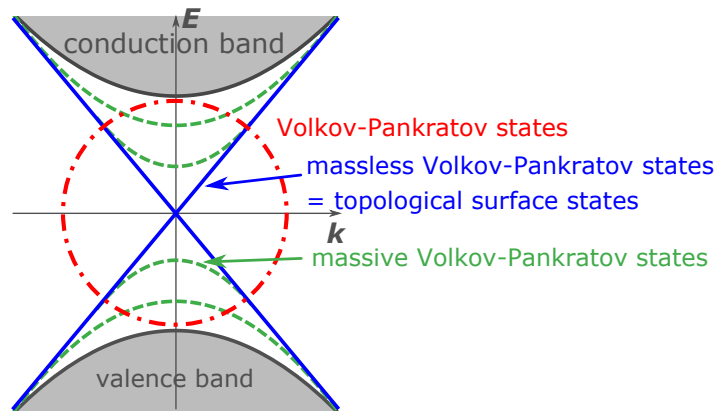
Figure 4.8: Shown are the interface states (surfaces states) at the interface between two materials with mutually inverted bands. The states are named Volkov-Pankratov states [16], after the authors first describing them, and are distinguished by their dispersion. Taken from Ref. [34].

transport measurements in the Dirac semi-metal compressively strained HgTe in Ref. [34], which is discussed in detail in Chapter 8. Perfectly quantized QH plateaus are observed over the whole accessible gate voltage range which covers densities of $n \sim \pm 10 \times 10^{11} \, \text{cm}^{-2}$. The electron transport is attributed to the topological surface states. Since the Dirac point and the hole regime of the TSS is not accessible, the hole transport can not have the same origin. The hole transport is traced to additional massive surface states which form due to the applied gate voltage. The formation of such massive surface states is shown by $6 \times 6 \, k \cdot p$ calculations which account for the applied gate voltage via a realistic Hartree potential. These states are dubbed massive Volkov-Pankratov states due to the above discussed first description by B. A. Volkov and O. A. Pankratov in Ref. [16].

Since the band structure of tensilely and compressively strained HgTe only differs for small k and energy window around the energy where for unstrained HgTe the quadratic band touching point would be. The formation of additional massive surface states is also likely in the three-dimensional insulator phase. The additional observed hole-like transport channel in parallel to the top and bottom topological surface states in the magneto-transport measurements presented in Sec. 3 are thus identified as massive VPS. The Landau level dispersion of the hole-like transport channel in parallel to the top and bottom TSS Landau level dispersion can be seen in Fig. 3.11 and its FFT analysis in Fig. 3.12. This assignment is confirmed by the self-consistent $k \cdot p$ calculations shown in Fig. 4.6, where a hole-like state, which is localized to the top side of the HgTe layer, is found for negative gate voltages. The probability distribution close to the top side is shown in Fig. 4.7c) for the potential shown in the inset. This is why the hole transport observed in tensilely strained HgTe is also attributed to the massive Volkov-Pankrtov states. Similar VPS are observed in Ref. [74] using high-frequency compressibility measurements that lead to the extension of the smooth material content variation over an interface to a smooth electric potential variation by Ref. [17] and hence to the name VPS. These measurements are discussed in the following Chapter 5.

5

HIGH FREQUENCY COMPRESSIBILTY MEASUREMENTS

The above described VPS have already been proposed to describe the high-frequency compressibility measurements on tensilely strained HgTe for high positive gate voltages. The high-frequency compressibility measurements give access to the DOS as a function of the electrochemical potential. The routine to access the DOS is described by introducing the device design used to measure the admittance and the model of distributed resistance-capacitance required to extract the capacitance and resistance values. These quantities can be transformed into the DOS and electrochemical potential. The results are interpreted with the help of additional $k \cdot p$ calculations accounting for the applied electric field and compared to the magneto-transport measurements.

5.1. THE MEASUREMENT SETUP

A complementary approach to investigate the 3D-TI tensilely strained HgTe is taken together with Inhofer *et.al.* as presented in Ref. [74, 82] via high frequency compressibility measurements. The surplus of these measurements over the quasi dc magneto-transport measurements presented before is the access to the DOS $D = \frac{\partial n}{\partial E_F}$ as a function of the chemical potential E_F [1]. To measure the high-frequency transport response a plate capacitor structure consisting of the HgTe layer as backplate a dielectric and an Au top gate is embedded into a co-planar waveguide, as shown in Fig. 5.1a) and schematically in Fig. 5.1b). The capacitor device is fabricated with optical lithography analogous to the Hall bar devices in Sec. 3.1.1. A stripe HgTe mesa is etched with an aqueous solution of $KI/I_2/HBr$ [45]. To contact this stripe, $50\,nm$ Au/Ge and $50\,nm$ Au are deposited via electron-beam evaporation on the with Ar^+ milling cleaned surface of the HgTe mesa. A top gate is fabricated using a self-aligned process for the insulator and gate deposition based on a negative optical resist with an undercut of $\sim 0.4\,\mu m$. As insulator 60 cycles of HfO_2 are grown by low-temperature atomic layer deposition at a temperature of $T = 30°C$ yielding a layer of $\sim 10\,nm$ thickness, which extends into the undercut of the resist [61, 83]. As gate electrode, a $100\,nm$ thick Au layer is deposited on top of a $5\,nm$ thick Ti sticking layer via in situ electron beam evaporation. This more directed electron beam deposition process compared to

---

[1]The chemical potential and Fermi energy will be used equivalently in this work as E_F to avoid confusion with the mobility μ.
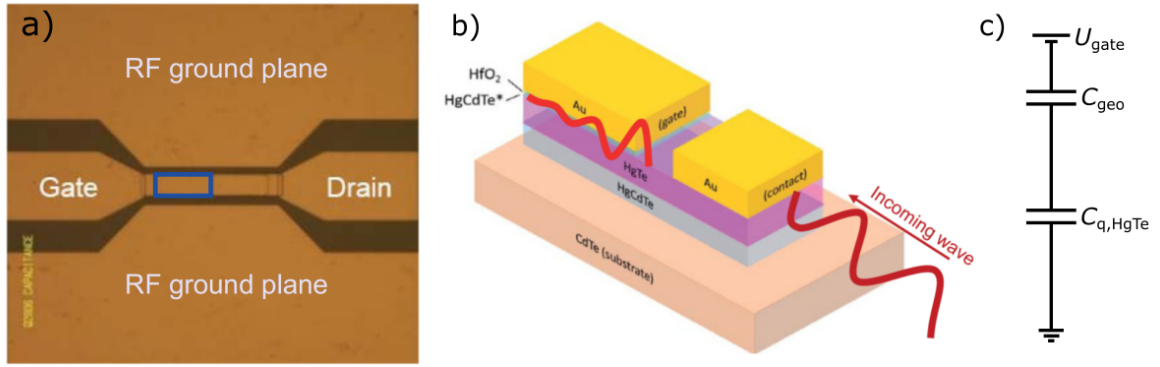
Figure 5.1: In a) a photograph of the plate capacitor device embedded into a co-planar waveguide is shown. In b) a schematic of the device is sketched to show the lateral structure of the device. The AC bias is indicated as a red wave. The Au gate on top of a HfO_2 dielectric/insulator covers an area of $44 \times 20\,\mu m$ of the stripe-shaped mesa [blue rectangle in a)] and allows together with the Au contact to apply a dc bias. In c) the corresponding circuit diagram is shown. The gate voltage U_{gate} drops over the geometric capacitance C_{geo} and the quantum capacitance $C_{q,HgTe}$. a) and b) are reprinted from A. Inhofer *et al.*, Observation of Volkov-Pankratov states in topological HgTe heterojunctions using high-frequency compressibility, PRB **96**, 195194 (2017) [74]. Copyright 2017 by The American Physical Society.

the atomic layer deposition growth restricts the Au gate layer to only reach up to $\sim 0.4\,\mu m$ to the edge of the HfO_2 insulator, thus preventing shorts to the HgTe layer. For the coplanar waveguides, 200 nm of Au/Ge and 200 nm Au are evaporated onto the sample. The detailed recipe can be found in Ref. [82]. The finished device is shown in Fig. 5.1a).

From a physical point of view, the device resembles a simple plate capacitor with an Au top plate, the HfO_2 and $Cd_{0.7}Hg_{0.3}Te$ layer as dielectric and the HgTe layer as the bottom plate. The area of the plate capacitor is given by the overlap of the Au gate with the HgTe layer, which has a length $L = 44\,\mu m$ and width $W = 20\,\mu m$. This plate capacitor can be extended to account for the quantum capacitance of the HgTe layer by using a capacitor circuit analogous to Sec. 4.1. Since the ground is connected via the HgTe layer, C_{tot} [2] is made up of a series connection of the quantum capacitance of the HgTe layer C_q and the geometric capacitance C_{geo} of the metal-topological insulator capacitor as schematically shown in Fig.5.1c) and 4.2b). This is the same equivalent capacitor circuit as for the Hall-bar device. The device is designed to maximize the measured admittance spectrum $Y(\omega)$ as a function of the angular frequency $\omega = 2\pi f$, where f is the frequency. The admittance $Y(\omega) = Z(\omega)^{-1}$ is the inverse of the complex impedance $Z(\omega)$. The co-planar waveguide matches the impedance of the structure to the $50\,\Omega$ impedance of the measurement circuit [82]. This prevents reflection of the measurement signal on the device. A thin insulator of 10 nm thick HfO_2 and a 5 nm thick $Cd_{0.7}Hg_{0.3}Te$ capping layer are chosen to maximize the capacitance of the device and consequently the amplitude of the admittance signal. HfO_2 is used as insulator layer due to its high expected dielectric constant of $\epsilon_{theoretical} = 25$ [84]. Even though the 10 nm thin HfO_2 layer grown by low-temperature atomic layer deposition only yields a value of $\epsilon \sim 3.6$ according to the analysis of Ref. [74], this still provides a sufficiently strong measurement signal. The deviation of the dielectric constant from the literature value is shortly assessed in the following. Thicker HfO_2 layers of 15 nm and 30 nm thickness grown by low-temperature atomic layer deposition yield $\epsilon \sim 7$, in Ref. [61]. The

---

[2]All capacitances are given as capacitance per unit square for convenience.
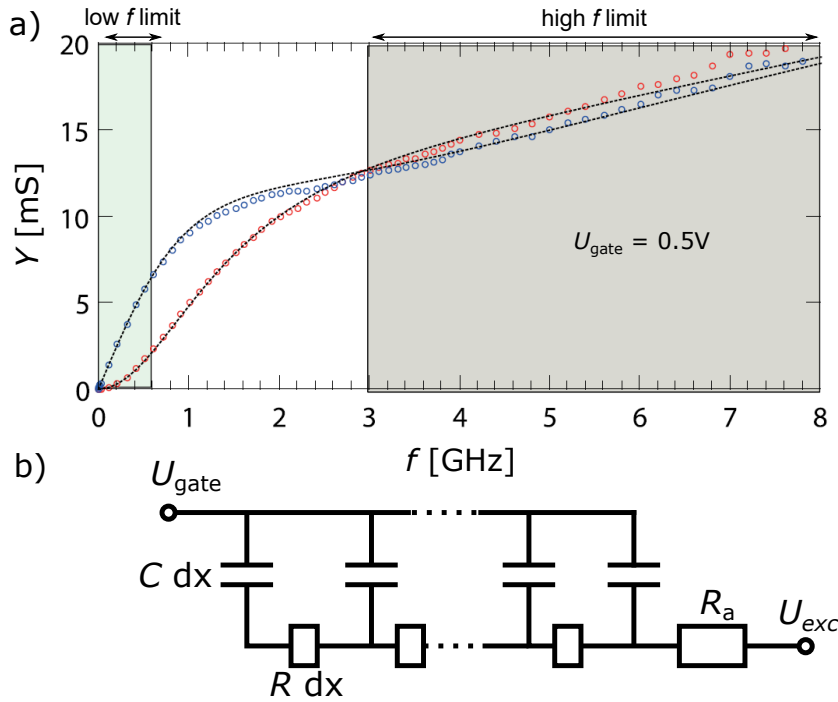
Figure 5.2: An exemplary complex admittance spectrum Y (Re(Y) in red and Im(Y) in blue) is shown as a function of the frequency f at a temperature of $T = 10\,$K in a). The low-frequency limit is shaded in green and the high-frequency limit in grey. In b) the circuit diagram for the distributed resistance-capacitance model is drawn. The infinitesimal resistances and capacitances are labeled by R dx and C dx. The contact resistance R_a and the DC gate voltage U_{gate} as well as the AC driving voltage U_{exc} are also indicated. a) is reprinted from A. Inhofer *et al.*, Observation of Volkov-Pankratov states in topological HgTe heterojunctions using high-frequency compressibility, PRB **96**, 195194 (2017) [74]. Copyright 2017 by The American Physical Society.

permittivity of HfO$_2$ is determined from the capacitance of the measured devices. This requires a value for the permittivity of Cd$_{0.7}$Hg$_{0.3}$Te. In Ref. [61] $\epsilon_{CdHgTe} \sim 10$ is used following Ref. [80], while in Ref. [74] a value of $\epsilon_{CdHgTe} \sim 8.5$ is taken based on Ref. [85]. Still, a factor of two is more than expected from the difference in the choice of ϵ_{CdHgTe}. This deviation could point towards some thickness dependence of ϵ_{HfO_2} for thin layers due to the complicated growth start [84]. In this work $\epsilon_{HfO_2} \sim 3.6$ and $\epsilon_{CdHgTe} \sim 8.5$ is used, following Ref. [74].

The measurements are performed with a vector network analyzer in a frequency range of $f = 50\,$kHz$-8\,$GHz in a cryogenic radiofrequency probe station at a temperature of $T = 10\,$K on samples fabricated from wafer Q2837. A standard in situ calibration technique is performed. Commercial calibration samples and fabricated dummy structures, which mimic the actual sample, are used to de-embed the admittance signal of the sample from contributions of the circuitry. The details of this procedure are described in Ref. [82]. An exemplary measurement of the frequency $f = \omega/2\pi$ dependent complex admittance $Y(\omega)$ is shown in Fig. 5.2a). To interpret the admittance spectrum $Y(\omega)$ and extract the quantities of interest, namely the capacitance and resistance, the distributed resistance-capacitance model from Ref. [86] is used. This model accounts for the actual device design, as schematically shown in Fig. 5.1b). The excitation signal is allowed to propagate inside the HgTe layer before transferring into the Au top plate.

The resistance and capacitance are defined as one-dimensional infinitesimal quantities as a function of the propagation direction as shown in Fig. 5.2b). This gives a set of coupled differential equations describing the complex admittance with the solution

$$Y(\omega)/W = iC_{\text{tot}}\omega L \frac{\tanh\left(\sqrt{i\sigma^{-1}C_{\text{tot}}\omega L^2}\right)}{\sqrt{i\sigma^{-1}C_{\text{tot}}\omega L^2}}, \tag{5.1}$$

where i is the imaginary unit. A fit of the model to the measurement data is shown as dashed lines in Fig. 5.2a). The model reproduces the measurement data well and thus allows to extract the overall capacitance C_{tot} and the conductivity σ. Before interpreting the extracted quantities first the seemingly complicated admittance spectrum shall be better understood by looking at the low and high-frequency limits. The complex admittance $Y(\omega)$ given by Eq. 5.1 reduces in the low frequency limit to

$$\text{Im}(Y(\omega \sim 0)) = C_{\text{tot}}L\omega \tag{5.2}$$

and

$$\text{Re}(Y(\omega \sim 0)) = \frac{C_{\text{tot}}^2}{\sigma}W\frac{L^3}{3}\omega^2. \tag{5.3}$$

A linear fit to $\text{Im}(Y(\omega \sim 0))$ yields the total capacitance C_{tot} according to Eq. 5.2. Knowing C_{tot} the conductance σ can be determined by a quadratic fit to $\text{Re}(Y(\omega \sim 0))$ following Eq. 5.3. Realistic devices possess a finite access resistance due to the contact to the device, which alters the measured resistance, but not the capacitance, for low frequencies. This access resistance can be determined and corrected by the analysis of the full measured frequency range, which is done for all presented resistance and capacitance values. The access resistance is not specifically addressed, since it is device geometry specific. A detailed description is given in Ref. [82]. The low-frequency part of the measured data is highlighted in green in Fig. 5.2a). The imaginary and real part of $Y(\omega)$ follow the expected linear and quadratic behavior, respectively. In the high frequency limit, Eq. 5.1 reduces to

$$\text{Re}(Y(\omega \rightarrow \infty)) \sim \text{Im}(Y(\omega \rightarrow \infty)) \sim W\sqrt{C_{\text{tot}}\frac{\sigma}{2}\omega}. \tag{5.4}$$

The high frequency limit is highlighted in grey in Fig. 5.2a), for which the measured real and imaginary part of $Y(\omega)$ are indeed alike. Since the low and high-frequency limit confirms the validity of the model, the focus is now shifted back to the results obtained with the fits of the admittance spectrum over the full frequency range.

The total capacitance and inverse conductance obtained by fitting the distributed resistance-capacitance model (Eq. 5.1) for the full measured frequency range in the hysteresis free gate voltage range of $U_{\text{gate}} = \pm 3\,\text{V}$ are summarized in Fig. 5.3a). The total capacitance C_{tot} and the inverse conductance σ^{-1} are shown as function of the chemical potential E_F where E_F is determined from

$$E_F(U_g) = e\int\frac{C_{\text{tot}}}{C_q}dU_g. \tag{5.5}$$

The total capacitance, shown in blue in Fig. 5.3a), features a clear minimum close to $E_F = 0\,\text{eV}$. Interestingly the maximum of the resistivity is shifted towards a more negative E_F in
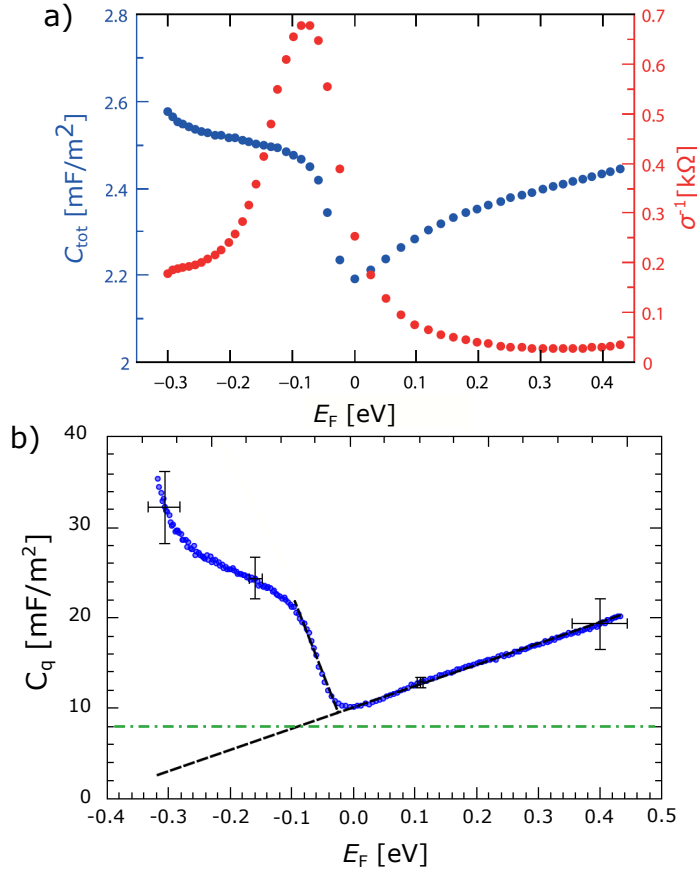
Figure 5.3: In a) the total capacitance C_{tot} and the inverse conductance σ^{-1} are shown as function of the electrochemical potential E_{F}. In b) the quantum capacitance C_{q} extracted by accounting for the insulator capacitance C_{ins} is shown together with error bars indicating the uncertainty due to the value of C_{ins}. The green dash-dotted line indicates the lowest expected quantum capacitance estimated by the $k \cdot p$ band structure of tensilely strained HgTe. The dashed black line is a guide to the eye to highlight the linear dependence of the quantum capacitance on the chemical potential for $E_{\text{F}} > 0\,\text{eV}$. The presented range of E_{F} corresponds to a gate voltage range of $U_{\text{gate}} = \pm 3\,\text{V}$. a) and b) modified from A. Inhofer *et al.*, Observation of Volkov-Pankratov states in topological HgTe heterojunctions using high-frequency compressibility, PRB **96**, 195194 (2017) [74]. Copyright 2017 by The American Physical Society.

comparison to the minimum of the capacitance. To get a more intuitive access to the physical origin of this offset, the quantum capacitance C_{q} is determined using

$$C_{\text{q}} = \left(C_{\text{tot}}^{-1} - C_{\text{geo}}^{-1} \right)^{-1}. \tag{5.6}$$

The geometric capacitance C_{geo} could be determined following Sec. 4.1.1 using the device dimensions and material parameters, but the necessary value, especially the dielectric constants, come with notable uncertainties. This is why the total capacitance is instead extracted from the admittance measurement for the highest available gate voltage. Since for high carrier densities the DOS can be taken as infinite, the quantum capacitance C_{q} becomes infinite as well. This yields $C_{\text{geo}} \sim C_{\text{tot}} \sim 2.6\,\text{mF/m}^2$. The resulting quantum capacitance C_{q} is shown as function of the electrochemical potential E_{F} in Fig. 5.3b). The quantum capacitance C_{q} still shows a minimum close to $E_{\text{F}} = 0$. The minimum of the DOS does not coincide with the maximum of the resistance. This observation is investigated further in the following Section by considering the band structure of HgTe.

5.2. Interpretation based on the Dirac screening model

In this Section the information about the DOS of the HgTe layer is extracted from the quantum capacitance spectrum $C_q(E_F)$. For a system like HgTe with multiple bands, the contributions due to the individual DOSs of the contributing bands to the total quantum capacitance have to be taken into account. As a starting point, the Dirac-screening model of Ref. [47] is used, which is summarized in the state of the art of research in Sec. 2.3.4. Only the top and bottom topological surface states are relevant according to this model. This is illustrated again in Fig. 5.4a), which shows the exclusive occupation of the TSS for a positive gate voltage within the Dirac-screening model.
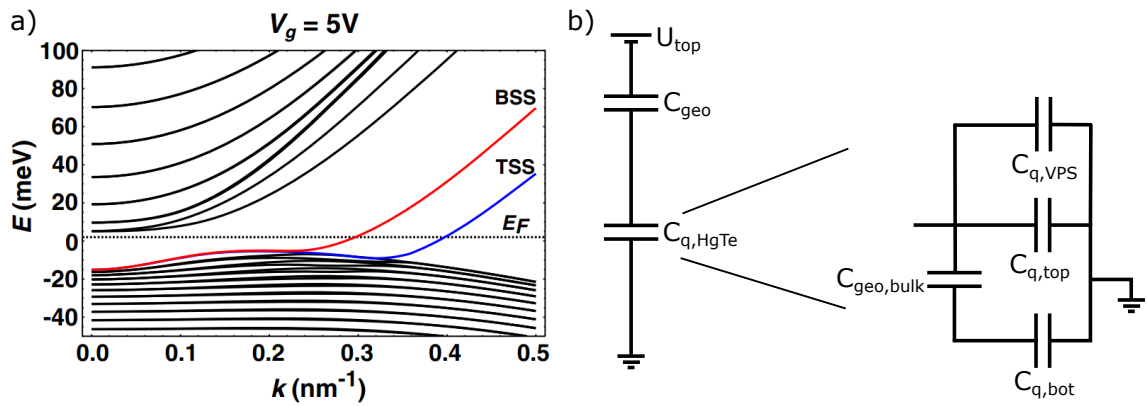

Figure 5.4: In a) the band structure of a 70 nm thick 0.3 % tensilely strained HgTe layer with a 6-band $k \cdot p$ Kane model which is shown, as already presented in Fig. 2.9c). The Fermi energy E_F is indicated as a dotted black line and the top and bottom TSS are highlighted in blue and red, respectively. Reprinted from C. Brüne *et al.*, Dirac-Screening Stabilized Surface-State Transport in a Topological Insulator, PRX **4**, 41045 (2014) [47], Attribution 3.0 Unported (CC BY 3.0). In b) the equivalent capacitor circuit is shown that represents the actual device by accounting for the quantum capacitance of the HgTe layer C_{HgTe}, which is calculated based on a further equivalent circuit including the quantum capacitances of the topological surface states $C_{q,top/bot}$, Volkov-Pankratov states $C_{q,VPS}$, and the geometric capacitance of the HgTe bulk $C_{geo,bulk}$, as already shown in Fig. 4.2a) and c).

Following the same procedure as in Sec. 4.1 a capacitor circuit diagram is designed to account for the quantum capacitances $C_{q,top}$ and $C_{q,bot}$, appropriately. The measured C_q is a parallel circuit of the quantum capacitance of the top TSS $C_{q,top}$ in parallel to the capacitance made up of the quantum capacitance of the bottom TSS $C_{q,bot}$ in series with the geometric capacitance of the HgTe bulk $C_{geo,bulk}$. The corresponding effective circuit diagram is shown in Fig. 4.2b) and again reprinted here in Fig. 5.4b). This capacitor circuit has some implications which account for the sensitivity of the capacitance measurements to different states. Since the quantum capacitance $C_{q,bot}(n > 0.5 \times 10^{11} \, \text{cm}^{-2}) > 6 \, \text{mF/m}^2$ (see Eq. 4.10) is in series with the smaller geometric capacitance of the HgTe layer $C_{geo,bulk} = \epsilon_0 \epsilon_{R,HgTe}/d_{HgTe} = 2.7 \, \text{mF/m}^2$, the total capacitance of this parallel channel is in good approximation given by the geometric capacitance of the HgTe layer $C_{parallel} \sim 2.7 \, \text{mF/m}^2$. A more precise value including $C_{q,bot}$ would yield $C_{parallel} \sim 2.4 \, \text{mF/m}^2$ which is not much different. The parallel path of $C_{geo,bulk}$ in series with $C_{q,bot}$ is expected to mainly act as constant "parasitic" capacitance. Or in other words, the measured capacitance depends only very weakly on the quantum capacitance of the bottom TSS. The negligible contribution of the bottom surface state is visualized in Fig. 4.4c). There the comparable small change in

the occupation of the bottom surface state with the top gate voltage is depicted. The quantum capacitance C_q consequently represents the gate voltage dependence of the quantum capacitance of the top TSS $C_{q,top}(U_{gate})$ including the constant offset $C_{parallel}$.

The minimum quantum capacitance $C_{q;min} \sim 10\,\text{mF/m}^2 > C_{parallel}$ at $E_F \sim 0.00\,\text{eV}$ is thus an meaningful and interesting quantity. Assuming a topological surface state with accessible Dirac point one would expect to find a zero DOS and thus $C_{parallel}$ as a minimum in contrast to the observed finite $C_{q;min}$. The zero DOS of a Dirac point would also be expected to be accompanied by a resistance maximum. Here the resistance maximum is shifted to $E_F \sim -0.08\,\text{eV}$, where hole transport would be expected. To explain this behavior the realistic band structure of tensily strained HgTe has to be considered. The corresponding band structure is shown in Fig. 2.6f) as calculated by $k \cdot p$ and in Fig. 2.6c) as determined by DFT calculations. The Dirac point of the TSS is buried in the bulk valence ($\Gamma_{8,\text{HH}}$) band. The position of the TSS Dirac point differs in the two calculations due to the different surface potentials accounted for. The $k \cdot p$ calculation in Fig. 2.6f) assumes an ideal interface to the $Cd_{0.7}Hg_{0}.3Te$ capping layers. The Dirac point then lies $\sim 80\,\text{meV}$ below the valence band edge. The DFT calculation also places the Dirac point inside the valence band edge, but closer to the valence band edge. The Dirac point is nevertheless inaccessible for both calculations. Consequently, zero DOS is unattainable in tensily strained HgTe, and the Dirac point of the top TSS can not be the origin of the observed minimum in C_q.

To find an alternative reason for the observed minimum capacitance, the focus is shifted back to the overall $C_q(E_F)$ spectrum. The quantum capacitance of the two-dimensional linear dispersing topological surface state depends according to Eq. 4.7 linearly on E_F. For $E_F > 0\,\text{eV}$ this resembles the experimental observation well, as indicated by the dashed black line in Fig. 5.3b). The minimal quantum capacitance can be estimated by reformulating Eq. 4.7 to include the Fermi wave vector k_F. The equation then reads

$$C_{q;\text{lin};2D}(k_F) = \frac{e^2}{h v_F} k_F. \tag{5.7}$$

In the $k \cdot p$ band structure, as shown in Fig. 2.6f), the smallest achievable DOS is found for E_F right above the valence band edge at $k_{F;min} = 0.10\,\text{nm}^{-1}$. Taking the Fermi velocity to be $v_{F;\text{lit}} = 0.5 \times 10^6\,\text{m/s}$ [51, 87], this yields based on Eq. 5.7 $C_{q,\text{lin};2D} \sim 8\,\text{mF/m}^2$ and is indicated as dash-dotted green line in Fig. 5.3b). This value is only slightly lower than the experimental observed minimal quantum capacitance. Alternatively, the surface state densities are also extracted from the FFT analysis of the gate voltage-dependent magneto-transport data shown in Fig. 3.12b). The valence band edge lies at $U_{gate} = -2\,\text{V}$ as indicated by a dash-dotted black line and yields $n_{top,min} \sim 0.6 \times 10^{11}\,\text{cm}^{-2}$. This density compares reasonable well with the extracted value of $k_{F;min} = 0.10\,\text{nm}^{-1}$ from the $k \cdot p$ calculations which corresponds to $n_{top,min} \sim 0.8 \times 10^{11}\,\text{cm}^{-2}$. Using the relation between k_F and n for a 2DEG given by Eq. 4.9, Eq. 5.7 is reformulated to include the density n explicitly as Eq. 4.10, which reads

$$C_{q,\text{TSS}} = \frac{e^2}{h v_F} \sqrt{4\pi n}. \tag{5.8}$$

With $n_{top,min}$ and Eq. 5.8 a minimum quantum capacitance of $C_{q,min,est} \sim 7\,\text{mF/m}^2$ is determined. Together with the above discussed "parasitic" parallel conductance due to the bottom surface state $C_{parallel} \sim 2.4\,\text{mF/m}^2$ these numbers reproduce the observed minimal capacitance of $C_{q;min} \sim 10\,\text{mF/m}^2$ well. The coexistence of electrons and holes, as seen in

the $k \cdot p$ calculation shown in Fig. 2.6f), also offers an explanation for the observed shift of the resistance maximum towards a more negative E_F compared to the minimum of the quantum capacitance $C_{q,min}$. The conductivity σ and consequently the resistance depends according to Eq. 3.2 not only the density n, and thus the DOS, but also the carrier mobility μ. The holes, which are introduced for $E_F < 0$, possess a much lower mobility due to their higher effective mass compared to the electrons, as determined in Sec. 2.3.3. This means the overall conductance can even reduce when the overall carrier density is increased. Additionally, the introduced holes can act as a new scattering source for the electrons reducing the overall conductance. The linear DOS which is observed for $E_f > 0$ eV, is consistent with the signal being dominated by the top TSS as expected from the Dirac screening model. The validity of this simple first assumption is examined in the next Section.

5.3. REINTERPRETATION BASED ON THE CAPACITOR CIRCUIT MODEL

The results of the high-frequency compressibility measurements allow extracting the Fermi velocity v_F. The quantum capacitance C_q as a function of the electrochemical potential E_F is analyzed using the Equation for the quantum capacitance of a two-dimensional linear dispersing band given by

$$C_{q,topSS}(E_F) = \frac{e^2}{2\pi\hbar^2}\frac{1}{v_F^2}E_F.$$ (5.9)

This equation resembles Eq. 4.7 under the assumption of no degeneracy ($g = 1$). A linear fit to the quantum capacitance data $C_q(E_F)$ is indicated in Fig. 5.3b) as dashed black line. The slope of this linear fit yields $v_F = 1.6 \times 10^6$ m/s. This Fermi velocity differs by a factor $2 - 3$ from $v_{F,exp} \sim 0.5 \times 10^6$ m/s obtained by other measurement techniques in Refs. [51, 87, 88], which is similar to $v_{F;kp} \sim 0.7 \times 10^6$ m/s determined by $k \cdot p$ calculations using the program "kdotpy" [29]. The theoretical value of $v_{F;kp}$ is obtained by a linear fit to the dispersion of the TSS for the energy range 50 meV< E < 150 meV and assuming the linear dispersion $E(k) = \hbar v_F k$ for the TSS. This procedure is visualized in Fig. 5.5, where the linear fit to the blue TSS is drawn as a dashed black line.
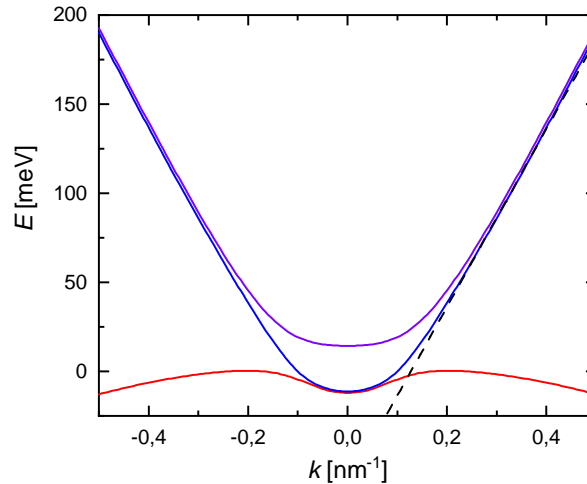

Figure 5.5: The band structure of HgTe determined by $k \cdot p$ calculation with the program "kdotpy" as shown in Fig. 2.6f) is shown. Only the band edges of the conduction (purple) and the valence band (red) are shown together with the topological surface state (blue). The dashed black line shows a linear fit to the dispersion of the surface state for the energies 50 meV< E < 150 meV.

To investigate the origin of the discrepancy of the Fermi velocity v_F by a factor of $2-3$, the assumptions made for the analysis are revisited. Using the Dirac-screening model and accounting for the capacitances of the top and bottom TSS only the top TSS is relevant according to the analysis in Sec. 5.2. In contrast, the magneto-transport measurements presented in Chapter 3 show the occupation of additional n-type transport channels, which are by $k \cdot p$ calculations in Chapter 4.3 identified as electron-like massive Volkov-Pankratov states. Even though a bandgap is observed in this measurements of $E_\text{gap} \sim 0.015\,\text{eV}$ before these electron-like massive VPS are observed, the bandgap is very small compared to the investigated energy range of $0.4\,\text{eV}$ in the compressibility measurements. Since the electron-like massive VPS are localized at the top surface, these states can be accounted for in the effective circuit diagram as additional parallel capacitance. The corresponding equivalent circuit diagram is shown in Fig. 4.2c) and again in Fig. 5.4b). The involvement of multiple bands makes the situation more complex and may make the extraction of band structure parameters from the quantum capacitance seem ambiguous. To qualify this statement, the band structure of HgTe calculated with $k \cdot p$ using the program "biscuit" is shown in Fig. 5.5. Only the band edges of the conduction and valence band together with the TSS is depicted. The dispersion of the conduction band edge is taken as an approximation for the dispersion of the electron-like massive VPS. For high energies ($E > 50\,\text{meV}$) the dispersion of the TSS and the electron-like massive VPS are approximately identical and linear. For sufficiently high energies the non-degenerate TSS and the double (spin) degenerate electron-like massive VPS can thus be treated as one linearly dispersing band with the degeneracy factor $g = 3$. The quantum capacitance is then again given by Eq. 5.9, which including the degeneracy factor explicitly reads

$$C_\text{q;realistic} = g\frac{e^2}{2\pi\hbar^2 v_\text{F}^2}E_\text{F} = gC_\text{q,topSS}. \qquad (5.10)$$

This equation allows to extract the Fermi velocity v_F using a linear fit to $C_\text{q}(U_\text{gate})$ as shown in Fig. 5.3b). The Fermi velocity is effectively renormalized by a factor of three, yielding the Fermi velocity $v_\text{F} \sim 0.5 \times 10^6\,\text{m/s}$. This Fermi velocity fits the before mentioned reported values of $v_\text{F,exp} \sim 0.5 \times 10^6\,\text{m/s}$. Furthermore, the involvement of three surface states agrees with the three two-dimensional transport channels observed in the magneto-transport.

This interim result supports the validity of the model for HgTe introduced in Chapter 4 based on the coexistence of topological surface states and Volkov-Pankratov states. The high-frequency compressibility measurements still provide some open questions. The quantum capacitance data for $E_\text{F} \sim 0\,\text{eV}$ and $E_\text{F} < 0\,\text{eV}$ is more complicated. A more in-depth analysis would be necessary, which is out of the scope of this work. It is unclear, why no indications for the occupation of the conduction band continuum are visible for the high positive electrochemical potentials E_F. A possible mechanism could be the screening of the applied electric field by the VPS. The self-consistent $k \cdot p$ calculations, as shown in Fig. 4.6c) and discussed in Sec. 4.3, show an energy shift of the electron-like massive VPS away from the band continuum. This energy shift is accompanied by a shift of the probability distribution of the state towards the top surface, as shown in Fig. 4.3c). The shift of the probability distribution towards the top surface is used to identify these states as electron-like massive Volkov-Pankratov states in Sec. 4.4. The questions about the screening properties of the TSS and the whereabouts of the conduction band are the motivation for the investigation of even stronger electric fields in the next Section.

5.4. OBSERVATION OF MASSIVE VOLKOV-PANKRATOV STATES

Measurements up to high gate voltages are performed to examine the dispersion of the TSS for high energies as well as their screening properties. These measurements revealed the formation of a related, but different, type of surface state in HgTe, which has been dubbed massive Volkov-Pankratov state [16, 17, 74] (see Sec. 4.4).

5.4.1. MEASUREMENTS UP TO HIGH GATE VOLTAGES

So far only the hysteresis free top gate voltage has been discussed. There, the quantum capacitance C_q shows a linear dependence on the electrochemical potential E_F for positive energies, as shown in Fig. 5.3b) up to $E_F \sim 0.43\,\text{eV}$. According to Eq. 5.9 a linear energy dependence can be taken as an indication for a linear energy dispersion in the momentum k. The big range of E_F with linearly dispersing states is surprising, even while accounting for the occupation of the electron-like massive VPS. The focus is thus shifted from the capacitance to the resistivity, which is shown as a function of the electrochemical potential in red in Fig. 5.3a). Starting from $E_F = 0\,\text{eV}$ the resistivity decreases with increasing E_F as expected with increasing charge carrier densities up to $E_F \sim 0.3\,\text{eV}$. For $E_F > 0.3\,\text{eV}$ the resistivity σ^{-1} appears nearly constant. This appearing constant resistivity is a minimum in the resistance. The minimum is verified by extracting the total capacitance C_{tot} and resistivity from complex admittance measurements for higher gate voltages. The extracted values are shown in Fig. 5.6a). The high applied gate voltages cause hysteresis, which can be seen by the saturation of the total capacitance C_{tot} and the resistivity σ_{-1} for gate voltages $U_{\text{gate}} > 6\,\text{V}$. Full hysteresis loops are shown in Ref. [74]. A similar hysteresis effect is observed in HgTe quantum wells in Ref. [89]. The hysteresis is attributed to a charge accumulation in the interface between the gate insulator and the $Cd_{0.7}Hg_{0.3}Te$ layer. The charge accumulation in the interface limits the maximum via the gate adjustable carrier density.
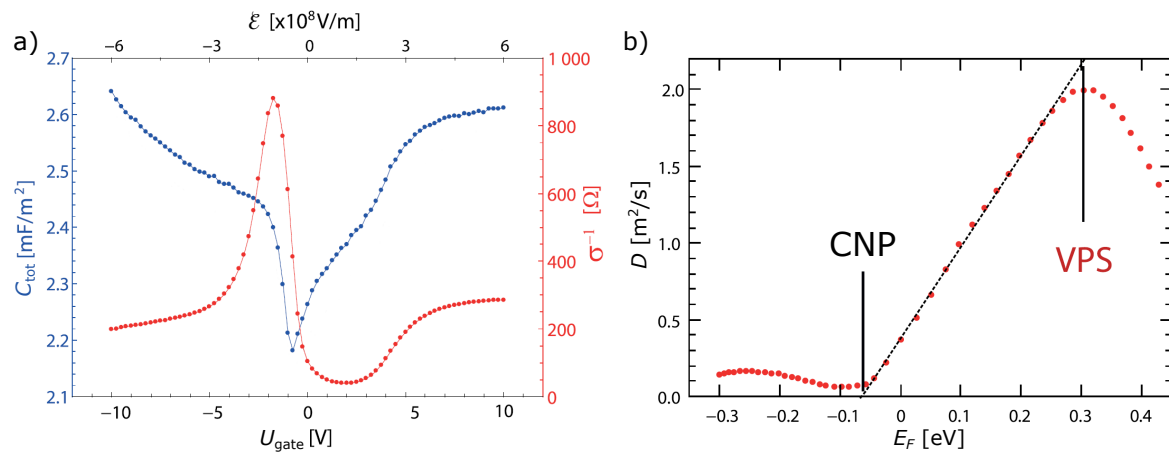
Figure 5.6: In a) the total capacitance C_{tot} and the inverse conductivity σ^{-1} are shown as function of the gate voltage U_{gate} and the electric field $\mathscr{E}$. In b) the Diffusion constant D extracted from the ac-compressibility measurements is shown as a function of the chemical potential E_F. The potential energetic position of the charge neutrality point and the onset of the massive Volkov-Pankratov state are marked as CNP and VPS, respectively. The dashed line is a guide to the eye. a) is modified and b) is reprinted from A. Inhofer *et al.*, Observation of Volkov-Pankratov states in topological HgTe heterojunctions using high-frequency compressibility, PRB **96**, 195194 (2017) [74]. Copyright 2017 by The American Physical Society.

The high gate voltage range verifies the observation of a minimum in the resistivity for positive gate voltage and justifies a more in-depth analysis of the measurements performed in the hysteresis free gate voltage range. In contrast to the observed minimum in the resistivity, a steady decrease of the resistivity is expected for the continuous occupation of one well-behaved band. The change from a decrease of the resistance to an increase with increasing gate voltage indicates either a change in the property of the band as a change of its effective mass or the onset of a new band. To investigate this weak trend in more detail another accessible quantity, the diffusion constant D, is introduced. The diffusion constant is determined by

$$D(E_F) = \frac{\sigma(E_F)}{C_q(E_F)}. \tag{5.11}$$

The diffusion constant D is shown as function of the electrochemical potential E_F in Fig. 5.6. For $E_F > -0.02\,\text{eV}$ the diffusion constant linearly increases with E_F up to a clear maximum at $E_F \sim 0.3\,\text{eV}$. For $E_F < -0.1\,\text{eV}$ the diffusion constant increases with more negative E_F, but much weak than the increase observed for $E_F > -0.02\,\text{eV}$. The maximum of the diffusion constant D at $E_F \sim 0.3\,\text{eV}$ is consistent with the position of the minimum of the resistivity. This decrease of the diffusion constant suggests the onset of some kind of transport hindering mechanism. The diffusion constant $D(E_F)$ can be translated into a mobility μ using the relation

$$\mu(E_F) = \frac{\sigma}{C_q} 2e \frac{D}{E_F}. \tag{5.12}$$

The observed linear dependence of $D(E_F)$ indicates a constant mobility of $\mu \sim 120 \times 10^3\,\frac{\text{cm}^2}{\text{Vs}}$, which compares well to the mobility determined by magneto-transport measurements for the electron transport regime, as shown in Fig. 5.7a). The observation of a low mobility for small carrier densities that increases up to a constant mobility for high electron densities is consistent with screened charged impurity scattering. This is usually the dominating scattering effect that limits the mobility in semiconductors at low temperatures [90]. For the region of interest $E_F > 0.0\,\text{eV}$ the electron density is sufficiently high to screen the charged impurities, yielding a constant mobility. The minimum of the diffusion constant lies as expected at $E_F \sim -0.1\,\text{eV}$, which is the poition of the resistance maximum in Fig. 5.3a)) and lower than the minimum of the DOS at $E_{F\text{minDOS}} \sim -0.02\,\text{eV}$. For $E_F < -0.1\,\text{eV}$ the diffusion constant only increases weakly with increasing hole density. This yields a hole mobility in the order of $\mu_{\text{hole}} \sim 20 \times 10^3\,\frac{\text{cm}^2}{\text{Vs}}$, also consistent with the value determined by magneto-transport measurements. To sum up the analysis of $D(E_F)$ yields consistent mobilities with the ones determined by magneto-transport measurements [see Fig. 5.7a)]. The observed maximum in the diffusion constant indicates the onset some transport hindering mechanism for $E_F > 0.3\,\text{eV}$. The onset of a new scattering mechanism should also be visible in DC magneto-transport, which is presented in the next Section.

5.4.2. Reference magneto-transport measurements

To perform magneto-transport measurements at high positive electric fields a Hall-bar is fabricated from wafer Q2837 following the recipe described in Sec. 3.1.1 with a few modifications. The mesa is etched with the aqueous solution of $KI/I_2/HBr$ (see Ref. [45]) and the 110 nm thick $SiO_2 Si_3N_4$ multilayer insulator is replaced by a 15 nm HfO_2 insulator is grown by low-temperature atomic layer deposition. These steps are equivalent to the fabrication process of the capacitor device described in Sec. 5.1. The insulator thickness is increased

from 10 to 15 nm to avoid insulator breakthrough due to the significantly increased area of the insulator in the Hall bar device. The longitudinal resistance as a function of the gate voltage $R_{xx}(U_{gate})$ is shown in Fig. 5.7a). A minimum in the high electron density regime is observed, which is reminiscent of the minimum observed for the capacitor structure in Fig. 5.3a). Its position is indicated in Fig. 5.7a) by the label VPS. The mobility μ and total carrier density n are extracted from the semi-classical magneto-transport regime following the procedure described in Sec. 3.1.2. The density values are shown as additional x-axis in Fig. 5.7a) together with the mobility as blue dots. The minimum in the longitudinal resistance R_{xx} coincides as expected with a maximum of the mobility μ. This is consistent with the reduction of the diffusion constant D found for the capacitor structure, as shown in Fig. 5.6b).
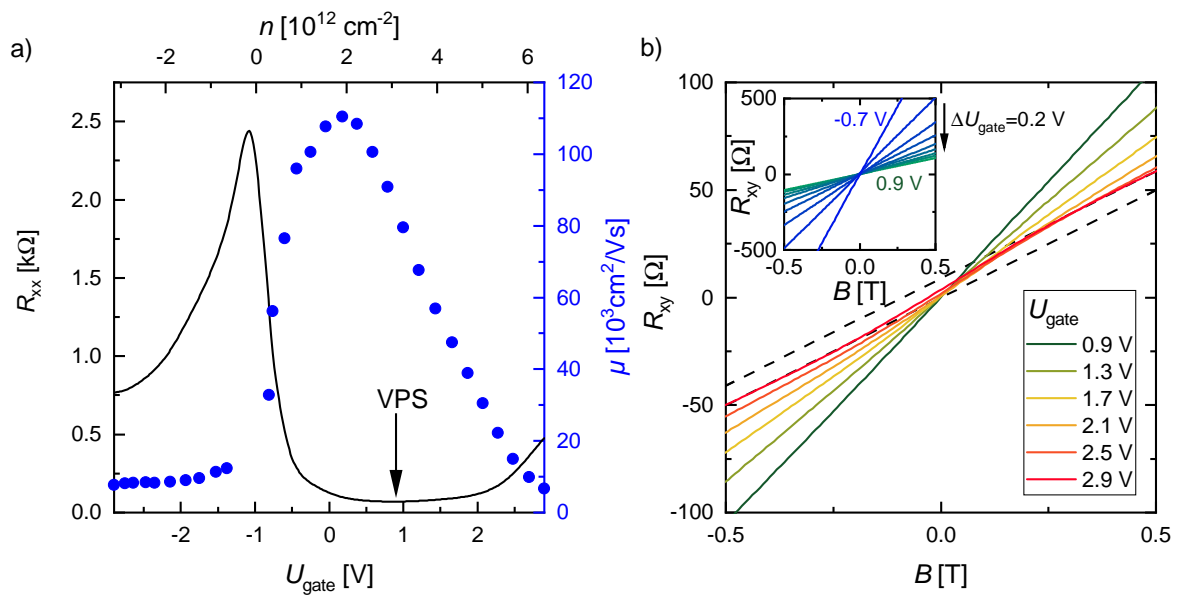
Figure 5.7: In a) the longitudinal resistance R_{xx} is shown in black together with the mobility μ as a function of the gate voltage U_{gate} and equivalently the overall density n. In b) exemplary measurements of the Hall resistance R_{xy} are shown as a function of the magnetic field B for high positive gate voltages U_{gate} as well as lower voltages representing lower electron densities in the inset. The dashed lines are guides to the eye.

The gate voltage dependence of the longitudinal resistance and the mobility of the Hall-bar is similar to the resistivity and diffusion constant determined by the compressibility measurement, respectively. For the Hall-bar is the Hall resistance signal R_{xy} additionally accessible. The semi-classical transport regime for low magnetic fields is analyzed. In the electron regime, the Hall resistance $R_{xy}(B)$ shows the expected linear dependence on the magnetic field B up to gate voltages of $U_{gate} \sim 0.9$ V, as indicated by the dashed olive line in Fig. 5.7b). For $U_{gate} > 0.9$ V, the Hall resistance R_{xy} starts to form an s-shape around $B = 0$ T as shown in Fig. 5.7b). This s-shape deviation from the expected linear behavior is emphasized by the black dashed extrapolation of the linear behavior for magnetic fields $B \sim \pm 1$ T and the gate voltage $U_{gate} = 2.9$ V. The simplest model to reproduce such a curved Hall signal is the Drude model for two channels with sufficiently different carrier densities and mobilities, as introduced in Sec. 3.1.2. According to the model, the development of the s-shape indicates the onset of a second sufficiently different transport channel. This second transport channel shows no specific temperature dependence up to temperatures of $T = 20$ K according to Ref. [91].

Considering the band structure of HgTe, as shown in Fig. 5.5, it is surprising that a linear Hall signal is observed for such a large electron density range of up to $n \sim 30 \times 10^{11}\,\text{cm}^{-2}$ in the first place. This is reminiscent of the observed linear DOS up to high U_{gate} in the compressibility measurements in Fig. 5.3b) of Sec. 5.1. This observation is traced in Sec. 5.3 to the fact that the top topological surface state and the conduction band edge possess a nearly identical dispersion for high energies E_F and thus high electron densities n. A matching dispersion implies the same effective mass and thus also a similar mobility. This means that the TSS and electron-like massive VPS should not be distinguishable in the semi-classical regime and behave like one single degenerate transport channel. The onset of a second transport channel in the Hall resistance R_{xy}, suggests the occupation of a new state as the source for the scattering identified by the observed reduction of the diffusion constant. To find the responsible state, $k \cdot p$ band structure calculations are used in the next Section.

5.4.3. BAND STRUCTURE CALCULATIONS FOR A FINITE GATE VOLTAGE

The discussion of the band structure of HgTe usually focuses on the energy regime a few hundred meV around the Γ_8 and Γ_6 band edges at the Γ point. The band structure of HgTe is shown for this energy range in Fig. 2.6 based on ARPES, DFT and $k \cdot p$. The energies reached by the compressibility measurements and the magneto-transport measurements discussed in this Chapter 5 exceed this energy window. The bulk band structure of tensilely strained HgTe calculated using the program "kdotpy" is shown up to higher energies in Fig. 5.8a). The electrochemical potential E_F of the compressibility measurements can be mapped to the energy of the band structure by assigning the minimum of C_q to the valence band edge based on the discussion in Sec. 5.2. The observed low diffusion constant and mobility for $E_F < -0.02\,\text{eV}$ in Fig. 5.6 is consistent with the flat dispersion of the bulk valence band edge. The high mobility determined by the linear fit to $D(E_F)$ for $E_F > -0.02\,\text{eV}$ similarly agrees with the high mobility expected for electrons with a linear dispersion. No resemblance for the breakdown of the diffusion constant at $E_F \sim 0.3\,\text{eV}$ is found in the bulk band structure of HgTe, as shown in Fig. 5.8a).

The bulk band structure does not consider any interfaces or any other intrinsic or external potentials. In principle, the self-consistent k·p calculations presented in Sec. 4.3 could be used to look for additional interface states for strong applied electric fields. Unfortunately, these calculations are only possible for very small gate voltages and consequently also very small changes in E_F of $\Delta E_F \sim 0.03\,\text{eV}$ compared to the relevant energy scale of $E_F \sim 0.3\,\text{eV}$ and are thus unsuitable to find the responsible mechanism. Following the same motivation, six-band $k \cdot p$ calculations are performed in Ref. [17, 74]. These calculations reveal the formation of an additional interface state at $E \sim 0.8\,\text{eV}$, as shown in Fig. 5.8b). This additional interface state is formed due to the drop of the electrical potential over the interface. Similar massive interface states are predicted by B. A. Volkov and O. A. Pankratov in Ref. [16] in an interface with a smooth material content variation. The authors of Ref. [17, 74] argue that a smooth electric potential is equivalent to a material content variation and also causes the formation of additional massive surface states. This creation mechanism is discussed in more detail in Sec. 4.4. Based on this resemblance these additional massive surface states due to the electric potential are called massive Volkov-Pankratov states to acknowledge the first description of such states by B. A. Volkov and O. A. Pankratov in Ref. [16]. These additional massive states should possess a different disper-
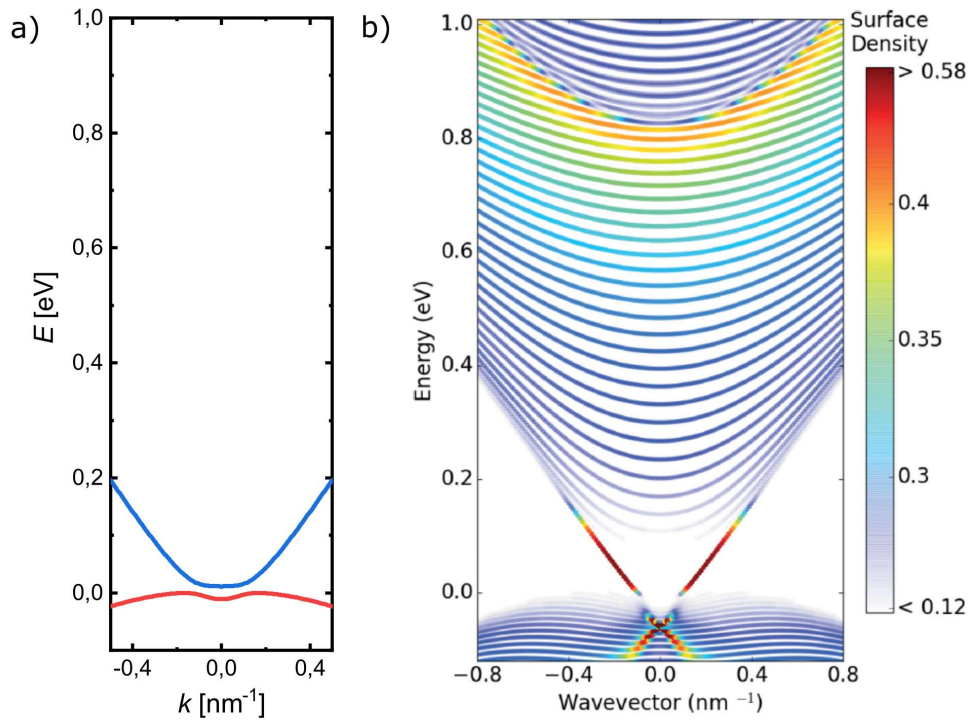
Figure 5.8: In a) the bulk band structure of tensilely strained HgTe is shown for higher positive energies as calculated with the eight-band $k \cdot p$ using the program "kdotpy" [29] and depicted before in Fig. 2.6e). In b) the energy dispersion along the interface direction is shown for an HgTe/CdTe interface obtained within a six-band Kane model. The color encodes the density of eigenstates in a region of 6 nm around the interface. b) is reprinted from A. Inhofer *et al.*, Observation of Volkov-Pankratov states in topological HgTe heterojunctions using high-frequency compressibility, PRB **96**, 195194 (2017) [74]. Copyright 2017 by The American Physical Society.

sion to the other occupied states and could constitute a new scattering mechanism. The massive VPS are thus a reasonable mechanism for the observed breakdown of the diffusion constant by the onset of a new scattering channel. These massive Volkov-Pankratov states found for very high electron densities and strong electric fields are different from the ones described in Sec. 4.4. The difference lies in the localization of these states. While the VPS here are localized 6 nm around the interface, the electron and hole VPS found in the magneto-transport experiments (see Sec. 4.4) for much smaller densities and weaker electric fields are mainly localized inside the HgTe layer. Both states are still a consequence of the shape of the Hartree potential across the heterostructure and interesting as well as not neglectable additional surface states.

5.5. SUMMARY OF HIGH FREQUENCY COMPRESSIBILITY MEASUREMENTS

The high-frequency compressibility measurements constitute a valuable complementary measurement technique to the magneto-transport investigations. These measurements grant access to the DOS as a function of the electrochemical potential. A linear DOS is observed over a wide range of electrochemical potentials indicating the existence of a state with linear energy dispersion. The observed reduction of the diffusion constant for strong electric fields hints at the onset of a new state. Magneto-transport experiments on a Hall bar device reveal an s-shaped curvature in the Hall resistance for low magnetic fields. Such an s-shaped curvature is consistent with the onset of an additional transport channel according to the two-channel Drude model. The modeling of this observation with the help of $k \cdot p$ calculations with a realistic interface and accounting for the applied electric field led to the discovery of an additional massive interface state. These states have been called to Volkov-Pankratov states to acknowledge the work of B.A. Volkov and O. A. Pankratov on inverted interfaces in e.g. Ref. [16].

Further insights could be gained by combining the complementary measurement techniques of high-frequency compressibility and magneto-transport measurements. As a first approach, measurements could be performed with Lock-In amplifiers at moderate frequencies in the order of 10 kHz in cryostats wired with coaxial cables. This frequency range avoids the need for special high-frequency equipment. This way the capacitance can be examined as a function of the magnetic field. The combination of resistance and capacitance measurements could allow determining the localization of different states similar to Ref. [76]. The observed transport features could thus be traced to the responsible states.

6

NEW INSIGHTS INTO THE THREE-DIMENSIONAL TOPOLOGICAL INSULATOR PHASE OF HGTE

Three-dimensional topological insulators have been theoretically predicted in 2008 by Ref. [92]. Shortly after $Bi_{1-x}Sb_x$ has been verified as experimental realizations using ARPES in Ref. [6] and tensilely strained HgTe using magneto-transport measurements in Ref. [8]. The development of topological materials has been reviewed in Ref. [38, 39]. Nevertheless, a convincing identification and manipulation of all observed surface states present a challenge up to the present day. The realization of a prototypical 3D-TI with purely topological surface state-driven transport either needs very high magnetic fields, as for $Bi_{2-x}Sb_xTe_{3-y}Se_y$ e.g. in Ref. [93], or is hindered by the existence of other states in parallel, as in tensilely strained HgTe in Ref. [71]. This is where this work contributes. The quality of tensilely strained HgTe samples has further improved. Additionally, the MBE grown layer stack and the lithographic fabrication recipe have been adjusted. In these samples, quantum Hall effect and Shubnikov-de Haas oscillations can be observed for low magnetic fields even below $B = 0.2\,T$. Because of this, six contributing transport channels have been found. The analysis of the Landau level spectrum together with $k \cdot p$ calculations enabled us to identify their respective origins. Two of these states are the top and bottom topological surface states, which exist over the full investigated gate voltage range. The four other transport channels are identified as additional surface states. The existence of such additional states was first proposed to explain the observations in high-frequency compressibility measurements. In these compressibility measurements, a strong electric field has been used to investigate the dispersion of the topological surface states for high energies and revealed their linear dispersion over a wide energy range. These strong electric fields have been shown with the help of $k \cdot p$ calculations in Ref. [17, 74] to cause the formation of additional massive surface states, dubbed massive Volkov-Pankratov states. Such Volkov-Pankratov states have been identified as the origin of the two hole-like transport channels observed in the magneto-transport experiments. This has been verified with the help of additional self-consistent $k \cdot p$ calculations. The additional observed electron type transport channels are likewise contributed to massive Volkov-Pankratov states. To sum up, a purely topological surface state-driven regime is found and the additional transport channels are identified as massive Volkov-Pankratov states created by the applied gate voltage.

This indicates tensilely strained HgTe as an ideal three-dimensional topological insulator for further more advanced experiments and devices.

For example, a first step towards the realization of topological qubits has already been made based on hybrid superconductor HgTe devices [40]. Experiments with superconductors on $65 - 90\,$nm thick tensile strained HgTe devices in Ref. [14] have already shown a $4 - \pi$ -periodic Josephson supercurrent. The $4 - \pi$ contribution was relatively small due to the coexistence of topological trivial surface states. Subsequent experiments on hybrid superconductor devices based on topological HgTe quantum wells in Ref. [94] showed a much stronger $4 - \pi$ contribution. An optimized MBE grown layer stack could suppress the formation of Volkov-Pankratov states and maximize the carrier density in the TSSs and thus the $4 - \pi$ contribution. The use of a $Cd_{0.7}Hg_{0.3}Te$ buffer layer with an iodine doping layer and a protective $Cd_{0.7}Hg_{0.3}Te$ capping layer is suggested. A minimal invasive etching method as wet etching with aqueous $KI/I_2/HBr$ solution or inductively coupled ion etching is necessary to provide an adequate interface for the superconductor to be able to induce superconductivity.

Next to this more ambitious long-term goal, exist also more immediate questions and potential developments. The bottom doping layer has been shown to change the occupation of the bottom TSS, while the top gate mainly alters the filling of the top TSS. Motivated by this observation, the growth of samples on a doped GaAs substrate is suggested, since the substrate can be used as a back gate. The combination of a top and back gate constitutes an ideal playground to investigate the interplay and interaction of the TSSs with each other and the massive Volkov-Pankratov states. The potential change in the occupation of the bottom surface states can be increased by the combined use of the iodine doping layer and the GaAs substrate as a back gate. The massive Volkov-Pankratov states are also interesting themselves due to their non-trivial dispersion. Especially the hole-like massive Volkov-Pankratov states with their "camelback"-like dispersion. These are predicted to potentially host additional quantum oscillations without a Fermi surface [53, 54] (see App. B). Due to the strong spin-orbit coupling in HgTe, an electric field can alter the symmetry of these hole-like VPSs due to the combination of the bulk and structural inversion asymmetry or equivalently the Dresselhaus and Rashba effect. An investigation on the shape and symmetry of these bands via magneto-transport is presented in Ref. [95] and also examined to some extent in Part III of this work.

III

HgTe as inversion induced Dirac semi-metals

7

BULK PROPERTIES OF INVERSION INDUCED DIRAC SEMI-METALS

The two-dimensional topological surface states are of special interest because of their topological protection, spin moment locking, and linear dispersion. It turns out that linear dispersions are also interesting in three dimensions, where they are predicted to cause a new magnetoresistance effect, the so-called chiral anomaly [11]. To address this new transport effect this Chapter is arranged as follows: Materials with a linear bulk dispersion, so-called topological semi-metals, are introduced. The focus lies on the subclass of inversion-induced Dirac semi-metals since the investigated material compressively strained HgTe belongs to this material class. Magneto-transport measurements reported on these topological semi-metals are reviewed. These show a reduction of the longitudinal resistance with a magnetic field applied parallel to the current. This so-called negative magnetoresistance is seen as a signature for the subsequently described chiral anomaly. This presents the starting point for the subsequent presented magneto-transport investigations on compressively strained HgTe. The fabrication process of the HgTe samples is described and the performed magneto-transport experiments are summarized. The magneto-transport experiments are performed with varying strength and angle of the magnetic field which yields results consistent with the chiral anomaly as a driving mechanism. This accordance is verified with the help of measurements with varying top gate voltage as well as impurity concentration and strain in the HgTe layer. Additionally, other transport effects, as the weak anti-localization, the planar Hall effect, and other band structure-dependent magnetoresistance effects, are found and investigated.

7.1. TOPOLOGICAL SEMI-METALS

Recently, a variety of materials have been proposed to be topological semi-metals with linear dispersing bulk bands. These are mainly novel materials of which only some have been successfully synthesized and measured. A comprehensive overview can be found in the recent review papers [11, 96, 97]. Here only a brief overview of topological materials is given to be able to place compressively strained HgTe within these. The class of topological semi-metals can be divided into Dirac and Weyl semi-metals. Dirac semi-metals host a linear crossing of degenerate bands that are protected by time-reversal symmetry T and

parity symmetry [1] P. Weyl semi-metals host non-degenerate linear crossing points. These linear crossing points are protected by either T or P symmetry. The broken symmetry is used to categorize the Weyl semi-metals into the magnetic Weyl semi-metals with broken time-reversal symmetry T and the non-centrosymmetric Weyl semi-metals with broken parity P.

The magnetic Weyl semi-metals are theoretically the simplest Weyl semi-metal with a minimum of two symmetry enforced non-degenerate linear crossing points and thus an ideal model system. Materials predicted as magnetic Weyl semi-metals are for example the magnetic pyrochlores $A_2Ir_2O_7$ [12], which turns out to have a more complex band structure with 24 Weyl nodes. Even though the material has been successfully experimentally synthesized in different phases, the Weyl semi-metal phase stays elusive [11]. DFT calculations predicted other materials like Co-based magnetic half Heusler compounds as magnetic Wely semi-metals [98], but these materials have not yet been experimentally realized. The other class of Weyl semi-metals contains the non-centrosymmetric Weyl semi-metals, which host four or a multitude of four Weyl nodes due to the T symmetry. The most prominent representative of these materials is the TaAs family, for example, TaP, NbAs, and NbP, which are predicted to host 24 Weyl nodes [99] and were successfully synthesized and experimentally examined [100]. ARPES measurements on these materials reveal the predicted disjoint surface states called Fermi-arcs. These Fermi-arcs and other surface states in topological semi-metals, specifically inversion induced Dirac semi-metals, are addressed in detail in the subsequent Chapter 8. The bulk of these topological semi-metals is predicted to cause another specific effect, the so-called chiral anomaly in Ref. [101], which is addressed in detail in Sec. 7.3. The chiral anomaly leads to a reduction of the longitudinal resistance with a magnetic field applied along the direction of the current. Initially, the observation of a negative MR in magneto-transport experiments on Weyl semi-metals led to a controversial discussion whether the negative MR really stems from the chiral anomaly or it is a measurement artifact due to a non-uniform current distribution, called current jetting [102–104]. The chiral anomaly has also been measured in Dirac semi-metals and is now widely accepted as the origin. The chiral anomaly is addressed in detail in Sec. 7.2 based on inversion induced Dirac semi-metals.

The complicated band structure of the experimentally realized Weyl semi-metals hinders a comparison to HgTe. This is why the list of Weyl semi-metals is not more comprehensive and the focus is shifted to the more comparable Dirac semi-metals. One realization of a Dirac semi-metal is the phase at the quantum critical point between the conventional and topological insulator phase. The first report of a negative MR in such a so-called composition tuned Dirac semi-metal is reported for $Bi_{0.97}Sb_{0.03}$ in Ref. [105] and later in $ZrTe_5$ [106]. Another realization is $Cd_xHg_{1-x}Te$ for the critical concentration $x = x_c \sim = 0.17$ [31]. This phase is due to an additional flat band called Kane semi-metal [31] and is studied in detail in Ref. [32]. The other realization of Dirac semi-metals are the band inversion induced Dirac semi-metals, as compressively strained HgTe [34], Cd_3As_2 [107], and Na_3Bi [108]. The investigation of inversion-induced Dirac semi-metals based on the material compressively strained HgTe is the focus of this work.

---

[1]spatial inversion symmetry

7.2. Inversion induced Dirac semi-metals

The state of the art of research on inversion induced Dirac semi-metals is summarized as starting point for the investigations on compressively strained HgTe conducted in this work. The inversion induced Dirac semi-metals Cd_3As_2 and Na_3Bi are introduced and the reported magneto-transport investigations are summarized. A reduction of the magnetoresistance with magnetic fields along the current direction is observed. Different origins for this negative MR are explored.

7.2.1. Cd_3As_2

Cd_3As_2 is the most widely studied inversion induced Dirac semi-metal. A comprehensive review can be found in Ref. [107]. Two possible phases of Cd_3As_2 are discussed in the literature for ambient conditions. Traditionally, Cd_3As_2 is assumed to crystallize in the non-centrosymmetric space group $I4_1cd$ (No. 110), but recently the centrosymmetric group $I4_1/acd$ (No. 142) has been preferred. In the $I4_1cd$ space group the Dirac nodes could be split into Weyl nodes, due to the lacking inversion symmetry. The $I4_1/acd$ is inversion symmetric which preserves the degeneracy of the Dirac node. The Cd_3As_2 crystal structure is given by a nonprimitive tetragonal unit cell shown in Fig. 7.1a). The unit cell can be described as being composed of 2x2x4 antifluorite cells with two missing cadmium cations as shown in Fig. 7.1a). The crystal lattice is nearly cubic with ($2a = 2b \sim c$) with a small elongation along the c-axis with ($c/2a \sim 1.006$) [107]. The symmetry of the crystal structure of Cd_3As_2 is reminiscent of the one of compressively strained HgTe discussed in Sec. 2.1. The only difference is that the lattice is intrinsically tetragonal, while for HgTe the lattice symmetry needs to be reduced from cubic to tetragonal, artificially by strain. Not the doubling of the lattice constant along c is the tetragonal distortion, but the deviation from perfect doubling $c = 2a = 2b$. The distortion from $c = 2a$ is roughly twice the elongation introduced by the strain of $\epsilon \sim 0.3\%$ in our compressively strained HgTe samples using the virtual substrates, as described in Sec. 7.4.1.

Traditionally, the low energy band structure of Cd_3As_2 is described by the six-band Bodnar model [109] as shown in Fig. 7.1b) . The two spin degenerate P-type bands, which cross linearly at finite $k_z = \pm k_0$, determine the low energy dispersion. The conduction band in light blue disperses linearly over the full momentum range and is called the light hole band (LH). The name already indicates the existence of a band inversion. The valence band (red) in contrast becomes flat for $k > k_D$ and is thus called heavy hole (HH) band. The second valence band (green) possesses an S-type character and disperses linearly. From the atomic limit, this S-type band is expected to lie above the two P-type bands, hence the traditional name electron band (E). The band structure is thus an inverted one as the band structure of HgTe presented in Fig. 2.3 on the left. The energy scale for the band gap E_D is determined by DFT calculations, scanning tunneling spectroscopy, and magneto-optics measurements to $E_D = 20 - 40\,meV$ [107]. Magneto-optic measurements yield a value of $E_g = -70\,meV$ for the inverted band gap between the E and LH bands [110]. This model is verified by ARPES measurements, shown in Fig. 7.1d). For comparison, the big k-range investigated by ARPES has to be considered. The ARPES measurement shows a linearly dispersing conduction band that touches the first valence band at $E \sim -0.3\,eV$ which possesses a flat dispersion for small k. Also, a second valence band with similarly steep linear dispersion as the conduction band is observed. The exact starting point of the band is not well resolved due to the limited resolution of the ARPES measurement. Since the linear crossing points are of

special interest, their position in the Brillouin zone is sketched in Fig. 7.1c). The investigated (001) surface is perpendicular to the expected splitting of the Dirac nodes. Because of this, not two linear crossing points at k_D, but one Dirac node at $k = 0$ are expected for this measurement direction. This is consistent with the observation in Fig. 7.1d) within the measurement resolution. Such a band structure can also be described by the Kane model given by Eq. 4.16 and is alternatively used to describe Cd_3As_2 [108]. The Kane model is also used to describe HgTe as discussed in Sec. 4.2.
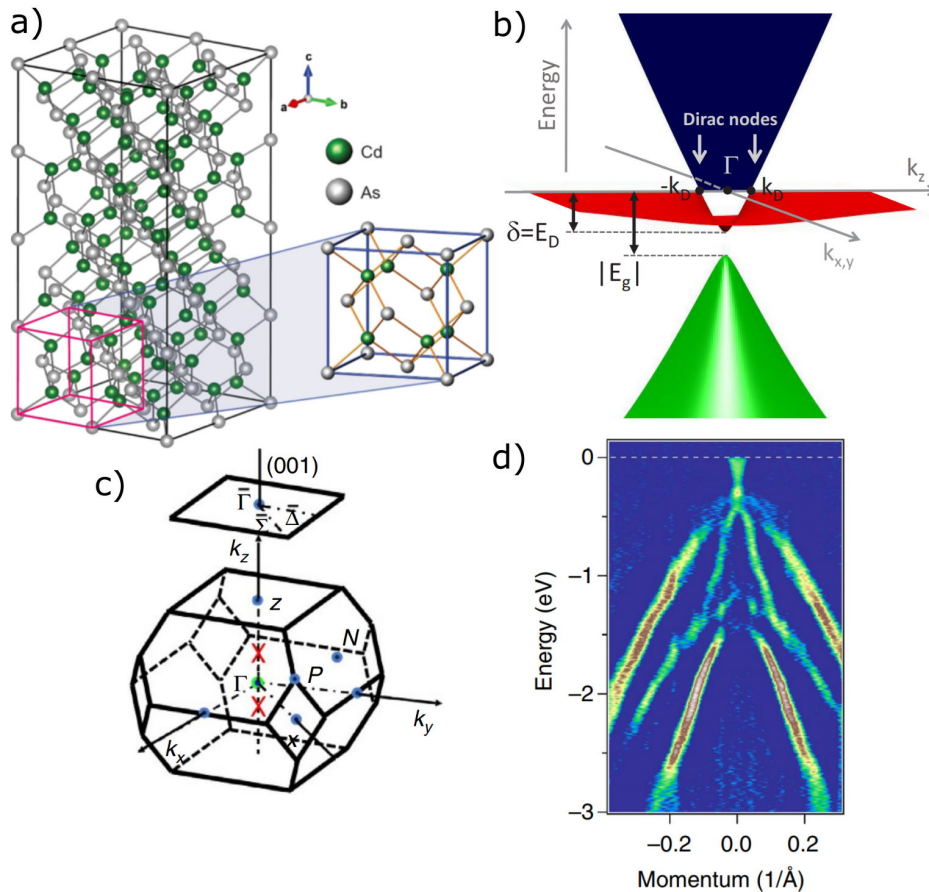
Figure 7.1: a) The non-primitive tetragonal unit cell of Cd_3As_2 is shown next to the weakly distorted antifluorite cell with two cadmium vacancies, which effectively composes the unit cell by taking it 2x2x4 times. b) Resulting band structure of Cd_3As_2 in the Bodnar model, where k_D mark the position of the Dirac nodes with the characteristic energy scales given by the bandgap E_D and the inverted band gap E_g. The bulk and (001) surface Brillouin zone of Cd_3As_2 is shown in c). In the surface Brillouin zone is the measurement direction indicated as a dash-dotted line. The second-derivative image of the band structures measured by ARPES along this direction is shown in d). a) and b) reprinted from I. Crassee *et al.*, 3D Dirac semimetal Cd_3As_2: A review of material properties, Phys. Rev. Mater. **2**, 120302 (2018) [107]. Copyright 2018 by The American Physical Society. c) and d) are reprinted with permission from Nature Publishing Group: Springer Nature, Nature Communications, Observation of a three-dimensional topological Dirac semimetal phase in high-mobility Cd_3As_2, Madhab Neupane *et al.*, *Copyright © 2014, Nature Publishing Group, a division of Macmillan Publishers Limited. All Rights Reserved.* (2014) [111].

7.2.2. NA$_3$BI

Another inversion induced Dirac semi-metal is the relatively novel material Na$_3$Bi [2]. Na$_3$Bi crystallizes in the hexagonal inversion symmetric space group $P6_3/mmc$ [108]. The hexagonally shaped Brillouin zone is shown in Fig. 7.2a). The Brillouin zone depicts the ARPES measurement results from Ref. [113]. These measurements show two solitary linear crossing points in the band structure, which are called Dirac nodes. The linear dispersion of the conduction band over a wide energy range is shown in Fig. 7.2b) [113]. The ARPES measurements shown in Fig. 7.2b) are consistent with the band structure calculations presented in Ref. [108]. The calculations are shown in Fig. 7.2c) and yield a linear crossing between the P-bands. The calculations show an additional third p-type valence band, but more importantly an S-type band energetically below the P-type bands. Na$_3$Bi consequently possesses the same inverted band structure as Cd$_3$As$_2$ and compressively strained HgTe.
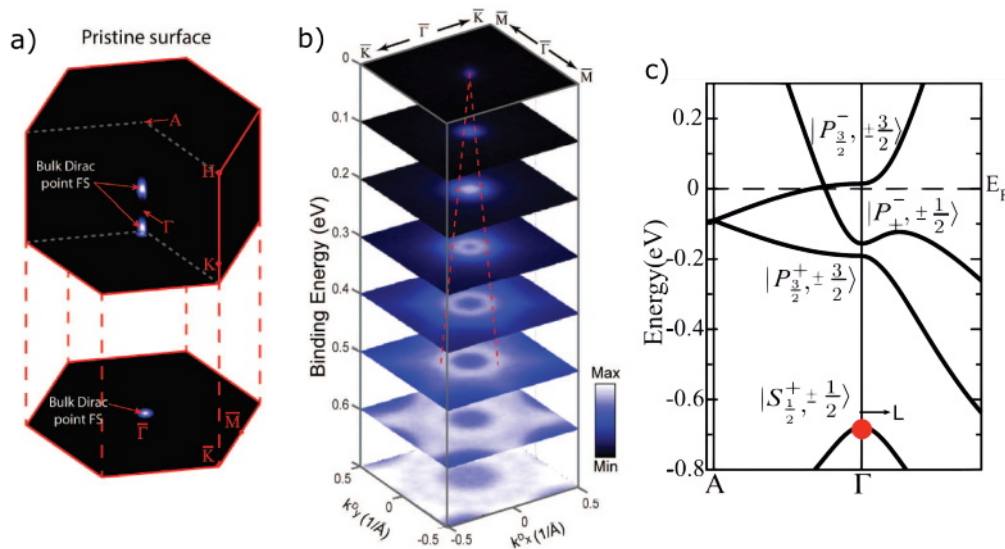
Figure 7.2: The ARPES measured map of the Fermi surface of Na$_3$Bi is shown in a) for the whole 3D Brillouin zone together with its surface projection. The measured constant energy contours for different binding energies are shown in b). The model low energy bulk band structure of Na$_3$Bi is shown along $A - \Gamma$ and $\Gamma - L$ direction in c). a) and b) from Discovery of a Three-Dimensional Topological Dirac Semimetal, Na$_3$Bi, K.L. Liu *et al.*, Science, **343**, 6173 (2014) [113]. Reprinted with permission from AAAS. c) reprinted from Z. Wang *et al.*, Dirac semimetal and topological phase transitions in A$_3$Bi(A=Na, K, Rb), PRB **85**, 195320 (2012) [108]. Copyright 2012 by The American Physical Society.

7.2.3. MAGNETO-TRANSPORT OF INVERSION INDUCED DIRAC SEMI-METALS

One goal of this work is to identify compressively strained HgTe as Dirac semi-metal using magneto-transport experiments. The magneto-transport features specific for the above introduced Dirac semi-metals are discussed in this Section. The magneto-transport data of Na$_3$Bi, first reported by Ref. [114], is used exemplary. The longitudinal specific resistance ρ_{xx} is shown in Fig. 7.3a) as a function of the magnetic field B for different magnetic field directions from B parallel to the current I to out of the transport plane. The usual magneto-transport configuration with the magnetic field applied out of the transport plane ($\Phi = 90°$)

---

[2]Special care must be taken here due to a second stable phase at ambient conditions namely NaBi exist, which is a bulk superconductor [112].

shows a monotonic increase of ρ_{xx} with B. This monotonic increase of the longitudinal resistivity appears linear for magnetic fields $B > 1\,\text{T}$. This increase of $\rho_{xx}(B)$ with B is called positive MR. For Na$_3$Bi decreases the positive MR with the rotation of the magnetic field into the sample plane towards the direction of the current. For angles $\phi < 45°$ the longitudinal resistivity ρ_{xx} reduces with the magnetic field for a limited range of B, which depends on the value of the angle Φ. This reduction of the longitudinal resistivity ρ_{xx} with the magnetic field B is called negative MR and increases with the rotation of B towards the transport plane and thus a decreasing ϕ. The negative MR is maximal for the magnetic field applied parallel to the current ($\phi = 0°$). For the whole reported magnetic field range of up to $\pm 9\,\text{T}$ a reduction of the ρ_{xx} with B is observed for B parallel I ($\phi = 0°$). For an ordinary three-dimensional metal, a magnetic field perpendicular to the current is expected to increase the resistance due to the increased path of the charge carriers due to the deflection by the Lorentz force. This deflection causes in ordinary metals a quadratic dependence of the resistance on the magnetic field $R_{xx}(B) \propto B^2$, which saturates for high magnetic fields [117]. In contrast, a magnetic field applied along the current direction does not alter the path of the charge carriers and thus does not change the resistance. The above described linear positive MR for B out of the transport plane and the negative MR for B parallel I of Na$_3$Bi, which is shown in Fig. 7.3a), deviates from this naive expectation and could thus in principle be a magneto-transport signature of Dirac semi-metals.

Indeed, the large linear positive MR for $\phi = 90°$ is suggested to be a signature for a linear bulk band structure in Ref. [118]. It is argued that the applied magnetic field lifts the protection from backscattering. The lifted backscattering protection is not the only physical mechanism proposed in the literature to cause a strong linear positive MR. A few mechanisms are given in the following. One of which is the so-called quantum magnetoresistance [119]. The specific resistance for a system with only the lowest Landau level partially occupied is described by

$$\rho_{xx}(B) = \rho_0 + \alpha B, \tag{7.1}$$

where $\rho_0 = \rho_{xx}(B = 0\,\text{T})$ and α is a proportionality factor which depends on the scattering in the sample. The condition of an only partially filled lowest LL only requires a low density, meaning a small Fermi surface. It does not pose any other restrictions on the dispersion. A system with the Fermi energy close to the Dirac point would be sufficient, but not required, for the observation of a positive linear MR. A linear positive MR is also reported for compensated materials, as InSb and Bi in Ref. [120]. Ref. [121] traces the linear positive MR to an electron-hole-recombination in finite-size samples due to an interplay of the bulk and edge of the sample. Also in a completely different system, a high mobility ($\mu = 25 \times 10^6\,\text{cm}^2\text{V}^{-1}\text{s}^{-1}$) n-type GaAs quantum well a linear positive MR is observed in Ref. [115]. In Fig. 7.3b) the longitudinal resistance R_{xx} is shown in black together with the resistance calculated according to the so-called resistance rule [122, 123]

$$R_{\text{diff}} = \frac{\text{d}R_{xy}}{\text{d}B} \cdot B \cdot \alpha \tag{7.2}$$

in red. For $T = 20\,\text{K}$ both resistances coincide and increase linearly with B. For lower temperatures oscillations due to the quantization in Landau levels are visible. The respective filling factors ν are indicated as dashed blue lines. The positive linear MR is already observed for low magnetic fields corresponding to filling factors $\nu > 2$ and thus a different mechanism than the quantum magnetoresistance must be at work. The linear MR is attributed to an admixture of the Hall resistivity, which is linear in B, to the longitudinal

resistivity. This admixture is consistent with the validity of the resistance rule according to Eq. 7.2. The admixture of the Hall resistance can be caused by variation of the density over the sample. This admixture of the Hall resistance is another mechanism for a linear MR are inhomogeneities of the sample that even exist for the well-established material GaAs that can be grown in high quality as high mobility quantum wells. The admixture can not only be due to density fluctuations but also mobility fluctuations inside the sample. Mobility fluctuations are shown as origin in Ref. [124] with the help of magneto-transport measurements on InAs and In(As,N) layers with varying N content, to vary the scattering center concentration and accompanying Monte Carlo simulations. Such density/mobility inhomogeneities are also used to explain the magnetoresistance of MBE grown layers of the Dirac semi-metal Cd_3As_2 in Ref. [116]. The MR as function of an out of plane magnetic field is shown in Fig. 7.3c) for Cd_3As_2 layers of thicknesses ranging from 85 nm to 370 nm. These layers also show a quasi-linear and non-saturating MR. The quantum magnetoresistance is excluded as the mechanism due to the densities of $n \sim 2 \times 10^{12}\,cm^{-2}$. These are still too high for transport only by the lowest Landau level for typical accessible magnetic fields in a lab, even though much lower than for example the density of the bulk samples in Ref. [118]. The magnetic field required to enter the lowest Landau level for such a density of $n \sim 2 \times 10^{12}\,cm^{-2}$ is $B_{ql} > 20$ T, which is a factor of 2 higher than the highest reported magnetic field of ± 10 T in Fig. 7.3c). In Ref. [116] it is argued, that the inhomogeneities as the origin of the observed strong linear MR are supported by the observation of a negative MR for a magnetic field applied parallel to the current in the same samples. These measurements are shown in Fig. 7.3d). For thin samples, only a weak magnetic field dependence of the longitudinal resistance is observed. The weak magnetic field dependence fits the expected magnetic field independence of an ideal metal of finite size and thus an ordinary 2DEG. For thicker samples, a strong negative MR is observed. The increasing negative MR with sample thickness is consistent with current distortions due to density/mobility fluctuations in the sample. The fluctuations lead to inhomogeneous equipotential lines. The effect is stronger in thicker samples since these allow for a deviation of the current flow also along the growth direction, The resulting inhomogeneous equipotential lines prevent a sensible measurement of the potential inside the sample with voltage probes on the edge of the sample. A similar deformation of the equipotential lines can be caused by the magnetic field for point-like contacts called current jetting [102–104].

Even though the linear positive MR is unusual, it is not a suitable indicator for a Dirac semi-metal phase due to the multitude of different possible origins. The attention is shifted to the negative MR observed for the magnetic field parallel to the current. Even though such a negative MR can also be due to measurement artifacts due to insufficient sample quality causing current jetting or non-well defined potential measurements due to density/mobility fluctuations in the sample, as mentioned above. Another physical mechanism requires the existence of linear crossing points in the bulk band structure and is called chiral anomaly. The negative MR observed in Na_3Bi in Ref. [114] is shown in Fig. 7.3a) and is in Ref. [114] attributed to this chiral anomaly, which will be introduced in the following Section.
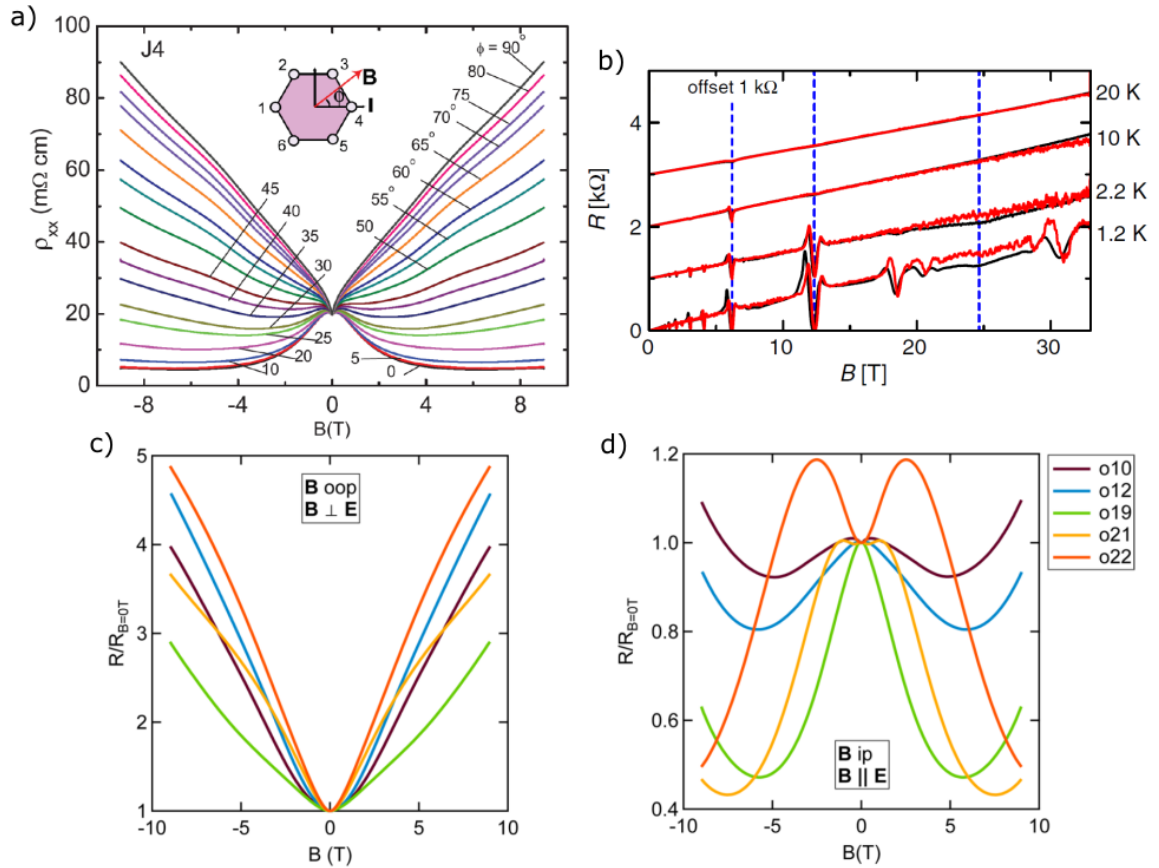
Figure 7.3: In a) the longitudinal resistance R_{xx} is shown as a function of the magnetic field B for different angles ϕ of the magnetic field with respect to the current I. The angels ϕ range from $\phi = 0°$ being B parallel to the current I to 90° being B out of the transport plane for Na_3Bi. In b) the longitudinal resistance R_{xx} of a ultra high mobility n-type GaAs quantum well is shown in black together with the calculated resistance based on the Hall resistance R_{xy} using $R_{\text{diff}} = dR_{xy}/dB \cdot B \cdot \alpha$ in red as function of an out-of-plane magnetic field B for different temperatures $T = 0.3, 1.2, 2.210$, and 20 K. The dashed blue lines indicate the positions of the filling factors $\nu = 2, 1$, and 0.5, respectively. The longitudinal resistance normalized to the resistance at zero magnetic field $R/R_{B=0\,T}$ is shown as a function of a magnetic field perpendicular to the transport plane in c) and along the current direction in d) for Cd_3As_2 layers of thickness $85, 120, 170, 340$, and $370\,nm$ indicated by the labels o10 to o20. a) from Evidence for the chiral anomaly in the Dirac semimetal Na_3Bi, J. Xiong *et al.*, Science, **350**, 6259 (2015) [114]. Reprinted with permission from AAAS. b) reprinted from T. Khouri *et al.*, Linear Magnetoresistance in a Quasifree Two-Dimensional Electron Gas in an Ultrahigh Mobility GaAs Quantum Well, PRL **117**, 256601 (2016) [115]. Copyright 2016 by The American Physical Society. c) and d) reprinted from T. Schumann *et al.*, Negative magnetoresistance due to conductivity fluctuations in films of the topological semimetal Cd_3As_2, PRB **95**, 241113 (2017) [116]. Copyright 2017 by The American Physical Society.

7.3. THE CHIRAL ANOMALY

The chiral anomaly is a neat example of a consequence of topology. It does not cause the formation of special states but leads to a directly measurable transport phenomenon. The chiral anomaly is a consequence of the topological character of the band structure of the material with its linear crossing points. The topological character of these nodes can be described as magnetic monopoles. The chirality gives the respective magnetic charges [11]. The involved chirality of the nodes lends the phenomenon its name chiral anomaly. Parallel applied electric and magnetic fields shift the energy of the linear crossing points with respect to each other. The occupation of nodes with one type of "magnetic charge" is increased, while the occupation of the opposite one is reduced. This occupation imbalance is released by an additional current I_c, reducing the resistance of the system [11, 125, 126].
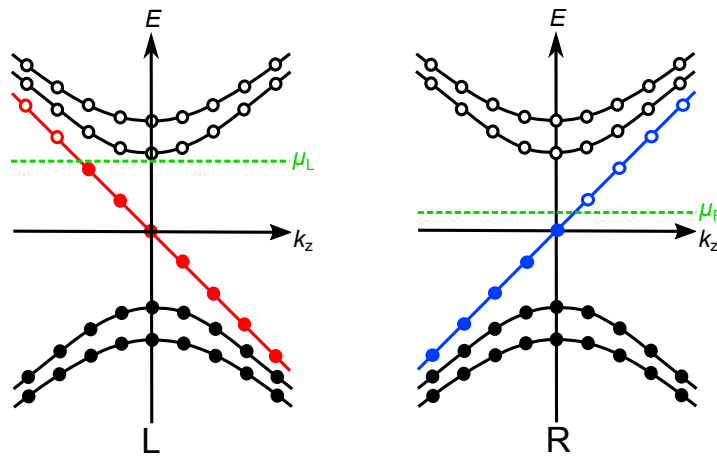
Figure 7.4: Shown are the Landau levels (ll) of two Weyl points with different chirality (L and R) with a magnetic field applied parallel to an electric field. Filled (empty) circles indicate filled (empty) states. The zeroth LLs are marked in red and blue.

The first description of this so-called anomaly for solid states systems is given in Ref. [101] and is shortly summarized here since it is the most picturesque one. The minimal required band structure consists of two Weyl nodes with opposite chirality. An applied magnetic field leads to the formation of LLs. The LLs for the two Weyl nodes are thereby identical except for the zeroth LL, which possess opposite velocities according to the different chiralities of the Weyl nodes, as shown in Fig. 7.4. For simplicity, the magnetic field is assumed to be strong enough, that only the lowest (= zeroth) LL is occupied and the system is in its so-called quantum limit. The electric field $\mathscr{E}$ changes the momentum of the charge carriers by $\delta k = e/\hbar \mathscr{E}$. This changes the occupation as soon as the change in momentum δk equals the size of one momentum space $k_{\min} = \frac{2\pi}{L}$, where L is the system size along the direction of interest. This process is indicated by the filled and empty circles in Fig. 7.4. The occupation of one Weyl node thereby increases, while the other one decreases due to their opposite velocity of the zeroth LL. The overall occupation is conserved. The rate of this change in local occupation is given by

$$\frac{dn_{R/L}^{3D}}{dt} = \pm \frac{e^2}{h^2} \mathscr{E} \cdot \boldsymbol{B}. \tag{7.3}$$

This local occupation imbalance is only stable when the intranode scattering ($1/\tau_a$) is faster than the internode scattering, which relaxes this imbalance. In Weyl semi-metals is the internode scattering suppressed by the separation of the Weyl nodes in k-space. For Dirac semi-metals, the suppression is due to the remaining symmetry of the lattice [127]. Because of this, the electric and magnetic field-induced occupation difference can be described as a chiral chemical potential difference. This chiral chemical potential difference drives an anomalous current I_c, analogous to usual chemical potential differences. To quantify this chiral current I_c the chiral magnetic effect, as described by Ref. [128], can be used according to Ref. [11]. The chiral current I_c depends linearly on the energy difference between the Weyl nodes ΔE_{nodes}, which can be written down as

$$I_c = \frac{e^2}{h^2} B \Delta E_{\text{nodes}} \tag{7.4}$$

Since the change in occupations given by Eq. 7.3 is due to the linear dispersion of the zeroth LL proportional to the change in energy, the overall dependence of the chiral current on the magnetic field is given by

$$I_c \propto B \mathscr{E} \cdot \boldsymbol{B} \tau_a. \tag{7.5}$$

The chiral magnetic effect can according to Ref. [11] be seen as a second successive use of the $\boldsymbol{E} \cdot \boldsymbol{B}$ term causing an equilibrium current due to the chiral chemical potential difference caused by its first use. This chiral current I_c causes an additional conductivity that increases quadratically with the magnetic field B. This result for the quantum limit is also reproduced by the semi-classical Boltzmann kinematic approach in Ref. [129] and using field theory in Ref. [127] yielding the relation

$$\sigma(B) = \sigma_0 + \frac{e^4 \tau_a B^2}{4\pi^4 D(E_{\text{F}})}. \tag{7.6}$$

To summarize, in Dirac and Weyl semi-metals a quadratic increase of the conductivity $\sigma(B) \propto B^2$ with the projection of the magnetic field B along the driving electric field (= current) is expected. Equivalently the resistance is expected to reduce according to $R_{xx}(B) \propto \left(\sigma_0 + B^2\right)^{-1}$. The chiral anomaly is the focus of the following section to verify compressively strained HgTe as Dirac semi-metal and to explore its properties in detail.

7.4. CHIRAL ANOMALY IN COMPRESSIVELY STRAINED HGTE

The above introduction of topological semi-metals, their magneto-transport properties, and the chiral anomaly set the basis for the investigation of the Dirac semi-metal compressively strained HgTe. First, the sample fabrication, including strain engineering, is described, and the possibility to adjust the carrier density and thus the electrochemical potential via gating is introduced. Second, magneto-transport measurements are performed to find indications for the chiral anomaly. A variety of different measurements are performed to verify the chiral anomaly as the origin. Lastly, the bulk properties of compressively strained HgTe are examined.

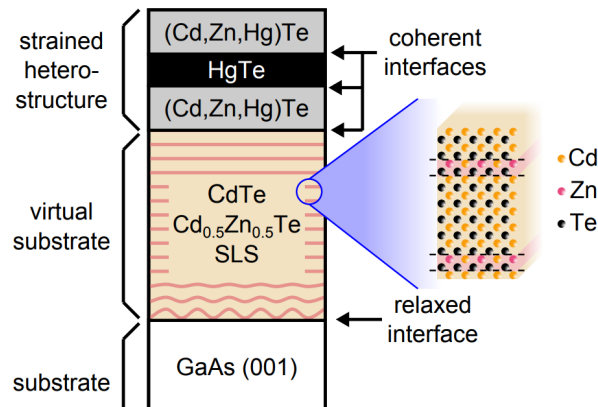## 7.4.1. Sample Fabrication and measurement setup

Figure 7.5: The MBE grown layer stack is shown on top of the commercial GaAs substrate with the virtual substrate composed of a superlattice of CdTe layers by self-limited monolayers of $Cd_{0.5}Zn_{0.5}Te$, followed by the HgTe layer sandwiched in the protective (Cd,Zn,Hg)Te layers. Reprinted from P. Leubner *et al.*, Strain Engineering of the Band Gap of HgTe Quantum Wells Using Superlattice Virtual Substrates, PRL **117**, 086403 (2016) [130]. Copyright 2016 by The American Physical Society.

The compressively strained HgTe samples are realized using the virtual substrate introduced by Leubner *et. al.* in Ref. [25, 130] to freely adjust the lattice constant between the one of CdTe and $Cd_{0.5}Zn_{0.5}Te$. Samples with strain values of $-0.3\% < \epsilon < 0.6\%$ for bulk HgTe layers of $d_{HgTe} = 60-120\,$nm [25] can be grown by MBE. A schematic of the MBE grown layer stack is shown in Fig. 7.5. The amount of strain is limited by the lattice constant of CdTe for negative values and the onset of relaxation in the HgTe layer for positive values. The virtual substrate is composed of a superlattice of MBE grown CdTe layers in variable thickness and mono-layers of $Cd_{0.5}Zn_{0.5}Te$ grown in a self-limiting atomic layer epitaxy fashion as sketched in Fig. 7.5. The resulting strain is given by the relative CdTe to $Cd_{0.5}Zn_{0.5}Te$ layer thickness. This ratio can be adjusted during MBE growth by choosing the appropriate Te flux and growth time of the CdTe layer. The fully strained grown HgTe layer of a thickness $d_{HgTe} = 60-120\,$nm is surrounded by protective $Cd_{0.7}Hg_{0.3}Te$ layers to increase the interface quality. The maximal thickness of the protective layers due to relaxation depends on the desired strain. For $d = 70\,$nm thick HgTe samples with a compressive strain of $\epsilon \sim 0.3\%$ protective $Cd_{0.7}Hg_{0.3}Te$ layers are limited to a thickness of $d_{HgCdTe} = 10-15\,$nm , while for tensilely strained samples on CdTe ($\epsilon \sim -0.3\%$) with thickness of up to $d_{HgCdTe} = 80\,$nm are feasible [25]. The realizable thickness of the HgTe layer can be increased using a lattice-matched $Cd_{1-x}Zn_xTe$ barriers. The measurements presented in this chapter are either performed in a dilution refrigerator with a base temperature of $T = 0.02\,$K and accessible magnetic fields up to $B = 16\,T$. Alternatively, a helium bath cryostat with a 1K-pot is used, which reaches $T \sim 2\,$K and is capable of magnetic fields up to $B = 14\,$T. For the bath cryostat, two dipsticks with two different one-axis rotation mechanisms are available. The dipsticks allow rotating the sample with respect to the magnetic field to cover a rotation inside the sample plane or rotating out of the sample plane. Some measurements have been performed in the high field magnet laboratory in Nijmegen in a He^3-cryostat at the temperature $T = 0.3\,$K in a bitter magnet capable of magnetic fields up to $B = 30\,$T.

7.4.2. ADJUSTING THE CARRIER DENSITY
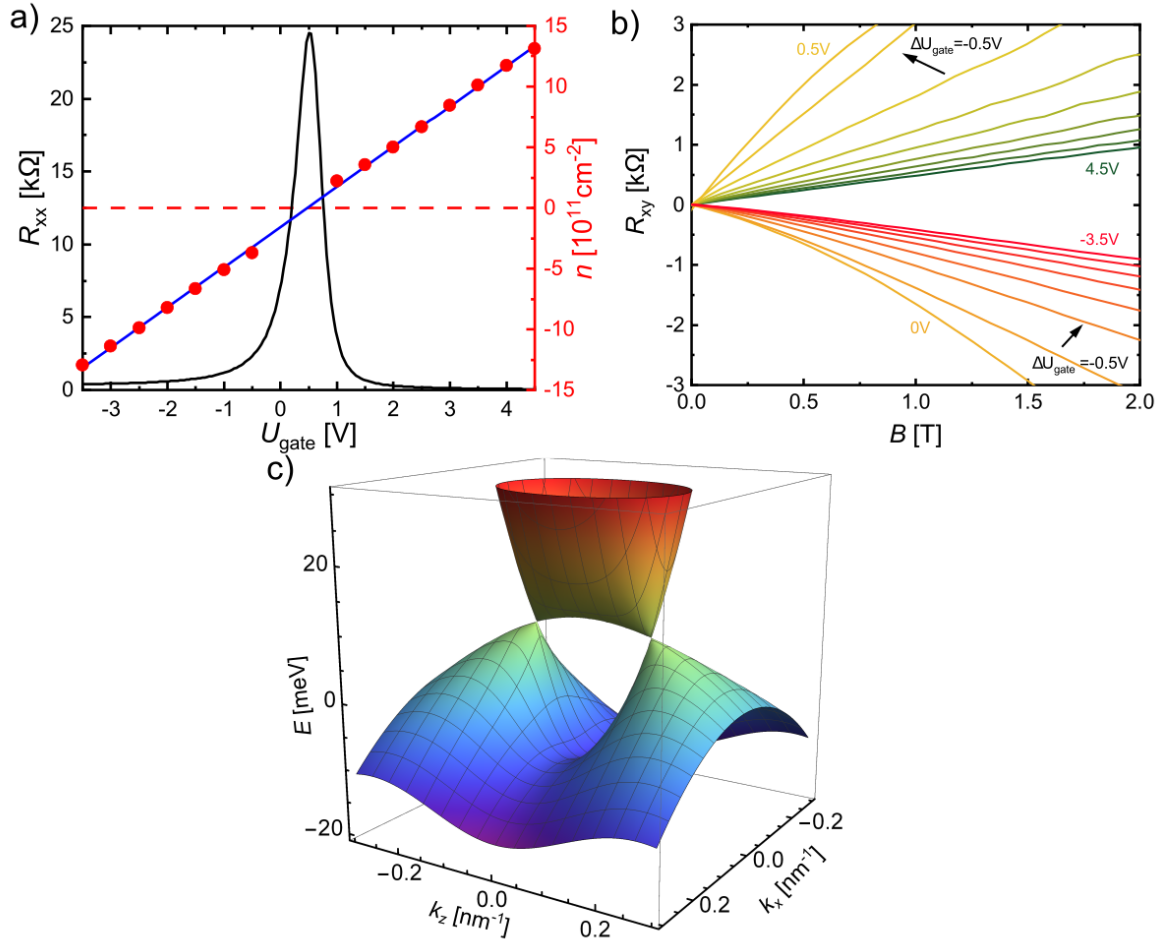
Figure 7.6: In a) the longitudinal resistance R_{xx} is shown in black together with the carrier density n as red dots of the gate voltage U_{gate} at zero magnetic field and the temperature $T = 20\,$mK. The blue line represents a linear fit to the carrier density n as a function of U_{gate}. In b) the Hall resistance R_{xy} is shown as a function of an out-of-plane magnetic field B for various gate voltages U_{gate}. In c) the low energy bulk $k \cdot p$ band structure based on the eight-band Kane-model calculated with the program "biscuit" is shown along k_z and k_x [29].

The chiral anomaly requires the band structure to host linear crossing points and the electrochemical potential to lie close to the linear crossing points, as described in Sec. 7.3. This is why being able to change the electrochemical potential is a powerful tool to verify the chiral anomaly as the underlying mechanism for the observed negative MR. The Hall-bar devices are equipped with a top gate making them plate capacitors, as shown in Fig. 3.1 and Fig. 3.2 and described in Sec. 4.1.1. The electrochemical potential is thus indirectly adjusted via changing the carrier density, as introduced in Sec. 4.1. The change in the carrier density is directly proportional to the applied gate voltage. The longitudinal resistance R_{xx} is shown as a function of the gate voltage U_{gate} in Fig. 7.6a). A sharp maximum is observed close to $U_{gate} = 0.5\,$V reaching $R_{xx,max} = 24.5\,$kΩ, which equals a sheet resistance of $r_\square \sim 8.2\,$kΩ. The lowest R_{xx} value is observed for $U_{gate} = 4.5\,$V with $R_{xx}(U_{gate} = 4.5\,V) = 62\,$Ω. For positive gate voltages, a change in resistance of 3 orders of magnitude is achieved. Negative gate voltages lead to a reduction of the resistance of 2 orders of magnitude to $R_{xx}(U_{gate} = -3.5\,V) = 400\,$Ω. Figure 7.6a) shows the carrier density as a function of the gate voltage. The accessible

gate range is equivalent to densities reaching from $n(U_\text{gate} = -3.5\,\text{V}) \sim -13 \times 10^{11}\,\text{cm}^{-2}$ to $n(U_\text{gate} = 4.5\,\text{V}) \sim 12 \times 10^{11}\,\text{cm}^{-2}$. The density as a function of the gate voltage shows the linear dependence expected for a plate capacitor, as indicated by the blue line. The carrier densities are determined by linear fits to the Hall resistance in the function of the out-of-plane magnetic field as shown in Fig. 7.6a).

The maximum of the longitudinal resistance $R_{xx}(U_\text{gate})$ at $U_\text{gate} \sim 0.5\,\text{V}$ coincides with the zero density determined by the blue linear fit. It thus marks the charge neutrality point and separates the electron and the hole transport regimes. The height and identification of the maximum of the longitudinal resistance $R_{xx}(U_\text{gate})$ with the charge neutrality point is different to the three-dimensional insulator phase of tensilely strained HgTe, for which no simple representation for the $R_{xx}(U_\text{gate})$ maximum can be found, as discussed in Sec. 3.3.1. The Hall resistance R_{xy} as function of an out of plane magnetic field B is shown in Fig. 7.6b). For the gate voltages $U_\text{gate} > 0.5\,\text{V}$ only positive (electron-like) Hall slopes are observed, while for gate voltages $U_\text{gate} < 0.5\,\text{V}$ only negative (hole-like) Hall slopes are measured. The 3D-TI tensilely strained HgTe also shows positive Hall slopes in the electron regime. In contrast, the hole transport regime only shows negative Hall slopes for high magnetic fields, which are always accompanied by a positive Hall slope for low magnetic fields, as shown in Fig. 3.8. To translate the observed magneto-transport properties into a band structure picture, the maximum of the longitudinal resistance R_{xx} indicates the transition from a purely electron-like to a hole-like state. The low energy bulk band structure is calculated with $k \cdot p$ using the program "biscuit" [29] based on the Kane Hamiltonian introduced in Sec. 4.2 for a biaxial compressive strain of $\epsilon = 0.3\,\%$ without accounting for the bulk inversion asymmetry and shown in Fig. 7.6c). The two low energy bands, namely the $\Gamma_{8,\text{HH}}$ and $\Gamma_{8,\text{LH}}$ bands cross linearly at finite $k_z = \pm k_{z,0}$. Based on this band structure the resistance maximum can be seen as an indicator for the electrochemical potential being located at linear band crossing points.

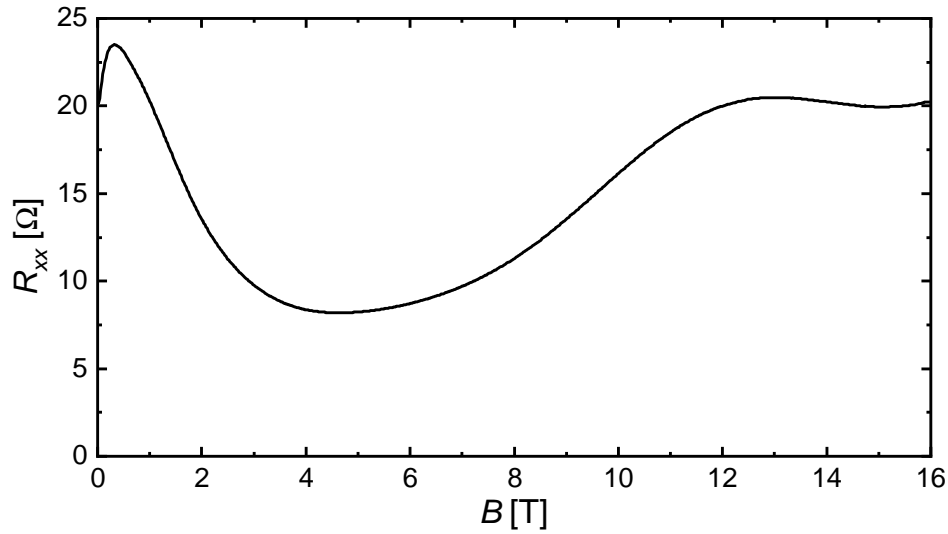### 7.4.3. NEGATIVE MAGNETORESISTANCE IN COMPRESSIVELY STRAINED HGTE

Figure 7.7: The longitudinal resistance R_{xx} is shown as a function of the magnetic field B applied parallel to the current path for the gate voltage at the charge neutrality point and the temperature $T = 0.02$ K.

The linear crossing points in the band structure are the identifying property of the Dirac semi-metals. The electrochemical potential is thus, as a starting point for the in-plane magnetic field dependent investigation, placed at the Dirac nodes. The gate voltage is chosen to correspond to the charge neutrality point according to Sec. 7.4.2. The magnetic field is applied parallel to the current path of the Hall bar. The resulting longitudinal resistance $R_{xx}(B)$ at a temperature of $T = 0.02$ K is shown in Fig. 7.7. The longitudinal resistance $R_{xx}(B = 0\,T)$ deviates slightly from its maximum of $R_{xx}(U_{gate})$ shown in Fig. 7.6. The reason for this deviation is multiple cooldowns of the sample which are necessary to change the alignment of the rotation axis of the sample stick with respect to the magnetic field. Different cooldowns can cause small varieties in the trapping of charges and insulator properties. These varieties lead to a different potential landscape seen by the active layer and thus an offset in the gate voltage or the mobility. As a consequence, the absolute value of the longitudinal resistance changes. Data from multiple cooldowns is presented in this Chapter. For low magnetic fields, the resistance increases quickly up to $B \sim 0.3$ T, where the resistance starts to decrease with further increasing magnetic field down to $B \sim 4.7$ T. The minimum observed resistance represents a relative reduction compared to resistance at zero magnetic field of $R_{xx,min}/R_{xx}(B = 0\,T) \sim 60\,\%$. For higher magnetic fields the resistance increases again with a local maximum at $B \sim 13$ T. To sum up, a reduction of the longitudinal resistance $R_{xx}(B)$ with increasing magnetic field, typically called negative MR, is observed as predicted by the chiral anomaly. But this negative MR is accompanied by other effects, namely a resistance increase for small magnetic fields and a non-monotonic MR for high magnetic fields.

To separate these different features, measurements are performed as a function of the magnetic field for different temperatures and shown in Fig. 7.8a) as longitudinal resistance R_{xx} and in Fig. 7.8b) as MR $R_{xx}/R_{xx}(B = 0\,T)$. The idea behind these measurements is that different underlying physical mechanisms should come with different temperature dependencies. The measurements are performed in a continuous-flow cryostat equipped with
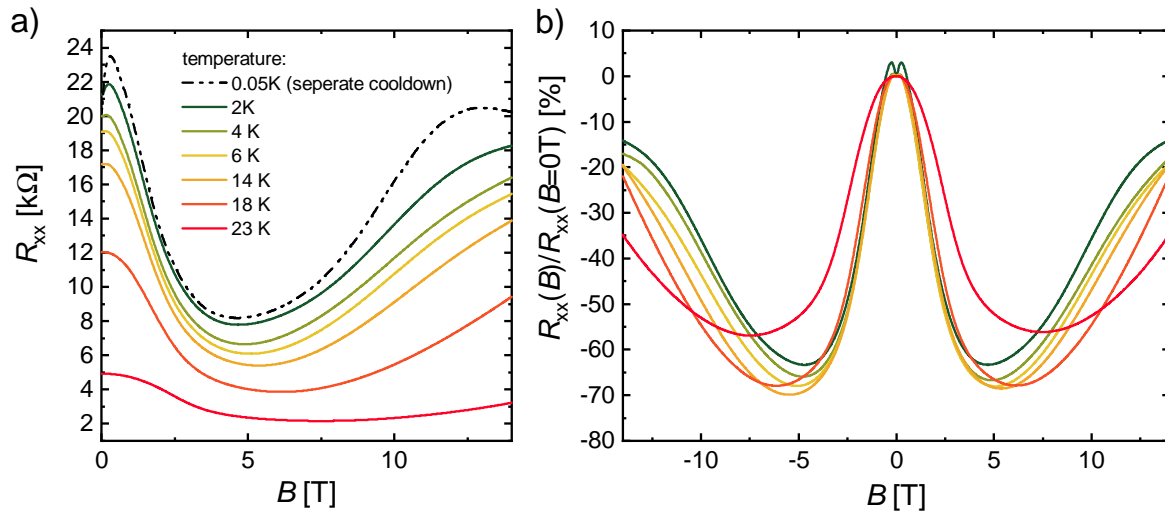
Figure 7.8: The longitudinal resistance R_{xx} and the magnetoresistance $R_{xx}(B)/R_{xx}(B=0\,\mathrm{T})$ is shown as function of a magnetic field B applied parallel to the current path for the gate voltage $U_{\mathrm{gate,max}}$ for temperatures of 2 K in dark green via 4 K, 6 K and 18 K to 23 K in red in a) and b), respectively. In a) the longitudinal resistance R_{xx} is shown for a different cooldown at the temperature $T = 0.02\,\mathrm{K}$ as dash-dotted black line. This is a repetition of the data shown in Fig. 7.7.

an electrical heater to allow for moderately high temperatures up to $T \sim 20\,\mathrm{K}$. The temperature of $T \sim 20\,\mathrm{K}$ is chosen as the upper limit, since for this temperature the influence of phonons is not neglectable anymore for HgTe [131]. The longitudinal resistance at zero magnetic field decreases with increasing temperature, as expected for an insulator. The strong positive MR for small magnetic fields reduces quickly with temperature. The relative increase of $\Delta\mathrm{MR} \sim 15\,\%$ for $T = 0.05\,\mathrm{K}$ becomes unresolvable for $T > 4\,\mathrm{K}$ as can be seen in Fig. 7.8a) and b). In contrast the negative MR, which is observed for magnetic fields up to $B \sim 4.6\,\mathrm{T}$ only shows a weak temperature dependence up to $T = 18\,\mathrm{K}$. The negative MR stays nearly unchanged even though the $R_{xx}(B = 0\,\mathrm{T})$ varies by a factor of two for the same change in temperature. The slight increase in MR with temperature is most likely due to the normalization to $R_{xx}(B = 0T)$ which is altered with temperature due to the temperature dependence of the strong positive MR for low magnetic fields. Only for $T = 23\,\mathrm{K}$ a significant change of the negative MR contribution is observed, which is probably due to phonons setting in.

The positive MR for low magnetic fields is due to its strong temperature dependence at low temperatures most likely WAL as already mentioned in Sec. 3.2.2. The positive MR for low magnetic fields is investigation in more detail in Sec. 7.5.1, which supports WAL as likely mechanism. Treating the positive MR for low magnetic fields B as WAL enables the modeling of the observed longitudinal resistance $R_{xx}(B)$ up to moderate magnetic fields of $B \lesssim 4\,\mathrm{T}$. Weak (anti)localization in two-dimensional systems is described by the Hikami-Larkin-Nagaoka equation [132], which reproduces the WAL observed in thin films of the Dirac semi-metals Cd_2As_3 [133] and Na_3Bi [134] well. In contrast the WAL signal, as shown in Fig. 7.8a) and b) and especially Fig. 7.18, is not well described by the Hikami-Larkin-Nagaoka equation. A different shape of the WAL signal is also observed for the Weyl semi-metal TaAs in Ref. [135]. An alternative expression for the WAL in disordered Weyl semi-metals is calculated with the Feynman diagram technique in Ref. [136]. This expression is used in Ref. [135] in a simplified form and reproduces their experimental data well.
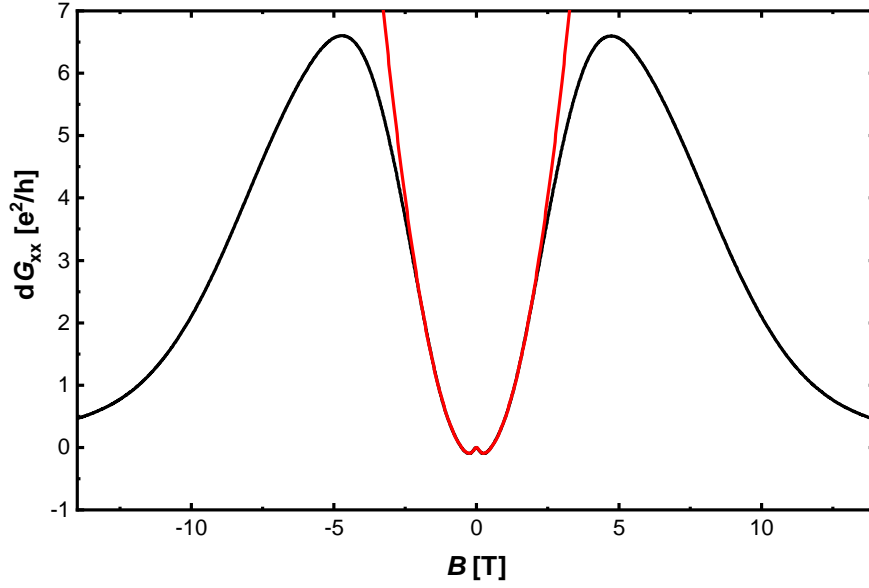
Figure 7.9: The change in longitudinal conductance $dG_{xx}(B) = G_{xx}(B) - G_{xx}(B = 0\,\mathrm{T})$ is shown as function of the magnetic field applied along the current direction B for the temperature $T = 2\,\mathrm{K}$ in black together with a fit according to Eq. 7.7 up to $B = \pm 1.5\,\mathrm{T}$ in red.

While also accounting for the chiral anomaly according to Eq. 7.6, the simplified WAL equation reads:

$$\sigma_{xx}(B) = -C_{\mathrm{WAL}}\left(\sqrt{B}\frac{B^2}{B^2 + B_c^2} + \gamma B^2 \frac{B_c^2}{B^2 + B_c^2}\right) + \sigma_0 + C_{\mathrm{CA}}B^2. \tag{7.7}$$

This formula effectively describes an initial B^2 behavior with the strength C_{WAL} with a transition at the critical crossover field B_c towards a $\sqrt{B}$ behavior with the strength $\gamma \cdot C_{\mathrm{WAL}}$. The Eq. 7.7 thus possess three fitting parameters to describe the low magnetic field behavior. The zero field conductivity $\sigma_{xx}(B = 0\,\mathrm{T})$ is accounted for by σ_0. The chiral anomaly driven part of the signal is accounted for by the additional term $C_{\mathrm{CA}}B^2$, which is quadratic in B and possess only the fitting constant C_{CA}. The longitudinal conductance G_{xx} is equivalent to the longitudinal conductivity σ_{xx} due to the neglectable small Hall signal for the magnetic field applied along the direction of the current, as shown in Fig. 7.20 for the angle $\theta = 0°$ in green. The change of the longitudinal conductance with the magnetic field $dG_{xx} = G_{xx}(B) - G_{xx}(B = 0\,\mathrm{T})$ is shown in Fig. 7.9 together with the fit of Eq. 7.7. The fitting of the WAL signal is only a tool to separate the WAL contribution from the rest of the signal. The $dG_{xx}(B)$ for moderate magnetic fields $B < 3\,\mathrm{T}$ follows the B^2 behavior expected for the chiral anomaly according to Eq. 7.6 and 7.7. For high magnetic fields positive MR effects expected for most systems [117] take over. This observation of a B^2 dependence of the positive magneto conductivity, which is equivalent to the negative MR, is encouraging for the chiral anomaly as driving mechanism.

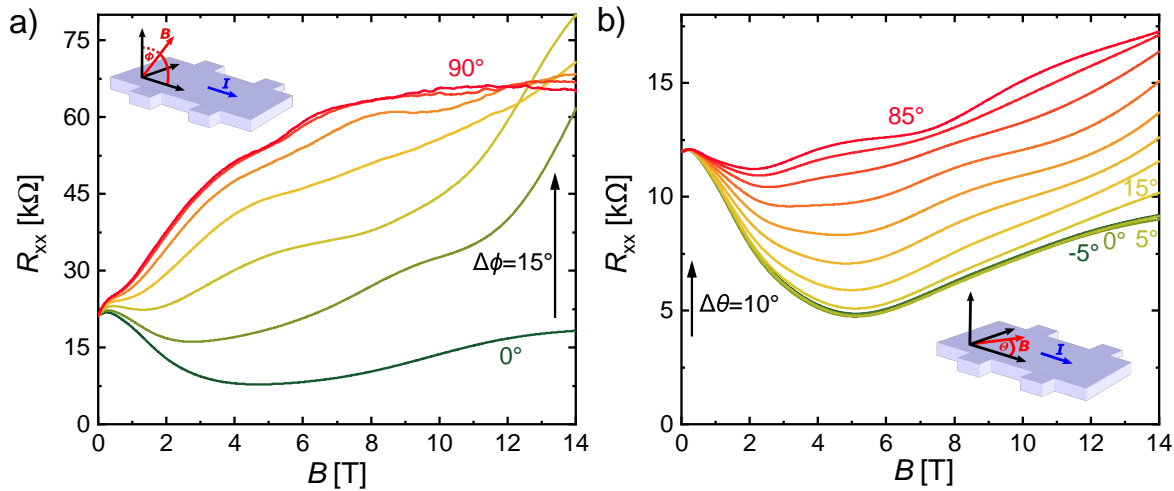**7.4.4.** ANGULAR DEPENDENCE OF THE NEGATIVE MAGNETORESISTANCE

Figure 7.10: The longitudinal resistance R_{xx} is shown as a function of the magnetic field B for various magnetic field directions for angles Φ out of the transport plane for the charge neutrality point of a compressively strained HgTe layer at $T = 2\,\text{K}$ in a). The R_{xx} is shown as a function of the magnetic field applied inside the transport plane along the angle Θ with respect to the current direction at the temperature $T = 0.3\,\text{K}$ in the high field magnet laboratory in Nijmegen in b). The magnetic field directions are indicated as schematics in the insets.

The chiral anomaly as a possible origin for the observed negative MR is verified by investigating the negative MR signal for various angles of the magnetic field with respect to the driving current. According to Eq. 7.5 the strength of the anomalous contribution is given by the scalar product of the magnetic field with the current-driving electric field. The strength of the negative MR thus depends on the component of the magnetic field alongside the current. In Fig. 7.10a) the longitudinal resistance R_{xx} is shown as function of the magnetic field for different magnetic field directions from B parallel to the current, labeled with $\Phi = 0°$, to B out of the transport plane for $\Phi = 90°$. The magnetic field range for which the negative MR is observed as well as its amplitude reduces quickly with the rotation of the magnetic field out of the transport plane (increasing angle Φ). For $\Phi \geq 45°$ a monotonically increasing positive MR is observed. A strong positive MR signal is expected in an out of plane magnetic field ($\Phi = 90°$) for systems with low carrier densities, as is the case here, according to the discussion in Sec. 7.2.3. This expected positive MR due to the out-of-plane magnetic field contribution overshadows the MR effects of the in-plane component of the magnetic field for angles $\Phi \geq 45°$. That the positive MR is driven by the out-of-plane component of the magnetic field is confirmed via the rotation of the magnetic field inside the sample plane. The corresponding longitudinal resistance R_{xx} is shown as function of the magnetic field along different in-plane angles Θ in Fig. 7.10b). The angle $\Theta = 0°$ represents the B parallel I case and the angle $\Theta = 85°$ the B nearly perpendicular to I, but inside the transport plane case. The real perpendicular direction of $\Theta = 90°$ could not be reached due to limitations in the rotation mechanism. A reduction of the negative MR with increasing angle Θ or decreasing parallel portion of the magnetic field is observed. The effectively in-plane perpendicular case ($\Theta = 85°$) shows compared to the out-of-plane case ($\Phi = 90°$) only a week overall positive MR, which in comparison can effectively be treated as magnetic field independent. Additional features in the form of local minima and maxima of the longitudi-

nal resistance $R_{xx}(B)$ are observed. These features are especially visible for the red $\Theta = 85°$ curve in Fig. 7.10b). These local extrema are present for all investigated angles, but they are obscured by the stronger overall MR. Similar features are also observed in the 3D-TI phase and thus not specific to the Dirac semi-metal phase. These local extrema are investigated in detail in Sec. 7.5.4 based on tensilely strained HgTe 3D-TI samples. To summarize, the negative MR is driven by the component of the magnetic field parallel to the current and is thus consistent with the chiral anomaly as the underlying mechanism.

7.4.5. Gate voltage dependence of the negative magnetoresistance
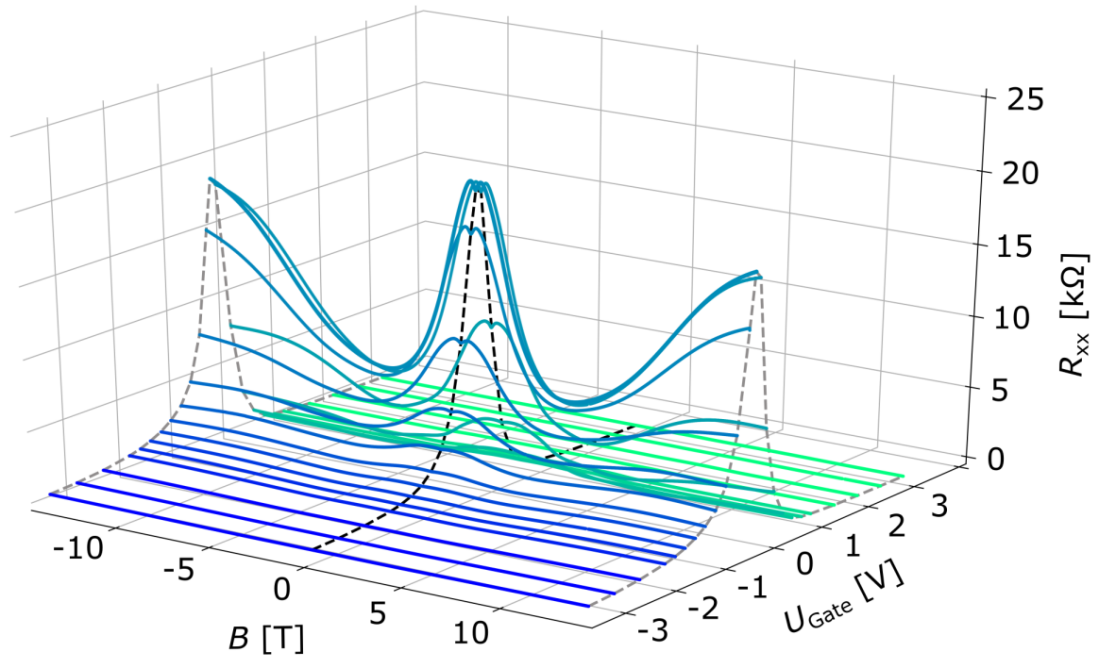
Figure 7.11: The longitudinal resistance R_{xx} of the compressively strained HgTe layer is shown as a function of the magnetic field B applied along the current direction for different gate voltages U_{gate} for the temperature $T \sim 2\,\text{K}$.

This Section examines the influence of the position of the electrochemical potential relative to the Dirac nodes on the observed negative MR and thus the magnetoresistance for the electron and hole transport regime. The top gate of the device is used to adjust the carrier density in the HgTe layer, as introduced in Sec. 7.4.2. An overview of the longitudinal resistance R_{xx} for different gate voltages as function of the magnetic field B applied along the current direction is shown in Fig. 7.11. The longitudinal resistance $R_{xx}(U_{\text{gate}})$ at $B = 0\,\text{T}$ is highlighted as dashed black line as reference. The turquoise line at the maximum of the black dashed $R_{xx}(U_{\text{gate}})$ at $B = 0\,\text{T}$ curve represents the same measurement as the dark green curves of $\Phi = 0°$ and $\Theta = 0°$ shown in Fig. 7.10a) and b). It shows the highest resistance over the full magnetic field range. The longitudinal resistance decreases quickly with more negative gate voltage (blue lines) as well as more positive gate voltages (green lines) for the whole magnetic field range. The longitudinal resistance R_{xx} depends stronger on the gate voltage U_{gate} than the magnetic field B. This is why it is insightful to look at the variation of R_{xx} with U_{gate} for different values of B. The change in resistance

with U_{gate} is strongest around $B \sim 0\,\text{T}$ along the dashed black line and high magnetic fields of $B \sim \pm 14\,\text{T}$ along the dashed grey lines. For moderate magnetic fields around $B \sim 5\,\text{T}$, the gate voltage dependence of the R_{xx} appears to be weaker than for zero and high magnetic fields. To quantify this impression, the data is re-plotted as MR in Fig. 7.12a) (Fig. 7.12b)) for the electron (hole) transport regime. With the introduction of more electrons (higher gate voltages) the overall change of resistance with magnetic field reduces from turquoise to green in Fig. 7.12a). The same happens by adding more holes (lower gate voltages) from turquoise to blue in Fig. 7.12b). The negative MR reduces with increasing carrier densities and is most prominent for gate voltages around $U_{\text{gate}} \sim -0.2\,\text{V}$. Since $U_{\text{gate}} \sim -0.2\,\text{V}$ is equivalent to the charge neutrality point, the negative MR is connected to low carrier densities and hence likely to the Fermi energy being located at the Dirac nodes, as discussed in Sec. 7.4.2. The oscillations like local extrema become very prominent for high positive gate voltages $U_{\text{gate}} = 3\,\text{V}$ [green curve in Fig. 7.12a)]. As already mentioned in Sec. 7.4.4 these features are not specific to the Dirac semi-metal phase of HgTe and are addressed in more detail in Sec. 7.5.4.
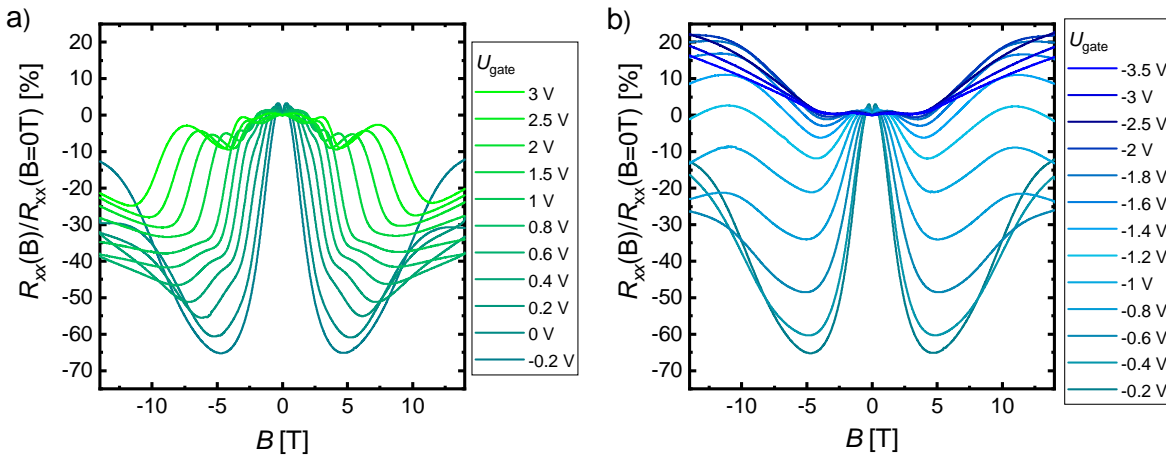
Figure 7.12: The longitudinal resistance normalized to the resistance at zero magnetic field $R_{xx}/R_{xx}(B = 0\,\text{T})$ of a compressively strained HgTe layer is shown as function of the magnetic field B applied along the direction of the current for different gate voltages $U_{\text{gate}} \geq -0.2\,\text{V}$ in a) and $U_{\text{gate}} \leq -0.2\,\text{V}$ in b) for the temperature $T \sim 2\,\text{K}$.

The observation of a reduction of the negative MR with increasing carrier density poses the question of why do not all carriers contribute to the chiral anomaly, or equivalently how does the gate voltage alter the underlying band structure. The simplest assumption is that all carriers occupy the bulk of the material and shift the Fermi energy accordingly. The bands of compressively strained HgTe are only for a small energy range around the Dirac nodes linear as shown in Fig. 7.6c). The further the Fermi energy is moved away from the Dirac nodes, the less linear the bands become. The non-linearity reduces the chiral charge pumping due to the magnetic field [11, 137]. The two Dirac nodes connect already 2 meV above the energy of the Dirac nodes, as can be seen in Fig. 7.6c). Such a connection of the two Dirac nodes is typically called Lifshitz transition. The Lifshitz transition could provide a relaxation process hindering the build-up of chiral charge on the Dirac nodes. It should be noted, that the splitting between the Dirac nodes is not relevant for the chiral current, but the splitting of the Weyl nodes, which for compressively strained HgTe is most likely due to the Zeeman effect of the applied magnetic field. This is investigated in detail in Sec. 7.4.7.

The Lifshitz transition is also an upper limit for the size of the Weyl node splitting. The corresponding carrier density is $n_{\text{Lifshitz}} \sim 0.1 \times 10^{11}\,\text{cm}^{-2}$, which is equivalent to a change in gate voltage of $\Delta U_{\text{gate}} < 0.1\,\text{V}$. A clear negative MR is observed over a much wider gate voltage range, as shown in Fig. 7.12. This observation could have a multitude of reasons: The Lifshitz transition is somehow irrelevant for the build-up chiral charges on the Dirac nodes. The correction to the band structure by the applied magnetic field, for example, due to the Zeeman effect is extraordinarily strong. The charge carriers do not simply occupy the bulk of the HgTe layer, but also other states that do not contribute to the chiral charge pumping. The chiral anomaly is only expected for three-dimensional states [101], which makes the occupation of surface states are potential mechanism.

Different types of surface states are proposed for compressively strained HgTe and examined in detail in subsequent Chapter 8. To test whether the occupation of surface states could explain the observed gate voltage dependence of the negative MR, a simple model is proposed. The model consists of two parallel transport channels. One transport channel represents the surface state, and the other one the bulk states. The conductance of the surface states is assumed to only to depend on the gate voltage and to be independent of the magnetic field. The conductance of the surface states $G_{\text{ss}}(U_{\text{gate}})$ is thus given by the gate voltage-dependent conductance without magnetic field $G_{\text{ss}}(U_{\text{gate}}) = 1/R_{xx}(U_{\text{gate}})$. The conductance of the bulk states is in contrast assumed to be independent of the gate voltage, but to host the chiral anomaly and hence to depend on the magnetic field. The conductance of the bulk states $G_{\text{anomaly}}(B)$ is for convenience assumed to be zero without a magnetic field and only describe the magnetic field dependence of the conductance at the charge neutrality point (CNP) $G_{\text{anomaly}}(B) = 1/R_{xx,\text{CNP}}(B) - 1/R_{xx,\text{CNP}}(B = 0\,\text{T})$. The longitudinal resistance at the charge neutrality point as a function of the magnetic field $R_{xx,\text{CNP}}(B)$ is shown as a turquoise curve in Fig. 7.11 at the maximum of the black dashed line. Since the surface states and bulk states exist in parallel their conductances add up. The expected resistance from this model is the inverse of the sum of these two conductances

$$R_{\text{model}}(U_{\text{gate}}, B) = \frac{1}{G_{\text{ss}}(U_{\text{gate}}) + G_{\text{anomaly}}(B)}. \tag{7.8}$$

The resistance determined by this model is shown as dashed red line together with the measured longitudinal resistance as function of the gate voltage for the magnetic fields $B = 2\,\text{T}, 6\,\text{T}$, and $10\,\text{T}$ in Fig. 7.13. The model reproduces the measurement data for $B = 2\,\text{T}$ perfectly, while for $B = 6\,\text{T}$ some deviations are visible around $0\,\text{V} < U_{\text{gate}} < 1\,\text{V}$. For $B = 10\,\text{T}$ bigger deviations can be seen. The assumption of no MR for the gate voltage-dependent channel is not realistic, as can be seen by the green and blue curves in Fig. 7.12a) and b), which correspond to high positive and negative gate voltages, respectively. The resemblance of the model with the experimental data, despite the oversimplification, encourages the occupation of surface states as the underlying mechanism. The origin and nature of these surface states are examined in the subsequent Chapter 8.

Here, the results obtained on compressively strained HgTe is compared to the reported observations in other Dirac semi-metals, as Cd_3As_2, which is described in Sec. 7.2.3. The carrier density of $n_{Cd_3As_2} \sim 2 \times 10^{12}\,\text{cm}^{-2}$, which is in Ref. [116] reported to be low for Cd_3As_2, is a factor of two higher than the highest investigated carrier density of $n_{\text{max}} \sim 1.2 \times 10^{12}\,\text{cm}^{-2}$ in our compressively strained HgTe samples. For the densities of $n \sim 1 \times 10^{12}\,\text{cm}^{-2}$, which corresponds to gate voltages $|U_{\text{gate}}| > \pm 3\,\text{V}$ the negative MR is already overshadowed by other magnetoresistance effects in compressively strained HgTe, as shown in Fig. 7.11.
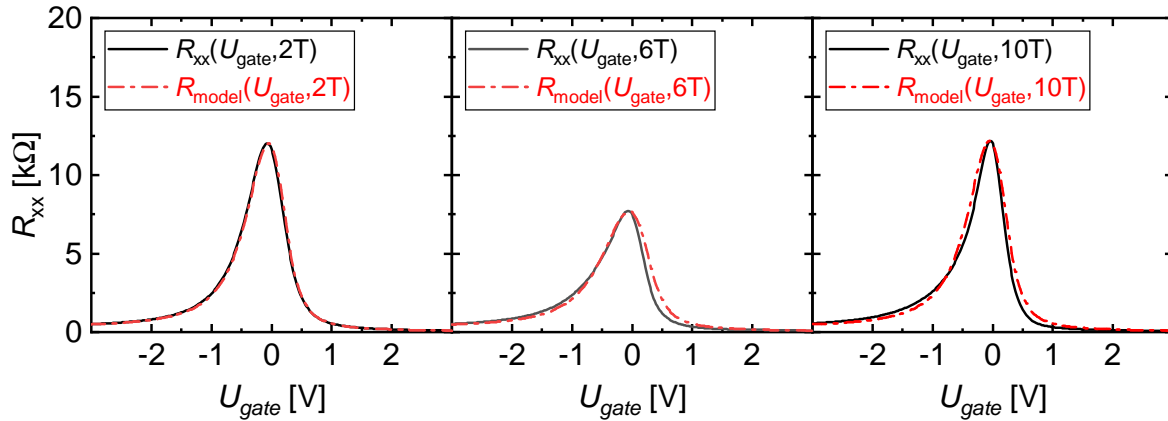
Figure 7.13: The longitudinal resistance R_{xx} is shown as a function of the gate voltage U_{gate} for a magnetic field of $B = 2\,T, 6\,T$, and $10\,T$ applied parallel to the current. The results of a model assuming one gate voltage-independent magnetic field dependent channel in parallel to a gate voltage-dependent magnetic field independent channel are shown simultaneously as dashed lines.

The different density regime could indicate a different mechanism for the negative MR. In Ref. [138] the observed negative MR in Cd_3As_2 is attributed to density/mobility fluctuations in the sample. Excluding inhomogeneities as the origin is always difficult. Nevertheless, their role for the observed negative MR is investigated in the next Section based on samples with different mobilities indicating different impurity concentrations. So far, it is encouraging, that the negative MR in our compressively strained HgTe samples is only observed in a limited gate voltage range around the charge neutrality point. This is consistent with the Fermi energy being located close to the Dirac nodes and no occupation of any other states and makes the chiral anomaly a likely mechanism.

7.4.6. MOBILITY DEPENDENCE OF THE NEGATIVE MAGNETORESISTANCE

The influence of impurities on the observed negative MR is investigated using samples fabricated from three different wafers with nominally the same compressive strain. These samples have been intended to investigate potential thickness dependencies and to exclude finite-size effects due to the limited thickness $d_{HgTe} = 66\,nm$ of sample QC0262. The longitudinal resistance R_{xx} of the three samples is shown in function of the gate voltage in Fig. 7.14a). The so far discussed thinnest sample shows the highest maximum of the longitudinal resistance $R_{xx}(U_{gate})$ and simultaneously the lowest $R_{xx}(U_{gate})$ for high positive and negative U_{gate} equivalent to high densities. The opposite behavior with the lowest maximum resistance and the highest resistance for high densities is observed for the sample with the intermediate thickness $d_{HgTe} = 94\,nm$. The position of the maximum longitudinal resistance R_{xx} shifts with reducing height to more negative gate voltages. Neither the height nor the position of the peak of the longitudinal resistance $R_{xx}(U_{gate})$ indicates a thickness-dependent trend. The total carrier densities and mobilities are determined for the three samples from the semi-classical low magnetic field regime and shown in Fig. 7.14b). The thinnest sample shows the highest mobility over the full density range, while the $d = 94\,nm$ thick sample shows the lowest mobility. The absence of a thickness dependence points to a difference in the layer quality and thus the number of impurities. The varying number of impurities in the samples explains the different longitudinal resistance for high positive and negative gate voltages. The peak in the longitudinal resistance $R_{xx}(U_{gate})$ indicates ac-

cording to the discussion in Sec. 7.4.2 the charge neutrality point is shifted with to more negative voltages with decreasing mobility. The shift could indicate increased unintentional doping in the HgTe layer and is consistent with an increased charged impurity density in the HgTe layer and thus reduced mobility. Unfortunately, the absolute position of the $R_{xx}(U_{\text{gate}})$ peak is not a reliable quantity. It can vary from cool down to cool down due to differences in the charge trapping at interfaces and inside the insulator while cooling down the sample. The focus is thus shifted to the mobility μ, which is shown as a function of the total density n In Fig. 7.14b). For low carrier densities n no values for the mobility μ can be determined indicating very low mobilities. The density region with indeterminably low mobilities is here called mobility gap. The size of the mobility gap increases with decreasing mobilities for high carrier densities n. This increase of this mobility gap corresponds to the observed broadening of the peak of the longitudinal resistance $R_{xx}(U_{\text{gate}})$ in Fig. 7.14a). The sharpness of the $R_{xx}(U_{\text{gate}})$ peak or equivalently the maximum of R_{xx} resembles thus an indicator for the mobility of the sample. The mobility gap is larger for holes than for electrons, which is consistent with the overall lower mobility observed for holes than for electrons. The lower mobility makes the holes more prone to localization due to potential inhomogeneities in the sample. Nevertheless, all three samples show a reduction of the longitudinal resistance with a magnetic field applied along the current direction, as shown in Fig. 7.14c). Despite the significant difference in the value of the longitudinal resistance at zero magnetic field the normalized longitudinal resistance shows a comparable reduction with the magnetic field of $R_{xx}(B)/R_{xx}(B0 = \text{T}) \sim 65\,\%$. The slightly higher amplitude of the negative MR for the thickest sample in red is an artifact due to the absence of the WAL correction around $B \sim 0\,\text{T}$. Still, differences exist in the MR of the three samples. For example, the magnetic field value of the minimal longitudinal resistance, the visibility of the additional oscillation like extrema, and the strength of the positive MR for high magnetic fields. Nevertheless, the resemblance of the MR of these three samples in Fig. 7.14d) is astonishing compared to the difference in $R_{xx,\text{max}}(B = 0\,\text{T})$. Since the strength of the negative MR does not vary significantly in these samples, has neither the thickness nor the mobility, and thus the number of impurities, a significant influence on the negative MR.

This observation raises the question, what the independence of the mobility of the negative MR implies for its physical origin. The mobility is a measure of the homogeneity and amount of impurities in the sample. The typical scattering mechanisms in layers as HgTe are density fluctuations and ionic scattering [90]. Both types of scattering are described to be able to cause negative MR. Fluctuations of the density or mobility are identified in Ref. [116] to cause the observed negative MR in Cd_3As_2 samples, which is described in Sec. 7.2.3 and shown in Fig. 7.3d). Ionic scattering, which is typically the dominating source of scattering in semiconductors for low temperatures [90], is described by Ref. [139] to cause a negative MR with a magnetic field parallel to the current. If either of the two mechanisms would be responsible for the observed negative MR, the measured MR signal should depend on the mobility. In contrast, the amplitude of the negative MR does not change with the mobility, even though the mobility of the investigated samples differs by more than a factor of three between the $d_{\text{HgTe}} = 94\,\text{nm}$ and $d_{\text{HgTe}} = 66\,\text{nm}$ thick samples. This independence of the amplitude of the negative MR on the mobility of the sample makes the scattering on charged impurities and density or mobility fluctuations an unlikely mechanism. The negative MR is because of this most likely due to a band structure effect, as the chiral anomaly.
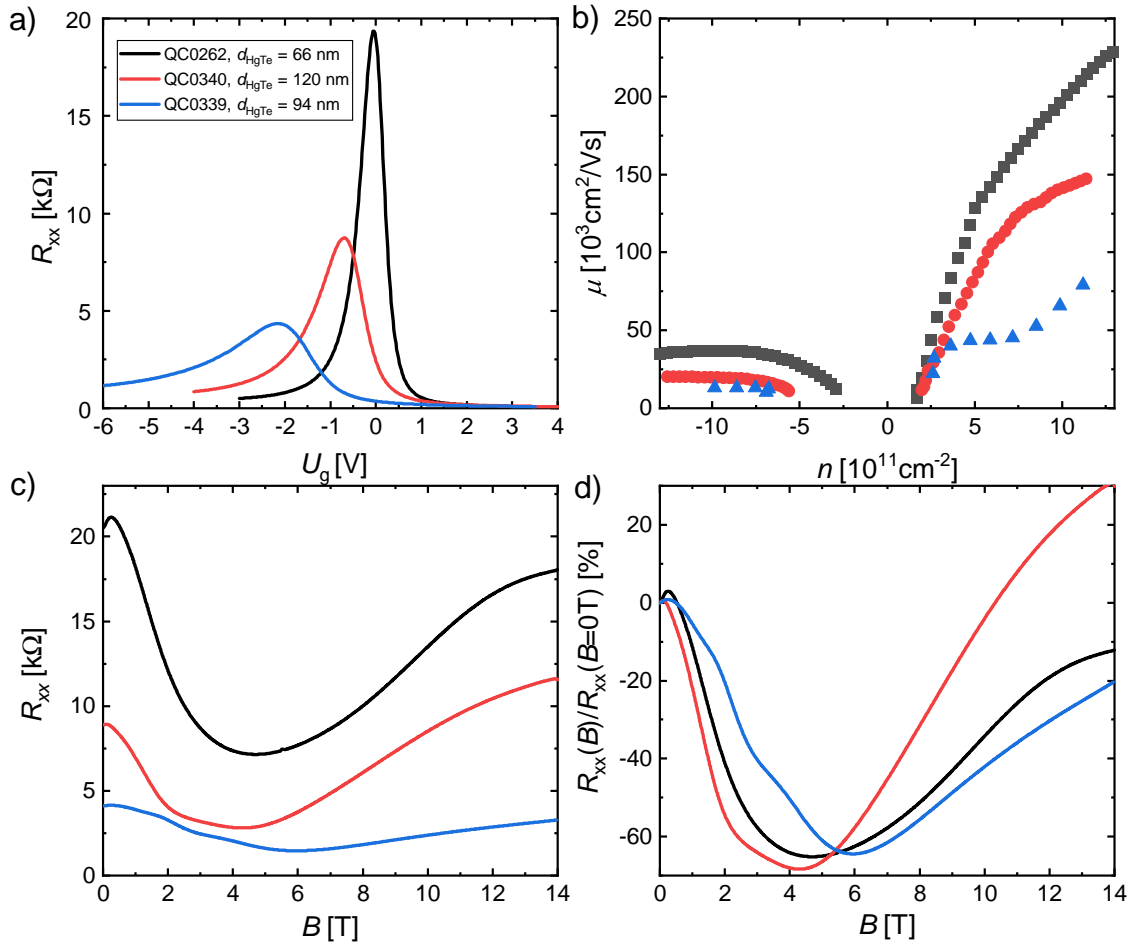
Figure 7.14: In a) the longitudinal resistances R_{xx} of HgTe layers of different thicknesses $d_{\mathrm{HgTe}} = 66\,\mathrm{nm}, 120\,\mathrm{nm}$, and $94\,\mathrm{nm}$ with a compressive strain of $\epsilon \sim 0,3\%$ strain are shown as function of the gate voltage U_{gate} for the magnetic field $B = 0\,\mathrm{T}$ and the temperature $T \sim 2\,\mathrm{K}$. In b) the mobility μ is shown as a function of the total charge carrier density n determined from the semi-classical transport regime. In c) the longitudinal resistance R_{xx} at the charge neutrality point is shown as a function of the magnetic field B applied parallel to the current direction at $T \sim 2\,\mathrm{K}$. In d) the same data as c) is presented as the longitudinal resistance normalized to the zero magnetic field resistance $R_{xx}(B)/R_{xx}(B = 0\,\mathrm{T})$.

7.4.7. STRAIN DEPENDENCE OF THE NEGATIVE MAGNETORESISTANCE

The possibility to alter the band structure of HgTe with bi-axial strain applied by the growth on a substrate with appropriate lattice constants, as introduced in Sec. 2.1.2 and 7.4.1, is used to investigate the relevance and influence of the splitting between the two Dirac cones for the negative MR. Samples with different strain ranging from a slight tensile strain of $\epsilon = -0.04\%$ to a compressive strain of $\epsilon = 0.47\%$ are compared. The longitudinal resistance R_{xx} at the charge neutrality point is shown as a function of the magnetic field applied along the direction of the current in Fig. 7.15a). The most prominent observation is that the longitudinal resistance $R_{xx}(B = 0\,\mathrm{T})$ varies up to a factor of 10 between the samples ranging from $R_{xx,\mathrm{QC0262}}(B = 0\,\mathrm{T}) = 20.5\,\mathrm{k\Omega}$ to $R_{xx,\mathrm{QC0426}}(B = 0\,\mathrm{T}) = 1.7\,\mathrm{k\Omega}$. The values of the longitudinal resistance do not follow the magnitude of the strain in an obvious fashion. The longitudinal resistance $R_{xx}(B = 0\,\mathrm{T})$ is thus probably not only determined by the strain in the HgTe layer but also by other factors as the growth quality of the layer, as discussed in

Sec. 7.4.6. Nevertheless, all samples show a negative MR up to $B \sim 6\,$T. A comparison of the respective amplitudes of the negative MR is hindered by the big variation of the values of the longitudinal resistance $R_{xx}(B = 0\,$T$)$. This is why the longitudinal resistance is normalized to the zero magnetic field resistance and shown in Fig. 7.15b). The maximum of the negative MR is for all samples around $B \sim 5\,$T observed. Only the sample QC0361, which possesses the highest strain, shows the maximum at a magnetic field of $B \sim 9\,$T. The amplitude of the maximum negative MR only varies by a factor of two between the values of $-37\,\%$ and $-65\,\%$. This factor of two is small compared to the variation in the longitudinal resistance $R_{xx}(B = 0\,$T$)$ by a factor of ten. The amplitude of the negative MR does not show any obvious trends in the function of the strain. In contrast, the amplitude of the negative MR amplitude increase with increasing longitudinal resistance $R_{xx}(B = 0\,$T$)$. The observed properties of the sample with varying strain are reminiscent of the MR observed for sample with varying mobility, but constant strain, in Fig. 7.14c) and d). As discussed in Sec. 7.4.6, the value of the maximum resistance in the Dirac semi-metal phase is a measure of the mobility of the sample. The different mobility of the investigated layers overshadows any potential strain influence. The different mobilities thereby are either due to differences in layer quality or due to different effective masses of the bands in the layers. For zero strain a semi-metal with a quadratic band touching point is expected. These samples could be more prone to potential fluctuations over the sample compared to their linear counterparts for higher compressive strain. The independence of the relative amplitude of the negative MR on the mobility of the HgTe layers observed in Sec. 7.4.6, seems only to hold above a certain layer quality. Fig. 7.15b) shows the longitudinal resistance normalized to its zero magnetic field value as a function of the magnetic field for samples with various strain and layer quality. The amplitude of the observed negative MR reduces for too low mobilities, or equivalently to disordered layers.
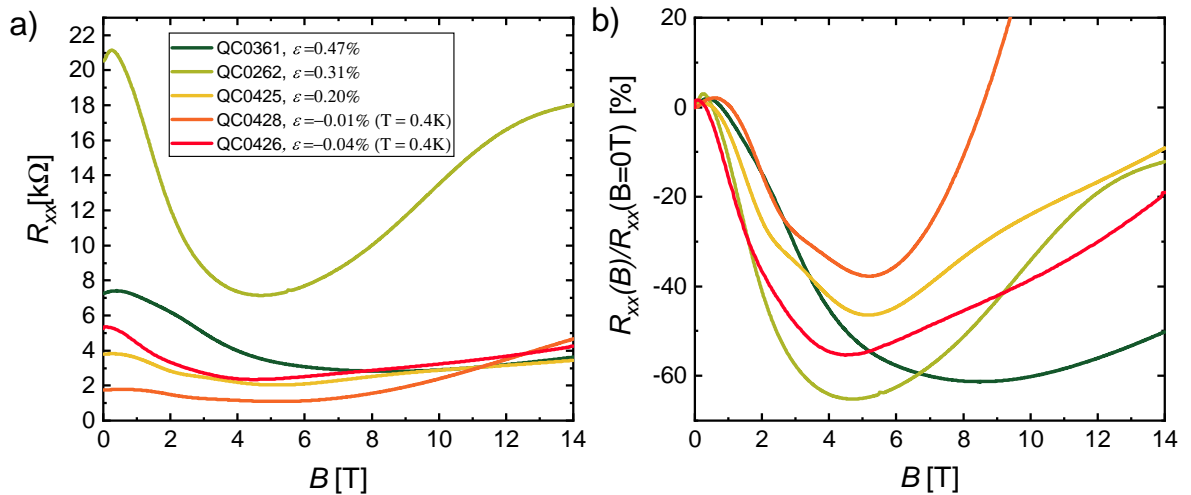
Figure 7.15: In a) the longitudinal resistance R_{xx} of HgTe samples with different strain ϵ, which ranges from a compressive strain of $\epsilon = 0.47\,\%$ to a slight tensile strain of $\epsilon = 0.04\,\%$, is shown as a function of the magnetic field B applied along the direction of the current. The temperature is $T \sim 2\,$K, as long as not otherwise indicated. In b) the same data is shown as longitudinal resistance normalized to the longitudinal resistance at zero magnetic field $R_{xx}(B)/R_{xx}(B = 0\,$T$)$.

It is surprising that also the two samples with a small tensile strain show a negative MR signal. The amplitude of the negative MR of the slightly compressively strained sample with $\epsilon = -0.04\%$ is even comparable to the highest observed negative MR of the sample QC0262. This sample can be treated as unstrained to a good approximation since the uncertainty in the strain is comparable to its size and the bandgap is neglectable small. Unstrained HgTe is a semi-metal with a quadratic band touching point, with no linear crossing points at zero magnetic field. In Ref. [140] it is pointed out that HgTe as inverted material of the point group T_d becomes a Weyl semi-metal in a magnetic field due to the energy shift by the Zeeman effect. Consequently, a chiral anomaly driven negative MR is expected for unstrained HgTe. Since the size of the negative MR is comparable for the unstrained and 0.31% and 0.47% strained HgTe, the Zeeman effect is likely the driving force for the chiral anomaly in the compressively strained Dirac semi-metal phase and the unstrained semi-metal phase with a quadratic band touching of HgTe.

7.4.8. MAGNETORESISTANCE IN THE ABSENCE OF A LINEAR CROSSING POINT IN THE BULK BAND STRUCTURE

In this Section, the question is addressed whether a band touching point is needed at all to observe the negative MR signal. The particular possibility to adjust the bulk band structure of HgTe by strain, while preserving all other properties is even further exploited. This allows a direct comparison to the in-plane magneto-transport of the 3D-TI tensilely strained HgTe. The sample is a tensilely strained HgTe layer of 90 nm thickness is grown surrounded by a 10 nm thick capping and a 50 nm thick $Cd_{0.7}Hg_{0.3}Te$ buffer layer on top of a commercial CdTe substrate. It is similar to the 3D-TI sample analyzed in detail in Part II. The longitudinal resistance R_{xx} and the carrier density n are shown as function of the gate voltage U_{gate} in Fig. 7.16a). The longitudinal resistance for high negative and positive gate voltages is with 0.4 kΩ and 0.08 kΩ, respectively, comparable to the longitudinal resistance of the Dirac semi-metal phase for such densities. For comparison see Fig. 7.6a). In contrast, the maximum of the longitudinal resistance $R_{xx,max}(U_{gate}) = 1.22$ kΩ is nearly 20 times smaller than the maximum resistance for the Dirac semi metal phase. The maximum of the longitudinal resistance is also shifted with respect to the charge neutrality point, as determined by the linear fit to the total densities shown in Fig. 7.16a). This difference in the longitudinal resistance curves $R_{xx}(U_{gate})$ enables a distinction between the 3D-TI and Dirac semi-metal phase. The low maximum resistance and its shift with respect to the charge neutrality point is a consequence of the coexistence of the electron-like topological surface states with the hole-like Volkov-Pankratov states. The interplay of these two states is discussed in Chapter 3 and more detailed in Ref. [58, 79]. For the comparison with the Dirac semi-metal phase, this shift is irrelevant, and the charge neutrality point is chosen as the reference point. The longitudinal resistance R_{xx} is shown as function of the magnetic field B parallel to the current and the gate voltage U_{gate} in Fig. 7.16b). The longitudinal resistance $R_{xx}(B)$ increases with the magnetic field B for the light blue curves around the charge neutrality point $U_{gate} \sim -0.8$ V. The observed positive MR in the 3D-TI phase around the charge neutrality point verifies the relevance of the Dirac nodes in the Dirac semi-metal phase or the magnetic field induced Weyl nodes in the unstrained semi-metal phase for the chiral anomaly driven negative MR. The comparison of Fig. 7.16b) to Fig. 7.11 nicely highlights the different magnetoresistance of the two phases.
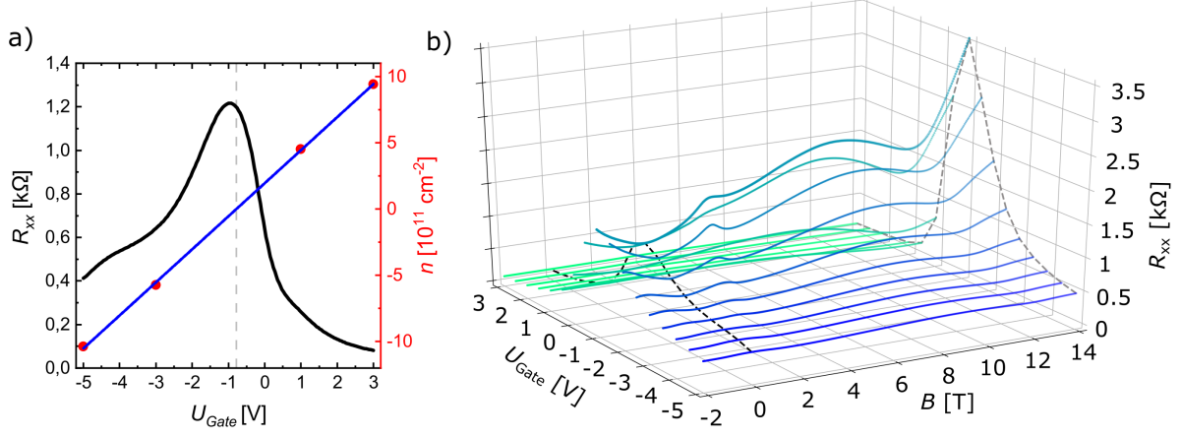
Figure 7.16: In a) the longitudinal resistance R_{xx} of the 90 nm thick tensilely strained HgTe sample Q2761 is shown in black as a function of the gate voltage U_{gate} together with the corresponding charge carrier densities n in red. The blue line represents a linear fit to the density $n(U_{\text{gate}})$ and the vertical dashed line indicates the charge neutrality point. In b) the longitudinal resistance R_{xx} is shown as function of the magnetic field B applied along the direction of the current for multiple gate voltages from $U_{\text{gate}} = 3\,\text{V}$ in blue to $U_{\text{gate}} = -5\,\text{V}$ in green. The $R_{xx}(U_{\text{gate}})$ shown in a) is indicated as dashed black line in b). The dashed grey line highlights the $R_{xx}(B = 14\,\text{T})$ values.

Despite this difference, also similarities are observed. The gate voltage mainly determines the value of the longitudinal resistance R_{xx}. The longitudinal resistance is non-monotonic and also shows oscillation-like local extrema. These local extrema and their potential origins are examined in Sec. 7.5.4. The MR of the 3D-TI sample is positive for all $U_{\text{gate}} \leq 0\,\text{V}$. For $U_{\text{gate}} > 0\,\text{V}$ and thus with $n > 2 \times 10^{11}\,\text{cm}^{-2}$ well in the electron transport regime, the resistance reduces with magnetic field. This negative MR is observable up to electron densities $n \sim 1 \times 10^{12}\,\text{cm}^{-2}$ for $U_{\text{gate}} = 3\,\text{V}$. This negative MR seems to originate from a different mechanism. The thin capping layer thickness makes density or mobility fluctuations over the sample a potential mechanism, as also suggested for the negative MR observed in Cd_3As_2 samples, as discussed in detail in Sec. 7.2.3.

To summarize, the positive MR around the charge neutrality point for the tensilely strained HgTe sample is opposite to the negative MR observed for the compressively strained HgTe samples. The linear crossing point in the bulk band structure of compressively strained HgTe is necessary to observe negative MR around the charge neutrality point. Furthermore, the linear crossing points of unstrained HgTe samples in a magnetic field also cause a negative MR signal. The chiral anomaly is thus likely the driving mechanism behind the observed negative MR.

7.5. ADDITIONAL IN-PLANE MAGNETO-TRANSPORT EFFECTS

The chiral anomaly-driven negative MR in the Dirac semi-metal compressively strained HgTe is accompanied by other interesting transport features. These effects are summarized in Fig. 7.17. The longitudinal resistance R_{xx} at the charge neutrality point is shown as a function of the in-plane magnetic field applied for various angles Θ. Three different transport regimes are identified: These are the magnetic field direction independent low magnetic field regime, the moderate magnetic field regime with a monotonic dependence of the longitudinal resistance on the angle Θ, and the high magnetic field regime. The magnetic field $B \sim 18\,\mathrm{T}$ is chosen as the starting point for the high magnetic field regime, since there the behavior of the longitudinal resistance $R_{xx}(B)$ changes indicated by the crossing of the $R_{xx}(B)$ curves. This magnetic field is highlighted as a dashed black vertical line. The negative MR observed in the moderate magnetic field regime is identified with the chiral anomaly in the previous Sec. 7.4. This Section focuses on the transport features, which are observed additionally to the negative MR. The low magnetic field regime is taken as starting point.
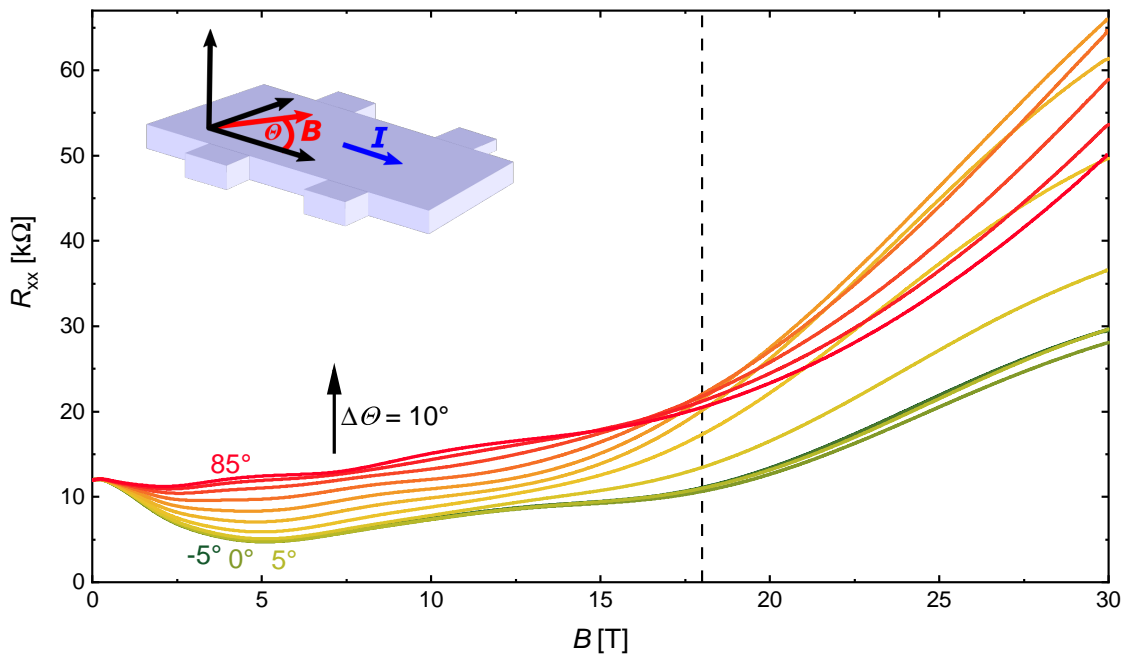
Figure 7.17: The longitudinal resistance R_{xx} at the charge neutrality point of compressively strained HgTe (QC0262) is shown as a function of an in-plane magnetic field B applied alongside various angles Θ, as indicated in the inset, at the temperature $T = 0.3\,\mathrm{K}$. The vertical dashed black line marks the magnetic field $B = 18\,\mathrm{T}$. The data is measured in the high field magnet laboratory in Nijmegen.

7.5.1. WEAK ANTI-LOCALIZATION

The low magnetic field regime shows a positive MR, which is in Sec. 7.4.3 interpreted as WAL correction. Weak anti-localization is predicted by Ref. [141] to cause a positive MR for metals with strong spin-orbit coupling. That WAL is relevant in HgTe layers is motivated from its observation in arrays of HgTe wires in Ref. [142]. The interpretation of WAL as driving mechanism for the positive MR is supported by the possibility to fit the observed MR up to $B \sim 3\,\mathrm{T}$ with Eq. 7.6, as shown in Fig. 7.9. The WAL and the chiral anomaly are taken into

account for the fit. To produce a satisfactory resemblance of MR for low magnetic fields, the formula for the WAL described by Ref. [135, 136] is used. This Equation deviates from the typically used Hikami-Larkin-Nagaoka formula [132]. The good resemblance makes the WAL a likely mechanism for the positive MR observed for low magnetic fields and highlights the WAL as peculiar and thus interesting. This Section shall be seen as a motivation for a future pursue a more in-depth examination of the observed WAL signal. Figure 7.18 shows a summary of the results obtained in this work.

Firstly, the temperature dependence of the positive MR signal is examined and emphasizes the WAL as a likely mechanism. The normalized longitudinal resistance is shown for various temperatures for low magnetic fields in Fig. 7.18a). This data is an excerpt of the low magnetic field regime from the data already shown in Fig. 7.8. A strong positive MR of up to 3 % is observed for $T = 2$ K. The amplitude of the positive MR reduces with increasing temperature. For a temperature of $T = 6$ K only an amplitude 0.2 % is observed. For a temperature of $T \sim 18$ K, the positive MR increases no longer. The MR decreases instead right away with increasing magnetic fields around $B = 0$ T. Since WAL is a self-interference effect, it depends on a sufficiently long coherence time and is thus strongly temperature-dependent. The strong observed temperature dependence of the positive MR is consistent with the WAL as the underlying mechanism.
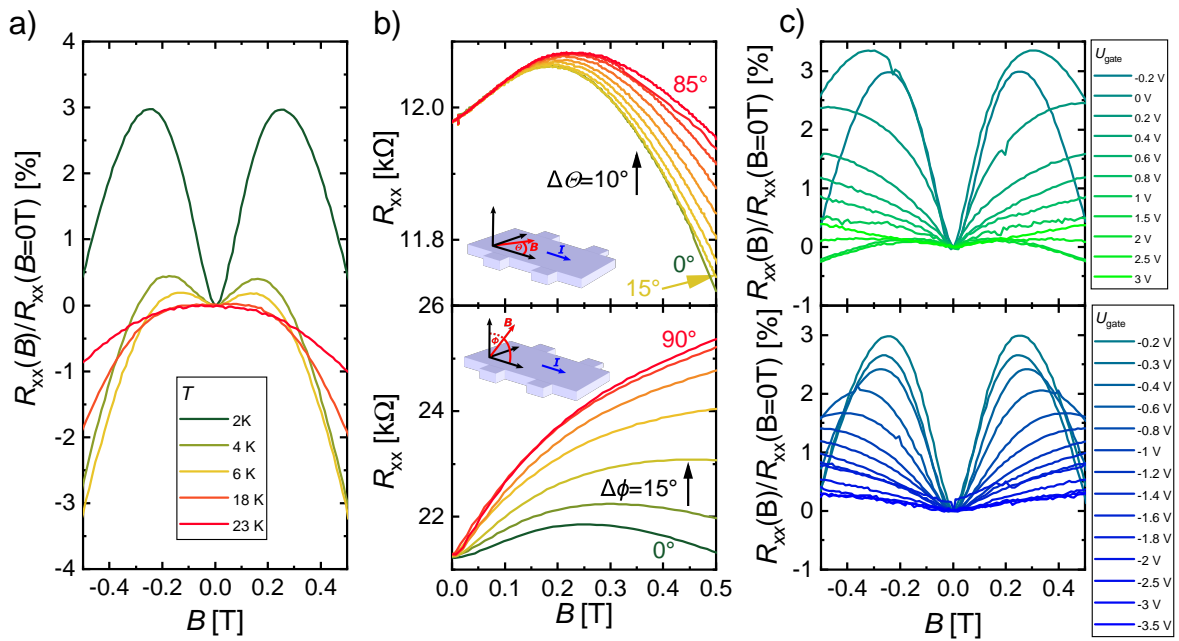
Figure 7.18: The figure shows an overview of the longitudinal resistance R_{xx} as a function of the magnetic field B observed in compressively strained HgTe layer QC0262. In a) the longitudinal resistance normalized to the zero magnetic field resistance $R_{xx}(B)/R_{xx}(B = 0$ T) at the charge neutrality point is shown as function of the magnetic field B along the current direction for different temperatures $T = 2$ K, 4 K, 6 K, 14 K, 18 K, and 23 K. In the upper panel of b) the longitudinal resistance R_{xx} is shown as a function of the magnetic field B for various angles Θ in the sample plane (see inset) and in the lower panel for angles Φ representing a rotation out of the sample plane (see inset). In c) the normalized longitudinal resistance $R_{xx}(B)/R_{xx}(B = 0$ T) is shown as function magnetic field B along the current direction for different gate voltages U_{gate}. The upper panel shows the electron regime, and the lower panel the hole regime. The sub-figures a), b), and c) are close ups of the low magnetic field regime of the data already presented in Fig. 7.8, Fig. 7.10, and Fig. 7.12, respectively.

Secondly, the positive MR and thus the WAL shows peculiarities. The positive MR for various angles of the magnetic field is summarized in Fig. 7.18b). The shown data represent a zoom onto the low magnetic field region of Fig. 7.10. The longitudinal resistance $R_{xx}(B)$ is up to magnetic fields of $B \sim 0.1\,\mathrm{T}$ independent of the angle Θ of the magnetic field with respect to the current inside the sample plane. This independence is also observed for TaAs in Ref. [135] and consistent with the calculations for a thin Weyl semi-metal of Ref. [143]. The positive MR in contrast increases with increasing inclination Φ and hence the out-of-plane component of the magnetic field. The origin could be twofold. It could be the additional positive MR expected due to an out-of-plane magnetic field by the deflection of the charge carriers by the Lorentz force. It could also be a property of the WAL itself. For a Weyl semi-metal, different WAL corrections for an out-of-plane and an in-plane magnetic field are given in Ref. [143]. A distinction between these two effects is not possible with the current data set.

Thirdly, the top gate is used to identify the transport regime with the most prominent positive MR and thus WAL. The normalized longitudinal resistance R_{xx} as function of the magnetic field B along the current direction is summarized for various gate voltages U_{gate} in Fig. 7.18c). The strongest positive MR is observed around $U_{\mathrm{gate}} \sim -0.2\,\mathrm{V}$ which resembles the position of the maximum of the longitudinal resistance $R_{xx}(U_{\mathrm{gate}})$ and thus the charge neutrality point as well as the strongest observed negative MR for moderate magnetic fields. In Sec. 7.4.2 this gate voltage is identified with the Fermi energy located at the Dirac nodes. The strong MR is thus likely connected to the Dirac nodes in the bulk band structure.

Lastly, the pure existence of a strong WAL correction in a three-dimensional layer makes the WAL interesting in itself. In contrast only a very weak WAL is observed in the 3D-TI tensilely strained HgTe in Ref. [144]. Together with the non-trivial dependence on the angle of the magnetic field and the gate voltage dependence, this effect would be interesting to investigate in more detail in a dilution refrigerator with a three-dimensional vector magnet.

7.5.2. Planar Hall effect

The longitudinal resistance $R_{xx}(B)$ for moderate magnetic fields $B > 1\,\mathrm{T}$ is dominated by negative MR which is traced to the chiral anomaly in Sec. 7.4. In this Section, the details of the angular dependence of the negative MR are investigated in more detail. The additional current driven by the chiral anomaly is described by Eq.7.5. Since the current-driving excitation voltage is constant in our experiment, the longitudinal conductance depends on the variation of the current due to the chiral anomaly. The longitudinal conductance $G_{xx}(\theta)$ is hence given by the scalar product of E and B and thus depends on $\cos(\theta)$. Since the dependence on B is quadratic the angular dependence of the conductance is given by

$$G_{xx}(\theta) \propto \cos^2(\theta). \tag{7.9}$$

An exemplary measurement of the longitudinal resistance $R_{xx}(\theta)$ at the charge neutrality point for a constant magnetic field $B = 5\,\mathrm{T}$ is shown in Fig. 7.19a). The longitudinal resistance R_{xx} is measured as a function of the in-plane angle θ by rotating the sample stick inside the constant magnetic field. The angle θ is determined with a Hall sensor mounted on the rotation mechanism next to the sample. Because of this, the absolute value of the angle θ possesses an uncertainty in the order of a few degrees. The longitudinal conductance $G_{xx}(\Theta) = 1/R_{xx}$ and the conductivity $\sigma_{xx}(\theta)$ are shown together with the longitudinal resistance $R_{xx}(\Theta)$ for $B = 5\,\mathrm{T}$ in Fig. 7.19a).
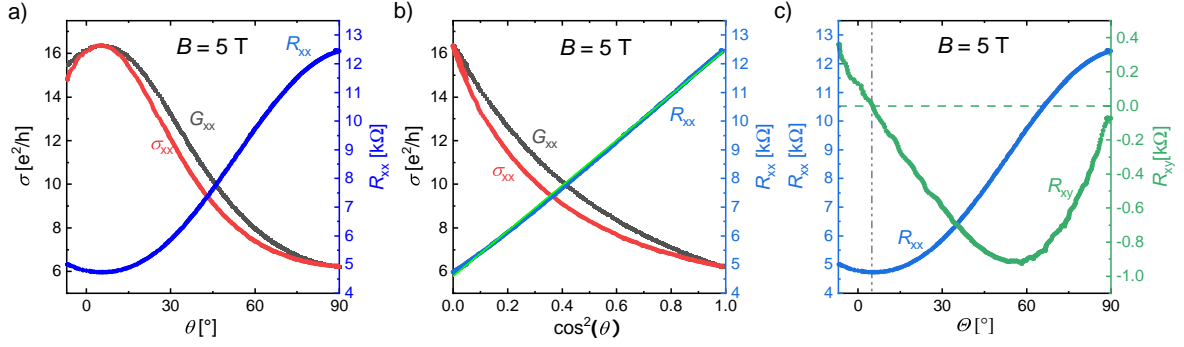
Figure 7.19: In a) the longitudinal conductance $G_{xx} = 1/\rho_{xx}$ (black), longitudinal conductivity σ_{xx} (red), and the longitudinal resistance R_{xx} (blue) at the charge neutrality point of the compressively strained HgTe layer QC0262 are shown as function of the angle Θ of a constant magnetic field $B = 5\,\text{T}$ in sample plane for the temperature $T = 0.3\,\text{K}$. The same data is shown in b) again, as a function of $\cos^2(\Theta)$. In c) the Hall resistance R_{xy} is shown in green together with the longitudinal resistance R_{xx} in blue as a function of the angle Θ. The dashed green line indicates $R_{xy} = 0\,\text{k}\Omega$ and the dash-dotted grey line highlights the corresponding angle $\Theta \sim 5°$. The data has been measured in the high field magnet laboratory in Nijmegen.

The longitudinal conductivity $\sigma_{xx}(\theta)$ is determined using

$$\sigma_{xx}(\theta) = \frac{w}{l} \frac{R_{xx}}{R_{xx}^2\left(\frac{l}{w}\right)^2 + R_{xy}^2}, \tag{7.10}$$

where $\frac{w}{l}$ is the ratio of the length l to the width w of the Hallbar. The longitudinal conductance $G_{xx}(\theta)$ (black) and longitudinal conductivity $\sigma_{xx}(\theta)$ (red) curves show a maximum close to the angle $\theta \sim 0°$ and the onset of a minimum for the angle $\theta \sim 90°$, as expected from Eq. 7.9. The connection of these two extrema deviates from the expected sinusoidal shape. In contrast, the longitudinal resistance $R_{xx}(\theta)$ (blue curve) appears to be sinusoidal. To quantify this impression, the same data is plotted as function of $\cos^2(\theta)$ in Fig.7.19b). The longitudinal resistance R_{xx} shows a linear dependence on $\cos^2(\theta)$, which is emphasized by the linear fit depicted as a green line. The longitudinal conductance and conductivity do not show a linear dependence in contradiction to the expectation from Eq. 7.9.

To sum up, the longitudinal resistance $R_{xx}(\theta)$ is proportional to $\cos^2(\theta)$. This proportionality is expected for the anisotropic magneto-resistance (AMR), as observed in ferromagnetic metals [145]. The anisotropic magnetoresistance is the manifestation of the scattering dependence on the magnetic field and current direction in the longitudinal resistance R_{xx}. This scattering also causes a voltage perpendicular to the current and consequently a Hall resistance R_{xy}. This effect is called planar Hall effect (PHE). The AMR and PHE signals are constrained by the crystal symmetry of the material. The space group of HgTe is given by the F$\bar{4}$3m space group of the zinc blende crystal. The applied bi-axial in-plane strain reduces the space group to F$\bar{4}$2m. The allowed terms of the longitudinal resistivity ρ_{xx} and Hall resistivity ρ_{xy} in an in-plane magnetic field are given in Ref. [146] for this space group. These terms read

$$\rho_{xx}(\vartheta) = C_0 + C_I \cos(2\vartheta - 2\varphi) + C_{IC} \cos(2\vartheta + 2\varphi) + C_C \cos(4\vartheta) \tag{7.11}$$

and

$$\rho_{xy}(\vartheta) = C_I \sin(2\vartheta - 2\varphi) + C_{IC} \sin(2\vartheta + 2\varphi), \tag{7.12}$$

where ϑ and φ are the angles of the magnetic field and current with respect to the crystallographic direction and C_0 resembles the average longitudinal resistivity ρ_{xx} and C_I, C_{IC} as well as C_C are respective amplitudes. Since the measured Hall bars are oriented such that the current flows along the high symmetry $\langle 110 \rangle$ direction, these equations reduce to

$$\rho_{xx}(\theta) = C_0 + C_a \cos(2\theta) + C_b \cos(4\theta) \tag{7.13}$$

and

$$\rho_{xy}(\theta) = C_a \sin(2\theta), \tag{7.14}$$

where θ is the angle between the magnetic field and the current, and C_a and C_b are treated as fitting parameters. According to the trigonometric identities is

$$\cos(2\theta) = 2\cos^2(\theta) - 1. \tag{7.15}$$

Equation 7.13 is thus consistent with the observation of the longitudinal resistance R_{xx} being linear in $\cos^2(\theta)$, as shown in Fig. 7.19b). The Hall resistance $R_{xy}(\theta)$ is shown together with the longitudinal resistance $R_{xx}(\theta)$ in Fig. 7.19c). The Hall resistance $R_{xy}(\theta)$ crosses zero at the minimum of the longitudinal resistance $R_{xx}(\theta)$ signal, which is consistent with the expected phase shift of $45°$ between the two signals by Eq. 7.13 and 7.14. Even though the Hall resistance $R_{xy}(\theta)$ deviates from the expected sinusoidal shape, it appears to have a zero-crossing at the position of the extrema in the longitudinal resistance $R_{xx}(\theta)$. The zero crossing is thus consistent with the two-fold symmetry $\sin^2$ expected for the PHE by Eq. 7.14. The amplitude of the Hall signal is with $\Delta \rho_{xy} = \Delta R_{xy} \sim 0.9\,\text{k}\Omega$ is similar to the amplitude of the longitudinal resistivity signal of $\Delta \rho_{xx} = \Delta R_{xx} \frac{w}{l} \sim 1.3\,\text{k}\Omega$. The amplitudes for the AMR and PHE are expected to coincide according to Eq. 7.13 and Eq. 7.14. A reason for the observed smaller amplitude in the Hall resistivity could be the misalignment of the sample with respect to the magnetic field. Such a misalignment is unavoidable in the used rotation mechanism. An out-of-plane magnetic field causes a contribution of the classical Hall to the Hall resistance $R_{xy}(\theta)$. The classical Hall contribution is expected to be proportional to $\sin(\theta + \theta_0)$. The phase θ_0 is unknown and depends on the direction of the misalignment. The presence of a PHE signal and the deviation of the negative MR from the naively expected $G_{xx} \propto \cos^2(\theta)$ behavior is emphasizing the importance of accounting for the resistivity as tensor as already pointed out in Ref. [147]. There is a narrowing of the negative MR and thus a deviation of the longitudinal conductance from $G_{xx} \propto \cos^2(\theta)$ due to the PHE described.

An overview over the Hall resistance R_{xy} as a function of the magnetic field B for various angles θ inside the sample plane for the full accessible magnetic field range is given in Fig. 7.20. The Hall resistance $R_{xy}(B)$ signal shows three different regimes:

The low to moderate magnetic field regime for $B < 10\,\text{T}$ (left of the dashed grey line) shows positive Hall resistance R_{xy} values for angles $\theta = -5°$ together with the strongest negative signals for the angle $\theta = 45°$ (thick orange line). For angles $\theta > 45°$ the Hall resistance R_{xy} increases again up to $\theta = 85°$, but stays below the value of $R_{xy}(\theta = -5°)$. This behavior resembles the measurement for fixed $B = 5\,\text{T}$ as function of the angle θ in Fig. 7.19c) and is thus assigned to the above discussed PHE related to the chiral anomaly.

The transition regime $10\,\text{T} < B < 18\,\text{T}$ (between the dashed lines) shows also a minimal Hall resistance R_{xy} for the angle $\theta \sim 45°$, but the Hall resistance $R_{xy}(\theta \geq 65°)$ exceeds the $R_{xy}(\theta = -5°)$ values. In contrast, the longitudinal resistance $R_{xx}(B)$ in Fig. 7.17 does not
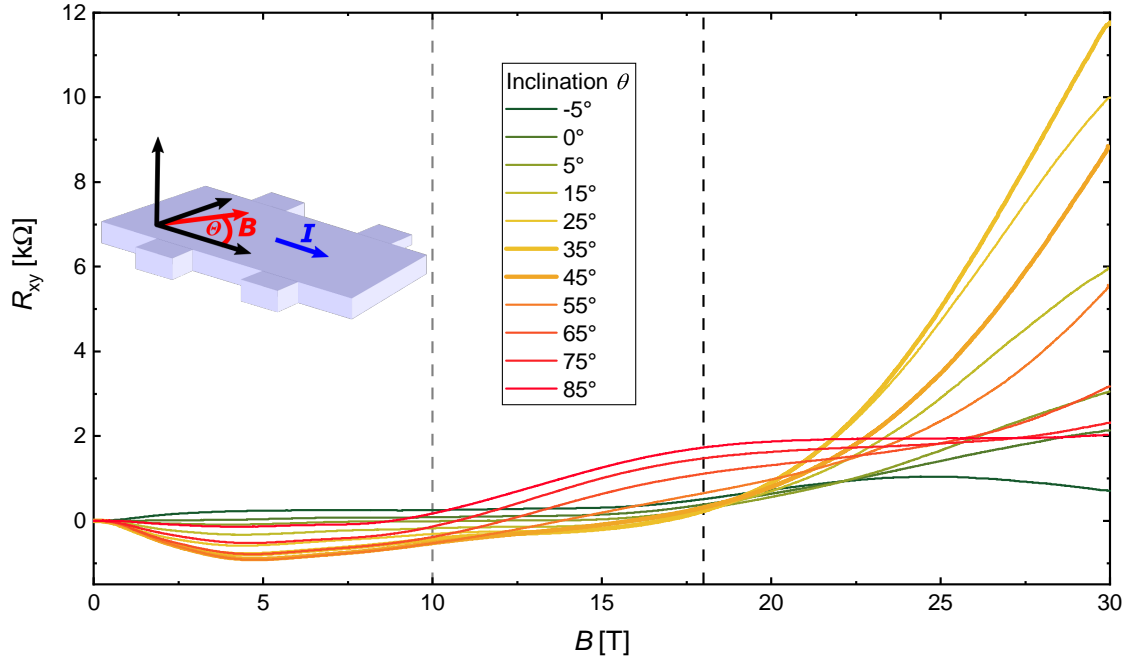
Figure 7.20: The Hall resistance R_{xy} at the charge neutrality point of the compressively strained HgTe layer QC0262 is shown as a function of an in-plane magnetic field B applied alongside various angles θ at the temperature $T = 0.3\,$K. The angle θ of the magnetic field B with respect to the current I is sketched in the schematic inset. The vertical dashed grey and black lines mark $B = 10\,$T and $B = 18\,$T, respectively. The data has been measured in the high field magnet laboratory in Nijmegen.

show a change in the transport behavior up to $B \sim 18\,$T. The here investigated low carrier density regime at the charge neutrality point is susceptible to artifacts due to classical Hall effect-like contributions. These classical Hall effect-like contributions to the Hall resistance R_{xy} are caused by a misalignment of the magnetic field with respect to the sample plane and can not easily be excluded. This transition regime is thus not investigated.

The high magnetic field regime $B > 18\,$T (right to the dashed black line) shows a strong increase with the magnetic field B of the longitudinal resistance $R_{xx}(B)$ and the Hall resistance $R_{xy}(B)$, as shown in Fig. 7.17 and 7.20, respectively. The Hall resistance $R_{xy}(\theta = 35°)$ (thick yellow line) is for magnetic fields $B < 18\,$T close to the most negative observed Hall resistance values $R_{xy}(\theta = 45°)$, but increase for high magnetic fields $B > 18\,$T quickly from negative to the maximal positive Hall resistance values. The Hall resistance $R_{xy}(\theta \sim 35°)$ increase for high magnetic fields $B > 18\,$T much stronger with the magnetic field than any magnetic field dependence of the Hall resistance observed for moderate magnetic fields $B < 18\,$T. Similar behavior is observed for the longitudinal resistance $R_{xx}(B)$ shown in Fig. 7.17. The maximum of the longitudinal resistance R_{xx} is for high magnetic fields $B > 18\,$T observed for the angle $\theta = 45°$ instead of the angle $\theta = 85°$ for moderate magnetic fields $B < 18\,$T. This observed strong positive MR contradicts the theoretically expected linear negative MR for high magnetic fields in Weyl and Dirac semi-metals [148]. To summarize, the in-plane magnetic field-dependent longitudinal and Hall resistance data seems to indicate the existence of two transport regimes. The moderate magnetic field regime for $B < 18\,$T, which is dominated by the chiral anomaly driven negative MR and PHE, and the high magnetic field regime for $B > 18\,$T with a strong positive magnetoresistance with so far unknown origin.

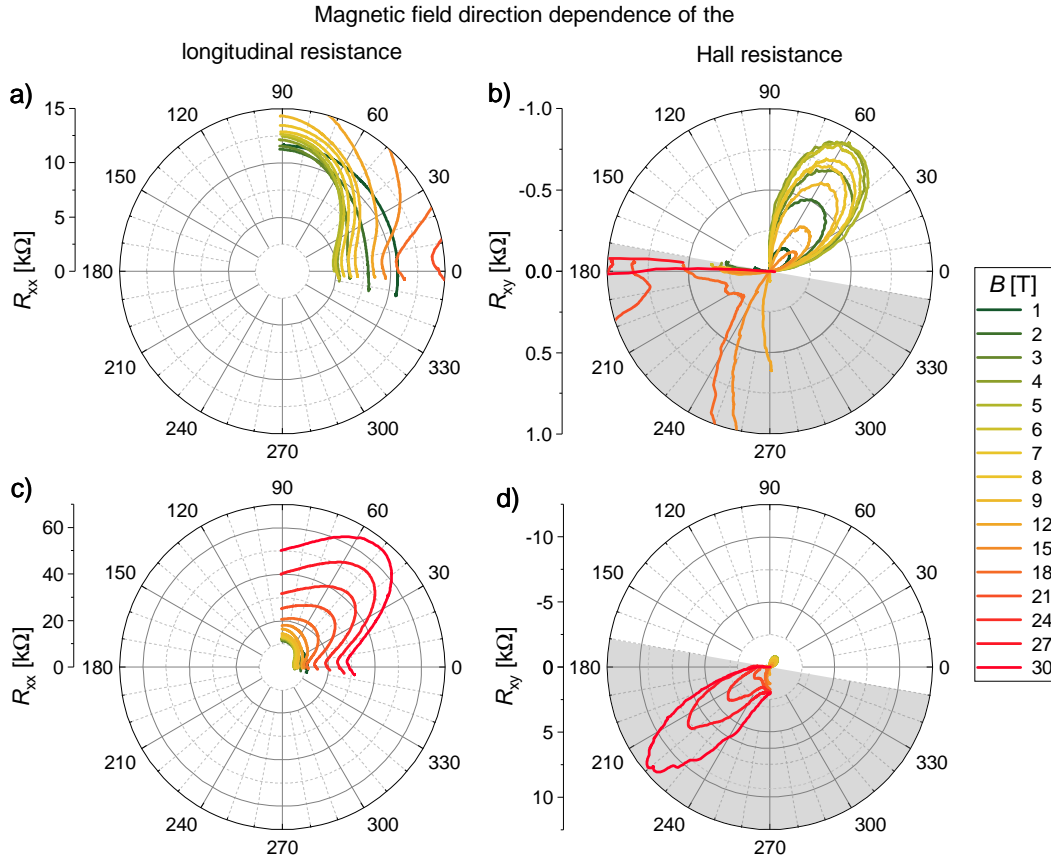### 7.5.3. POTENTIAL METAL-INSULATOR TRANSITION IN HIGH MAGNETIC FIELDS

Figure 7.21: The longitudinal resistance R_{xx} and Hall resistance R_{xy} of the compressively strained HgTe layer QC0262 are shown as polar plots as a function of the angle of the magnetic field with respect to the current Θ between $-10°$ and $90°$ for various constant magnetic field values B and the charge neutrality point at the temperature $T = 0.3\,\text{K}$. The longitudinal resistance $R_{xx}(\Theta)$ and the Hall resistance $R_{xy}(\Theta)$ are shown up to magnetic fields $B = 12\,\text{T}$ in a) and b) and up to $B = 30\,\text{T}$ in c) and d), respectively. The grey background indicates positive values of the Hall resistance $R_{xy}(\Theta)$ in b) and d). The data has been measured in the high field magnet laboratory in Nijmegen.

The observed strong increase of the longitudinal and Hall resistance for high magnetic fields is addressed in this Section. The angular resolution is improved by measuring the longitudinal and Hall resistance for various constant magnetic fields B as a function of the angle θ. The measurement results are shown as polar plots in Fig. 7.21. The polar plot of the longitudinal resistance R_{xx} in Fig. 7.21a) emphasizes the reduced longitudinal resistance R_{xx} for the angle $\theta \sim 5°$ compared to the maximal resistance for $\theta = 90°$ due to the chiral anomaly. This AMR is accompanied by the negative PHE signal in the Hall resistance R_{xy} with a maximum at the angle $\theta \sim 50°$, as shown in Fig. 7.21b). The PHE signal increases with the magnetic field up to a maximum for $B = 5\,\text{T}$, before it decreases with higher magnetic fields again until it changes sign and becomes positive. So far this resembles only an alternative illustration of the decently understood chiral anomaly-driven moderate magnetic field regime. The representation of the data as polar plot in Fig. 7.21c) is chosen to emphasize the shift of the maximum of the longitudinal resistance $R_{xx}(\theta)$ for magnetic fields $B > 12\,\text{T}$ from the angle $\theta = 90°$ towards $\theta \sim 50°$, where it stays for high magnetic fields $B \geq 18\,\text{T}$. A similar shift is observed for the Hall resistance R_{xy} in Fig. 7.21b) and d). There

a maximal negative Hall resistance signal is observed around the angle $\theta \sim 50°$ for magnetic fields $B \leq 12\,\mathrm{T}$, which transforms via a complicated intermediate regime into a positive maximum around $\theta \sim 40°$ for $B > 24\,\mathrm{T}$. In Fig. 7.21d) the positive maximum of the Hall resistance R_{xy} around the angle $\theta \sim 40°$ appears like a negative maximum around $\theta \sim 220°$ due to the chosen radial axis for the polar plot. The angular dependence of the longitudinal resistance appears for the available range of angles to transform from a two-fold symmetry for moderate magnetic fields in a) to a four-fold symmetry for high magnetic fields $B > 18\,\mathrm{T}$ in c).
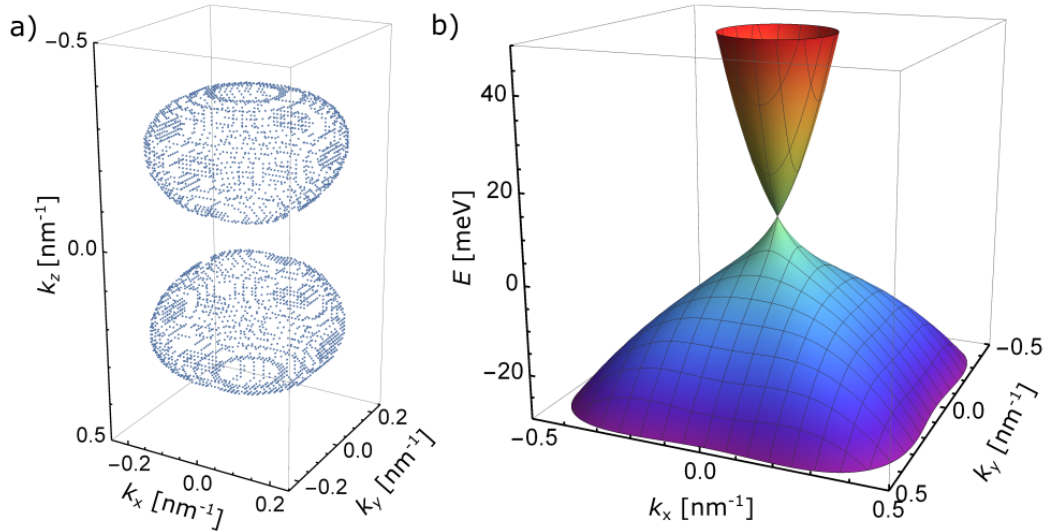

Figure 7.22: In a) a constant energy contour is shown for $E = -5\,\mathrm{meV}$, which equals $14\,\mathrm{meV}$ below the Dirac nodes, in the three-dimensional momentum space for a $\epsilon = 0.3\,\%$ compressively strained HgTe layer, which is calculated with the program "kdotpy" [29]. In b) the energy E dispersion of lowest valence and conduction band is shown with respect to the momenta k_x and k_y for $k_z = 0.12\,\mathrm{nm}^{-1}$, which resembles the position of the Dirac node in k_z.

The significant increase in the longitudinal and Hall resistance with the magnetic field is reminiscent of a magnetic field-driven metal-insulator transition. Such metal-insulator transitions are observed in narrow gap semiconductors, but typically in out-of-plane magnetic fields [149]. For two-dimensional holes in GaAs, a metal-insulator transition is also observed with in-plane magnetic fields in Ref. [150]. There the necessary magnetic field strength for the metal-insulator transition varies with the crystal direction along which the magnetic field is applied. A similar angular dependence is observed for the strength of the increase of the longitudinal resistance with magnetic field in Fig. 7.17 and the Hall resistance in Fig. 7.20 as well as summarized as polar plots in Fig. 7.21. To check the possibility of a metal-insulator transition as the underlying mechanism, the symmetry of the band structure of HgTe is examined. The bulk band structure of $\epsilon = 0.3\,\%$ compressively strained HgTe is shown in Fig. 7.22, as calculated using the program "kdoptpy" [29]. The equal energy contour for $E = -5\,\mathrm{meV}$, which equals $14\,\mathrm{meV}$ below the Dirac nodes, is shown in Fig. 7.22a). This energy contour resembles exemplarily the hole-transport regime and not the low-density regime directly at the Dirac nodes. It nevertheless emphasizes the quadratic distortion of the bandstructure due to the four-fold symmetry of the lattice. It also shows that the extremal contour in the $k_x - k_y$-plane lies close to the middle of the Fermi surfaces, which are positioned around position of the Dirac nodes at $k_z = \pm 0.12\,\mathrm{nm}^{-1}$. The investi-

gated magneto-transport relevant extremal energy dispersion of the $k_x - k_y$-plane is centered around $k_z = \pm 0.12 \, \text{nm}^{-1}$, which is shown in Fig. 7.22b). The quadratic distortion of the dispersion is already a few meV away from the Dirac node visible, which also makes the effective mass depending on the k-direction. The measured Hall-bar is aligned along the $\langle 110 \rangle$-direction. For the angle $\theta = 0°$, the magnetic field is aligned with the largest extension of the Fermi area along k and the highest effective mass. For $\theta = 45°$, the magnetic field points towards the smallest elongation of the Fermi area along k and lowest effective mass. The strongest increase of the longitudinal and Hall resistance with the magnetic field is observed according to Fig. 7.21c) and d) around the angle $\theta_{\text{max,R}_{xx}} \sim 50°$ and $\theta_{\text{max,R}_{xy}} \sim 40°$ and thus along the $\langle 100 \rangle$ direction. If a metal-insulator transition is responsible for the observed increase in the longitudinal and Hall resistance for high magnetic fields, then the smallest extension of the Fermi area in k or the lowest effective mass would cause the earliest onset of the metal-insulator transition in the magnetic field. A magnetic field-driven metal-insulator transition seems a reasonable mechanism for the observed strong MR and its angular dependence for high magnetic fields.

7.5.4. Oscillations in the in-plane magnetoresistance

Figure 7.23: The longitudinal resistance normalized to the resistance at zero magnetic field $R_{xx}/R_{xx}(B = 0 \, \text{T})$ is shown for the 90 nm thick tensilely strained HgTe layer Q2761 as function of the magnetic field B applied along the current direction for different gate voltages $U_{\text{gate}} > -0.8 \, \text{V}$ in a) and $U_{\text{gate}} < -0.8 \, \text{V}$, in b) for the temperature $T \sim 2 \, \text{K}$. This resembles a different presentation of the longitudinal resistance R_{xx} data already shown in Fig. 7.16b). The gate voltage $U_{\text{gate}} > -0.8 \, \text{V}$ depicts the charge neutrality point as indicated by the vertical grey dashed line in Fig. 7.16a).

The magnetoresistance data, for example depicted in Fig. 7.23, shows oscillation-like extrema. These extrema are already mentioned in Sec. 7.4.4 and shown in Fig. 7.12. The extrema are in our group referred to as "in-plane oscillations" and are not specific to the Dirac semi-metal phase. The 3D-TI tensilely strained HgTe also shows these extrema, as shown in Fig. 7.16b) and investigated in Ref. [95, 151]. The presumably simpler 3D-TI phase is thus used in this Section to discuss these extrema and their potential physical origins. An overview of the longitudinal resistance R_{xx} as a function of a magnetic field B applied along

the direction of the current of tensilely strained HgTe is already given in Fig. 7.16b). The overall trend of the MR as a function of the magnetic field is discussed in Sec. 7.4.8. The focus lies there on the absence of a negative MR around the charge neutrality point. To enhance the visibility of the oscillations the same data is presented again in Fig. 7.24a) and b) as longitudinal resistance normalized to the zero magnetic field resistance for the electron and hole regime, respectively. The MR for the gate voltage $U_{gate} = 3\,V$ (green) representing high electron densities only shows one weak local extrema. The only distinct feature is a maximum around $B \sim 4\,T$. The maximum moves with decreasing gate voltage U_{gate} towards lower magnetic fields B until it can not be identified anymore for $U_{gate} = 0.5\,V$. For $U_{gate} = 0.5\,V$ a minimum starts to form at $B \sim 13\,T$ instead. This minimum becomes more pronounced for low electron densities ($U_{gate} \leq 0\,V$) and shifts to $B \sim 12\,T$. The hole regime is summarized in Fig. 7.23b) and shows the same pronounced minimum at $B \sim 12\,T$ (dashed grey vertical line) for all investigated negative gate voltages. This minimum is accompanied by a maximum at $B \sim 9\,T$. A second maximum exist for lower $B < 4\,T$ which shifts with more negative U_{gate} and thus increasing hole density towards lower B until it vanishes for $U_{gate} < -4\,V$.
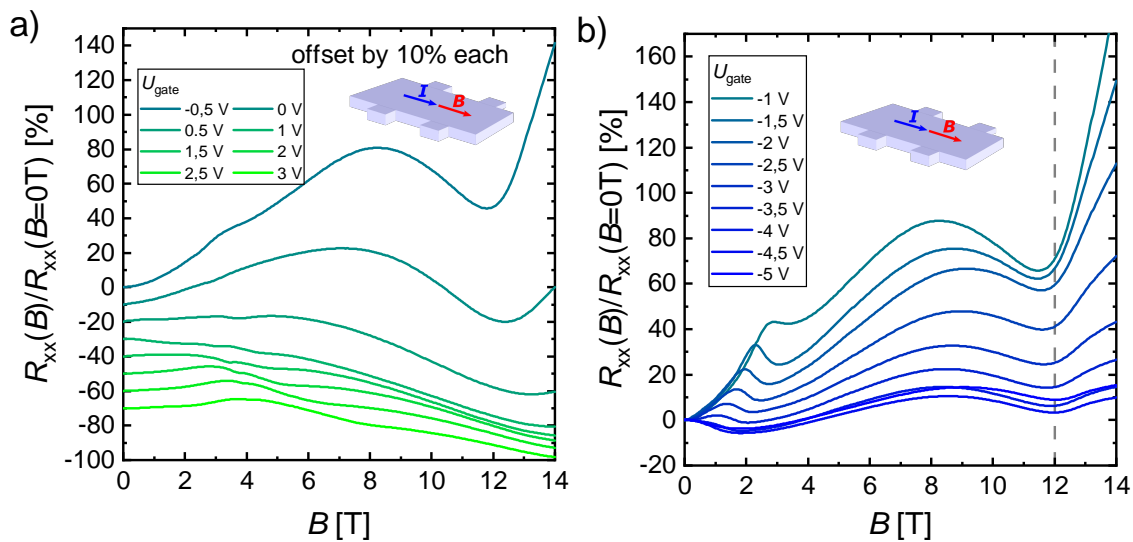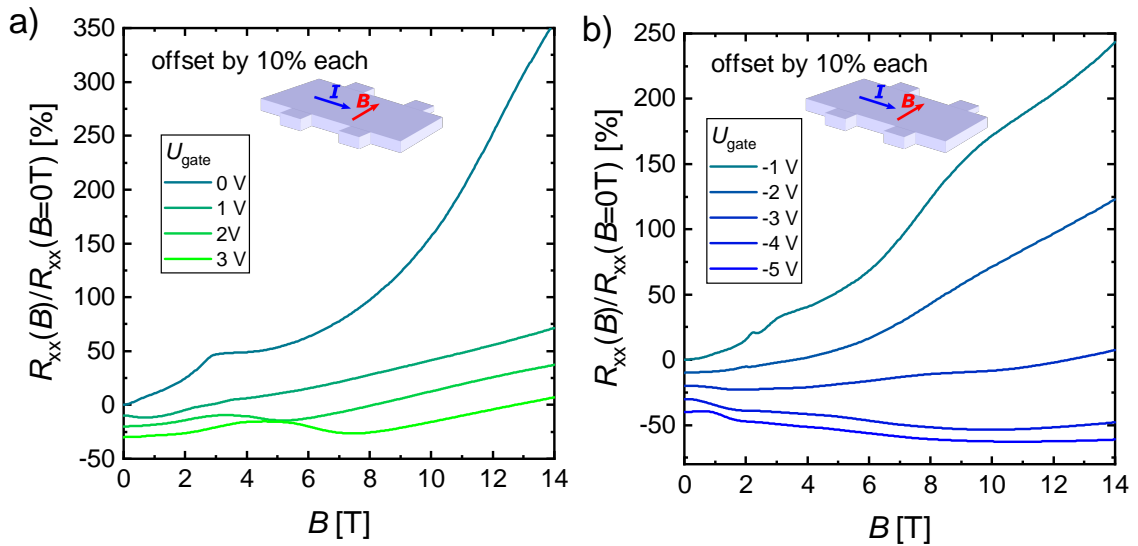

Figure 7.24: The longitudinal resistance normalized to the resistance at zero magnetic field $R_{xx}/R_{xx}(B = 0\,T)$ is shown for the 90 nm thick tensilely strained HgTe layer Q2761 as function of the magnetic field B applied inside the sample plane perpendicular to the current direction for different gate voltages $U_{gate} \geq 0\,V$ in a) and $U_{gate} < 0\,V$, in b) for the temperature $T \sim 2\,K$.

The angular dependence of these extrema is investigated by reproducing the measurement with the magnetic field applied perpendicular to the direction of the current, but still in the sample plane, shown in Fig. 7.24. The MR is positive for the electron regime, very strong for the low-density regime, and negative for the hole regime. The additional extrema observed in the high electron densities for $U_{gate} \geq 2$ and shown in Fig. 7.24a) are similar in shape and amplitude to the ones seen in the measurements with a parallel magnetic field. The hole regime is shown in Fig. 7.24b). It only shows weak features and lacks the pronounced extrema and their clear gate voltage dependence as observed for the parallel magnetic field case. There are still non-monotonicities visible, but much smaller in amplitude.
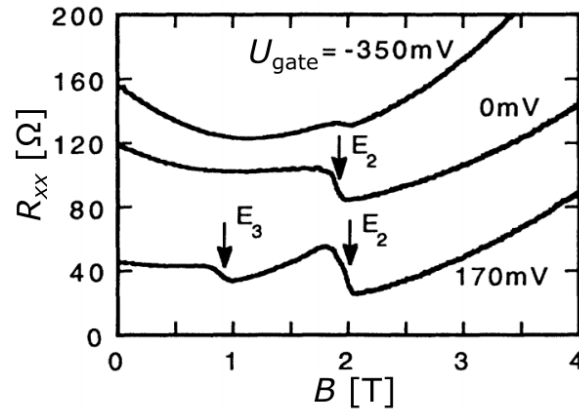
Figure 7.25: The longitudinal resistance R_{xx} of a remotely doped wide parabolic AlGaAs quantum well as a function of a magnetic field B applied in the direction of the current is shown for different gate voltages U_{gate}. The sharp oscillations are labeled with arrows and the corresponding subband labels E_2 and E_3. The middle curve ($U_{gate} = 0$ mV) is offset by $60\,\Omega$ for clarity. Reprinted from J. Jo *et al.*, Probing the subband structure of a wide electron system in a parabolic quantum well via capacitance-voltage measurements, PRB **47**, 4056 (1993) [152]. Copyright 1993 by The American Physical Society.

Different potential, but not satisfying ideas to explain these oscillations-like features exist. Only considering the n-regime of the B in-plane perpendicular to the current case, the oscillation-like features are reminiscent of the cyclotron resonances with the finite size of the device, which are called Weiss oscillations [153]. Since the same features are also observed in the parallel magnetic field case, cyclotron orbits can not be the origin. To form cyclotron orbits, the charge carriers need to be deflected by the Lorentz force of a magnetic field perpendicular to the current. For thin 3D-TI a change in the tunneling probability between the TSS with the strength of an in-plane magnetic field is predicted [154]. The magnetic field shifts the Dirac cones of the top and bottom TSS in opposite directions in k-space. The shift leads to a maximum in the tunnel coupling for exactly touching Dirac cones due to the matched spin and momentum direction of the top and bottom TSS. Since this tunneling process only causes one extremum, it can also not be the origin of all the observed extrema.

To find other possible mechanism measurements of other material systems showing similar signatures are reviewed. The magnetoresistance of a two-dimensional hole-gas in a remotely doped wide parabolic AlGaAs quantum well shows similar oscillation-like extrema for a magnetic field applied along the direction of the current in Ref. [152], as shown in Fig. 7.25. The observed minima of the longitudinal resistance R_{xx} are explained by the magnetic field-induced depopulation of hole subbands. Even though no subbands are involved in the transport in HgTe, the VPS, introduced in Sec. 4.4, are similar. Magnetic field dependence of these VPS would cause a similar redistribution of charge carriers in an in-plane magnetic field and thus extrema in the magnetoresistance. Calculations to determine the magnetic field dependence of the VPSs to verify this hunch are still pending.

7.6. Bulk properties of inversion induced Dirac semi-metals

One achievement of this work is the verification of compressively strained HgTe as Dirac semi-metal. The procedure has been as follows: As a starting point, the in the literature established inversion induced Dirac semi-metals Cd_3As_2 and Na_3Bi have been introduced. In the literature, two transport features are identified with Dirac semi-metals. These are the strong linear positive MR in an out-of-plane magnetic field and the negative MR for a magnetic field aligned with the current. The chiral anomaly driven negative MR is identified as the more reliable signature. Nevertheless, strong positive and negative MR are also reported for non-topological materials without linear band structure. The tunability of compressively strained HgTe has been used to find the physical origin of the magnetoresistance and to pinpoint the chiral anomaly as the driving mechanism. The nobs are the strain engineering of the band structure, and the low intrinsic doping, and thus gateablility. These nobs have been used to trace the negative MR to the chiral anomaly. The negative MR is only observed for samples, which have a linear bulk band crossing and for which the Fermi energy is located close to the Dirac nodes. The magnetic field strength and angle dependence also fit the expectations for the chiral anomaly. Interestingly, the strength of negative MR does not scale with the splitting of the Dirac nodes in k-space. Even unstrained HgTe layers show a negative MR. The splitting of the quadratic band touching point due to the Zeeman effect into linear crossing points is identified as the underlying mechanism. A scattering-driven mechanism has been excluded based on a series of samples with different mobilities and consequently different impurity densities. The strength of the negative MR signal reduces with increasing impurity density. This observation excludes a scattering-driven mechanism. It confirms that an intrinsic band structure effect is likely the driving mechanism. The chiral anomaly as the driving mechanism is consistent with the negative MR signal only depending on the magnetic field contribution parallel to the current.

Additionally, an accompanying planar Hall effect, and a strong positive MR for high magnetic fields, has been observed. These two effects possess a different angular dependence than the negative MR signal, which is consistent with the cubic symmetry of the HgTe crystal. For low magnetic fields, a positive MR has been measured and is due to its temperature dependence identified as WAL. The WAL shows an atypical magnetic field dependence, consistently with the observations in the Weyl semi-metal TaAs. Such a strong WAL in a three-dimensional material is peculiar and notable. In the moderate magnetic field regime, oscillation-like extrema have been observed. These features exist in the Dirac semi-metal as well as in the 3D-TI phase. Their origin is still unclear but could be related to the magnetic field dependence of the VPS, which exist in both phases.

The measurements which establish compressively strained HgTe as Dirac semi-metal brought up quite a few interesting questions: Most of which arise around angular dependencies. A profound analysis of these would be ambitious in this work due to the shortcomings of the used rotation mechanism, as the unavoidable and unknown misalignment. It would be interesting to investigate the samples with a three-dimensional vector magnet in a dilution refrigerator. These effects reach from the peculiar strong WAL signal at low magnetic fields via the observed PHE and oscillation-like extrema to the strong positive MR at very high magnetic fields. The assignment of this strong MR for high magnetic fields to a metal-insulator transition could be tested using temperature-dependent measurements. The origin of the AMR and PHE signals could be examined by fabricating and measuring Hall bars on one chip for multiple crystal directions or Corbino disc structures. These mea-

surements could reveal whether these effects depend on the angle of the magnetic field with respect to the current or the crystal axis. Additionally to hosting the chiral anomaly, the quadratic semi-metal unstrained HgTe is predicted to host a magnetic field-induced phase transition. It also depicts the phase with the lower limit for the achievable density in the topological surface states by strain engineering. A low carrier density makes single quantum Hall channels already at low magnetic fields accessible. The single QH channels are beneficial for some superconductor hybrid devices or even metrology. A more in-depth analysis of unstrained HgTe samples would thus be interesting.

7

SURFACE STATES IN INVERSION INDUCED DIRAC SEMI-METALS

Weyl and Dirac semi-metals are not only interesting because of the linear crossing points in their bulk band structure and the consequential anomalous magneto-transport effects. Weyl semi-metals are predicted to host a new type of disjoint surface state, called Fermi-arc. This raises the question, whether these disjoint surface states are also present in Dirac semi-metals. The existence of the name-giving band inversion in inversion induced Dirac semi-metals additionally raises the question, whether the band inversion causes the formation of topological surface states. These questions are addressed in this Chapter with the help of magneto-transport measurements on compressively strained HgTe layers. The measurement results are interpreted with the help of DFT and $k \cdot p$ band structure calculations. The insights won by the magneto-transport investigation of the compressively strained HgTe layers, and the band structure calculations are generalized and compared to reported measurements and models for Cd_3As_2, the most widely studied inversion induced Dirac semi-metal, to find one coherent description.

8.1. OUT OF PLANE MAGNETO-TRANSPORT MEASUREMENTS

To search for potential surface states, a three-dimensional slab of compressively strained HgTe of thickness $d = 66\,nm$ is investigated for signs of two-dimensional transport features, namely the QHE. The observation of two-dimensional transport features requires the existence of two-dimensional states, which due to the three-dimensional extension of the slab can not be due to its bulk and thus indicates the existence of surface states. The same procedure is extensively used to investigate the surface states of the 3D-TI tensilely strained HgTe in Chapter II. The tool of choice are magneto-transport experiments with an out-of-plane applied magnetic field. Exemplary measurements of the longitudinal and Hall resistance are shown in Fig. 8.1. The electron-regime, in Fig. 8.1a), shows well pronounced QH plateaus in the Hall resistance R_{xy} (red) and SdH oscillations in the longitudinal resistance R_{xx} (black). The peaks of the SdH oscillations in the longitudinal resistance R_{xx} coincide with the position of the QH plateau transitions in the Hall resistance R_{xy}. The values of the QH-plateaus match the theoretical expected values of $R_{\text{theo},xy} = \frac{1}{j}\frac{h}{e^2}$, where j is the integer QH index. The agreement is better than the accuracy of 1 % of the used "SR124" and "SR810" Lock-In amplifiers from Stanford Research Systems [155]. The QH-
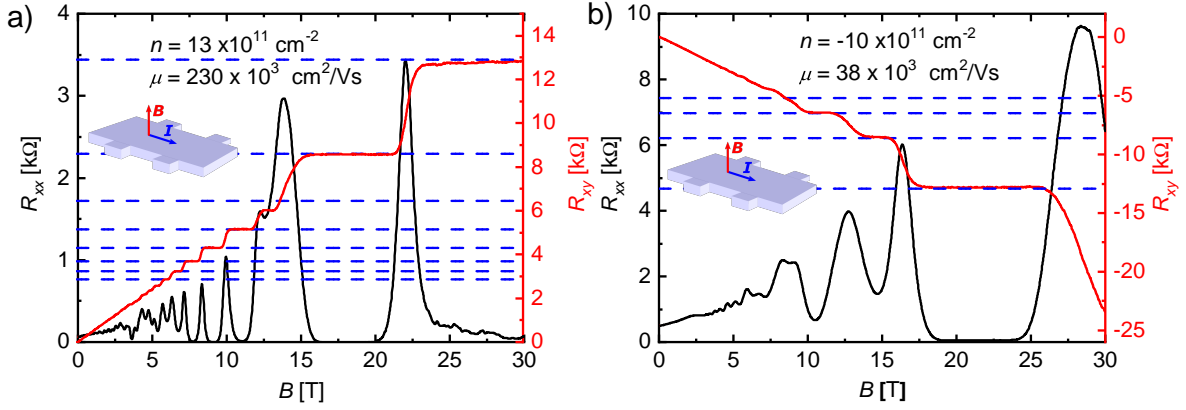
Figure 8.1: The longitudinal resistance R_{xx} (black) and Hall resistance R_{xy} (red) are shown as function of the out of plane magnetic field B at the temperature $T = 0.3\,\text{K}$ for a gate voltage $U_{\text{gate}} = 4\,\text{V}$, which corresponds to an electron density of $n = 13 \times 10^{11}\,\text{cm}^{-2}$ in a), and $U_{\text{gate}} = -4\,\text{V}$, which corresponds to a hole density of $n = -10 \times 10^{11}\,\text{cm}^{-2}$ in b). The indicated charge carrier density n and mobility μ are extracted from the semi-classical low magnetic field regime. The measurements were performed in the high field magnet laboratory of the Radboud University in Nijmegen.

plateaus in the Hall resistance R_{xy} are accompanied by zeros in the longitudinal resistance R_{xx} for magnetic fields $B > 7\,\text{T}$. Except for very high magnetic fields $B > 22\,\text{T}$, where the longitudinal resistance $R_{xx}(B > 22\,\text{T})$ shows finite and fluctuating values. These fluctuations are most likely an artifact due to a magnetic freeze-out of the contacts, which is discussed in Ref. [58]. The qualitatively same behavior is observed for the hole-regime shown in Fig. 8.1b). Quantum Hall plateaus are observed in the Hall resistance R_{xy}, which quantize to the literature value and are accompanied by a zero in the longitudinal resistance R_{xx} for high magnetic fields. The main difference is the negative sign of the Hall resistance R_{xy}, which indicates the hole character of the transport regime. Additionally, the SdH oscillations and the QH-plateau transitions are broader compared to the electron-regime. The broadening is consistent with the about five times lower mobility, which is determined from the semi-classical low magnetic field regime and indicated in Fig. 8.1.

The observed QHE and SdH oscillations are reminiscent of the magneto-transport of the 3D-TI tensilely strained HgTe shown in Fig. 2.8 and 3.3 and described in Chapter 3 and Sec. 2.3.3. The three-dimensional extension of the HgTe layer together with the observation of QHE, which is a purely two-dimensional phenomenon, infers the existence of surface states. The same argument can be made for the Dirac semi-metal compressively strained HgTe. The exact quantization of QH-plateau values to the theoretical values and the zeros in the longitudinal resistance R_{xx} indicate a purely two-dimensional transport for magnetic fields $B > 7\,\text{T}$. Electron and hole type surface states are thus expected to exist. To investigate the properties of these surface states further the same approach, as for 3D-TI HgTe layers presented in Sec. 3.3.2, is taken. The LL dispersion in the magnetic field is investigated over the full available gate voltage range and shown in Fig. 8.2. The derivative of the Hall conductance with respect to the gate voltage $\partial\sigma_{xy}/\partial U_{\text{gate}}$ is therefore shown as a color plot as a function of the magnetic field and the gate voltage. High values of $\partial\sigma_{xy}/\partial U_{\text{gate}}$ indicate the transition between QH-plateaus and thus the position of LLs. Zeros in $\partial\sigma_{xy}/\partial U_{\text{gate}}$ indicate the position of QH-plateaus and their respective QH-indices are indicated as white numbers based on the value of the Hall conductivity $\sigma_{xy}(U_{\text{gate}}, B)$.

The LL show a surprisingly regular pattern, especially compared to the LL dispersion of the tensilely strained HgTe layers shown in Fig. 3.9. The LL dispersion of the 3D-TI phase shows multiple intersecting sets of LL as emphasized in Fig. 3.11a). The LL dispersion of the compressively strained Dirac semi-metal phase of HgTe shown in Fig. 8.2 in contrast consists of two separate sets of LL. An electron-like set for $U_{gate} > 0.5\,V$ and a hole-like set for $U_{gate} < 0.5\,V$. The character of the LLs is given by their slope. Electron-like LL possess a positive slope and hole-like LL a negative slope. The hole-like LLs do not cross and show a periodic pattern of alternating smaller and bigger spacing. Such a pattern is expected for a regular spin degenerate 2DEG, where the splitting of the LL is caused in an alternating fashion by the orbital and Zeeman effect of the magnetic field. This hole regime is separated from the electron regime via a zero plateau in σ_{xy} at $U_{gate} \sim 0.5\,V$. The electron LL are well resolved and show a regular and equidistantly spaced pattern. The only exception is the QH-plateau with QH-index $j = 4$. For the QH-index $j = 4$ a LL crosses through. Additional crossings at high positive gate voltages and low magnetic fields can neither be directly observed nor excluded due to the limited resolution and broadening of the LL. The discussion and reconstruction of the details in the LL dispersion is postponed to Sec. 8.2.4. The main result is the observation of LL and thus two-dimensional transport over the full available gate voltage range. Potential origins of the observed two-dimensional transport are the Fermi-arcs predicted for Weyl semi-metals and topological surface states due to the inherent band inversion.
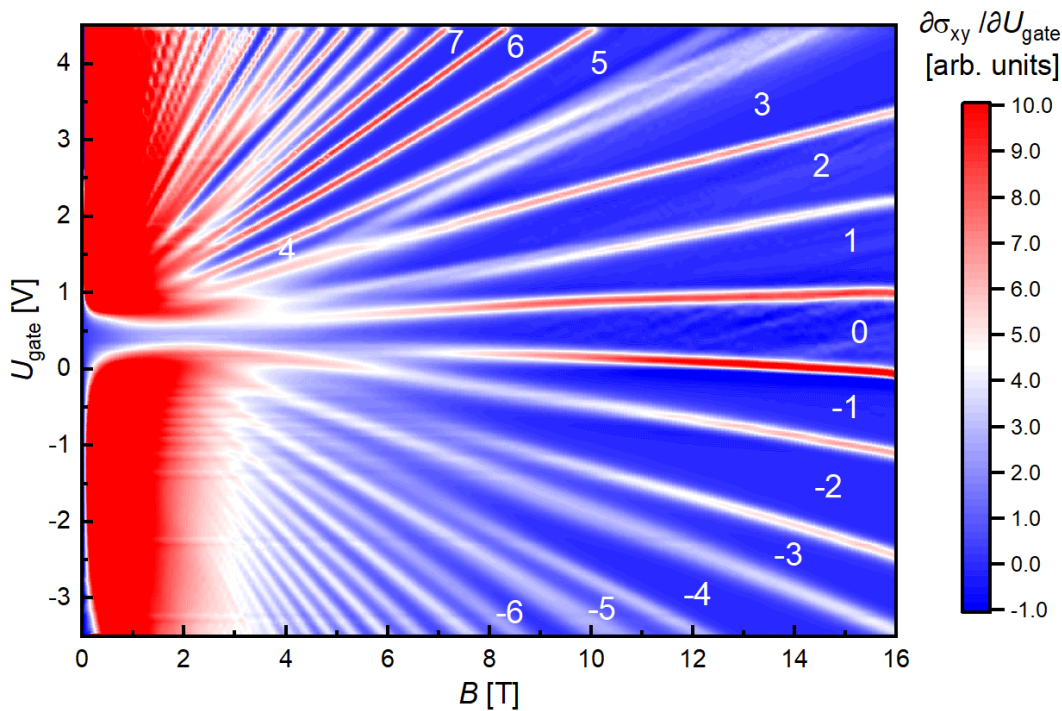

Figure 8.2: The derivative of the Hall conductivity σ_{xy} with respect to the gate voltage U_{gate} is shown as a function of the gate voltage U_{gate} and the out of plane magnetic field B at the temperature $T = 0.05\,K$. The white labels indicate the QH-plateau index determined by the values of the Hall conductivity $\sigma_{xy}(U_{gate}, B)$.

8.2. ORIGIN OF THE SURFACE STATES

This Section investigates the origin of the observed two-dimensional transport in the Dirac semi-metal compressively strained HgTe. The different potential surface states of the Dirac semi-metal compressively strained HgTe are introduced. The missing inversion symmetry of the zinc blende crystal makes compressively strained HgTe actually a Weyl semi-metal, even though this symmetry breaking is small. Because of this, Fermi-arcs are expected to exist. Their relevance for the observed magneto-transport is discussed. Topological surface states are expected due to the inherent band inversion of HgTe. The possibility of the formation of VPS due to the similarity to the three-dimensional insulator phase of tensilely strained HgTe is examined. Finally, observed LL dispersion is reproduced using a toy model accounting for the TSS and massive VPS.

8.2.1. FERMI-ARCS

The broad interest in Weyl semi-metals is fueled by their disjoint surface states predicted in Ref. [12] and named Fermi-arcs. The simplest possible model which hosts such Fermi-arcs represents the material class of magnetic Weyl semi-metals. A magnetic Weyl semi-metal consists of linearly dispersing bands with at least two non-degenerate linear crossing points. An overview over topological semi-metal is given in Sec. 7.1. The Brillouin zone of such a magnetic Weyl semi-metal is shown in Fig. 8.3a). The position of the linear crossing points called Weyl nodes are highlighted as red balls. The chirality of the Weyl nodes is indicated by the plus and minus signs. The projection of the bulk Weyl nodes onto the surface Brillouin zone (grey area) is shown as red circles. The projected Weyl nodes of opposite chirality are connected via the so-called Fermi-arc indicated in yellow in Fig. 8.3a). The name Fermi-arc stems from their open arc-like contour. The shown upper surface only hosts one Fermi-arc connecting the projected Weyl nodes from positive to negative chirality, while the opposite connection is located at the bottom surface. Accounting for both surfaces the Fermi-arcs form together again a closed Fermi contour which is connected via the bulk Weyl nodes. The Fermi-arcs are similar to the TSS of a 3D-TI. The two TSS located on opposite surfaces also possess different chirality [11]. In Weyl semi-metals the Fermi-arc are thus also protected by the separation of the Weyl nodes in k-space. The degenerate Dirac nodes in Dirac semi-metals are effectively multiple Weyl nodes on top of each other, which impedes the protection of the Fermi-arcs. Even though Fermi-arcs do thus not necessarily have to exist in Dirac semi-metals, in principle there is nothing preventing their formation. The magnetic field used to probe the properties of these semi-metals anyways lifts the degeneracy of the Dirac nodes due to the Zeeman effect. Dirac semi-metals in a magnetic field are thus effectively Weyl semi-metals. The Zeeman provides the splitting of the Weyl nodes relevant for the formation of Fermi-arcs.

With this general introduction of Fermi-arcs, the attention is shifted to the Weyl nodes in compressively strained HgTe and its Fermi-arcs. The bulk Brillouin zone of compressively strained HgTe is shown in Fig. 8.3b) together with the surface Brillouin zone of the (001) surface on top and the (010) surface on the right. The broken inversion symmetry of the zinc blende crystal splits the Dirac nodes at $k_z = \pm k_{z,0}$, as shown in Fig. 7.6c) and Fig. 2.2c), into four Weyl nodes each inside the k_x, k_y plane. The positions of the Weyl nodes in the Brillouin zone are marked as balls. The balls are colored according to their chirality in red (positive) and blue (negative). The experimentally investigated surface is the (001) surface, which is shown on the top in Fig. 8.3b). The projection process is graphically rep-

resented in Fig. 8.3b) by the red plane sketched in the bulk Brillouin zone which reduces to the red line in the (001) surface Brillouin zone. For the (001) surface one of the Weyl nodes around $k_z = -k_{z,0}$ is projected on top of the equivalent Weyl node around $k_z = +k_{z,0}$. This yields in total four projected Weyl nodes in the (001) surface Brillouin zone as indicated by the colored dots. The chiralities of the surface Weyl nodes are the sum of the projected bulk Weyl node chiralities. The red and blue dots thus possess the chirality $+2$ and -2, respectively. This yields a total of eight chiral charges, which corresponds to four expected Fermi-arcs for the top (001) and bottom (00$\bar{1}$). The resulting Fermi-arcs of the (001) surface are determined with DFT calculations in Ref. [156] and shown in Fig. 8.3c). The four Fermi-arcs look together like a slightly deformed Fermi annulus.

The contribution of the Fermi-arcs to the observed magneto-transport in Sec. 8.1 is estimated by calculating their size in k-space. The Fermi-arcs are approximately annuli and their diameter depends on the position of the Fermi energy with respect to the Weyl nodes. As an upper boundary, the full area of a circle is estimated instead. For the radius $k = 0.1\,\text{nm}$ extracted from Fig. 8.3c) and using the equation for the DOS in k-space for a non-degenerate 2DEG

$$n = \frac{1}{4\pi} k^2 \tag{8.1}$$

this yields the density $n_{\text{Fermi arc}} \sim 0.8 \times 10^{11}\,\text{cm}^{-2}$. This density is small compared to the maximal accessed density of $n_{\text{max}} \sim 13 \times 10^{11}\,\text{cm}^{-2}$. The assumed strain of 1 % for the DFT calculations is a factor of three larger than the experimental strain of 0.3 % strain. Density functional theory calculations with a strain of 0.3 % of Ref. [34] yield a much smaller splitting of the Weyl nodes of $\Delta k \sim 0.02\,\text{nm}$, as shown in Fig. 8.3d). This size in k-space corresponds to a density of $n_{\text{Fermi arcs}} \sim 0.03 \times 10^{11}\,\text{cm}^{-2}$, which is neglectable for magneto-transport experiments. This neglectable small density excludes the Fermi-arcs as the surface states carrying the observed magneto-transport of Sec. 8.1. These DFT calculations depicted in Fig. 8.3d) show additional surface localized states which disperse along the valence band edge. The origin of these surface states and their relevance for the magneto-transport are the topic of the next Section.
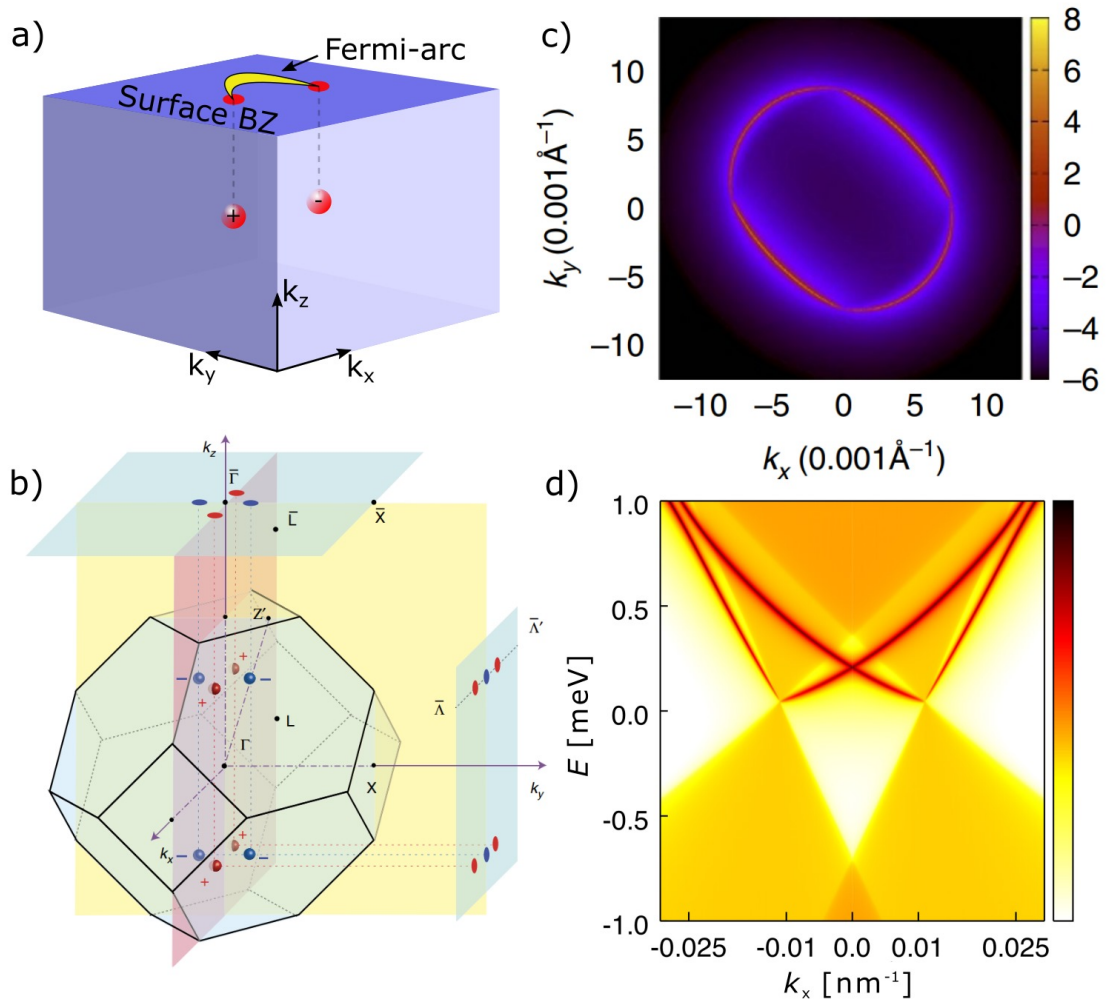
Figure 8.3: In a) two Weyl nodes with different chirality, indicated by the plus and minus sign, are shown as two red balls in the bulk Brillouin zone (BZ). The resulting disjoint surface state, called Fermi-arc is sketched in yellow in the surface Brillouin zone which connects the projected Weyl nodes (red circles). In b) a schematic of the bulk Brillouin zone of HgTe is shown. The positions of its eight Weyl nodes are indicated as circles. These circles are according to their chirality red or blue. The surface Brillouin zone of the (001) surface, investigated experimentally in this work, and the corresponding projections of the Weyl nodes are shown on top and equivalently for the (010) surface on the right. In c) the surface Fermi-arcs are shown in the (001) surface for a HgTe layer with 1% compressive strain determined with DFT calculations. In d) the band structure of a 0.3% compressively strained semi-infinite HgTe layer calculated with DFT is shown. The color code represents the spectral function. Dark red colors indicate the surface character, while lighter colors show the bulk states. b) and c) are reprinted from J. Ruan *et al.*, Symmetry-protected ideal Weyl semimetal in HgTe-class materials, Nature Communications **7**, 11136 (2014), Creative Commons Attribution 4.0 International License [156]. d) is reprinted from D. M. Mahler, Interplay of Dirac Nodes and Volkov-Pankratov Surface States in Compressively Strained HgTe, PRX **9**, 031034 (2019), Creative Commons Attribution 4.0 International License [34].

8.2.2. TOPOLOGICAL SURFACE STATES

Figure 8.4: In a) the band structure of 0.3 % compressively strained semi-infinite HgTe layer calculated with DFT is shown as in Fig. 8.3d) only for a bigger momentum range k. The color code represents the spectral function, and dark red colors thus indicate surface character, while lighter colors show the bulk states. The band structure of a 70 nm thick 0.3 % com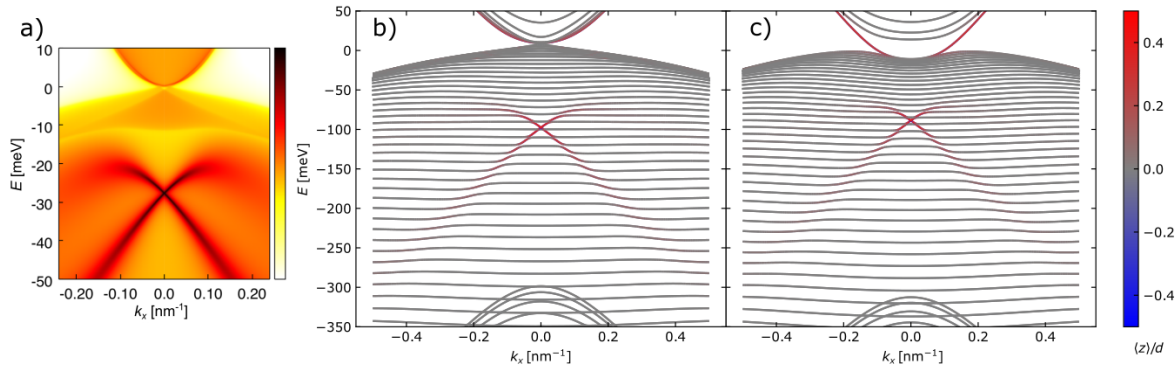pressively and tensilely strained HgTe calculated with the program "kdpotpy" [29] is shown along the k_x direction in b) and c), respectively. The color code indicates the localization of the states along the finite z-direction. a) is taken from D. M. Mahler, Interplay of Dirac Nodes and Volkov-Pankratov Surface States in Compressively Strained HgTe, PRX **9**, 031034 (2019), Creative Commons Attribution 4.0 International License [34].

Since Fermi-arcs are not sufficient to explain the observed two-dimensional magneto-transport, the question arises whether other surface states exist in compressively strained HgTe. The band structure of a semi-infinite slab of ~ 0.3 % compressively strained HgTe determined by DFT calculations is already shown in Fig. 8.3d) and here again in Fig. 8.4a) for a wider momentum and energy range. Additionally to the bulk bands (orange) are two surface states (dark red) visible. The character of the states is identified by the amplitude of their spectral function on the surface. One surface state follows the bulk conduction band edge, while the other is buried in the bulk valence band. The buried surface state disperses linearly for low energies, crosses at $E \sim -27$ meV linearly, and finally hybridizes in an anti-crossing-like fashion with the bulk valence band for $E > -20$ meV. The dispersion of the seemingly two surface states is reminiscent of the TSS in the three-dimensional topological insulator phase of HgTe, as shown in Fig. 2.6.

To simplify the comparison, the band structures of 70 nm thick HgTe layers is shown for -0.3 % compressive and 0.3 % tensile strain in Fig. 8.4b) and c), respectively. The band structures are determined by $k \cdot p$ calculations using the program "kdotpy" [29] with $Cd_{0.7}Hg_{0.3}CdTe$ layers as the boundary conditions. The dispersion of the surface states highlighted in red only differs around $E \sim 0$ meV. For higher energies $E > 0$ meV, the surface state disperses along the bulk conduction band edge for both phases. For lower energies $E < 0$ meV, the surface states hybridize for both phases with the bulk valence band and show a linear crossing inside the bulk valence band at $E \sim -100$ meV. The surface state found by the DFT and $k \cdot p$ calculations for the compressively strained HgTe slab resembles the topological surface state of the 3D-TI tensilely strained HgTe. This accordance suggests the band inversion as the origin for the surface states observed in the compressively strained HgTe Dirac semi-metal phase. Thereby, the different positions obtained for the linear crossing of the TSS with the DFT and $k \cdot p$ calculations are only a consequence of the different surface potentials assumed for the calculations. The position of the Γ_6 bulk band is indeed nearly unaffected by the different strain directions and lies at $E \sim -300$ meV

below the Γ_8 bands for both strain directions in Fig. 8.4b) and c). The order of the bands is inverted to the atomic limit, which classifies compressively strained HgTe as inversion induced Dirac semi-metal (see Chapter 7). The strain only changes the details of the band structure around $E \sim 0\,$meV and not the topology of the system. For high momenta k, the order of the bands is the same for all phases: The $\Gamma_{8,LH}$, $\Gamma_{8,HH}$, and then the Γ_6 bands. Because of this, topological surface states due to the inversion of the Γ_6 band with respect to the $\Gamma_{8,LH}$ band are expected to form in the Dirac semi-metal phase of HgTe exactly as in its 3D-TI phase. The details of its dispersion can of course vary, for example, due to the hybridization of the TSS with the $\Gamma_{8,HH}$ bands. These band inversion-induced surface states in compressively strained HgTe are thus also called topological surface states. An important side note: The existence of the topological surface states also in compressively strained HgTe, for which the valence and conduction band touch, emphasizes that no bulk bandgap is necessary for the formation of topological surface states.

8.2.3. Volkov Pankratov states

With the existence of TSS also in the Dirac semi-metal phase of HgTe established, the focus is now shifted onto the modeling of the experimentally observed Landau level dispersion. The TSS in Dirac semi-metal phase follows the edge of the bulk conduction band as shown in Fig. 8.4a) and b). The TSS disperses thus like the TSS in the 3D-TI phase, as shown in Fig. 8.4c) for comparison. For positive gate voltages U_{gate} and thus electron densities, the TSS of the Dirac semi-metal phase of HgTe should consequently behave similar to the TSS of the 3D-TI phase of HgTe. To verify this, the influence of the top gate voltage is investigated using $k \cdot p$ calculations for a 66nm thick $\epsilon = 0.3\,\%$ compressively strained HgTe layer based on the six-band Kane Hamiltonian (see Sec. 4.2) in Ref. [34]. The calculations use Hard-wall boundary conditions and include the bulk inversion symmetry breaking term. Appropriate toy Hartree potentials are included to account for the applied top gate voltage. The resulting band structure is shown in Fig. 8.5a) together with the shape of the applied Hartree potential $V_{Hartree}$ [1] in black in Fig. 8.5b). The TSS are separated from the conduction sub-bands and are preferentially occupied in the same fashion as for the 3D-TI case shown in Fig. 4.6b). The degeneracy of TSS (blue) is lifted by the Hartree potential. The observed electron-type two-dimensional transport is thus assigned to the topological surface states.

This raises the question of whether the hole-type transport is also carried by the TSS. To answer this question a short detour via the 3D-TI phase is taken. The motivation of the TSS also being responsible for the hole-type transport comes from the Dirac screening model described in Sec. 2.3.4. In Ref. [49] two dimensional electron and hole transport is observed in 3D-TI tensile strained HgTe samples. To explain the observed hole transport it is proposed that the Dirac node of the TSS can be pulled into the bulk bandgap for sufficiently strong gate voltages. The hole-side of the TSS would thus be accessible. In the 3D-TI phase, the $\Gamma_{8,LH}$ band lies above the $\Gamma_{8,HH}$ band, which is followed by the Γ_6 band, as shown in Fig. 8.6b). Since the inverted bands are the $\Gamma_{8,LH}$ and Γ_6 band, the Dirac point can in principle be moved above the $\Gamma_{8,HH}$ band and consequently into the bulk bandgap. In the Dirac semi-metal phase in contrast, the order of the Γ_8 bands at the Γ point is inverted compared to the 3D-TI phase, as shown in Fig. 8.6a). As mentioned above, the band inversion creating the TSS is between the $\Gamma_{8,LH}$ and the Γ_6 band. In the Dirac semi-metal phase, the Dirac point of the TSS can thus not be moved through the $\Gamma_{8,LH}$ band. The TSS would

---

[1]In this notation a negative Hartree potential represents a positive gate voltage.

hybridize and vanish as far as it touches the $\Gamma_{8,LH}$ band. The hole-part of the TSS thus only exists in parallel to the bulk valence $\Gamma_{8,HH}$ band. The large DOS of the Γ_8 band overshadows the TSS, as shown in Fig. 8.4a) and b). The TSS can consequently not be the origin of the observed two-dimensional hole-type transport.
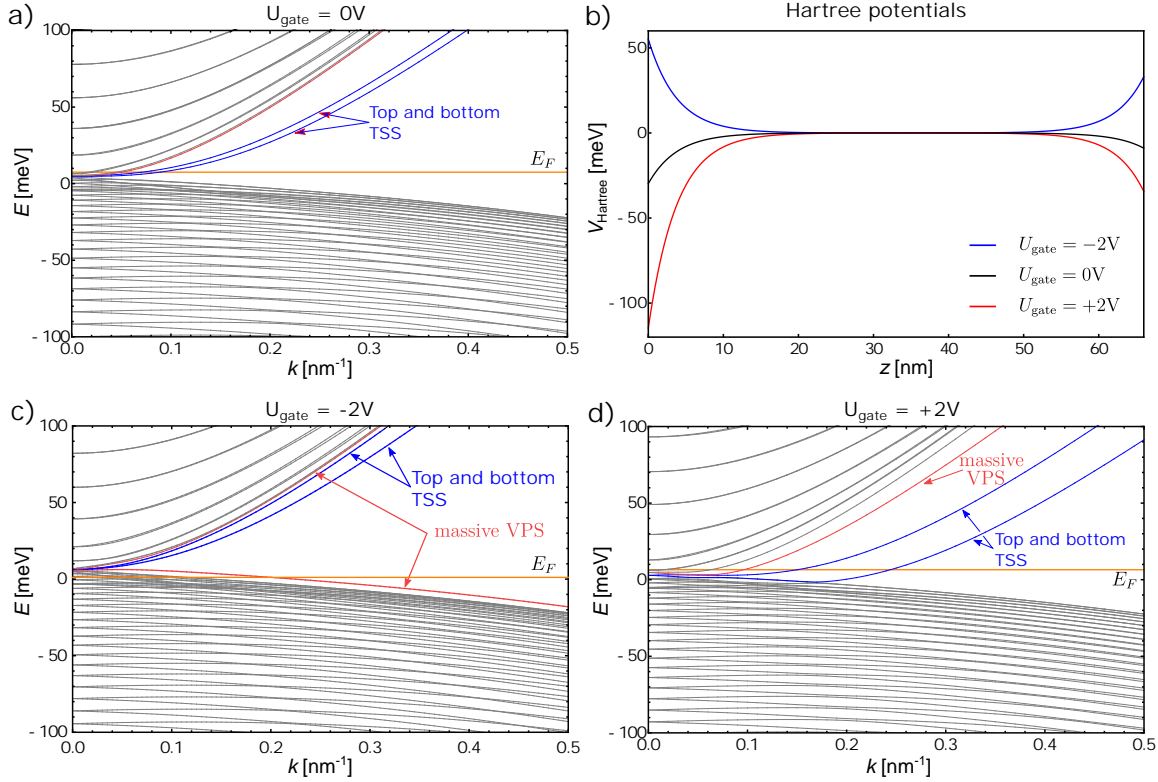

Figure 8.5: The band structure of a 66 nm thick 0.3 % compressively strained HgTe slab is shown. It is calculated using the Kane model including the bulk inversion asymmetry terms and accounting for a Hartree potential $V_{Hartree}$, which represents a small electron density, a moderate hole density, and a moderate electron density in a), c) and d), respectively. The Fermi energy is indicated as orange line the topological surface state (TSS) and massive Volkov-Pankratov states (VPS) are highlighted in red and blue, respectively. The respective Hartree potentials are presented as a function of the z coordinate in b). Taken from D. M. Mahler, Interplay of Dirac Nodes and Volkov-Pankratov Surface States in Compressively Strained HgTe, PRX **9**, 031034 (2019), Creative Commons Attribution 4.0 International License [34]. .

Different kinds of hole-type surface states must be present. Further $k \cdot p$ calculations are performed in Ref. [34] for a positive Hartree potential representing a negative gate voltage. The Hartree potential is shown in blue in Fig. 8.5b) and the resulting band structure in Fig. 8.5c). The topological surface states are pushed close to the conduction band, and the electrochemical potential shifts slightly down. The first valence bulk sub-band, highlighted in red, is shifted away from the remaining valence sub-bands. This state is preferentially occupied and is consequently responsible for the hole-like transport. This red valence band is localized at the top surface as shown for the 3D-TI-phase in Fig. 4.7c) and discussed in Sec. 4.3. Such additional massive surface states have been already described by B. A. Volkov and O. A. Pankratov in Ref. [16] for an interface of insulators with mutually inverted bands. To acknowledge this work, the red state is called massive Volkov-Pankratov state. A more detailed discussion can be found in Sec. 4.4. The introduction of hole-like massive Volkov-Pankratov state in this work based on the 3D-TI tensilely strained HgTe is

chosen out of didactic reasons. Actually, the conceptional inaccessibility of the hole-side of the TSS in compressively strained HgTe helped to identify the massive VPS in the 3D-TI tensilely strained HgTe phase, as described in Sec. 4.4.

The calculation for the positive Hartree potential in Fig. 8.5c) shows not only a hole-type massive VPS but also an electron-type massive VPS. The electrochemical potential lies below this electron-type massive VPS and is thus not occupied. This nevertheless raises the question, whether for higher negative potentials the transport is purely TSS driven or whether electron-type massive VPS also contributes. The band structure for a moderately strong negative Hartree potential [Fig. 8.5b) (red)] is shown in Fig. 8.5d). An electron-type massive VPS is found and highlighted in red. At the electrochemical potential E_F, the DOS of this massive VPS is small, especially compared to the DOS of the TSS. Assuming no degeneracy, Eq. 4.9 can be used to estimate the density n from the respective size in k-space. This yields $n_{VPS} \sim 0.7 \times 10^{11}\,\mathrm{cm}^{-2}$ for the massive VPS, $n_{\mathrm{bot\,TSS}} \sim 1.8 \times 10^{11}\,\mathrm{cm}^{-2}$ and $n_{\mathrm{top\,TSS}} \sim 4.8 \times 10^{11}\,\mathrm{cm}^{-2}$ for the bottom and top TSS, respectively. The quantum limit for n_{VPS} is according to the definition of the filling factor (Eq. 3.7) $B_{ql;VPS} \sim 3$ and thus close to the not well resolved low magnetic field regime of Fig. 8.2 and Fig. 8.7. The top and bottom TSS thus dominate the magneto-transport in the electron-regime of the Dirac semi-metal compressively strained HgTe.
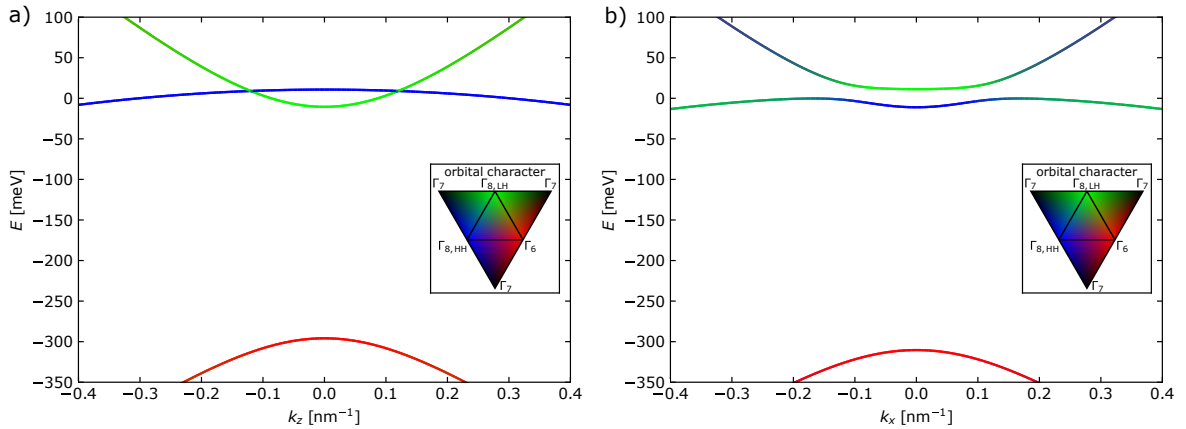
Figure 8.6: The band structure of a 70 nm thick 0.3 % HgTe layer is shown for compressive strain along the k_z-direction in a) and for tensile strain along the k_x-direction in b). The color code indicates the band character as indicated in the inset. Both band structures are calculated using the program "kdpotpy" [29].

8.2.4. Identification of the Landau levels

The $k \cdot p$ calculations with Hartree potentials identify three relevant states for the magneto-transport, namely the top and bottom TSS as well as the hole-type massive VPS. Theoretically, the LL dispersion of the full band structure, as shown in Fig. 8.5, can be calculated. The amount of involved bands and their complex dispersions hinders the assignment of the LL with their respective bands. Additionally, the theoretical determined dispersion in energy into the measured dispersion in gate voltage U_{gate} or equivalently carrier density n is not straightforward, as discussed in Chapter 4. This is why the focus is shifted back to measured LL dispersion already shown in Fig. 8.2. The LL are expected to disperse linearly as function of the density and thus gate voltage U_{gate} (see the discussion in Chapter 3). The measured LL dispersion is shown again in Fig. 8.7. The observed LL are extrapolated

to $B \to 0\,\mathrm{T}$. The extrapolation yields two starting points for the LL. The LL are color-coded according to their starting point. The dash-dotted blue lines emerge from the lower starting point at $U_{\mathrm{gate}} \sim 0.5\,\mathrm{V}$ and the dashed red lines from $U_{\mathrm{gate}} \sim 0.7\,\mathrm{V}$. All dash-dotted blue lines disperse electron-like and all, except one, dashed red lines are hole-like. The origin of the electron-like LL below the origin of the hole-like LL is unusual. This behavior can be explained considering the band structure of compressively strained HgTe. The dispersion of the surface states is reminiscent of the dispersion of the corresponding bulk bands [compare Fig. 8.5c)]. Because of this, the simpler dispersion of the bulk bands, as shown in Fig. 8.6, is discussed representatively. Consistently, the electron-like conduction band (green) minimum lies below the hole-like valence band (blue) maximum at the Γ-point. More puzzling is the origin of the single electron-like dispersing red dashed LL.
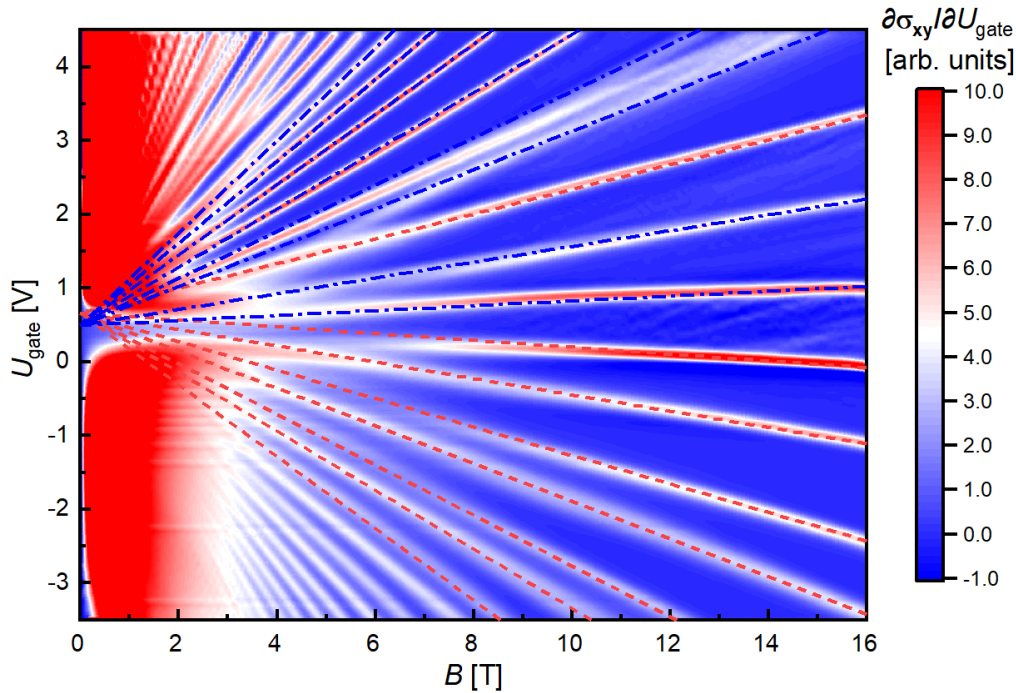
Figure 8.7: The derivative of the Hall conductivity σ_{xy} with respect to the gate voltage U_{gate} is shown as function of U_{gate} and the out of plane magnetic field B at the temperature $T = 0.05\,\mathrm{K}$. The blue dash-dotted and red dashed lines are guides to highlight the two sets of Landau levels with a different origin for $B = 0\,\mathrm{T}$.

To investigate this odd LL, an analytically solvable toy model is used to qualitatively reproduce the *LL* dispersion. This is done following the approach of Ref. [157]. The model is the two-dimensional version of the "simple for band model" (Eq. 8.8) widely used to describe topological materials and discussed in detail in Sec. 8.4.1. The non-degenerate Hamiltonian reads

$$H_{\mathrm{toy}}(k_x, k_y) = \begin{pmatrix} C_0 + M_0 + (C_2 - M_2)(k_x^2 + k_y^2) & A k_+ \\ A k_- & C_0 - M_0 + (C_2 + M_2)(k_x^2 + k_y^2) \end{pmatrix} \quad (8.2)$$

with $k_{\pm} = k_x \pm i k_y$. Two copies of this Hamiltonian are used to represent the top and bottom TSS as well as the massive VPS, respectively. The parameters are chosen to create a simplified version of the band structure determined with $k \cdot p$ calculations for a negative gate voltage $U_{\mathrm{gate}} = 2\,\mathrm{V}$ shown in Fig. 8.5c). The resulting model band structure is shown in

Fig.8.8a) for the parameters given in table 8.1. The model reproduces the qualitative dispersion of the top and bottom TSS in blue and light blue as well as the massive hole and electron-type VPS in red and green. The Landau level dispersion of these bands can be obtained analytically following the usual procedure, as described in Ref. [157] and Ref. [158]. First, the Peierls substitution $\boldsymbol{k} \to \boldsymbol{\Pi} = \boldsymbol{k} + \frac{e}{\hbar}\boldsymbol{A}$ is used to introduce the magnetic field dependence. The gauge potential $\boldsymbol{A}$ represents the magnetic field via $\boldsymbol{\nabla} \cdot \times \boldsymbol{A} = \boldsymbol{B} = B\hat{e}_z$ with $\hat{e}_z$ being the unit vector along the z-direction pointing perpendicular to the surface. Second, the momenta $\boldsymbol{\Pi}$ are expressed in second quantization as ladder operators:

$$\Pi_x = \sqrt{\frac{eB}{2\hbar}}\left(\hat{a}^\dagger + \hat{a}\right), \quad \Pi_y = \sqrt{\frac{eB}{2\hbar}}\left(\hat{a}^\dagger - \hat{a}\right), \quad \Pi_- = \sqrt{\frac{eB}{2\hbar}}\hat{a}, \quad \text{and} \quad \Pi_+ = \sqrt{\frac{eB}{2\hbar}}\hat{a}^\dagger \quad (8.3)$$

The ladder operators applied to the Eigenstate $|n\rangle$ obey the following conditions:

$$\hat{a}^\dagger \langle n| = \sqrt{n+1}\,|n+1\rangle, \quad \hat{a}\langle n| = \sqrt{n}\,|n-1\rangle, \quad \text{and} \quad \hat{a}^\dagger \hat{a}|n\rangle = \hat{n}|n\rangle = n|n\rangle \quad (8.4)$$

Third, the Eigenvalues of the Hamiltonian (Eq. 8.2 including the Peierls substitution and expressed in second quantization using Eq. 8.3 are calculated to

$$E_{\text{LL}}(B) = C_0 - C2\frac{e}{\hbar}Bn \mp \sqrt{A2\frac{e}{\hbar}Bn + (M_0 + M_2\frac{e}{\hbar}Bn)^2}$$

$$E_{\text{LL}=0}(B) = C_0 - M_0 - (C_2 - M_2)\frac{e}{\hbar}B \quad (8.5)$$

These Eigenvalues represent the LL dispersion and are shown in Fig. 8.8b) for the parameters of table 8.1. The hole-type transport is solely carried by the LL of the hole-type massive VPS (red). For magnetic fields $B > 3\,\text{T}$ the electron-type transport is determined by the LL of the top (blue) and bottom (light blue) TSS except for one LL. Only one LL of the massive VPS crosses through the LL of the TSS. This LL is the LL with index $v = 0$, which possesses a positive dispersion despite originating from the hole-like massive VPS. The LL of the electron-like massive VPS only contribute to the not well resolved low magnetic field regime ($B < 3\,\text{T}$).

To sum up, the magneto-transport of the compressively strained HgTe samples is carried by the topological surface states and the hole-like massive Volkov-Pankratov states. No signatures of Fermi-arcs could be found. This observation emphasizes the importance of the inherent band inversion in materials.

band	C_0	C_2	M_0	M_2	A
massive VPS	0 eV	$-0.9\,\text{eVnm}^2$	1 eV	$0.002\,\text{eVnm}^2$	$0.08\,\text{eVnm}^2$
TSS	$-0.01\,\text{eV}$	$-1\,\text{eVnm}^2$	0.1 eV	$0\,\text{eVnm}^2$	$0\,\text{eVnm}^2$

Table 8.1: The table shows the parameters of the simple four band model (Eq. 8.2 used to represent the massive Volkov-Pankratov states and the topological surface states of the Dirac semi-metal compressively strained HgTe. These are used to qualitatively reproduce the measured LL dispersion.
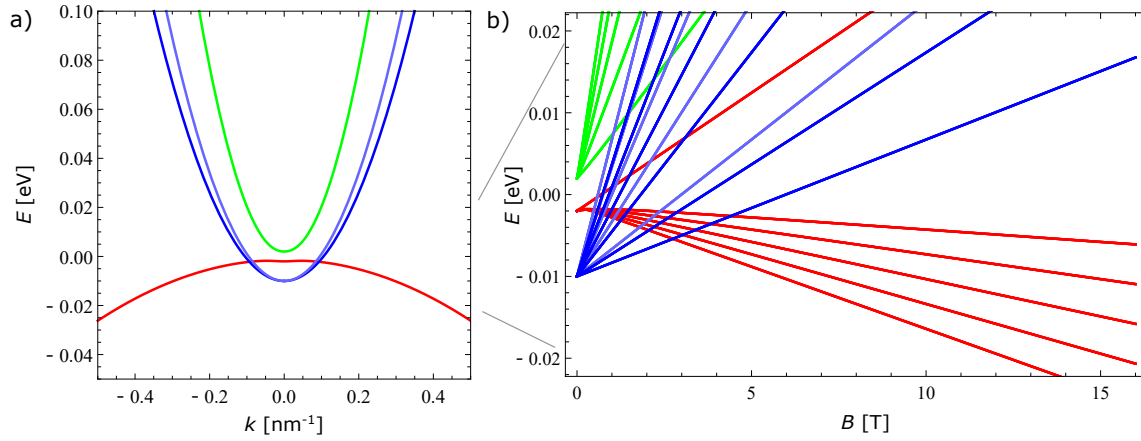
Figure 8.8: In a) the qualitative band structure of an inversion induced Dirac semi-metal with an applied gate voltage is shown based on the simple four-band model (Eq. 8.2). The blue and light blue bands are the top and bottom topological surface states and the red and green bands are the hole and electron-type massive Volkov-Pankratov states. In b) the corresponding Landau level dispersion concerning the magnetic field B and the energy E are shown up to the Landau level index $v = 5$.

8.3. SURFACE STATES IN OTHER INVERSION INDUCED DIRAC SEMI-METALS

The magneto-transport measurements on compressively strained HgTe reveal the existence of topological surface states and VPSs in inversion induced Dirac semi-metals. In this context, the reported observations of magneto-transport effects in the Dirac semi-metals Cd_3As_2 are reviewed and the theoretical predicted magneto-transport phenomena, as the SdH oscillations and QHE carried by Fermi-arcs are summarized. This overview is used as the foundation to find a consistent description of inversion-induced Dirac semi-metals.

8.3.1. QUANTUM OSCILLATIONS IN THE DIRAC SEMI-METAL Cd_3As_2

As a starting point, the expected magneto-transport phenomena for a simple Dirac semi-metal with two double degenerate linearly crossing bands is described. Fermi-arcs are predicted to cause unconventional quantum oscillations in the longitudinal resistance as a function of the magnetic fields [159]. For simplicity, the mechanism is described based on a Weyl semi-metal, which can be straightforwardly transferred to Dirac semi-metals. A slab of a Weyl semi-metal is shown in Fig. 8.9a), where the projection of the Weyl nodes onto the top and the bottom surface is indicated as circles. A magnetic field applied alongside the z-direction forces the charge carriers in the Fermi-arc on the top surface to fulfill one-half of a cyclotron orbit. To execute the other half of the cyclotron orbit the charge carrier has to move through the bulk parallel to the magnetic field into the Fermi-arc of the bottom surface. On the bottom surface, the charge carrier can finish its cyclotron orbit by moving back to the projection of the first Weyl node and tunneling back to the top surface. The overall path can be treated as one cyclotron orbit, as long as the movement through the bulk is coherent, e.g. tunnel-like. This full cyclotron orbit is sketched in Fig. 8.9a). The magnetic fields B_j corresponding to these cyclotron orbits is given by

$$\frac{1}{B_j} = \frac{e}{k_0}\left(\frac{\pi v_F}{E_F}(j+\gamma) - d\right), \tag{8.6}$$
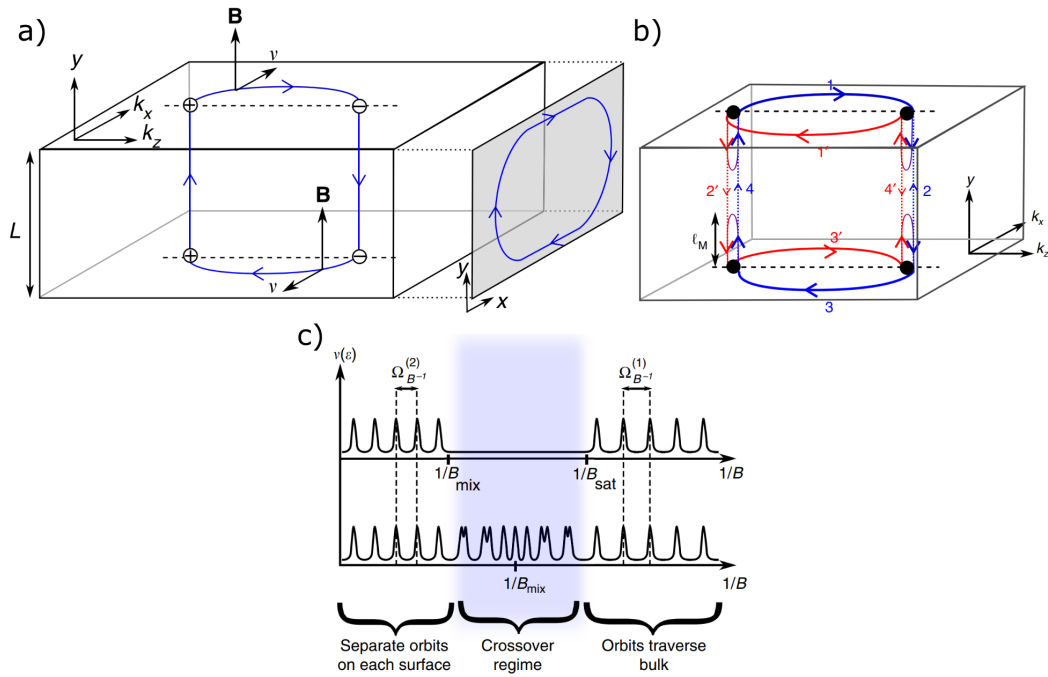
Figure 8.9: In a) the semi-classical orbits of quantum oscillations in the Fermi-arcs of a finite Weyl semi-metal slab are shown in real space for the y-direction and momentum space for x and z. The same semi-classical orbits are shown in b) for a Dirac semi-metal with two Fermi-arcs per surface. The potential intermixing of surface and bulk states due to a magnetic field is indicated as arrows. In c) the corresponding quantum oscillations are shown for three different possible regimes due to the intermixing. Reprinted by permission from Nature Publishing Group: Springer Nature, Nature Communications, Quantum oscillations from surface Fermi arcs in Weyl and Dirac semi-metals, A. C. Potter *et al.*, *Copyright © 2014, Nature Publishing Group, a division of Macmillan Publishers Limited. All Rights Reserved.* (2014) [159].

where k_0 is the length of the Fermi-arc, j the Landau level index, γ a constant, which accounts for quantum corrections for low Landau level indices, and d the thickness of the device [159]. The path in a Dirac semi-metal can be imagined as the sum of the path for two opposite Weyl semi-metals. The cyclotron orbits are thereby separated by the suppressed backscattering between nodes with different chirality due to the leftover symmetry of the crystal [11]. The corresponding semi-classical orbit for a Dirac semi-metal is shown in Fig. 8.9b The expected resulting quantum oscillations are depicted in 8.9c). The tunnel-like motion through the bulk has multiple consequences [159]. It restricts the thickness of the samples not to exceed the mean free path. It also causes a bulk thickness phase dependence as visible in Eq. 8.6, and a saturation magnetic field B_{sat} as an upper limit for the occurrence of these oscillations

$$B_{\mathrm{sat}} \sim \frac{k_0}{d}. \tag{8.7}$$

Such Fermi-arc mediated quantum oscillations have first been reported for the Dirac semi-metal Cd_3As_2 in Ref. [160]. The results of this work are shortly summarized in the following. These devices are produced via focused ion beam etching. The resulting device is shown in Fig. 8.10a) as false color scanning electron microscope picture. The active Cd_3As_2 structure is highlighted in purple and the gold leads in yellow. The longitudinal resistivity shows quantum oscillations as a function of the magnetic field. For the magnetic field applied parallel or perpendicular to the surface different frequencies are observed, as

can be seen in Fig. 8.10b). The corresponding frequencies of these oscillations are determined using a FFT analysis and shown in Fig. 8.10c). For the parallel (0°) case only one frequency is obtained, while in the perpendicular (90°) case an additional frequency is found. An overview of the angular dependence of the frequencies is given in Fig. 8.10f). One frequency is angle independent. The other frequency scales with $\cos(\Theta)$, where Θ is the angle of the magnetic field with respect to the normal of the transport plane. The angle independent frequency is assigned to the bulk carriers. The other frequency is attributed to the Fermi-arcs based on its angular dependence, which is consistent with the expectation for a two-dimensional system. Since for Fermi-arc mediated quantum oscillations a bulk thickness-dependent phase is expected according to Eq. 8.6, also a triangular shape is fabricated as shown in Fig. 8.10d). The corresponding results of the FFT analysis are shown in Fig. 8.10e). The FFT analysis of the triangular shape only shows the frequency f_B assigned to the bulk. The absence of the Fermi-arc assigned frequency is in Ref. [160] interpreted as consistent with the canceling of the quantum oscillations due to the different phases picked up by the different path lengths through the bulk in the triangular geometry.
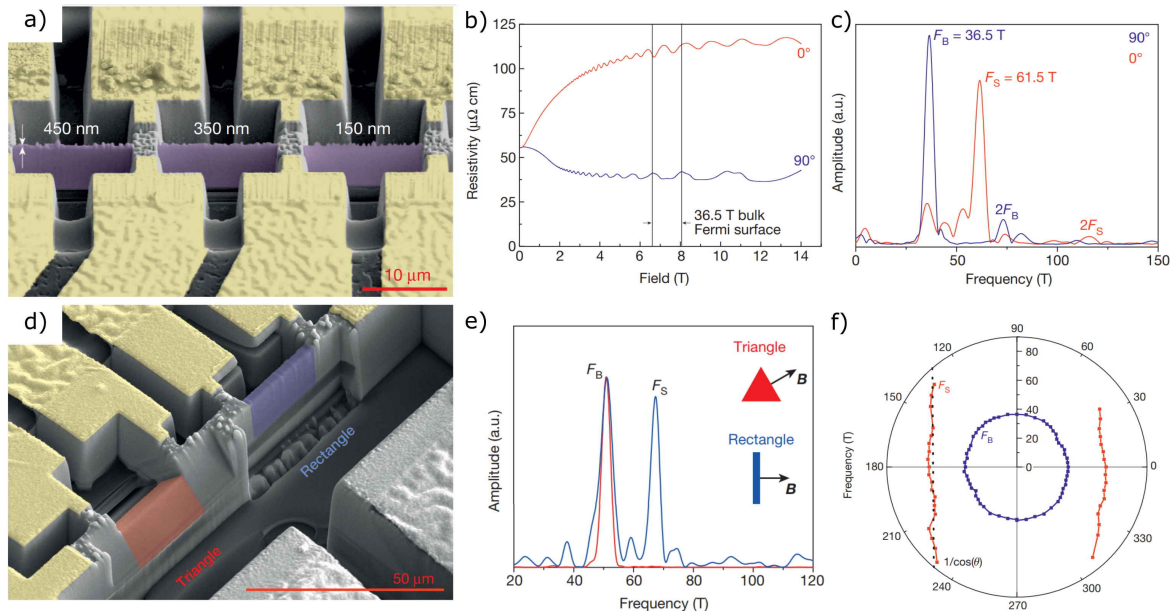
Figure 8.10: In a) a false-color scanning electron microscope picture of the Cd_3As_2 devices prepared by focused ion beam as free-standing $4\,\mu m \times 10\,\mu m$ sheets are shown. The free-standing Cd_3As_2 structures are highlighted in purple and the Au contacts in yellow. The longitudinal resistivity as a function of the magnetic field is shown in b). The two horizontal lines indicate the expected peak positions in the magnetic field B for the oscillations periodic in the inverse magnetic field with a frequency of $f = 36.5\,T$. The corresponding FFT analysis of the resistivity in function of the inverse magnetic field is shown in c) for a magnetic field applied parallel to the surface (0°) in red and perpendicular to it (90°) in blue. An overview of the angular dependence of the FFT determined frequencies is given in f). In d) an additional prepared and measured triangular geometry is highlighted in light red. The results of the FFT analysis of the magneto-transport of the triangular structure are shown in e) in light red together with the results for the rectangular reference structure in light blue. The direction of the magnetic field is indicated schematically in the inset. Reprinted by permission from Nature Publishing Group: Springer Nature, Nature, Transport evidence for Fermi-arc-mediated chirality transfer in the Dirac semimetal Cd3As2, P. J. W. Moll *et al.*, *Copyright ©2016, Nature Publishing Group, a division of Macmillan Publishers Limited. All Rights Reserved.* (2016) [160].

The presented interpretation possesses a few shortcomings, which are discussed in the following. As pointed out by the authors of Ref. [160], the maximum magnetic field B_{sat} for the Fermi-arc assigned quantum oscillations is not consistent with the predicted thickness dependence of Eq. 8.7. The maximum magnetic field B_{sat} instead fits the quantum limit expected for conventional quantum oscillations. Also, the frequency of a three-dimensional state is only expected to be independent of the magnetic field direction for a spherical Fermi surface. Following the discussion of Ref. [137] Fermi-arcs only exist around the Weyl/Dirac nodes, as long as the Fermi contour does not wrap both Dirac nodes completely, which would cause the chiral charge of the Dirac nodes to cancel. In other words, Fermi-arcs only exist for energies inside the anti-crossing gap. In this energy window, the assumption of a spherical Fermi surface, which would correspond to an angle independent frequency as shown in Fig. 8.10f), is non-trivial and the Fermi contour could as well be asymmetric.
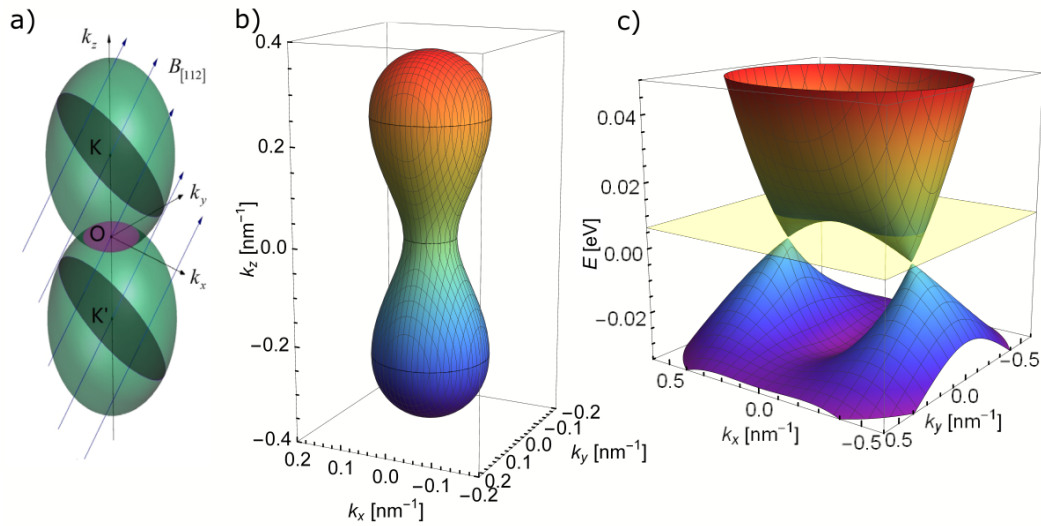
Figure 8.11: In a) the suggested 3D nested anisotropic Fermi surface in Cd_3As_2 is shown based on magnetic field angle-dependent magneto-transport measurements. In b) the Fermi surface of Cd_3As_2 calculated with an simple four band model (Sec. 8.4.1) using the parameters of Ref. [161] is shown for the Fermi energy $E_F = 0.0065\,eV$. The Fermi energy $E_F = 0.0065\,eV$ is indicated as transparent yellow plane in the corresponding band structure for $k_z = 0$ in c). a) is taken from Y. Zhao *et al.*, Anisotropic Fermi Surface and Quantum Limit Transport in HighMobility Three-Dimensional Dirac Semimetal Cd_3As_2, PRX **5**, 031037 (2015), Creative Commons Attribution 3.0 License [162].

An anisotropic three-dimensional Fermi surface can also lead to a similar angular dependence of the magnetic field as an isotropic two-dimensional Fermi circle and thus be responsible for the observed angular dependent frequency assigned to Fermi-arcs. In Ref. [162], the shape of the Fermi contour is analyzed with the help of crystal direction-dependent magneto-transport measurements. These measurements yield either one single frequency or two frequencies depending on the crystal direction. Summarizing the observations for multiple crystal directions, a Fermi surface composed of two nested ellipsoids is suggested, as shown in Fig. 8.11a). The expected Fermi energy is estimated to be $E_F = 200\,meV$ above the Dirac nodes, consistent with the observed high carrier density of $n \sim 6 \times 10^{18}\,cm^{-3}$. To motivate, that this mechanism is responsible, an example Fermi surfaces is shown for a Fermi energy ($E_F = 6.5\,meV$) slightly above the so-called Lifshitz transition in Fig. 8.11b).

A Lifshitz transition is the conversion from two Fermi surfaces to one Fermi surface with changing Fermi energy, here increasing Fermi energy. The Lifshitz transition happens when the Fermi energy E_F hits the upper edge of the anti-crossing gap, as indicated by the transparent yellow plane in Fig. 8.11c). The shown Fermi surface is probably not the exact Fermi surface of the device investigated in Ref. [160] but motivates the possibility of the existence of a Fermi surface with such a symmetry in Cd_3As_2. To calculate this Fermi surface a simple four-band model is used, as described in Eq. 8.8, with the parameters for Cd_3As_2 given by Ref. [161]. The values of the simple four-band model should not be taken as absolute quantities, since the exact band structure of Cd_3As_2 is still under discussion, as discussed in Sec. 7.2.1 and the review paper Ref. [107]. Unfortunately, different reports on the same material Cd_3As_2 can also not simply be compared. Very different magneto-transport properties are observed in Ref. [163] on nanoplates of Cd_3As_2 with thicknesses between 80 nm and 150 nm with various carrier densities. For lower doped samples, even QHE is observed.

8.3.2. QUANTUM HALL EFFECT IN Cd_3As_2

The observation of QHE is a more reliable indicator for the dimensionality of a system since it only exits in two-dimensional systems. In Ref. [163], plateaus in the Hall resistance R_{xy} are observed in Cd_3As_2 samples with a low carrier concentration of $n_{3D} \sim 5 \times 10^{17} \, cm^{-3}$, as shown in Fig. 8.12a). The observation of QHE requires a two-dimensional transport layer. The three-dimensional extension with a thickness of $70 - 150$ nm of the investigated Cd_3As_2 nanoplates suggests the existence of surface states. The authors of Ref. [163] assign this surface transport to Fermi-arcs. To prove that Fermi-arcs are the underlying mechanism for the observed QHE in Cd_3As_2, the phase of the QHE in a wedge-shaped sample is investigated in Ref. [164]. The proposed mechanism by Fermi-arcs is sketched in Fig. 8.9 and predicts that the phase scales with the sample thickness d according to Eq. 8.6. The wedge design is chosen to probe three different thicknesses in one sample piece and compare the phase of the observed quantum oscillations and QHE. Indeed a shift of the phase for the different thicknesses is observed.

In contrast, in Ref. [138] a different approach is taken to test the thickness dependence of the phase. Layers of different thicknesses grown with MBE are defined in Hall bar structures and equipped with a gate, which allows matching the carrier densities for the different layers. Their experiment yields no clear dependence of the phase on the sample thickness. Instead, the observed shifts between the onset of QH plateaus and SdH oscillations in different devices are traced to small differences in the carrier density in the samples. These small differences are unavoidable since it is impossible to precisely match the carrier density only based on the classical Hall slope for low magnetic fields. The reported phases do not match the expectations for the QHE carried by Fermi-arcs. Arguably the chosen layers are with up to 38 nm relatively thin, but according to the estimate by Ref. [163] the Fermi wavelength is of the same size, making at least the thicker devices quasi three-dimensional.

So far, it is implicitly assumed that the proposed mechanism of cyclotron orbits through the Fermi-arcs on opposite surfaces not only cause SdH oscillations but also QHE. The expected magneto-transport is explicitly calculated for finite slabs of Weyl and Dirac semi-metals, namely Cd_3As_2 and Na_3Bi, in Ref. [161]. The mechanism thereby is the same as proposed for the quantum oscillations in Sec. 8.3.1 and sketched in Fig. 8.9. The simple four band model described by Eq. 8.8 with $B(\boldsymbol{k}) = 0$ is used and solved for a 100 nm thick slab of Cd_3As_2 along the [110] direction. The resulting band structure is shown in Fig. 8.12b) to-
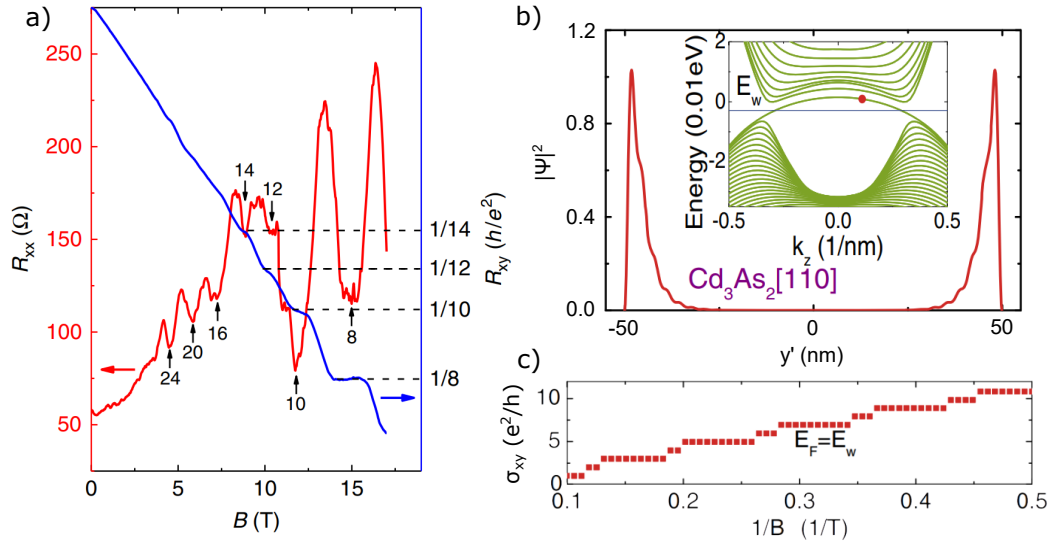
Figure 8.12: In a) the measured longitudinal resistance R_{xx} and Hall resistance R_{xy} as a function of the magnetic field B on a Cd_3As_2 nanoplate is shown. The band structure of a 100 nm slab of Cd_3As_2 determined with a simple four-band model is shown in b) together with the wave function distribution along the finite direction for $k_z = 0.01$ nm^{-1} indicated as red dot. The corresponding Hall conductance σ_{xy} is shown in c). a) is taken from C. Zhang *et al.*, Evolution of Weyl orbit and quantum Hall effect in Dirac semimetal Cd3As2, Nat. Commun. **8**, 1272 (2017), Attribution 4.0 International (CC BY 4.0) [163]. b) and c) are taken from C. M. Wang *et al.*, 3D Quantum Hall Effect of Fermi Arcs in Topological Semimetals, PRL **119**, 136806 (2017) Copyright 2017 by the American Physical Society. [161].

gether with the probability distribution $|\Phi|$ of the occupied state for $k_z = 0.01$ nm^{-1}. A surface state localized on both surfaces is found, which is nevertheless identified as a Fermi-arc state. The corresponding Hall conductivity σ_{xy} is calculated showing the formation of QH-plateaus. The Hall conductivity σ_{xy} is shown as function of the inverse mangetic field in Fig. 8.12c).

To sum up, in Cd_3As_2 SdH oscillations and QHE are reported, which are similar to the observation in compressively strained HgTe in this work. The magnetic field direction dependence of the reported SdH oscillation and the observation of QHE characterizes the transport in Cd_3As_2 as two-dimensional. The necessary surface states are typically identified as Fermi-arcs. In contrast, the two-dimensional magneto-transport observed in compressively strained HgTe is assigned to the topological surface states and the massive Volkov-Pankratov states.

8.4. MODEL HAMILTONIANS FOR INVERSION INDUCED DIRAC-SEMI-METALS

The magneto-transport indicates the existence of surface states in compressively strained HgTe and Cd_3As_2. To understand the origin of these surface states in these inversion induced Dirac semi-metals the most popular model Hamiltonians are reviewed and compared. These Hamiltonians are a simple four-band model, a Luttinger-like model, and the already in Sec. 4.2 introduced Kane model. The origin and stability of the observed surface states are addressed with the help of these models.

8.4.1. SIMPLE FOUR BAND MODEL

The most widely used model is the simple four-band model already used in Sec. 8.3 to visualize the band structure of Cd_3As_2 [165]. This simple four band model is also used to describe Na_3Bi [108] and the three-dimensional insulators chalcogenides Bi_2Se_3, Bi_2Te_3 and Sb_2Te_3 [166]. One convention for the Hamiltonian is

$$H_\Gamma(\boldsymbol{k}) = \epsilon_0(\boldsymbol{k}) + \begin{pmatrix} M(\boldsymbol{k}) & Ak_+ & 0 & B^*(\boldsymbol{k}) \\ Ak_- & -M(\boldsymbol{k}) & B^*(\boldsymbol{k}) & 0 \\ 0 & B(\boldsymbol{k}) & M(\boldsymbol{k}) & -Ak_- \\ B(\boldsymbol{k}) & 0 & -Ak_+ & -M(\boldsymbol{k}) \end{pmatrix} \begin{matrix} |E,\uparrow\rangle \\ |H,\downarrow\rangle \\ |E,\downarrow\rangle \\ |H,\uparrow\rangle \end{matrix} \tag{8.8}$$

where $k_\pm = k_x \pm i k_y$ and

$$\epsilon_0(\boldsymbol{k}) = C_0 + C_1 k_z^2 + C_2(k_x^2 + k_y^2)$$

as well as

$$M(\boldsymbol{k}) = M_0 - M_1 k_z^2 - M_2(k_x^2 + k_y^2) \tag{8.9}$$

to account for the non-cubic crystal structures of these materials (tetragonal for Cd_3As_2 and hexagonal for Na_3Bi and the chalcogenides). The parameters M_0, M_1, M_2 have to be negative ($M_0, M_1, M_2 < 0$) to realize the necessary band inversion. To describe a Dirac semi-metal like Cd_3As_2 and Na_3Bi the off-diagonal element $B(\boldsymbol{k})$ is set to zero ($B(\boldsymbol{k}) = 0$). The other parameters C_0, C_1, C_2 and A are effectively fitting parameters to reproduce the dispersion of the low energy bands obtained by DFT or ARPES.

It is instructive to look at the different phases that can be described by this model and their connection. A picturesque way to obtain the Dirac semi-metals phase is by starting with a fully quadratic dispersion and reducing the symmetry until the target band structure with the linear band crossings is achieved. The additional fitting term $\epsilon_0(\boldsymbol{k})$ is set to zero ($\epsilon_0(\boldsymbol{k}) = 0$) for simplicity. The effective mass terms in Eq. 8.9 are chosen to be $M_1 = M_2$ and $M_0 = 0$. Setting all off-diagonal elements to zero, the dispersion is given by the diagonal elements of Eq. 8.8, namely

$$E_{\text{quadratic}}(\boldsymbol{k}) = \mp M_2 \boldsymbol{k}^2,$$

making the system a semi-metal with quadratically dispersing bands as shown in Fig. 8.13a). An intuitive approach to create a linear crossing between two bands is to figuratively speaking push the two bands into each other. This can be done by introducing an energy offset between the two bands via setting $M_0 < 0$ and results in the dispersion given by

$$E_{\text{nodal-line}}(\boldsymbol{k}) = \pm \left(M_0 - M_2 \boldsymbol{k}^2 \right),$$

which describes a so-called nodal-line semi-metal phase, as shown in Fig. 8.13b). This nodal-line semi-metal phase disperses linearly along the radial direction of the circular nodal line and quadratically in the other directions. The simplest possible Dirac semi-metal hosts two linear crossing points, called Dirac nodes. These two Dirac nodes are chosen to reside on the k_z-axis. The degeneracy along the nodal line is therefore lifted via the introduction of the coupling terms Ak_+ and Ak_- linear in k. The resulting band structure of a Dirac semi-metal is given by

$$E_{\text{Dirac}}(\boldsymbol{k}) = \mp \sqrt{A^2 \left(k_x^2 + k_y^2 \right) + \left(M_0 - M_2 \boldsymbol{k}^2 \right)^2}$$
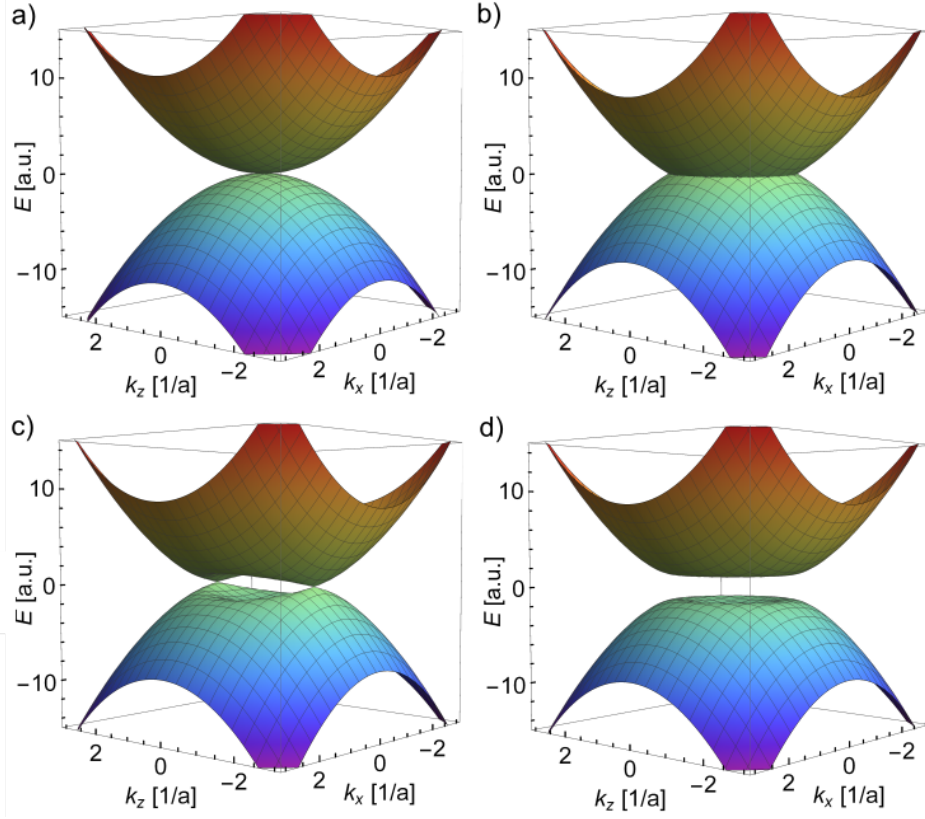
Figure 8.13: The evolution of the band structure from a quadratic semi-metal [a)] via a nodal-line semi-metal [b)] and a Dirac semi-metal [c)] into a topological insulator [d)] is shown based on the simple four band model (see Sec. 8.4.1).

and shown in Fig. 8.13c). When the left over degeneracy at $k_z = k_0$ is lifted via the additional linear coupling term $B(\boldsymbol{k}) = A_z k_z$ in the Hamiltonian (Eq. 8.8), the topological insulator phase with the dispersion

$$E_{\text{3D-TI}}(\boldsymbol{k}) = \mp\sqrt{A^2\left(k_x^2 + k_y^2\right) + A_z^2 k_z^2 + \left(M_0 - M_2 \boldsymbol{k}^2\right)^2}$$

is realized as shown in Fig. 8.13d). The Dirac semi-metal phase is thus except for the protected crossing points at $k_z = k_0$ virtually identical to the topological insulator phase. This similarity of the Dirac semi-metal and topological insulator raises the question of whether topological surface states also exist in the Dirac semi-metal phase.

8.4.2. Surface states in the simple four band model
To investigate the properties of the surface states in inversion-induced Dirac semi-metals, their band structure is calculated for a finite slab. In Ref. [167] the simple four-band model, introduced in the above Sec. 8.4.1 and given by Eq. 8.8, is expressed in a tight binding like fashion. The simple four-band model in a tight binding like fashion reads

$$H(\boldsymbol{k}) = \epsilon_{\boldsymbol{k}}^0 + \left[t\left(\cos k_x + \cos k_y - 2\right) + t_z\left(\cos k_z - \cos Q\right)\right]\tau_z + \lambda\,\sin k_x \sigma_x \tau_x + \lambda\,\sin k_y \sigma_y \tau_x,$$
$$(8.10)$$

where $\boldsymbol{\sigma}$ ($\boldsymbol{\tau}$) are the Pauli matrices acting on the spin (orbital space), t and t_z are hopping amplitudes, and λ is the spin-orbit coupling parameter. The obtained surface states are

shown in Fig. 8.14a) with respect to the position of the Dirac nodes in the Brillouin zone indicated as red dots. Fig. 8.14b) shows the connection of the two Dirac nodes on the k_z-k_y surface via two surface states. The dispersion of these surface states looks like the dispersion expected for Fermi-arcs. The authors of Ref. [167] show that they can deform the surface state and move it away from the Dirac nodes via adding a perturbation term, which conserves the symmetry and does not shift the bulk nodes. This perturbation term has the form

$$\delta H_4(\boldsymbol{k}) = m' \left(\cos k_x - \cos k_y \right) \sin k_z \sigma_z \tau_x.$$

This possibility to detach the surface states from the Dirac nodes, questions the Dirac nodes as the origin for the surface states and thus them being Fermi-arcs.
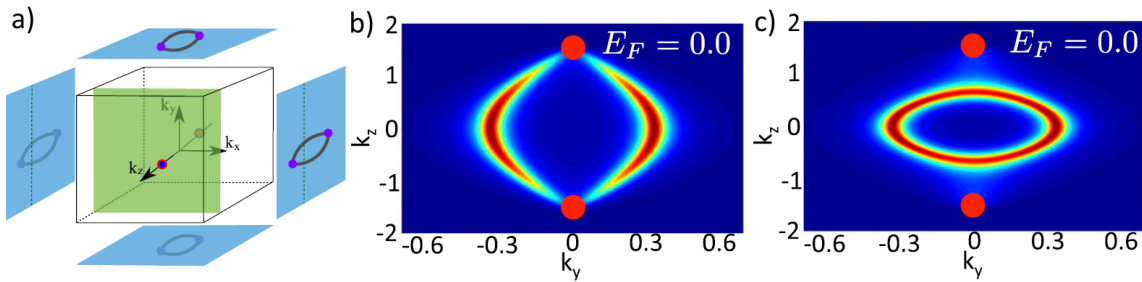

Figure 8.14: In a) the bulk Brillouin zone is shown in the middle, and the position of the two Dirac nodes of the simple four-band model is marked as red dots. The equivalent surface Brillouin zones of the four surfaces parallel to k_z are shown in blue. The Fermi-arc-like surface states connect the projections of the Dirac node onto the respective surface Brillouin zone, which are indicated as red dots. The Fermi-arcs-like surface states on the k_z-k_y surface calculated using the simple four-band model are shown in b) without perturbation and in c) with perturbation for the electrochemical potential E_F positioned at the Dirac nodes ($E_F = 0$). Reprinted from M. Kargarian *et al.*, Are the surface Fermi arcs in Dirac semimetals topologically protected?, PNAS **113**, 8648 (2016), Copyright 2016 National Academy of Sciences [167].

As mentioned in Sec. 8.4.1, the band structure and Hamiltonian of the Dirac semi-metal phase and the topological insulator only differ around $k_z = k_0$. This difference comes from an off-diagonal term breaking the symmetry protection at $k_z = k_0$. This similarity suggests some affinity between the observed surface states in both phases. Since the TSS in topological insulators is connected to the $\mathbb{Z}_2$ topological invariant indicating a topologically nontrivial character for $\mathbb{Z}_2 = 1$, the authors of Ref. [168] determine the topological invariant of the Dirac semi-metal phase. The Dirac semi-metal phase also possesses the topological invariant $\mathbb{Z}_2 = 1$ and thus an unwanted or at least hidden band inversion. A quite pictorial approach is taken in Ref. [168] to negate the band inversion in the Dirac semi-metal phase, by adding a set of mutually inverted bands. They use that the addition of two $\mathbb{Z}_2 = 1$ invariants yields $\mathbb{Z}_2 = 0$ and thus a topologically trivial system. The corresponding robust Dirac semi-metal eight-band model with the topological invariant $\mathbb{Z}_2 = 0$ of Ref. [168] reads:

$$H_8(\boldsymbol{k}) = \begin{pmatrix} H(\boldsymbol{k}) & M(\boldsymbol{k}) \\ M^\dagger(\boldsymbol{k}) & H_{\text{TI},} \end{pmatrix}, \tag{8.11}$$

$$H_{\text{TI}} = \epsilon'_{\boldsymbol{k}} + t' \left(\cos k_x \cos k_y + \cos k_z - 2 \right) \tau_z + \left[\lambda_{xy} \left(\sin k_x \sigma_x - \sin k_y \sigma_y \right) + \lambda_z \sin k_z \sigma_z \right] \tau_x, \tag{8.12}$$

$$M(\boldsymbol{k}) = m_0 \left(1 - \tau_z \right) \tag{8.13}$$

with m_0 being real. This Hamiltonian describes the superposition of a Dirac semi-metal and a topological insulator. Each of the two is described by a copy of Eq. 8.10. The off-diagonal terms mix the Dirac semi-metal and 3D-TI blocks of the Hamiltonian. The corresponding bulk band structure is shown in Fig. 8.15a).
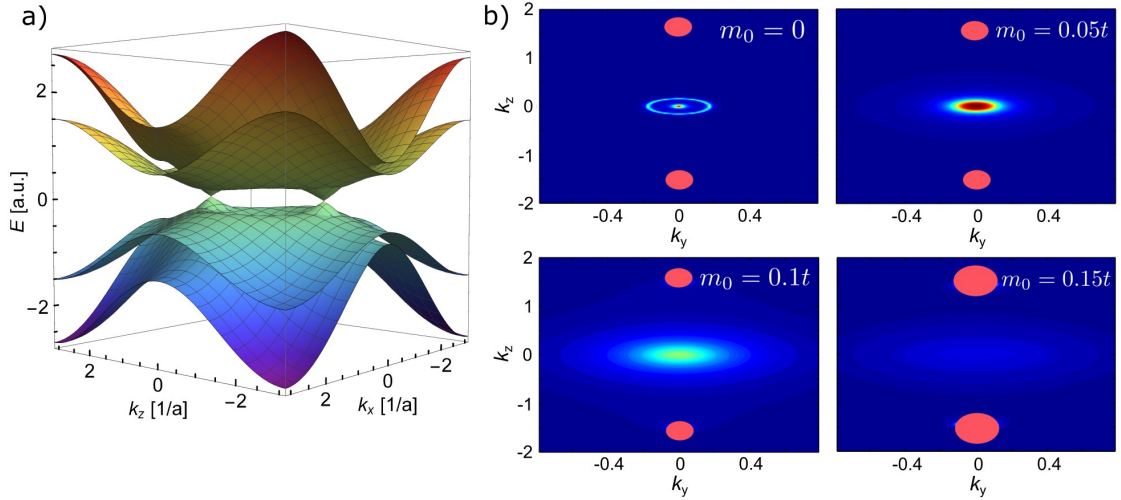

Figure 8.15: In a) the bulk band structure of the non-topological Dirac semi-metal phase proposed by Ref. [168] is shown. In b) the resulting surface state is shown in the surface Brillouin zone for various values of the model parameter m_0 for the Dirac semi-metal model with the topological invariant $\mathbb{Z}_2 = 0$. The projection of the Dirac nodes is indicated as red circles. b) taken from M. Kargarian *et al.*, Deformation and stability of surface states in Dirac semimetals, PRB **97**, 165129 (2018), Copy- right 2018 by the American Physical Society [168].

The resulting surface state for different strength of the mixing term m_0 in Eq. 8.13 is shown in Fig. 8.15b). The surface state can be destroyed by increasing the strength of the mixing term m_0. The mixing term adds a mass term to the surface state, which opens a gap around $k_z = 0$. The surface states are thus only observed in the topologically non-trivial ($\mathbb{Z}_2 = 1$) effective four-band Dirac semi-metal model, and not in the topologically trivial ($\mathbb{Z}_2 = 0$) eight-band Dirac semi-metal model. Because of this, the authors of Ref. [168] argue that the surface states are not related to the Dirac nodes, but instead are an extension of the usual bulk boundary correspondence due to the band inversion. This suggests, that the surface states in Cd_3As_2 and compressively strained HgTe are related to their topologically non-trivial bulk character.

8.4.3. Luttinger-like model

The Luttinger model [23] and the Kane model are widely used to describe the band structure of HgTe. The surplus of the Luttinger-like model over the above described simple four-band model is its connection to the Kane model. The Kane model is well established for the tensilely strained 3D-TI phase of HgTe and the contribution of each band is well-understood [8, 77], as described in Sec. 4.2. The Luttinger-like Hamiltonian can be created by downfolding of the six-band Kane Hamiltonian, as presented in Ref. [24, 169]. In this downfolding process also the basis is adjusted accordingly.
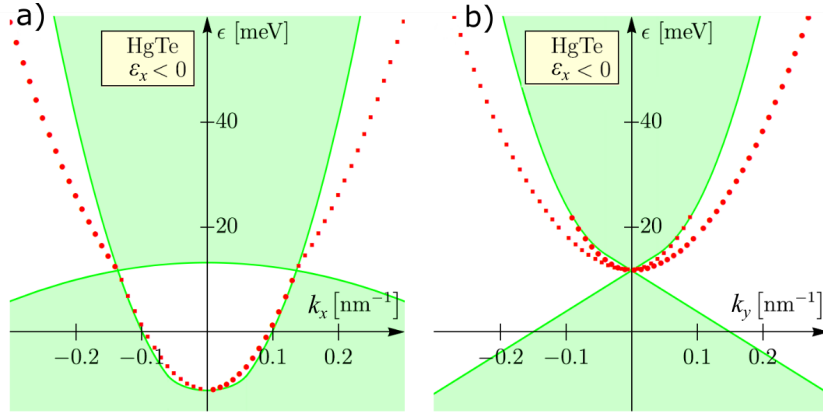
Figure 8.16: The bulk spectrum of the Dirac semi-metal phase of HgTe in the Luttinger-like model is shown for the momentum $k_z = 0$. In a) the energy ϵ is shown for $k_y = 0$ as function of k_x, which is the momentum along the direction of the uni-axial strain ϵ_x. In b) the energy is shown for $k_x = 0$ as function of k_y. The calculated surface state dispersion is highlighted as red dots. Taken from M. Kharitonov *et al.*, Universality and Stability of the Edge States of Chiral-Symmetric Topological Semimetals and Surface States of the Luttinger Semimetal, PRL **119**, 266402 (2017), Copyright 2017 by the American Physical Society [169].

The Luttinger-like Hamiltonian for unstrained HgTe, a semi-metal with quadratically dispersing bands, reads

$$
H_{\text{Luttinger}} = \begin{pmatrix} \alpha_0 \boldsymbol{k}^2 + E_{\alpha_z}(\boldsymbol{k}) & -2\sqrt{3}\alpha_z k_- k_z & -\sqrt{3}\alpha_z k_-^2 & 0 \\ -2\sqrt{3}\alpha_z k_+ k_z & \alpha_0 \boldsymbol{k}^2 - E_{\alpha_z}(\boldsymbol{k}) & 0 & -\sqrt{3}\alpha_z k_-^2 \\ -\sqrt{3}\alpha_z k_+^2 & 0 & \alpha_0 \boldsymbol{k}^2 - E_{\alpha_z}(\boldsymbol{k}) & 2\sqrt{3}\alpha_z k_- k_z \\ 0 & -\sqrt{3}\alpha_z k_+^2 & 2\sqrt{3}\alpha_z k_+ k_z & \alpha_0 \boldsymbol{k}^2 + E_{\alpha_z}(\boldsymbol{k}) \end{pmatrix} \begin{matrix} |HH_{\text{L}};\uparrow\rangle \\ |LH_{\text{L}};\uparrow\rangle \\ |LH_{\text{L}};\downarrow\rangle \\ |HH_{\text{L}};\downarrow\rangle \end{matrix}
$$

$$(8.14)$$

with $E_{\alpha_z}(\boldsymbol{k}) = \alpha_z \left(k_x^2 + k_y^2 - 2kz^2 \right)$, where the effective Luttinger parameter are related to the Kane model parameters by

$$
\alpha_0 = \gamma_1 - \frac{E_{\text{P}}}{3E_{\text{g}}}, \quad \alpha_z = \gamma_2 - \frac{E_{\text{P}}}{6E_{\text{g}}}. \tag{8.15}
$$

The Kane model parameters are listed in Table 4.1. In Ref. [169] the same analysis is extended to the Dirac semi-metal and topological insulator phase. These phases are accessed from the quadratic semi-metal phase by elongating the cubic unit cell via uni-axial strain, which lifts degeneracy at the Γ-point. The band structure of the Dirac semi-metal phase is shown in Fig. 8.16. The shown surface states are similar to the surface states obtained by the simple four-band model [Sec. 8.4.1, Fig. 8.14b)], and by the eight-band Kane model [Fig. 8.4b)]. A three-dimensional semi-metal with quadratic dispersion, as unstrained HgTe, also hosts stable surface states, as already reported in Ref. [81] and shown in Ref. [24] using the four-band Luttinger-like model given by Eq. 8.14. The band structure of unstrained HgTe determined with the Luttinger-like model is shown in Fig. 8.17a). The surface states found for the unstrained HgTe phase is identical to the one determined for the Dirac semi-metal phase. Since the unstrained HgTe Hamiltonian is much simpler, it is exemplary analyzed in the following.

The phase diagram of this model is tested by varying the parameter of the Hamiltonian. The resulting phase diagram, as determined by Ref. [24] is shown as a function of the effective Luttinger parameters β in Fig. 8.17b). The used effective Luttinger parameters are
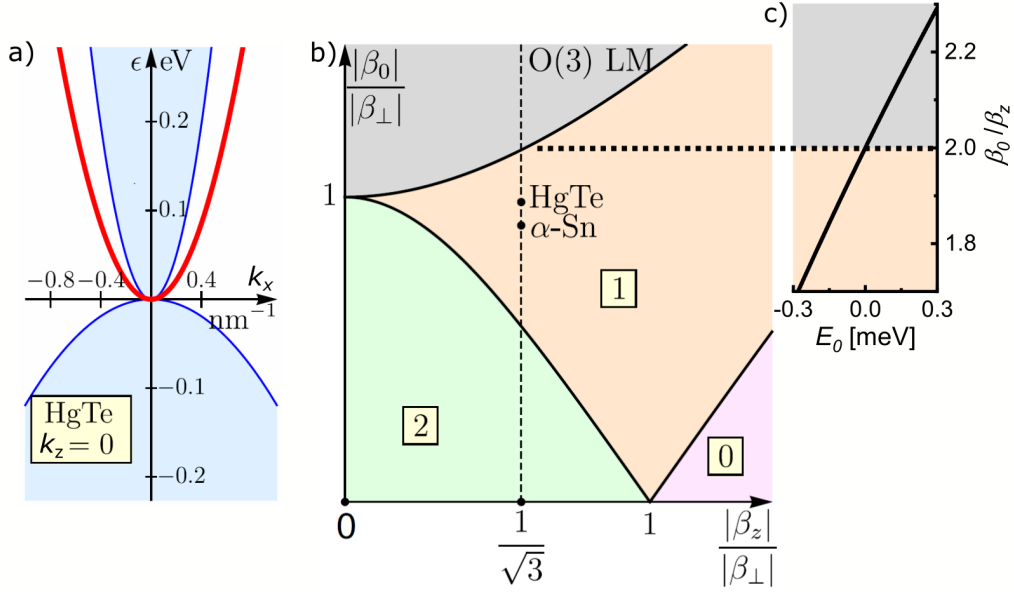
Figure 8.17: In a) the band structure of a semi-infinite unstrained HgTe slab in the Luttinger-like model is shown for the momentum $k_z = 0$. The bulk states are shown in blue and the surface state in red. In b), the edge-state stability phase diagram is shown as function of the normalized effective Luttinger parameters $\beta_0/\beta_\perp$ and $\beta_z/\beta_\perp$. The position of the Luttinger-like model (Eq. 8.14) inside this stability phase diagram is indicated by the narrow dashed black line. The orange area hosts one surface state, the green area two surface states, and the grey area no surface states. In c) the band gap $E_0 = E_{\Gamma_6-\Gamma_8}$ of the Kane model is shown as function of the effective Luttinger parameters β_0/β_z. a) and b) reprinted from M. Kharitonov *et al.*, Universality and Stability of the Edge States of Chiral-Symmetric Topological Semimetals and Surface States of the Luttinger Semimetal, PRL **119**, 266402 (2017) [24], Copyright 2017 by The American Physical Society.

8

$\beta_0 = \alpha_0$ and $\beta_z = \alpha_z$, which are normalized to $\beta_\perp = \sqrt{3}\alpha_z$. The parameterization of the Luttinger-like model given by Eq. 8.14 is indicated by the thin black dashed vertical line in Fig. 8.17b). Multiple phases hosting different numbers of surface states are found. The phase of interest is colored in orange. The Section of the dashed line on the orange background indicates the range of the effective Luttinger parameters capable of hosting these surface states. Since the effective Luttinger parameters are determined by downfolding the parameters of the Kane Hamiltonian the question is, whether the parameters of the Kane model give a more intuitive access to the observed transition from a phase hosting a surface state to a phase without a surface state. Here especially the inverted band gap between the Γ_6 and Γ_8 bands $E_0 = E_{\Gamma_6-\Gamma_8}$ comes to mind. The existence of an inverted band gap between bands with different parity offers more intuitive access to the topological character of the material than calculating the topological invariant as done in Sec. 8.4.2. In Fig. 8.17c) the size of the band gap E_0 is shown as function of the normalized downfolded effective Luttinger parameter β_0/β_z. The phase of the Luttinger-like model hosting surface states is equivalent to an inverted bandgap in the Kane model. The transition to the phase with no surface state happens via closing the inverted bandgap and the transformation to a non-inverted bandgap and thus the band order. To correlate the effective Luttinger parameters to the inverted bandgap, the solution of the Luttinger-like Hamiltonian (Eq. 8.14) is analyzed in the $k_z = 0$ plane. This solution reads

$$E_\pm(k_\perp) = \left(\alpha_0 \pm \sqrt{3\alpha_z^2 + \alpha_z^2}\right)k_\perp^2 \tag{8.16}$$

with $k_\perp = \sqrt{k_x^2 + k_y^2}$. To describe a semi-metallic phase, as shown in Fig. 8.18a), the two solutions need to have effective masses with opposing signs. This restricts the effective Luttinger parameters due to Eq. 8.16 to $\alpha_0 < 2\alpha_z$ or equivalently $\beta_0 < 2\beta_z$. Using the effective Luttinger parameter definition given by Eq. 8.15 the above condition translates to $E_0 < 0$. In the six-band Kane model, the semi-metallic phase is thus accompanied by an inverted band order. The relation of the inverted band gap E_0 to the normalized downfolded effective Luttinger parameter β_0 / β_z is shown in Fig. 8.17c). To get a better understanding of the phases involved in this phase transition the corresponding band structures of the different phases of the Luttinger-like model are shown in Fig. 8.18. The quadratic semi-metal phase, which hosts surface states, is shown in a). The phase transitions happen via a phase with a quadratic conduction band and a completely flat valence band, as shown in b). The surface state lacking phase possesses only conduction bands, as shown in c). To summarize, the models typically used to describe inversion-induced Dirac semi-metal are inherently topologically non-trivial, and topological surface states are thus expected to exist.
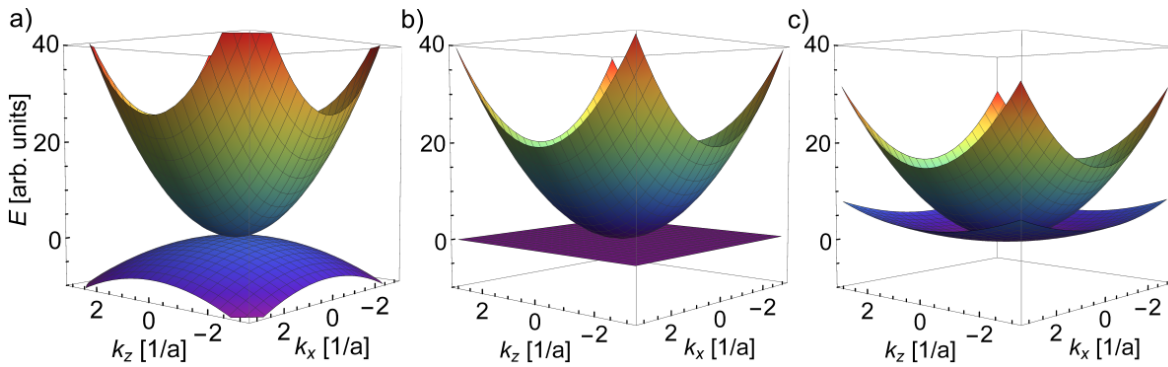
Figure 8.18: The band structure of the Luttinger-like model is shown for the semi-metal phase in a), the phase transition in b), and the non-semi-metal phase in c).

8.5. COMMON PROPERTIES OF INVERSION INDUCED DIRAC SEMI-METALS

The most important common property of the inversion-induced Dirac semi-metals is their name-giving inherent band inversion and thus topologically non-trivial character. These Dirac semi-metals are typically described with the help of two-band models since these already reproduce the characteristic linear band crossing. The band inversion in these systems is often not between these two low energy bands but between the conduction band and a higher valence band. The band structure of Cd_3As_2 and Na_3Bi with its band inversion is shown in Sec. 7.2. The order of the bands is identical to the band order in HgTe, which can be seen in Fig. 2.1. The topologically non-trivial character stems from the inversion of the S-type band with the P-type bands, which determines the low energy dispersion.

The possibility to alter the low energy dispersion via strain engineering in HgTe from an insulating to a Dirac semi-metal phase is described in Sec. 2.1.2 and visualized in Fig. 2.2. The simple transition via strain emphasizes the relationship of the inversion-induced semi-metals with the three-dimensional topological insulators. The underlying band inversion is thus expected to also cause the formation of topological surface states in inversion-induced Dirac semi-metals. This band inversion tends to be hidden in the parameterization of four

Figure 8.19: The ARPES measurement of the dispersion of the energy with respect to the Fermi energy $E - E_F$ is shown is function of the momentum of the Cd_3As_2 (112) surface in a) together with dispersion calculated with DFT in b). The bands are labeled and numbered according to their character. BV means bulk valence ba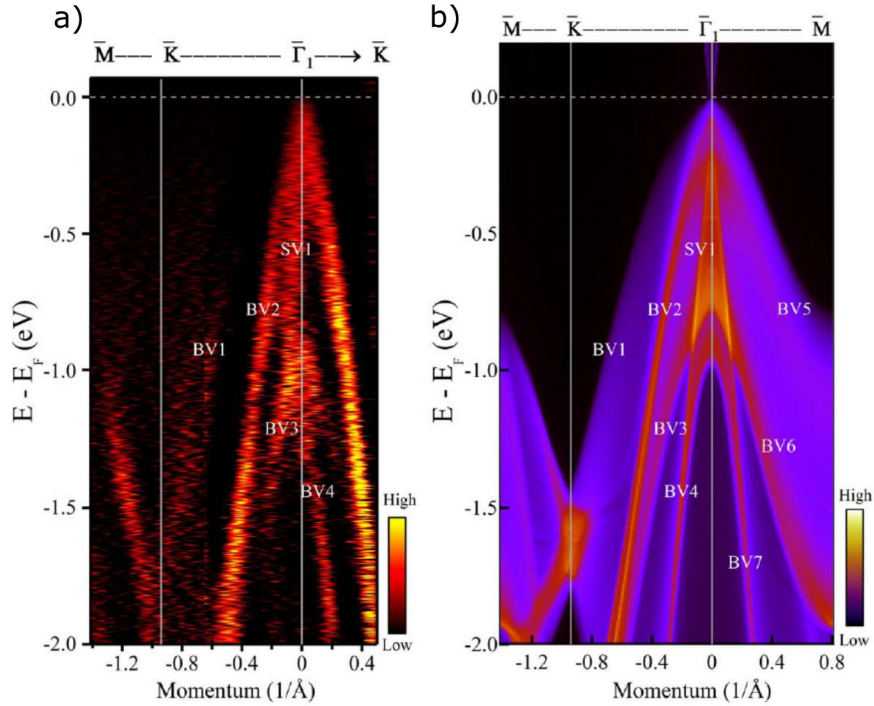nds and SV surface valence bands. Taken from X. Liu *et al.*, Evidence of Topological Surface State in Three-Dimensional Dirac Semimetal Cd_3As_2, Sci. Rep. **4**, 6106 (2014), Attribution-NonCommercial-NoDerivatives 4.0 International (CC BY-NC-ND 4.0) [162] [170].

band models, as discussed in Sec. 8.4. Because of this, it is proposed that the signatures of surface states found in inversion Dirac semi-metals are due to the topological surface states or the massive Volkov-Pankratov states also found in HgTe.

This statement is supported by the observation of topological surface states in ARPES measurements on Cd_3As_2 in Ref. [170, 171]. The measurements of Ref. [170] are shown exemplary in Fig. 8.19. A linearly dispersing surface state is observed over a broad energy range. The energy range is much wider than the finite energy window of the anti-crossing gap of the order of $20 - 40\,meV$ [107]. This observation is in contrast to the expected behavior of Fermi-arcs. The observed broad energy range, however, fits the expectation for topological surface states. The existence of TSS also offers a simple and consistent explanation for the observed SdH oscillations and QHE for compressively strained HgTe in this work and also reported for Cd_3As_2. This contradicts the initially in the literature favored assignment of the observed SdH oscillations and QHE in Cd_3As_2 to Fermi-arcs (see Sec. 8.3), which is also questioned by other works, as Ref. [138]. The existence of topological surface states becomes more present in the literature, as Ref. [172]. To sum up, topological surface states and massive Volkov-Pankratov states offer a simple, and consistent explanation for the two-dimensional transport phenomena observed in inversion-induced Dirac semi-metals.

IV

CONCLUSION

SUMMARY

The motivation for this work has been contributing a step to the advancement of technology. A next leap in technology would be the realization of a scalable quantum computer. One potential route is via topological quantum computing. A profound understanding of topological materials is thus essential. My work contributes by the investigation of the exemplary topological material HgTe. The focus lies on the understanding of the topological surface states and new possibilities to manipulate them appropriately. Traditionally top gate electrodes are used to adjust the carrier density in such semi-conductor materials. We found that the electric field of the top gate can further alter the properties of the HgTe layer. The formation of additional massive Volkov-Pankratov states limits the accessibility of the TSS. The understanding of these states and their interplay with the TSS is necessary to appropriately design devices and to ensure their desired properties. Similarly, I observed the existence and stability of TSSs even without a bandgap in the bulk band structure in the inversion induced Dirac semi-metal phase of compressively strained HgTe. The finding of topological surface states in inversion-induced Dirac semi-metals provides a consistent and simple explanation for the observation reported for Cd_3As_2.

These observations have only been possible due to the high quality of the MBE grown HgTe layers and the access of different phases of HgTe via strain engineering. As a starting point I performed Magneto-transport measurements on 67 nm thick tensilely strained HgTe layers grown on a CdTe substrate. We observed multiple transport channels in this three-dimensional topological insulator and successfully identified them. Not only do the expected topological surface states exist, but also additional massive surface states have been observed. These additional massive surface states are formed due to the electrical field applied at the top gate, which is routinely used to vary the carrier density in the HgTe layer. The additional massive surface states are called Volkov-Pankratov states after B. A. Volkov and O. A. Pankratov. They predicted the existence of similar massive surface states at the interface of materials with mutually inverted bands. We first found indications for such massive Volkov-Pankratov states in high-frequency compressibility measurements for very high electron densities in a fruitful collaboration with LPA in Paris. Magneto-transport measurements and $k \cdot p$ calculations revealed that such Volkov-Pankratov states are also responsible for the observed hole transport. We also found indications for similar massive VPS in the electron regime, which coexist with the topological surface states. The topological surface states exist over the full investigated gate range including a regime of pure topological insulator transport. To increase the variability of the topological surface states we introduced a modulation doping layer in the buffer layer. This modulation doping layer also enabled us to separate and identify the top and bottom topological surface states.

We used the variability of the bulk band structure of HgTe with strain to engineer the band structure of choice using virtual substrates. The virtual substrates enable us to grow compressively strained HgTe layers that do not possess a bandgap, but instead linear crossing points. These layers are predicted to be Dirac semi-metals. Indeed I observed also topological surface states and massive Volkov-Pankratov states in the compressively strained

Dirac semi-metal phase. The observation of topological surfaces states also in the Dirac semi-metal phase has two consequences: First, it highlights that no bulk bandgap is necessary to observe topological surface states. Second, the observation of TSS also in the Dirac semi-metal phase emphasizes the importance of the underlying band inversion in this phase. I could not find any clear signatures of the predicted disjoint topological surface states, which are typically called Fermi-arcs. The presence of topological surface states and massive Volkov-Pankratov states offer a simple explanation for the observed quantum Hall effect and other two-dimensional transport phenomena in the class of inversion induced Dirac semi-metals, as Cd_3As_2. This emphasizes the importance of the inherent bulk band inversion of different topological materials and provides a consistent and elegant explanation for the observed phenomena in these materials. Additionally, it offers a route to design further experiments, devices, and thus the foundation for the induction of superconductivity and thus topological quantum computing.

Another possible path towards quantum computing has been proposed based on the chiral anomaly. The chiral anomaly is an apparent transport anomaly that manifests itself as an additional magnetic field-driven current in three-dimensional topological semimetals with a linear crossing point in their bulk band structure. I observed the chiral anomaly in compressively strained HgTe samples and performed multiple control experiments to identify the observed reduction of the magnetoresistance with the chiral anomaly. First, the dependence of the so-called negative magnetoresistance on the angle and strength of the magnetic field has been shown to fit the expectation for the chiral anomaly. Second, extrinsic effects as scattering could be excluded as a source for the observed negative MR using samples with different mobilities and thus impurity concentrations. Third, the necessity of the linear crossing point has been shown by shifting the electrochemical potential away from the linear crossing points, which diminished the negative magnetoresistance. Fourth, I could not observe a negative magnetoresistance in the three-dimensional topological insulator phase of HgTe. These observations together prove the existence of the chiral anomaly and verify compressively strained HgTe as Dirac semi-metal. Surprisingly, the chiral anomaly is also present in unstrained HgTe samples, which constitute a semi-metal quadratic band touching point. This observation reveals the relevance of the Zeeman effect for the chiral anomaly due to the lifting of the spin-degeneracy in these samples.

Additionally to the chiral anomaly, the Dirac semi-metal phase of compressively strained HgTe showed other interesting effects. For low magnetic fields, a strong weak-anti-localization has been observed. Such a strong weak-anti-localization correction in a three-dimensional layer is surprising and interesting. Additionally, non-trivial magnetic field strength and direction dependencies have been observed. These include a strong positive magnetoresistance for high magnetic fields, which could indicate a metal-insulator transition. On a more device-oriented note, the semi-metal phase of unstrained HgTe constitutes the lower limit of the by strain engineering adjustable minimal carrier density of the topological surface states and thus of very high mobility.

To sum up, topological surface states have been observed in the three-dimensional topological insulator phase and the Dirac semi-metal phase of HgTe. The existence and accessibility of topological surface states are thus independent of the existence of a bandgap in the bulk band structure. The topological surface states can be accompanied by massive Volkov-Pankratov states. These VPS are created by electric fields, which are routinely applied to adjust the carrier density in semiconductor devices. The theoretical predicted

chiral anomaly has been observed in the Dirac semi-metal phase of HgTe. In contrast to theoretical predictions, no indications for the Fermi-arc called disjoint surface states have been observed, but instead the topological and massive Volkov-Pankratov surface states have been found. These states are thus expected for all inversion-induced topological materials.

ZUSAMMENFASSUNG

Der technologische Fortschritt schreitet immer schneller voran. Um diese Entwicklung zu ermöglichen werden die Strukturen immer kleiner. Das Erreichen atomarer Größen könnte bald die Abkehr von der üblichen Miniaturisierung erfordern und den Sprung zu einer neuen Technologie erzwingen. Die Motivation dieser Arbeit ist es das Verständnis topologischer Materialien zu erweitern und so einen Beitrag zu der Realisierung eines solchen potenziellen Technologiesprungs zu leisten. Eine vielversprechende Möglichkeit zur Aufrechterhaltung der aktuellen Entwicklungsgeschwindigkeit ist die Realisierung eines skalierbaren Quantencomputers. Eine mögliche Umsetzung ist das topologische Quantum-Computing, das zum Beispiel durch induzierte Supraleitung in topologische Oberflächenzustände realisiert werden könnte. Das tiefgehende Verständnis der topologischen Oberflächenzustände und deren Manipulation ist ein Schwerpunkte dieser Arbeit. Der zweite Schwerpunkt wurde kürzlich auch als ein potenzieller Pfad zur Realisierung eines Quantencomputers basierend auf „chiralen Qubits" vorgeschlagen, nämlich dem Nachweis und die Untersuchung des Transportphänomens der sogenannten chiralen Anomalie in Dirac- und Weyl-Halbmetallen.

Die Untersuchungen in dieser Arbeit wurden am MBE gewachsenen topologischen Material HgTe durchgeführt. HgTe zeichnet sich dadurch aus, dass verschiedene topologische Phasen realisierbar sind. Dazu wird die HgTe-Schicht durch die Wahl entsprechender Substrate verspannt. Als Startpunkt für die Analyse der topologischen Oberflächenzustände habe ich die topologische Isolator-Phase gewählt. Diese wird durch ein gedehntes MBE-Wachstum der HgTe-Schicht auf einem CdTe-Substrat realisiert. Eine hohe Qualität der HgTe-Schicht und Oberfläche wurde dabei mit Hilfe von schützenden $Cd_{0.7}Hg_{0.3}Te$-Schichten gewährleistet. Wir haben zusätzlich eine Modulationsdoping Schicht in der unteren $Cd_{0.7}Hg_{0.3}Te$-Schicht eingeführt, die für eine kleine endliche Elektronendichte in der HgTe-Schicht sorgt. Diese Dotierung gewährleistet eine zuverlässige elektrische Kontaktierung. Aus diesen Waferstücken haben wir mit Hilfe optischer Lithografie und trocknen Ätzens so genannte Hall-Bars strukturiert, die aus einem Strompfad mit vier längs und quer angeordneten Spannungsabgriffen besteht. Eine Möglichkeit zur Kontrolle der Ladungsträgerdichte in der HgTe-Schicht wird über eine aufgedampfte Gate-Elektrode geschaffen. Diese Hall-Bars habe ich mit Hilfe von niedrig frequenten Wechselspannungsmessungen unter hohen Magnetfeldern bis zu 30 T bei tiefen Temperaturen von 2 K in Helium-Kryostaten bzw. 0.1 K in He^3/He^4-Misch-Kryostaten untersucht.

Die hohe Qualität der HgTe-Schicht spiegelt sich in den zuverlässig erreichten hohen Beweglichkeiten in der Größenordnung von $0.5 \times 10^6 \frac{cm^2}{Vs}$ im Elektronenregime und $0.03 \times 10^6 \frac{cm^2}{Vs}$ im Lochregime wieder. Eine Quantisierung des Magneto-Transport ist dadurch schon für kleine Magnetfelder von $B \gtrsim 0.5\,T$ beobachtbar. Dies ermöglichte mir die Analyse der Dispersion der Landau Levels und damit der Nachweis der Existenz von sechs zweidimensionalen Transportkanälen. Zwei dieser Kanäle konnten wir mit den topologischen Oberflächenzuständen identifizieren. Den Einfluss der Spannungen, die an der Gate-Elektrode angelegt wurden, haben wir in hoch frequenten Kompressibilitätsmessungen fest-

gestellt. In diesen Messungen haben wir für sehr hohe Elektrodenspannungen Hinweise auf zusätzliche massive Volkov-Pankratov Zustände gefunden. Der Name ist dabei gewählt worden, um die Vorhersage derartiger Zustände durch B. A. Volkov und O. A. Pankratov zu würdigen. Den Ursprung der vier weiteren Transportkanäle konnten wir mit Hilfe von Bandstrukturberechnungen auf zusätzliche Oberflächenzustände zurückführen. Die Berechnung haben wir mit Hilfe des Kane Models in der $k \cdot p$ Näherung unter Beachtung der Hatree Potentiale, welche die angelegte Spannung an der Gate-Elektrode repräsentieren, durchgeführt. Die elektronenartigen topologischen Oberflächenzustände konnten für den ganzen untersuchten Elektrodenspannungsbereich nachgewiesen werden. Wir haben aber auch ein signifikantes und manipulierbares Elektrodenspannungsfenster gefunden, in welchem nur topologische Oberflächenzustände besetzt sind.

Eine Möglichkeit zur Manipulation der Eigenschaften der topologischen Oberflächenzustände ist die Variation der Verspannung mit Hilfe des MBE-Wachstums auf virtuellen Substraten aus alternierenden $Cd_{0.5}Zn_{0.5}Te$- und CdTe-Schichten mit einstellbarer Gitterkonstante. Die HgTe-Schicht haben wir durch das Wachstum auf ein entsprechendes virtuelles Substrates druck- anstatt zugverspannt. Die HgTe-Schicht befindet sich dadurch in der Dirac-Halbmetall anstatt der dreidimensionalen topologischen Isolator-Phase. Dirac-Halbmetalle zeichnen sich durch einen linearen Kreuzungspunkt der Volumenmaterialbänder aus. Ich konnte topologische Oberflächenzustände und massive Volkov-Pankratov Zustände auch in der Dirac-Halbmetall-Phase nachweisen. Dieser Umstand weist die Existenz und Stabilität der topologischen Oberflächenzustände auch ohne Bandlücke in der Bandstruktur des Volumenmaterials nach. Des Weiteren betont die Anwesenheit der topologischen Oberflächenzustände die Relevanz der inhärenten Bandinversion für die Klasse der inversionsinduzierten Dirac-Halbmetalle. In druckverspanntem HgTe habe ich QHE beobachtet, der nur in zweidimensionalen Systemen auftritt. Ähnliche Beobachtungen wurden auch für andere Dirac-Halbmetalle, wie Cd_3As, berichtet. Die topologischen Oberflächenzustände schlage ich als einfache und einheitliche Erklärung für diesen zweidimensionalen Transport vor.

Die Anwesenheit linearer Kreuzungspunkte in der Volumenmaterialbandstruktur druckverspannten HgTes konnte ich durch die Beobachtung der chiralen Anomalie nachweisen. Damit konnte ich nicht nur druckverspanntes HgTe als Dirac-Halbmetall nachweisen, sondern auch einen Beitrag zum besseren Verständnis der chiralen Anomalie leisten. Des Weiteren haben elektrodenspannungsabhängige Messungen gezeigt, dass parallel anwesende Oberflächenzustände das Signal der chiralen Anomalie zwar überlagern, dieses aber nicht verhindern. Außerdem habe ich Untersuchungen an unterspannten HgTe Schichten durchgeführt, welche Halbmetalle mit einem Berührungspunkt zweier Bänder mit quadratischer Dispersion darstellen. Auch in diesen Schichten wurde die chirale Anomalie beobachtet. Dies verdeutlicht die Relevanz des Zeeman-Effektes für die Ausbildung der chiralen Anomalie in HgTe. Die chirale Anomalie zeigte eine unerwartet Magnetfeldrichtungsabhängigkeit im Bezug zur Stromrichtung. Diese Magnetfeldrichtungsabhängigkeit betont die Notwendigkeit der Beschreibung des Widerstandes als Tensor, damit die dreidimensionale Ausdehnung der experimentellen Proben und der daraus folgenden Effekte, wie dem Planar-Halleffekt, korrekt beschrieben werden. Des Weiteren habe ich eine für dreidimensionale Proben außergewöhnlich stark ausgeprägte Weak-Antilokalisierung beobachtet. Diese könnte spezifisch für topologische Halbmetalle sein, da ähnliche Beobachtungen auch für das Weyl Halbmetall TaA berichtet wurden.

Das Ziel dieser Arbeit war es einen Beitrag zum technologischen Fortschritt durch das bessere Verständnis topologischer Materialen zu leisten. Dieses Ziel konnte somit erreicht werden. Wir können alle Zustände, die wir in dem dreidimensionalen topologischen Isolator zugverspanntes HgTe beobachtet haben, ihrem Ursprung zuordnen. Dies ermöglicht uns die Präparation und Manipulation der gewünschten Zustände für komplexe Bauteile, wie topologische und supraleitende Hybridstrukturen, zu optimieren. Ich konnte auch zum besseren Verständnis der Materialklasse der inversionsinduzierten Dirac-Halbmetalle beigetragen, indem ich die an druckverspannten HgTe gewonnen Erkenntnisse auf die gesamte Materialklasse der inversionsinduzierten Dirac-Halbmetalle verallgemeinern konnte. Dies ist zum Beispiel anhand des Nachweises der Anwesenheit von topologischen Oberflächenzuständen geschehen. Außerdem konnte ich neue Einblicke in die chirale Anomalie gewinnnen. Die Existenz linearer Kreuzungspunkte in der Volumenmaterialbandstruktur wurde dabei als notwendige Bedingung bestätigt. Damit konnte ich einen Beitrag zum Verständnis der Grundbausteine für zwei mögliche Pfade zu einem potenziellen Quantencomputer in der Form von zug- und druckverspanntem HgTe leisten.

8

A

THOMAS FERMI SCREENING

A significant part of this thesis evolves around the change of the occupation of different states with the help of an electric field in a plate capacitor like device. Since topological material are surrounded by topological surface states, the screening properties of these states are especially of interest. A simple estimation of the screening properties can be made by comparing the Thomas Fermi screening length l_{TF} of the TSS to its localization length l_{loc}. The localization length is determined using the program "kdotpy" [29] to calculate the probability distribution of the TSS along the stacking direction z, which is shown in Fig. A.1a) and yields a localization length of $l_{\mathrm{loc}} \sim 10\,\mathrm{nm}$. The screening length l_{TF} of the TSS is estimated following Ref. [173]. The TSS is assumed to disperse linearly with quadratic corrections due to the hybridization with bulk bands, which yields

$$l_{\mathrm{TF}} = \frac{1 + \mathrm{sgn}(n)\sqrt{\frac{|n|}{n_0}}}{r_s k_F} \tag{A.1}$$

with the parameters

$$r_s = \frac{e^2}{\epsilon_{\mathrm{TSS}} \epsilon_0 \hbar v_F}, \quad n_0 = \frac{m_{\mathrm{eff}}^2 v_F^2}{3\pi \hbar^2}, \tag{A.2}$$

where

$$k_F = \sqrt{4\pi n} \tag{A.3}$$

is the Fermi wave vector for a non-degenerate 2DEG and ϵ_{TSS} is the dielectric constant of the TSS. Since the exact value of ϵ_{TSS} is unknown, the screening length is calculated for multiple values of the dielectric constant. The resulting screening lengths are shown as function of the carrier density n in Fig. A.1. The bulk value of $\epsilon_{\mathrm{HgTe}} \sim 21$ [47] is chosen as upper limit for the estimation, which gives the longest screening length. Alternative values for the dielectric constant of the TSS are half the bulk value and the dielectric constant of graphene $\epsilon_{\mathrm{graphene}} = 3$ as suggested in Ref. [173] and Ref. [47], respectively. Even for the most pessimistic estimation based on the bulk dielectric constant $\epsilon = 21$, the Thomas Fermi screening lengths l_{TF} is already for $n \sim 0.5 \times 10^{-11}\,\mathrm{cm}^{-2}$ shorter than the localization length $l_{\mathrm{loc}} \sim 10\,\mathrm{nm}$. The minimal accessible density in 0.3 % tensilely strained HgTe is given by the DOS of the TSS at the valence band edge. The corresponding Fermi wave vector of the TSS estimated with the program "kdoptpy" $k_{\mathrm{F;kp}} \sim 0.95 \times 10^6\,\mathrm{cm}^{-1}$ as shown for example in Fig. 2.6g), yields using Eq. A.3 a minimal density $n \sim 0.5 \times 10^{-11}\,\mathrm{cm}^{-2}$. By this estimation, the TSS is expected to always be able to screen the applied electric fields.

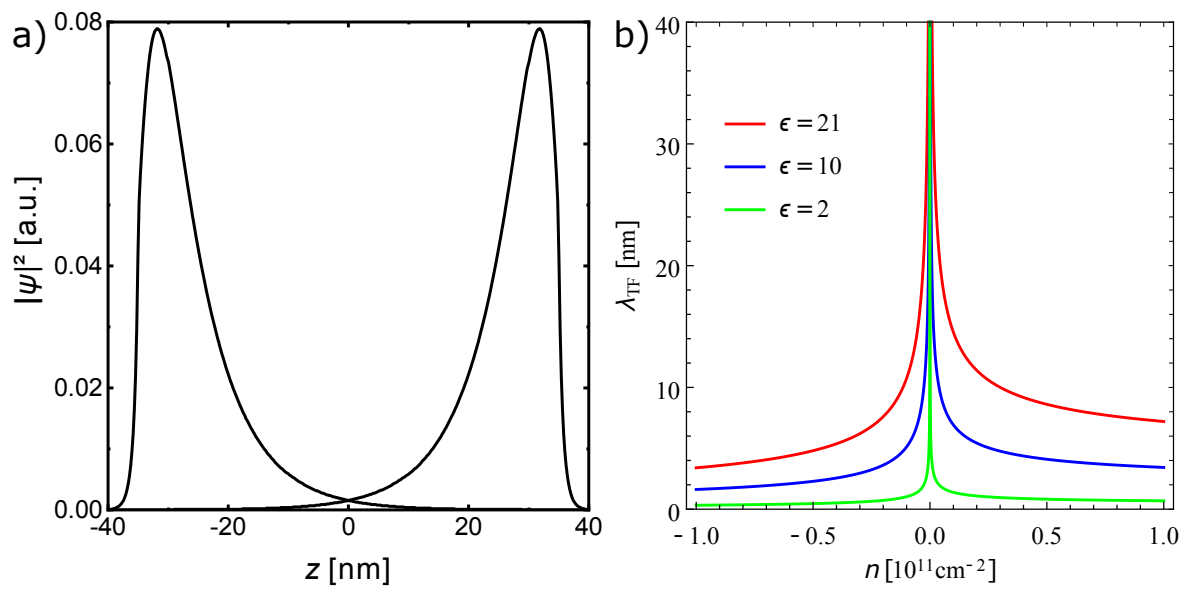Figure A.1: In a) the probability distribution $|\Phi|^2$ of the TSS is shown for a 70 nm thick 0.3 % tensilely strained HgTe layer for $k = 0.15\,\mathrm{nm}^{-1}$ calculated with the program "kdotpy" [29]. In b) the Thomas-Fermi screening length l_{TF} is shown as function of the carrier density n for a TSS with linear dispersion and quadratic corrections for different dielectric constants ϵ.

B

QUANTUM OSCILLATIONS WITHOUT A FERMI SURFACE

Quantum oscillations are a common occurrence in measurements on conductors in a magnetic field. The magnetic field pushes Landau Levels (LL) through the Fermi level causing oscillations in the DOS which manifest in well-known effects such as de Haas-van Alphen and Shubnikov-de Haas (SdH). It has recently been discovered that this description of quantum oscillations may be incomplete. Tan *et al.* reported $1/B$-quantum oscillations in the magnetization in the Kondo insulator SmB_6 when the Fermi level is in the gap of the material [55]. There are various interpretations discussed in the literature as addressed in Ref. [56]. A common one is to interpret this observation as resulting from Landau levels crossing, instead of the Fermi level, an extremum in the DOS. Such an extremum can be induced by the presence of a hybridization gap that leads to a non-monotonic dispersion of the bulk bands [53, 54].

The mechanism is illustrated in the cartoon of Fig. B.1 based on the band structure of tensilely strained HgTe. The crucial feature is that the hybridization causes a non-monotonic energy dispersion at the top of the valence band. Because of this, as the magnetic field is increased, Landau levels (yellow) first move up in energy until they reach the local extrema of the valence band (red), and then start moving downwards in energy. Since the carriers reside in the Landau levels, the effective position of the valence band maximum is thus modulated, as these LLs flow through the local extrema of the valence band (red). The effective size of the gap between the valence and conduction bands thus slightly oscillates as a function of the magnetic field.

We observed very pronounced $1/B$ period oscillations down to magnetic fields below $0.1\,\text{T}$ with a frequency $f = 2.5\,\text{T}$ as shown in Fig. 2.8c). Their oscillation frequency varied only about $\pm 25\,\%$ for tensilely strained HgTe layers grown on CdTe substrates. A strong change of this frequency has only been observed for less tensilely strained HgTe layers. Such a low variation in the occupation of the topological surface state across these samples seemed unlikely. The band structure and hence the shape of the valence band, in contrast, should be comparable across these samples, which makes the mechanism of quantum oscillations without a Fermi surface intriguing [42]. Further investigations with modulation doping and back gates trace these oscillations to the topological surface states (see Chapter 3 and Ref. [58]).
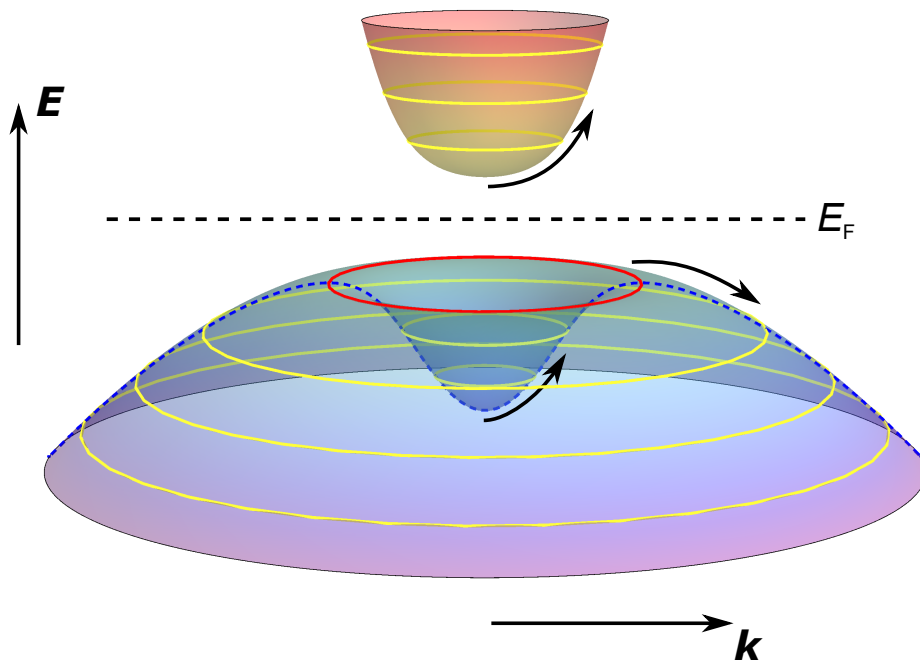
Figure B.1: A diagram of the bottom of the conduction and top of the valence band is shown for a finite magnetic field. The emerging Landau levels are represented by yellow circles. The black arrows indicate the direction of flow of the Landau levels as the magnetic field is increased. The red circle highlights the area surrounded by the top of the valence band in the absence of the magnetic field. The bulk Fermi level located inside the gap is indicated by the dashed line.

C

TEMPERATURE DEPENDENCE OF THE SEMI-CLASSICAL REGIME

In the 3D-TI tensilely strained HgTe is a dip in the longitudinal resistance R_{xx} for low magnetic fields around $B = 0\,$T observed. This dip is not due to WAL, but due to the involvement of multiple carrier densities. This is verified by the temperature dependence of this dip in the longitudinal resistance. The longitudinal resistance R_{xx} is shown as function of the magnetic field B for multiple temperatures T in Fig. C.1. The dip in the longitudinal resistance R_{xx} is stable up to the highest measured temperature of $T = 4\,$K. For low temperatures are also well pronounced SdH oscillations observed. The SdH oscillations are a consequence of the formation of Landau levels and thus a quantum effect. Similarly, the WAL describes a correction to the conductance due to self-interference and hence is also a quantum correction. Consequently, the higher temperature should diminish the WAL in a similar fashion as the SdH oscillations, which is not observed. The WAL dip observed in the Dirac semi-metal compressively strained HgTe shows a strong temperature dependence for this temperature range, as discussed in Sec. 7.5.1 and shown in Fig. 7.18. This makes WAL an unlikely mechanism. In contrast, the dip in the longitudinal resistance is likely a consequence of the involvement of multiple transport channels, which does not possess a strong temperature dependence, as observed in Fig. C.1.
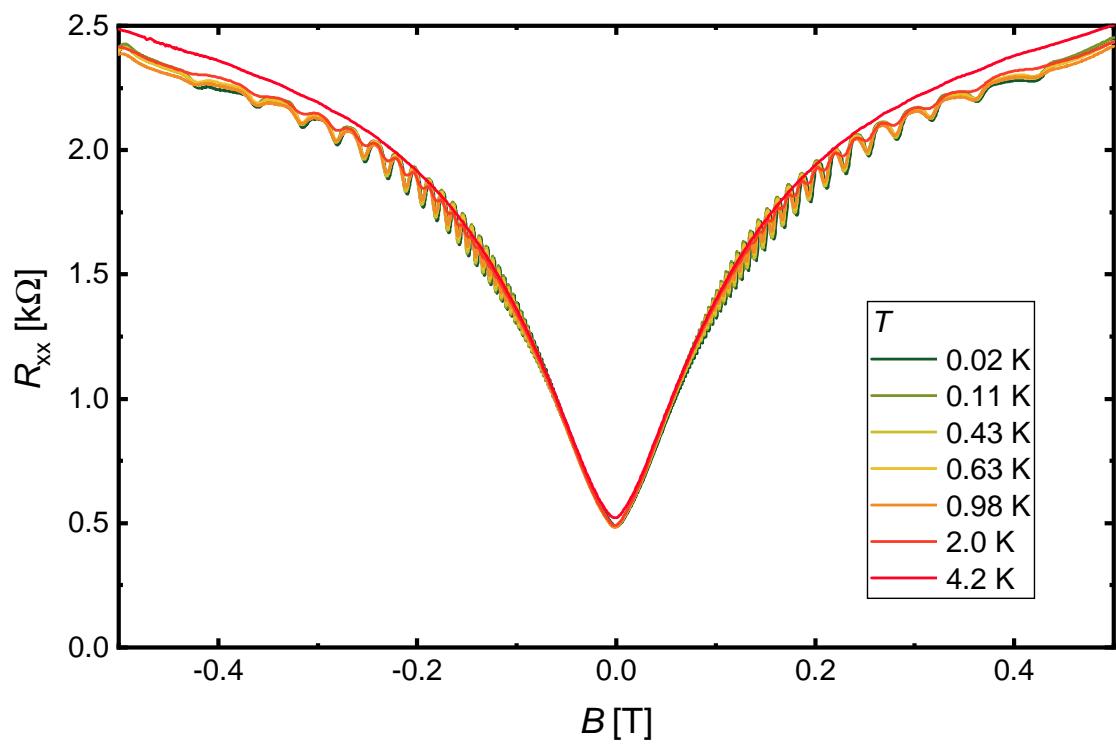
Figure C.1: The longitudinal resistance R_{xx} of the tensilely strained HgTe sample Q2584 is shown as a function of the magnetic field B at a low overall hole density for different temperatures T.

D

REPRODUCIBILITY OF THE FAST FOURIER ANALYSIS RESULTS

The high mobility of the samples enables the observation of well-pronounced SdH oscillations in the longitudinal resistance down to low magnetic fields $B < 0,2\,\mathrm{T}$. For these low magnetic fields, the SdH oscillations are still nicely sinusoidal, in contrast to the peak-like shape observed for high magnetic fields. This enables the analysis of the observed oscillations with the help of a FFT analysis. Since the measurement signal is nevertheless neither perfectly sinusoidal nor infinite, the reliability and credibility of the FFT analysis are addressed in this Section. The FFT results shown in this work are either obtained using the program "Wolfram Mathematica 12" [175] which provides its own FFT routine or the program "OriginPro 2018/2020" [174] which uses the adaptive software architecture for FFT library "fftw" [176]. The reliability and reproducibility of the FFT analysis is summarized in Fig. 3.12. As starting point the longitudinal resistance R_{xx}, its second derivative with respect to the magnetic field $d^2 R_{xx}/dB^2$ and the derivative of the Hall resistance with respect to the magnetic field dR_{xy}/dB are shown as exemplary measurement signals in Fig. D.1a). The presented data resembles a cut through the Landau level dispersion shown in Fig. 3.9 for the gate voltage $U_{\mathrm{gate}} = -1\,\mathrm{V}$. The data is interpolated to provide constant steps in the inverse magnetic field B^{-1} to provide equidistant sampling points for the FFT analysis. The resulting FFT spectrum determined with the program "OriginPro 2018/2020" is shown in Fig. D.1b). The x-axis is converted from frequency into density using $n = \frac{e}{h} f$ under the assumption of no degeneracy. All FFT results presented elsewhere in this work are based on the longitudinal resistance R_{xx} data to minimize the necessary data processing steps, as the numeric differentiation. All three obtained FFT spectra show two pronounced peaks at $n_2 = 1.7 \times 10^{11}\,\mathrm{cm}^{-2}$ and $n_3 = 2.0 \times 10^{11}\,\mathrm{cm}^{-2}$ as well as a peak at $n_1 = 0.6 \times 10^{11}\,\mathrm{cm}^{-2}$. The absolute amplitude of the peaks depends on the chosen signal. The variation is consistent with the strong variation in the amplitudes of the oscillations in the data shown in Fig. D.1a). The quantity of interest is not the amplitude, but the number of peaks that correspond to the number of conducting channels and their respective peak positions in density n representing their carrier density. Since the amplitude and shape of the oscillations depend on the magnetic field, the FFT analysis is repeated for different ranges of the magnetic field. The resulting FFT spectra are shown in Fig. D.1c) and yield consistent peak positions. The limitation of the analyzed spectrum to moderate magnetic fields $B < 5\,\mathrm{T}$ the n_1 peak is revealed as a double peak. For higher magnetic fields the QH regime deforms

the SdH oscillations from sinusoidal to separated peaks which hampers the FFT analysis and thus broadens the observed features. This is why a limited magnetic field range is used for the FFT in this work and especially for the spectrum presented in Sec. 3.4. To perform a FFT analysis the measured data has to be effectively repeated consecutively and infinitely. The data is therefore folded with a so-called window function to create an infinite periodic signal. The FFT spectra obtained using different window function are shown in Fig. D.1d). The chosen window functions are known to be appropriate to preserve the frequency and thus the density [177]. The "Hamming" window does not seem to be appropriate for the analyzed signal type. The other three window functions, namely "Dreieck", "Hanning" and "Welch" yield very similar results. The "Hanning" window resolves the double peak at n_1 also for the full magnetic field range but yields a factor of 10 smaller amplitudes in total. To summarize the FFT results presented in this work are obtained using the program "Origin 2018/2020" with the "Welch" window and an appropriate magnetic field range or the internal FFT routine of the program "Wolfram Mathematica 12".
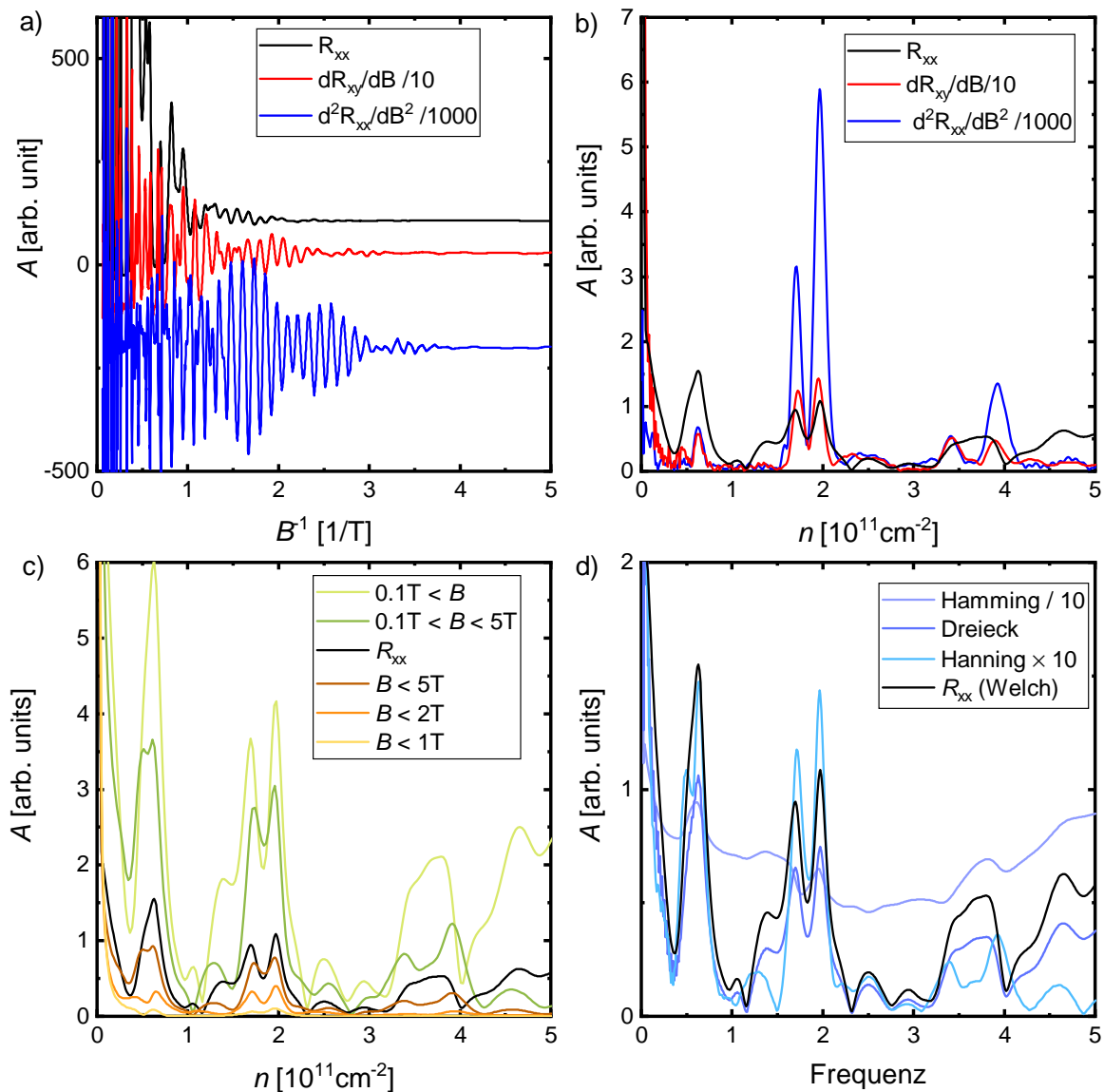
Figure D.1: In a) the exemplary measurement data of QC0501 for $U_{\text{gate}} = -1\,\text{V}$ is shown as the longitudinal resistance R_{xx} in black, the derivative of the Hall resistance with respect to the magnetic field dR_{xy}/dB in red and the second derivative of the longitudinal resistance with respect to the magnetic field d^2R_{xx}/dB^2 in blue in function of the inverse magnetic field B^{-1}. The curves are offset by 100, respectively. In b) the corresponding FFT spectrum of the data determined using a Welch window is shown as a function of the carrier density n, which is calculated from the determined frequency assuming no degeneracy. The FFT analysis of the longitudinal resistance R_{xx} data is shown for various ranges of the magnetic field B in c) and for different window functions in d). The analysis is performed using the program "Origin 2020" [174].

LIST OF PUBLICATIONS

- OBSERVATION OF VOLKOV-PANKRATOV STATES IN TOPOLOGICAL HGTE HETERO-JUNCTIONS USING HIGH-FREQUENCY COMPRESSIBILITY.
  A. Inhofer, S. Tchoumakov, G. Fève, J. M. Berroir, V. Jouffrey, D. Carpentier, M. O. Goerbig, B. Plaçais, K. Bendias, **D. M. Mahler**, E. Bocquillon, R. Schlereth, C. Brüne, H. Buhmann, and L. W. Molenkamp,
  Phys. Rev. B **96**, 195104 (2017).

- INTERPLAY OF DIRAC NODES AND VOLKOV-PANKRATOV SURFACE STATES IN COMPRESSIVELY STRAINED HGTE.
  D. M. Mahler, J.-B. Mayer, P. Leubner, L. Lunczer, D. Di Sante, G. Sangiovanni, R. Thomale, E. M. Hankiewicz, H. Buhmann, C. Gould and L.W. Molenkamp,
  Phys. Rev. X **9**, 031034 (2019).

- MASSIVE AND TOPOLOGICAL SURFACE STATES IN TENSILE STRAINED HGTE.
  D. M. Mahler, V. L. Müller, C. Thienel, L. Lunczer, J. Wiedenmann, W. Beugeling, H. Buhmann, and L.W. Molenkamp,
  Nano Letters **21**, 23, 9869–9874 (2021).

ACKNOWLEDGEMENTS

This work would not have been possible without the help of a large group of people. Here, I would like to sincerely thank all of you.

- Laurens, thank you for giving me the opportunity to work as a Ph.D. student in your chair EP III and your guidance.

- Hartmut, thank you for accepting me as a Ph.D. student, the positive and supportive work atmosphere in your group, and your support and trust in me.

- Charles, thank you for treating me as one of your Ph.D. students and for your help in the lab and with manuscripts.

- Wouter, thank you for providing such an easy to use and powerful band structure calculations tool and your patient explanations.

- I am also very grateful for the numerous fruitful discussions, explanations, and calculations from our theoretical collaborators Ewelina, Jan, and Benny from TP4 as well as Giorgio, Domenico, and Ronny from TP1.

- Thomas and Steffen, thank you for the sleep robing, but nevertheless very enjoyable and productive measurement session in the high field magnet laboratory in Nijmegen as well as your input on equipment design.

- Erwann, Andreas, and Bernard, thank you for the excursion into the world of high-frequency measurements and Paris.

- Cornelius and Jonas, thank you for introduction into the world of topological materials and magneto-transport.

- Budy, thank you for the rescue from any technical issues in the lab and for always creating a positive atmosphere.

- Kalle, thank your for the sample fabrication and the good time in Paris.

- Christopher, Raimund, Philipp, and Lukas, thank you for "just growing that stuff".

- Valentin, thank you for the headache-causing puzzling, but fruitful discussions and collaboration in the lab.

- I also appreciate the support of the work by Fabian as a master student and several bachelor students: Janice, Philip, Philipp, Alexander B., and Alexander W.

- I am also very thankful for the technical support and patience with an "only things breaking physicist" from the electronic and mechanic workshop, especially Roland, Cornelius, Utz, and Rainer, and the EP3-technicians Martin and Volkmar.

- Mirko thank you for design the new in-plane rotation stick.

- Madder thank you for sharing the journey towards this thesis with me and for the occasional detours in the strange world of metals.

- Gracy for your legendary motivational speeches and the introduction to Brazilian cuisine.

A big thank you to all members of EP3 for your help and the friendly and productive working atmosphere. Especially I want to mention our EP3 skiing, volleyball, wine fest, and coffee team: Madder, Lukas, Simon, Jonas, Mirko, Gracy, Steffen, Erwann, Philipp, Cornelius, and our EP7 substitute Tim.

I am also grateful for the funding by the SFB 1170 and the Elitenetzwerk Bayern.

Finally, I want to thank my family, especially my mom Simone, my sister Lena, and my girlfriend Kathi, but also my aunts and uncles, cousins, and grandparents for their continuous support and interest in my endeavors.

References

[1] O. Vafek and A. Vishwanath, *Dirac Fermions in Solids: From High-T_c Cuprates and Graphene to Topological Insulators and Weyl Semimetal,* Annu. Rev. Condens. Matter Phys. **5**, 83 (2014).

[2] C. L. Kane and E. J. Mele, *Z_2 Topological Order and the Quantum Spin Hall Effect,* Phys. Rev. Lett. **95**, 146802 (2005).

[3] B. A. Bernevig, T. L. Hughes, and S. C. Zhang, *Quantum Spin Hall Effect and Topological Phase Transition in HgTe Quantum Wells,* Science **314**, 1757 (2006).

[4] M. König, S. Wiedmann, C. Brüne, A. Roth, H. Buhmann, L. W. Molenkamp, X.-L. Qi, and S.-C. Zhang, *Quantum Spin Hall Insulator State in HgTe Quantum Wells,* Science **318**, 766 (2007).

[5] L. Fu and C. L. Kane, *Topological insulators with inversion symmetry,* Phys. Rev. B **76**, 045302 (2007).

[6] D. Hsieh, D. Qian, L. Wray, Y. Xia, Y. S. Hor, R. J. Cava, and M. Z. Hasan, *A topological Dirac insulator in a quantum spin Hall phase,* Nature **452**, 970 (2008).

[7] P. Roushan, J. Seo, C. V. Parker, Y. S. Hor, D. Hsieh, D. Qian, A. Richardella, M. Z. Hasan, R. J. Cava, and A. Yazdani, *Topological surface states protected from backscattering by chiral spin texture,* Nature **460**, 1106 (2009).

[8] C. Brüne, C. X. Liu, E. G. Novik, E. M. Hankiewicz, H. Buhmann, Y. L. Chen, X. L. Qi, Z. X. Shen, S. C. Zhang, and L. W. Molenkamp, *Quantum Hall effect from the topological surface states of strained bulk HgTe,* Phys. Rev. Lett. **106**, 126803 (2011).

[9] P. A. M. Dirac, *The quantum theory of the electron,* Proc. R. Soc. London. Ser. A, Contain. Pap. a Math. Phys. Character **117**, 610 (1928).

[10] H. Weyl, *GRAVITATION AND THE ELECTRON,* Proc. Natl. Acad. Sci. **15**, 323 (1929).

[11] N. P. Armitage, E. J. Mele, and A. Vishwanath, *Weyl and Dirac semimetals in three-dimensional solids,* Rev. Mod. Phys. **90**, 015001 (2018).

[12] X. Wan, A. M. Turner, A. Vishwanath, and S. Y. Savrasov, *Topological semimetal and Fermi-arc surface states in the electronic structure of pyrochlore iridates,* Phys. Rev. B **83**, 205101 (2011).

[13] V. Lahtinen and J. Pachos, *A Short Introduction to Topological Quantum Computation,* SciPost Phys. **3**, 021 (2017).

[14] J. Wiedenmann, E. Bocquillon, R. S. Deacon, S. Hartinger, O. Herrmann, T. M. Klapwijk, L. Maier, C. Ames, C. Brüne, C. Gould, A. Oiwa, K. Ishibashi, S. Tarucha, H. Buhmann, and L. W. Molenkamp, *4π-periodic Josephson supercurrent in HgTe-based topological Josephson junctions,* Nat. Commun. **7**, 10303 (2016).

[15] D. E. Kharzeev and Q. Li, *The Chiral Qubit: quantum computing with chiral anomaly,* (2019), arXiv:1903.07133 .

[16] B. A. Volkov and O. A. Pankratov, *Two-dimensional massless electrons in an inverted contact,* J. Exp. Theor. Phys. Lett. **42**, 145 (1985).

[17] S. Tchoumakov, V. Jouffrey, A. Inhofer, E. Bocquillon, B. Plaçais, D. Carpentier, and M. O. Goerbig, *Volkov-Pankratov states in topological heterojunctions,* Phys. Rev. B **96**, 201302 (2017).

[18] D. J. Chadi, J. P. Walter, M. L. Cohen, Y. Petroff, and M. Balkanski, *Reflectivities and electronic band structures of CdTe and HgTe,* Phys. Rev. B **5**, 3058 (1972).

[19] A. Pfeuffer-Jeschke, *Bandstruktur und Landau-Niveaus quecksilberhaltiger II-VI Heterostrukturen*, Ph.D. thesis, Universität Würzburg (2000).

[20] L. Voon and M. Willatzen, *The k p Method: Electronic Properties of Semiconductors* (Springer, 2009) p. 445.

[21] S. Bloom and T. K. Bergstresser, *Band structure of HgSe and HgTe,* Phys. status solidi **42**, 191 (1970).

[22] E. O. Kane, *Band structure of indium antimonide,* J. Phys. Chem. Solids **1**, 249 (1957).

[23] J. M. Luttinger, *Quantum theory of Cyclotron Resonance in Semiconductors: General Theory,* Phys. Rev. **102**, 1030 (1956).

[24] M. Kharitonov, J.-B. B. Mayer, and E. M. Hankiewicz, *Universality and Stability of the Edge States of Chiral-Symmetric Topological Semimetals and Surface States of the Luttinger Semimetal,* Phys. Rev. Lett. **119**, 266402 (2017).

[25] P. Leubner, *Strain-engineering of the Topological Insulator HgTe*, Ph.D. thesis, Universität Würzburg (2016).

[26] G. L. Pikus and G. E. Bir, *Symmetry and strain-induced effects in semiconductors* (Wiley, 1974) p. 484.

[27] L. Liu and W. Leung, *Transport property of zero-gap semiconductors under tensile stress,* Phys. Rev. B **12**, 2336 (1975).

[28] G. Dresselhaus, A. F. Kip, and C. Kittel, *Cyclotron resonance of electrons and holes in silicon and germanium crystals,* Phys. Rev. **98**, 368 (1955).

[29] W. Beugeling, *kdotpy: kp bandstructure calculation program,* (2017).

[30] I. Tsidilkovski, G. Harus, and N. Shelushinina, *Impurity states and electron transport in gapless semiconductors,* Adv. Phys. **34**, 43 (1985).

[31] M. Orlita, D. M. Basko, M. S. Zholudev, F. Teppe, W. Knap, V. I. Gavrilenko, N. N. Mikhailov, S. A. Dvoretskii, P. Neugebauer, C. Faugeras, A. L. Barra, G. Martinez, and M. Potemski, *Observation of three-dimensional massless Kane fermions in a zinc-blende crystal,* Nat. Phys. **10**, 233 (2014).

[32] R. Schlereth, *New techniques and improvements in the MBE growth of Hg-containing narrow gap semiconductors*, Ph.D. thesis, Universität Würzburg (2020).

[33] O. A. Pankratov, S. V. Pakhomov, and B. A. Volkov, *Supersymmetry in heterojunctions: Band-inverting contact on the basis of* $Pb_{1-x}Sn_xTe$ *and* $Hg_{1-x}Cd_xTe$, Solid State Commun. **61**, 93 (1987).

[34] D. M. Mahler, J.-B. Mayer, P. Leubner, L. Lunczer, D. Di Sante, G. Sangiovanni, R. Thomale, E. M. Hankiewicz, H. Buhmann, C. Gould, and L. W. Molenkamp, *Interplay of Dirac Nodes and Volkov-Pankratov Surface States in Compressively Strained HgTe*, Phys. Rev. X **9**, 031034 (2019).

[35] T. Royal Swedish Academy of Sciences, *Press Release - The Nobel Prize in Physics 2016*, (2016).

[36] D. Hsieh, Y. Xia, D. Qian, L. Wray, J. H. Dil, F. Meier, J. Osterwalder, L. Patthey, J. G. Checkelsky, N. P. Ong, A. V. Fedorov, H. Lin, A. Bansil, D. Grauer, Y. S. Hor, R. J. Cava, and M. Z. Hasan, *A tunable topological insulator in the spin helical Dirac transport regime*, Nature **460**, 1101 (2009).

[37] F. Ortmann, S. Roche, and S. O. Valenzuela, *Topological Insulators: Fundamentals and Perspectives* (Wiley, 2015) p. 407.

[38] M. Z. Hasan and C. L. Kane, *Colloquium : Topological insulators*, Rev. Mod. Phys. **82**, 3045 (2010).

[39] X.-L. Qi and S.-C. Zhang, *Topological insulators and superconductors*, Rev. Mod. Phys. **83**, 1057 (2011).

[40] J. Wiedenmann, *Induced topological superconductivity in HgTe based nanostructures*, Ph.D. thesis, Universität Würzburg (2018).

[41] C. Liu, G. Bian, T.-R. R. Chang, K. Wang, S.-Y. Y. Xu, I. Belopolski, I. Miotkowski, H. Cao, K. Miyamoto, C. Xu, C. E. Matt, T. Schmitt, N. Alidoust, M. Neupane, H.-T. T. Jeng, H. Lin, A. Bansil, V. N. Strocov, M. Bissen, A. V. Fedorov, X. Xiao, T. Okuda, Y. P. Chen, and M. Z. Hasan, *Tunable spin helical Dirac quasiparticles on the surface of three-dimensional HgTe*, Phys. Rev. B **92**, 115436 (2015).

[42] D. M. Mahler, J. Wiedenmann, C. Thienel, C. Ames, J. Böttcher, P. Leubner, R. Schlereth, F. Schmitt, C. Brüne, H. Buhmann, D. Di Sante, C. Gould, E. M. Hankiewicz, G. Sangiovanni, and L. W. Molenkamp, *Observation of 1/B oscillations from an insulating topological state of matter*, to be published .

[43] X. C. Zhang, A. Pfeuffer-Jeschke, K. Ortner, V. Hock, H. Buhmann, C. R. Becker, and G. Landwehr, *Rashba splitting in n-type modulation-doped HgTe quantum wells with an inverted band structure*, Phys. Rev. B **63**, 245305 (2001).

[44] C. Ames, *Molecular Beam Epitaxy of 2D and 3D HgTe, a Topological Insulator*, Ph.D. thesis, Universität Würzburg (2015).

[45] K. Bendias, S. Shamim, O. Herrmann, A. Budewitz, P. Shekhar, P. Leubner, J. Kleinlein, E. Bocquillon, H. Buhmann, and L. W. Molenkamp, *High Mobility HgTe Microstructures for Quantum Spin Hall Studies*, Nano Lett. **18**, 4831 (2018).

[46] D. A. Kozlov, Z. D. Kvon, E. B. Olshanetsky, N. N. Mikhailov, S. A. Dvoretsky, and D. Weiss, *Transport Properties of a 3D Topological Insulator based on a Strained High-Mobility HgTe Film,* Phys. Rev. Lett. **112**, 196801 (2014).

[47] C. Brüne, C. Thienel, M. Stuiber, J. Böttcher, H. Buhmann, E. G. Novik, C.-X. Liu, E. M. Hankiewicz, and L. W. Molenkamp, *Dirac-Screening Stabilized Surface-State Transport in a Topological Insulator,* Phys. Rev. X **4**, 041045 (2014).

[48] Y. Xu, I. Miotkowski, C. Liu, J. Tian, H. Nam, N. Alidoust, J. Hu, C.-K. Shih, M. Z. Hasan, and Y. P. Chen, *Observation of topological surface state quantum Hall effect in an intrinsic three-dimensional topological insulator,* Nat. Phys. **10**, 956 (2014).

[49] A. Jost, M. Bendias, J. Böttcher, E. Hankiewicz, C. Brüne, H. Buhmann, L. W. Molenkamp, J. C. Maan, U. Zeitler, N. Hussey, and S. Wiedmann, *Electron–hole asymmetry of the topological surface states in strained HgTe,* Proc. Natl. Acad. Sci. **114**, 3381 (2017).

[50] C. Thienel, *Exploring the transport properties of the three-dimensional topological insulator material HgTe,* Ph.D. thesis, Universität Würzburg (2015).

[51] J. Wiedenmann, *Quanten-Hall-Effekt eines relativistischen Systems,* Master thesis, Universität Würzburg (2013).

[52] L. Bockhorn, P. Barthold, D. Schuh, W. Wegscheider, and R. J. Haug, *Magnetoresistance in a high-mobility two-dimensional electron gas,* Phys. Rev. B **83**, 113301 (2011).

[53] J. Knolle and N. R. Cooper, *Quantum Oscillations without a Fermi Surface and the Anomalous de Haas–van Alphen Effect,* Phys. Rev. Lett. **115**, 146401 (2015).

[54] L. Zhang, X.-Y. Song, and F. Wang, *Quantum Oscillation in Narrow-Gap Topological Insulators,* Phys. Rev. Lett. **116**, 046404 (2016).

[55] B. S. Tan, Y. T. Hsu, B. Zeng, M. Ciomaga Hatnean, N. Harrison, Z. Zhu, M. Hartstein, M. Kiourlappou, A. Srivastava, M. D. Johannes, T. P. Murphy, J. H. Park, L. Balicas, G. G. Lonzarich, G. Balakrishnan, and S. E. Sebastian, *Unconventional Fermi surface in an insulating state,* Science **349**, 287 (2015).

[56] O. Erten, P. Ghaemi, and P. Coleman, *Kondo Breakdown and Quantum Oscillations in SmB6,* Phys. Rev. Lett. **116**, 046403 (2016).

[57] Y. Baum, J. Böttcher, C. Brüne, C. Thienel, L. W. Molenkamp, A. Stern, and E. M. Hankiewicz, *Self-consistent k·p calculations for gated thin layers of three-dimensional topological insulators,* Phys. Rev. B **89**, 245136 (2014).

[58] V. Müller, *Transport signatures of topological and trivial states in the three-dimensional topological insulator HgTe,* Ph.D. thesis, Universität Würzburg (to be published).

[59] C. R. Becker, C. Brüne, M. Schäfer, A. Roth, H. Buhmann, and L. W. Molenkamp, *The influence of interfaces and the modulation doping technique on the magneto-transport properties of HgTe based quantum wells,* Phys. status solidi **4**, 3382 (2007).

[60] F. Goschenhofer, J. Gerschütz, A. Pfeuffer-Jeschke, R. Hellmig, C. R. Becker, and G. Landwehr, *Investigation of iodine as a donor in MBE grown $Hg_{1-x}Cd_xTe$*, J. Electron. Mater. **27**, 532 (1998).

[61] M. K. Bendias, *Quantum Spin Hall Effect - A new generation of microstructures*, Ph.D. thesis, Universität Würzburg (2018).

[62] J. Dubowski, T. Dietl, W. Szymańska, and R. Gałazka, *Electron scattering in $Cd_xHg_{1-x}Te$*, J. Phys. Chem. Solids **42**, 351 (1981).

[63] C. W. Beenakker and H. van Houten, *Quantum Transport in Semiconductor Nanostructures*, Solid State Phys. - Adv. Res. Appl. **44**, 1 (1991).

[64] R. REIFENBERGER, *Magnetic Oscillations*, Science **227**, 1026 (1985).

[65] J. Chen, H. J. Qin, F. Yang, J. Liu, T. Guan, F. M. Qu, G. H. Zhang, J. R. Shi, X. C. Xie, C. L. Yang, K. H. Wu, Y. Q. Li, and L. Lu, *Gate-voltage control of chemical potential and weak antilocalization in Bi_2Se_3*, Phys. Rev. Lett. **105**, 176602 (2010).

[66] Y. V. Sharvin, *A possible method for studying Fermi surfaces*, Sov. Phys. JETP **21**, 655 (1965).

[67] B. Büttner, C. X. Liu, G. Tkachov, E. G. Novik, C. Brüne, H. Buhmann, E. M. Hankiewicz, P. Recher, B. Trauzettel, S. C. Zhang, and L. W. Molenkamp, *Single valley Dirac fermions in zero-gap HgTe quantum wells*, Nat. Phys. **7**, 418 (2011).

[68] C. Li, B. de Ronde, A. Nikitin, Y. Huang, M. S. Golden, A. de Visser, and A. Brinkman, *Interaction between counter-propagating quantum Hall edge channels in the 3D topological insulator $BiSbTeSe_2$*, Phys. Rev. B **96**, 195427 (2017).

[69] L. Wang, F. Schmitt, L. Lunczer, H. Buhmann, and L. W. Molenkamp, *Counterpropagating quantum Hall edge mode in Mn doped topological insulator $Hg_{1-x}Mn_xTe$*, to be published .

[70] K. Zolleis, C. Barnes, A. Davies, M. Simmons, D. Ritchie, and M. Pepper, *Onset of subband locking in double-quantum-well structures as the signature of wave function delocalization*, Phys. B Condens. Matter **249-251**, 850 (1998).

[71] J. Ziegler, D. A. Kozlov, N. N. Mikhailov, S. A. Dvoretsky, and D. Weiss, *Quantum Hall effect and Landau levels in the 3D topological insulator HgTe*, Phys. Rev. Res. **2**, 033003 (2020).

[72] C. H. W. Barnes, A. G. Davies, K. R. Zolleis, M. Y. Simmons, and D. A. Ritchie, *Intrinsic coupling mechanisms between two-dimensional electron systems in double quantum well structures*, Phys. Rev. B **59**, 7669 (1999).

[73] A. G. Davies, C. H. W. Barnes, K. R. Zolleis, J. T. Nicholls, M. Y. Simmons, and D. A. Ritchie, *Hybridization of single- and double-layer behavior in a double-quantum-well structure*, Phys. Rev. B **54**, R17331 (1996).

[74] A. Inhofer, S. Tchoumakov, B. A. Assaf, G. Fève, J. M. Berroir, V. Jouffrey, D. Carpentier, M. O. Goerbig, B. Plaçais, K. Bendias, D. M. Mahler, E. Bocquillon, R. Schlereth, C. Brüne, H. Buhmann, and L. W. Molenkamp, *Observation of Volkov-Pankratov states in topological HgTe heterojunctions using high-frequency compressibility,* Phys. Rev. B **96**, 195104 (2017).

[75] Jan Böttcher, *Anomalous Dirac Surface Screening versus Self-Consistent Hartree Band Structure Calculations for the 3D TI HgTe,* Master thesis, Universität Würzburg (2014).

[76] D. A. Kozlov, D. Bauer, J. Ziegler, R. Fischer, M. L. Savchenko, Z. D. Kvon, N. N. Mikhailov, S. A. Dvoretsky, and D. Weiss, *Probing Quantum Capacitance in a 3D Topological Insulator,* Phys. Rev. Lett. **116**, 166802 (2016).

[77] E. G. Novik, A. Pfeuffer-Jeschke, T. Jungwirth, V. Latussek, C. R. Becker, G. Landwehr, H. Buhmann, and L. W. Molenkamp, *Band structure of semimagnetic $Hg_{1-y}Mn_yTe$ quantum wells,* Phys. Rev. B **72** (2004).

[78] E. M. Hankiewicz, *personal communication,* (2019).

[79] D. M. Mahler, V. L. Müller, C. Thienel, J. Wiedenmann, W. Beugeling, H. Buhmann, and L. W. Molenkamp, *Massive and Topological Surface States in Tensile-Strained HgTe,* Nano Lett. **21**, 9869 (2021).

[80] P. Capper and J. Garland, *Mercury Cadmium Telluride: Growth, Properties and Applications* (Wiley Blackwell, 2010) pp. 1–556.

[81] M. I. D'yakonov and A. V. Khaetskiĭ, *Surface states in a gapless semiconductor,* Pis'ma Zh. Eksp. Teor. Fiz. **33**, 115 (1981).

[82] A. Inhofer, *Probing AC electronic compressibility of 3D HgTe and Bi_2Se_3 topological insulators at high electric fields: evidence for excited massive surface states,* Ph.D. thesis, Laboratoire Pierre Aigrain (2017).

[83] P. Shekhar, S. Shamim, S. Hartinger, J. Kleinlein, M. K. Bendias, R. Schlereth, H. Buhmann, and L. W. Molenkamp, *Room temperature atomic layer deposition of hafnium oxide for microelectronics application,* to be published .

[84] J. Robertson, *High dielectric constant oxides,* EPJ Appl. Phys. **28**, 265 (2004).

[85] J. Baars and F. Sorger, *Reststrahlen spectra of HgTe and $Cd_xHg_{1-x}Te$,* Solid State Commun. **10**, 875 (1972).

[86] E. Pallecchi, A. C. Betz, J. Chaste, G. Fève, B. Huard, T. Kontos, J.-M. Berroir, and B. Plaçais, *Transport scattering time probed through rf admittance of a graphene capacitor,* Phys. Rev. B **83**, 125408 (2011).

[87] A. M. Shuvaev, G. V. Astakhov, G. Tkachov, C. Brüne, H. Buhmann, L. W. Molenkamp, and A. Pimenov, *Terahertz quantum Hall effect of Dirac fermions in a topological insulator,* Phys. Rev. B **87**, 121104 (2013).

[88] J. N. Hancock, J. L. M. van Mechelen, A. B. Kuzmenko, D. van der Marel, C. Brüne, E. G. Novik, G. V. Astakhov, H. Buhmann, and L. W. Molenkamp, *Surface State Charge Dynamics of a High-Mobility Three-Dimensional Topological Insulator,* Phys. Rev. Lett. **107**, 149903 (2011).

[89] J. Hinz, H. Buhmann, M. Schäfer, V. Hock, C. R. Becker, and L. W. Molenkamp, *Gate control of the giant Rashba effect in HgTe quantum wells,* Semicond. Sci. Technol. **21**, 501 (2006).

[90] T. Ihn, *Semiconductor Nanostructures: Quantum States and Electronic Transport* (Oxford University Press, 2010) pp. 1–568.

[91] P. Stein, *Ladungsträger Kontrolle im Drei-Dimensionalen topologischen Isolator HgTe,* Bachelor thesis, Universität Würzburg (2017).

[92] L. Fu, C. L. Kane, and E. J. Mele, *Topological Insulators in Three Dimensions,* Phys. Rev. Lett. **98**, 106803 (2007).

[93] R. Yoshimi, A. Tsukazaki, Y. Kozuka, J. Falson, K. S. Takahashi, J. G. Checkelsky, N. Nagaosa, M. Kawasaki, and Y. Tokura, *Quantum Hall effect on top and bottom surface states of topological insulator ($Bi_{1−x}Sb_x$)Te_3 films,* Nat. Commun. **6** (2015).

[94] E. Bocquillon, R. S. Deacon, J. Wiedenmann, P. Leubner, T. M. Klapwijk, C. Brüne, K. Ishibashi, H. Buhmann, and L. W. Molenkamp, *Gapless Andreev bound states in the quantum spin Hall insulator HgTe,* Nat. Nanotechnol. **12**, 137 (2017).

[95] G. Santos, *Spin-Orbit Torques and Galvanomagnetic Effects Generated by the 3D Topological Insulator HgTe,* Ph.D. thesis, Universität Würzburg (to be published).

[96] B. Yan and C. Felser, *Topological Materials: Weyl Semimetals,* Annu. Rev. Condens. Matter Phys. **8**, 337 (2017).

[97] A. Bernevig, H. Weng, Z. Fang, and X. Dai, *Recent progress in the study of topological semimetals,* (2018).

[98] Z. Wang, M. G. Vergniory, S. Kushwaha, M. Hirschberger, E. V. Chulkov, A. Ernst, N. P. Ong, R. J. Cava, and B. A. Bernevig, *Time-Reversal-Breaking Weyl Fermions in Magnetic Heusler Alloys,* Phys. Rev. Lett. **117**, 236401 (2016).

[99] H. Weng, C. Fang, Z. Fang, B. A. Bernevig, and X. Dai, *Weyl Semimetal Phase in Noncentrosymmetric Transition-Metal Monophosphides,* Phys. Rev. X **5**, 011029 (2015).

[100] B. Q. Lv, H. M. Weng, B. B. Fu, X. P. Wang, H. Miao, J. Ma, P. Richard, X. C. Huang, L. X. Zhao, G. F. Chen, Z. Fang, X. Dai, T. Qian, and H. Ding, *Experimental Discovery of Weyl Semimetal TaAs,* Phys. Rev. X **5**, 031013 (2015).

[101] H. Nielsen and M. Ninomiya, *The Adler-Bell-Jackiw anomaly and Weyl fermions in a crystal,* Phys. Lett. B **130**, 389 (1983).

[102] K. Yoshida, *Transport of spatially inhomogeneous current in a compensated metal under magnetic fields. II. Dynamical properties of the current system,* J. Appl. Phys. **50**, 4166 (1979).

[103] F. Arnold, D. Sokolov, M. O. Ajeesh, S.-C. Wu, C. Shekhar, E. Hassinger, N. Kumar, B. Yan, M. Naumann, R. D. dos Reis, C. Felser, H. Borrmann, A. G. Grushin, M. Baenitz, M. Schmidt, M. Nicklas, J. H. Bardarson, and Y. Sun, *Negative magnetoresistance without well-defined chirality in the Weyl semimetal TaP,* Nat. Commun. **7**, 11615 (2016).

[104] R. D. Reis, M. O. Ajeesh, N. Kumar, F. Arnold, C. Shekhar, M. Naumann, M. Schmidt, M. Nicklas, and E. Hassinger, *On the search for the chiral anomaly in Weyl semimetals: The negative longitudinal magnetoresistance,* New J. Phys. **18**, 085006 (2016).

[105] H. J. Kim, K. S. Kim, J. F. Wang, M. Sasaki, N. Satoh, A. Ohnishi, M. Kitaura, M. Yang, and L. Li, *Dirac versus weyl fermions in topological insulators: Adler-Bell-Jackiw anomaly in transport phenomena,* Phys. Rev. Lett. **111** (2013).

[106] Q. Li, D. E. Kharzeev, C. Zhang, Y. Huang, I. Pletikosić, A. V. Fedorov, R. D. Zhong, J. A. Schneeloch, G. D. Gu, and T. Valla, *Chiral magnetic effect in ZrTe$_5$,* Nat. Phys. **12**, 550 (2016).

[107] I. Crassee, R. Sankar, W. L. Lee, A. Akrap, and M. Orlita, *3D Dirac semimetal Cd$_3$As$_2$: A review of material properties,* Phys. Rev. Mater. **2**, 120302 (2018).

[108] Z. Wang, Y. Sun, X. Q. Chen, C. Franchini, G. Xu, H. Weng, X. Dai, and Z. Fang, *Dirac semimetal and topological phase transitions in A$_3$Bi(A=Na, K, Rb),* Phys. Rev. B **85**, 195320 (2012).

[109] J. Bodnar, *Band structure of Cd$_3$As$_2$ from Shubnikov - de Haas and de Haas - van Alphen effects,* (2017), arXiv:1709.05845 .

[110] M. Hakl, S. Tchoumakov, I. Crassee, A. Akrap, B. A. Piot, C. Faugeras, G. Martinez, A. Nateprov, E. Arushanov, F. Teppe, R. Sankar, W.-l. Lee, J. Debray, O. Caha, J. Novák, M. O. Goerbig, M. Potemski, and M. Orlita, *Energy scale of Dirac electrons in Cd$_3$As$_2$,* Phys. Rev. B **97**, 115206 (2018).

[111] M. Neupane, S.-Y. Xu, R. Sankar, N. Alidoust, G. Bian, C. Liu, I. Belopolski, T.-R. Chang, H.-T. Jeng, H. Lin, A. Bansil, F. Chou, and M. Z. Hasan, *Observation of a three-dimensional topological Dirac semimetal phase in high-mobility Cd$_3$As$_2$,* Nat. Commun. **5**, 3786 (2014).

[112] S. K. Kushwaha, J. W. Krizan, B. E. Feldman, A. Gyenis, M. T. Randeria, J. Xiong, S. Y. Xu, N. Alidoust, I. Belopolski, T. Liang, M. Zahid Hasan, N. P. Ong, A. Yazdani, and R. J. Cava, *Bulk crystal growth and electronic characterization of the 3D Dirac semimetal Na$_3$Bi,* APL Mater. **3**, 041504 (2015).

[113] Z. K. Liu, B. Zhou, Y. Zhang, Z. J. Wang, H. M. Weng, D. Prabhakaran, S.-K. Mo, Z. X. Shen, Z. Fang, X. Dai, Z. Hussain, and Y. L. Chen, *Discovery of a three-dimensional topological dirac semimetal, Na$_3$Bi,* Science **343**, 864 (2014).

[114] J. Xiong, S. K. Kushwaha, T. Liang, J. W. Krizan, M. Hirschberger, W. Wang, R. J. Cava, and N. P. Ong, *Evidence for the chiral anomaly in the Dirac semimetal Na$_3$Bi,* Science **350**, 413 (2015).

[115] T. Khouri, U. Zeitler, C. Reichl, W. Wegscheider, N. E. Hussey, S. Wiedmann, and J. C. Maan, *Linear Magnetoresistance in a Quasifree Two-Dimensional Electron Gas in an Ultrahigh Mobility GaAs Quantum Well,* Phys. Rev. Lett. **117**, 256601 (2016).

[116] T. Schumann, M. Goyal, D. A. Kealhofer, and S. Stemmer, *Negative magnetoresistance due to conductivity fluctuations in films of the topological semimetal Cd_3As_2,* Phys. Rev. B **95**, 241113 (2017).

[117] Pippard, Alfred Brian and A. B. Pippard, *Magnetoresistance in Metals* (Cambridge University Press, 2009).

[118] T. Liang, Q. Gibson, M. N. Ali, M. Liu, R. J. Cava, and N. P. Ong, *Ultrahigh mobility and giant magnetoresistance in the Dirac semimetal Cd_3As_2,* Nat. Mater. **14**, 280 (2015).

[119] A. A. Abrikosov, *Quantum magnetoresistance,* Phys. Rev. B **58**, 2788 (1998).

[120] H. Weiss and H. Welker, *Zur transversalen magnetischen Widerstandsänderung von InSb,* Zeitschrift für Phys. **138**, 322 (1954).

[121] P. S. Alekseev, A. P. Dmitriev, I. V. Gornyi, V. Y. Kachorovskii, B. N. Narozhny, M. Schütt, and M. Titov, *Magnetoresistance in two-component systems,* Phys. Rev. Lett. **114**, 156601 (2015).

[122] A. Chang and D. Tsui, *Experimental observation of a striking similarity between quantum hall transport coefficients,* Solid State Commun. **56**, 153 (1985).

[123] S. H. Simon and B. I. Halperin, *Explanation for the Resistivity Law in Quantum Hall Systems,* Phys. Rev. Lett. **73**, 3278 (1994).

[124] N. Kozlova, N. Mori, O. Makarovsky, L. Eaves, Q. Zhuang, A. Krier, and A. Patanè, *Linear magnetoresistance due to multiple-electron scattering by low-mobility islands in an inhomogeneous conductor,* Nat. Commun. **3**, 1097 (2012).

[125] P. Hosur and X. Qi, *Recent developments in transport phenomena in Weyl semimetals,* Comptes Rendus Phys. **14**, 857 (2013).

[126] A. Burkov, *Weyl Metals,* Annu. Rev. Condens. Matter Phys. **9**, 359 (2018).

[127] A. A. Burkov, *Negative longitudinal magnetoresistance in Dirac and Weyl metals,* Phys. Rev. B **91**, 245157 (2015).

[128] A. A. Zyuzin and A. A. Burkov, *Topological response in Weyl semimetals and the chiral anomaly,* Phys. Rev. B **86**, 115133 (2012).

[129] D. T. Son and B. Z. Spivak, *Chiral anomaly and classical negative magnetoresistance of Weyl metals,* Phys. Rev. B **88**, 104412 (2013).

[130] P. Leubner, L. Lunczer, C. Brüne, H. Buhmann, and L. W. Molenkamp, *Strain Engineering of the Band Gap of HgTe Quantum Wells Using Superlattice Virtual Substrates,* Phys. Rev. Lett. **117**, 086403 (2016).

[131] K. Takita and G. Landwehr, *Very Large Phonon-Drag Thermoelectric Power of HgTe in Strong Magnetic Fields,* Phys. status solidi **106**, 259 (1981).

[132] S. Hikami, A. I. Larkin, and Y. Nagaoka, *Spin-Orbit Interaction and Magnetoresistance in the Two Dimensional Random System,* Prog. Theor. Phys. **63**, 707 (1980).

[133] B. Zhao, P. Cheng, H. Pan, S. Zhang, B. Wang, G. Wang, F. Xiu, and F. Song, *Weak antilocalization in Cd_3As_2 thin films,* Sci. Rep. **6**, 22377 (2016).

[134] J. Hellerstedt, M. T. Edmonds, N. Ramakrishnan, C. Liu, B. Weber, A. Tadich, K. M. O'Donnell, S. Adam, and M. S. Fuhrer, *Electronic Properties of High-Quality Epitaxial Topological Dirac Semimetal Thin Films,* Nano Lett. **16**, 3210 (2016).

[135] C.-L. Zhang, S.-Y. Xu, I. Belopolski, Z. Yuan, Z. Lin, B. Tong, G. Bian, N. Alidoust, C.-C. Lee, S.-M. Huang, T.-R. Chang, G. Chang, C.-H. Hsu, H.-T. Jeng, M. Neupane, D. S. Sanchez, H. Zheng, J. Wang, H. Lin, C. Zhang, H.-Z. Lu, S.-Q. Shen, T. Neupert, M. Zahid Hasan, and S. Jia, *Signatures of the Adler–Bell–Jackiw chiral anomaly in a Weyl fermion semimetal,* Nat. Commun. **7**, 10735 (2016).

[136] H.-Z. Lu and S.-Q. Shen, *Weak antilocalization and localization in disordered and interacting Weyl semimetals,* Phys. Rev. B **92**, 035203 (2015).

[137] F. D. M. Haldane, *Attachment of Surface "Fermi Arcs" to the Bulk Fermi Surface: "Fermi-Level Plumbing" in Topological Metals,* (2014), arXiv:1401.0529 .

[138] L. Galletti, T. Schumann, D. A. Kealhofer, M. Goyal, and S. Stemmer, *Absence of signatures of Weyl orbits in the thickness dependence of quantum transport in cadmium arsenide,* Phys. Rev. B **99**, 201401 (2019).

[139] P. Goswami, J. H. Pixley, and S. Das Sarma, *Axial anomaly and longitudinal magnetoresistance of a generic three-dimensional metal,* Phys. Rev. B **92**, 075205 (2015).

[140] J. Cano, B. Bradlyn, Z. Wang, M. Hirschberger, N. P. Ong, and B. A. Bernevig, *Chiral anomaly factory: Creating Weyl fermions with a magnetic field,* Phys. Rev. B **95**, 161306 (2017).

[141] G. Bergmann, *Weak anti-localization—An experimental proof for the destructive interference of rotated spin 1/2,* Solid State Commun. **42**, 815 (1982).

[142] M. Mühlbauer, A. Budewitz, B. Büttner, G. Tkachov, E. M. Hankiewicz, C. Brüne, H. Buhmann, and L. W. Molenkamp, *One-dimensional weak antilocalization due to the berry phase in hgTe wires,* Phys. Rev. Lett. **112** (2014).

[143] W. E. Liu, E. M. Hankiewicz, and D. Culcer, *Quantum transport in Weyl semimetal thin films in the presence of spin-orbit coupled impurities,* Phys. Rev. B **96**, 045307 (2017).

[144] M. Stuiber, *Dreidimensionale Topologische Isolatoren,* Master thesis, Universität Würzburg (2011).

[145] T. McGuire and R. Potter, *Anisotropic magnetoresistance in ferromagnetic 3d alloys,* IEEE Trans. Magn. **11**, 1018 (1975).

[146] M. Baussenwein, *Symmetry breaking in the planar anisotropic magnetoresistance of NiMnSb,* Ph.D. thesis, Universität Würzburg (to be published).

[147] A. A. Burkov, *Giant planar Hall effect in topological metals,* Phys. Rev. B **96**, 041110 (2017).

[148] T. Louvet, M. Houzet, and D. Carpentier, *Signature of the Chiral Anomaly in Ballistic Magneto-Transport,* (2017), arXiv:1711.06657 .

[149] M. Shayegan, V. Goldman, H. Drew, N. Fortune, and J. Brooks, *Magnetic-field induced metal-insulator transition in InSb and $Hg_{0.79}Cd_{0.21}Te$ at very low temperatures,* Solid State Commun. **60**, 817 (1986).

[150] S. J. Papadakis, E. P. De Poortere, M. Shayegan, and R. Winkler, *Anisotropic Magnetoresistance of Two-Dimensional Holes in GaAs,* Phys. Rev. Lett. **84**, 5592 (2000).

[151] F. Schmidt, *Transporteigenschaften von druck- und zugverspannten HgTe-Epi-Schichten,* Master thesis, Universität Würzburg, Würzburg (2016).

[152] J. Jo, E. A. Garcia, K. M. Abkemeier, M. B. Santos, and M. Shayegan, *Probing the subband structure of a wide electron system in a parabolic quantum well via capacitance-voltage measurements,* Phys. Rev. B **47**, 4056 (1993).

[153] D. Weiss, K. V. Klitzing, K. Ploog, and G. Weimann, *Magnetoresistance Oscillations in a Two-Dimensional Electron Gas Induced by a Submicrometer Periodic Potential,* Europhys. Lett. **8**, 179 (1989).

[154] S. S. Pershoguba and V. M. Yakovenko, *Spin-polarized tunneling current through a thin film of a topological insulator in a parallel magnetic field,* Phys. Rev. B **86**, 165404 (2012).

[155] Stanford Research Systems, *Digital Lock-In Amplifiers: SR810 and SR830, Analog Lock-In Amplifiers SR124 and SR2124 — Analog lock-in amplifiers,* .

[156] J. Ruan, S.-K. Jian, H. Yao, H. Zhang, S.-C. Zhang, and D. Xing, *Symmetry-protected ideal Weyl semimetal in HgTe-class materials,* Nat. Commun. **7**, 11136 (2016).

[157] J.-B. Mayer, *Note on Landau in Weyl HgTe with Pankratov states,* (2018).

[158] D. Tong, *Lectures on the Quantum Hall Effect,* (2016), arXiv:1606.06687 .

[159] A. C. Potter, I. Kimchi, and A. Vishwanath, *Quantum oscillations from surface Fermi arcs in Weyl and Dirac semimetals,* Nat. Commun. **5**, 5161 (2014).

[160] P. J. W. Moll, N. L. Nair, T. Helm, A. C. Potter, I. Kimchi, A. Vishwanath, and J. G. Analytis, *Transport evidence for Fermi-arc-mediated chirality transfer in the Dirac semimetal Cd_3As_2,* Nature **535**, 266 (2016).

[161] C. M. Wang, H. P. Sun, H. Z. Lu, and X. C. Xie, *3D Quantum Hall Effect of Fermi Arc in Topological Semimetals*, Phys. Rev. Lett. **119**, 136806 (2017).

[162] Y. Zhao, H. Liu, C. Zhang, H. Wang, J. Wang, Z. Lin, Y. Xing, H. Lu, J. Liu, Y. Wang, S. M. Brombosz, Z. Xiao, S. Jia, X. C. Xie, and J. Wang, *Anisotropic Fermi Surface and Quantum Limit Transport in High Mobility Three-Dimensional Dirac Semimetal Cd$_3$As$_2$*, Phys. Rev. X **5**, 031037 (2015).

[163] C. Zhang, A. Narayan, S. Lu, J. Zhang, H. Zhang, Z. Ni, X. Yuan, Y. Liu, J.-H. Park, E. Zhang, W. Wang, S. Liu, L. Cheng, L. Pi, Z. Sheng, S. Sanvito, and F. Xiu, *Evolution of Weyl orbit and quantum Hall effect in Dirac semimetal Cd$_3$As$_2$*, Nat. Commun. **8**, 1272 (2017).

[164] C. Zhang, Y. Zhang, X. Yuan, S. Lu, J. Zhang, A. Narayan, Y. Liu, H. Zhang, Z. Ni, R. Liu, E. S. Choi, A. Suslov, S. Sanvito, L. Pi, H.-Z. Lu, A. C. Potter, and F. Xiu, *Quantum Hall effect based on Weyl orbits in Cd$_3$As$_2$*, Nature **565**, 331 (2019).

[165] Z. Wang, H. Weng, Q. Wu, X. Dai, and Z. Fang, *Three-dimensional Dirac semimetal and quantum transport in Cd$_3$As$_2$*, Phys. Rev. B **88**, 125427 (2013).

[166] C.-X. Liu, X.-L. Qi, H. Zhang, X. Dai, Z. Fang, and S.-C. Zhang, *Model Hamiltonian for topological insulators*, Phys. Rev. B **82**, 045122 (2010).

[167] M. Kargarian, M. Randeria, and Y.-M. Lu, *Are the surface Fermi arcs in Dirac semimetals topologically protected?* Proc. Natl. Acad. Sci. **113**, 8648 (2016).

[168] M. Kargarian, Y. M. Lu, and M. Randeria, *Deformation and stability of surface states in Dirac semimetals*, Phys. Rev. B **97**, 165129 (2018).

[169] J.-B. Mayer, *Topological insulators and semimetals within 4-band Luttinger model*, Master thesis, Universität Würzburg (2017).

[170] X. Liu, G. Liu, Y. Feng, J. He, C. Chen, K. Shimada, J. Zhang, S. He, H. Namatame, L. Zhao, Z. Fang, Z. Wang, M. Taniguchi, Y. Peng, M. Nakatake, Y. Liu, C. Chen, Z. Xie, X. Dai, H. Yi, X. J. Zhou, Y. Shi, X. Dong, M. Arita, Z. Xu, and A. Liang, *Evidence of Topological Surface State in Three-Dimensional Dirac Semimetal Cd$_3$As$_2$*, Sci. Rep. **4**, 6106 (2014).

[171] S. Roth, H. Lee, A. Sterzi, M. Zacchigna, A. Politano, R. Sankar, F. C. Chou, G. Di Santo, L. Petaccia, O. V. Yazyev, and A. Crepaldi, *Reinvestigating the surface and bulk electronic properties of Cd 3 As 2*, Phys. Rev. B **97**, 165439 (2018).

[172] B. C. Lin, S. Wang, S. Wiedmann, J. M. Lu, W. Z. Zheng, D. Yu, and Z. M. Liao, *Observation of an Odd-Integer Quantum Hall Effect from Topological Surface States in Cd$_3$As$_2$*, Phys. Rev. Lett. **122** (2019).

[173] S. Adam, E. H. Hwang, and S. Das Sarma, *Two-dimensional transport and screening in topological insulator surface states*, Phys. Rev. B **85**, 235413 (2012).

[174] O. Corporation, *Origin(Pro)*, (2020).

[175] I. Wolfram Research, *Mathematica,* (2020).

[176] M. Frigo and S. G. Johnson, *FFTW: An adaptive software architecture for the FFT,* in *ICASSP, IEEE Int. Conf. Acoust. Speech Signal Process. - Proc.,* Vol. 3 (1998) pp. 1381–1384.

[177] J. O. Smith, *Cent. Comput. Res. Music Acoust.* (2011) pp. 1–674.